GDAŃSK UNIVERSITY OF TECHNOLOGY

The author of the doctoral dissertation: **Daniel Paweł Jaworski**
Scientific discipline: **Materials engineering**

DOCTORAL DISSERTATION

Title of doctoral dissertation: **Structure, microstructure and electrical properties of high-entropy perovskite oxides exhibiting proton conductivity**

Title of doctoral dissertation (in Polish): **Struktura, mikrostruktura oraz właściwości elektryczne wysokoentropowych tlenków perowskitowych wykazujących przewodnictwo protonowe**

Supervisor *signature*
Prof. Ph.D., D.Sc., Eng. Maria Gazda
Auxiliary supervisor *signature*
Ph.D., Eng. Tadeusz Miruszewski

Gdańsk, year 2025

POLITECHNIKA GDAŃSKA

STATEMENT

The author of the doctoral dissertation: **Daniel Paweł Jaworski**

I, the undersigned, declare that I am aware that in accordance with the provisions of Art. 27 (1) and (2) of the Act of 4th February 1994 on Copyright and Related Rights (Journal of Laws of 2021, item 1062), the university may use my doctoral dissertation entitled:
"**Structure, microstructure and electrical properties of high-entropy perovskite oxides exhibiting proton conductivity"**
for scientific or didactic purposes.[1]

Gdańsk, 27.01.2025 .....
signature of the PhD student

Aware of criminal liability for violations of the Act of 4th February 1994 on Copyright and Related Rights and disciplinary actions set out in the Law on Higher Education and Science(Journal of Laws 2021, item 478), as well as civil liability, I declare, that the submitted doctoral dissertation is my own work.

I declare, that the submitted doctoral dissertation is my own work performed under and in cooperation with the supervision of Prof. Ph.D., D.Sc., Eng. Maria Gazda and the auxiliary supervision of Ph.D., Eng. Tadeusz Miruszewski.

This submitted doctoral dissertation has never before been the basis of an official procedure associated with the awarding of a PhD degree.

All the information contained in the above thesis which is derived from written and electronic sources is documented in a list of relevant literature in accordance with Art. 34 of the Copyright and Related Rights Act.

I confirm that this doctoral dissertation is identical to the attached electronic version.

Gdańsk, 27.01.2025 .....
signature of the PhD student

I, the undersigned, agree to include an electronic version of the above doctoral dissertation in the open, institutional, digital repository of Gdańsk University of Technology.

Gdańsk, 27.01.2025 .....
signature of the PhD student

[1] Art 27. 1. Educational institutions and entities referred to in art. 7 sec. 1 points 1, 2 and 4–8 of the Act of 20 July 2018 – Law on Higher Education and Science, may use the disseminated works in the original and in translation for the purposes of illustrating the content provided for didactic purposes or in order to conduct research activities, and to reproduce for this purpose disseminated minor works or fragments of larger works.

2. If the works are made available to the public in such a way that everyone can have access to them at the place and time selected by them, as referred to in para. 1, is allowed only for a limited group of people learning, teaching or conducting research, identified by the entities listed in paragraph 1.

GDAŃSK UNIVERSITY OF TECHNOLOGY

DESCRIPTION OF DOCTORAL DISSERTATION

The Author of the doctoral dissertation: Daniel Paweł Jaworski

Title of doctoral dissertation: Structure, microstructure and electrical properties of high-entropy perovskite oxides exhibiting proton conductivity

Title of doctoral dissertation in Polish: Struktura, mikrostruktura oraz właściwości elektryczne wysokoentropowych tlenków perowskitowych wykazujących przewodnictwo protonowe

Language of doctoral dissertation: English

Supervisor: Prof. Ph.D., D.Sc., Eng. Maria Gazda

Auxiliary supervisor: Ph.D., Eng. Tadeusz Miruszewski

Date of doctoral defense:

Keywords of doctoral dissertation in Polish: przewodnictwo protonowe, tlenki wysokoentropowe, uwodnienie, struktura perowskitu, synteza w fazie stałej,

Keywords of doctoral dissertation in English: proton conductivity, high-entropy oxides, hydration, perovskite structure, solid state synthesis,

Summary of doctoral dissertation in Polish:

Obszerna baza różnych pierwiastków i nieporządek obecne w wieloskładnikowych materiałach wysokoentropowych mogą wpływać m.in. na koncentrację, czy ruchliwość nośników ładunku. Co więcej, przewodnictwo protonowe w tlenkach wieloskładnikowych wykazujących wysoką entropię jest interesującą i słabo poznaną właściwością.

Celem niniejszej pracy była synteza wieloskładnikowych tlenków na bazie cyrkonianu baru o strukturze perowskitu i określenie szeregu właściwości fizykochemicznych tych związków. Tlenki te wytworzono metodą syntezy w fazie stałej i scharakteryzowano przy użyciu m. in. dyfrakcji rentgenowskiej, dylatometrii, rentgenowskiej spektroskopii absorpcyjnej, obrazowania skaningowym mikroskopem elektronowym, termograwimetrii, kalorymetrii typu drop-solution, elektrochemicznej spektroskopii impedancyjnej oraz relaksacji przewodnictwa elektrycznego.

Wszystkie otrzymane materiały wykazywały regularną strukturę perowskitu o grupie $Pm\bar{3}m$. Mimo, że uwadniały się w atmosferze bogatej w parę wodną, to koncentracje protonów były o wiele niższe od tych obserwowanych w znanych przewodnikach protonowych na bazie ceranów-cyrkonianów baru. Ponadto, pomiary właściwości elektrycznych wykazały niższą przewodność elektryczną od podstawianych itrem ceranów-cyrkonianów baru, z dużym wkładem granic międzyziarnowych do oporu elektrycznego próbek.

Summary of doctoral dissertation in English:

The extensive base of various elements and disorder present in multi-component high-entropy materials can influence, among other things, the concentration and mobility of charge carriers. Moreover, proton conductivity in multi-component oxides exhibiting high entropy is an interesting and poorly understood property.

This work aimed to synthesize multi-component oxides based on barium zirconate with a perovskite structure and determine a range of physicochemical properties of these compounds. These oxides were synthesized by the solid-state synthesis method and characterized using various techniques, including X-ray diffraction, dilatometry, X-ray absorption spectroscopy, scanning electron microscopy, thermogravimetry, drop-solution calorimetry, electrochemical impedance spectroscopy, and electrical conductivity relaxation.

All obtained materials exhibited a regular perovskite structure with the $Pm\bar{3}m$ space group. Although they hydrated in a steam-rich atmosphere, the proton concentrations were much lower than those observed in well-known proton conductors based on barium cerate-zirconates. Moreover, electrical property measurements revealed lower electrical conductivity than in yttrium-doped barium cerate-zirconates, with a significant contribution from grain boundaries to the electrical resistance of the samples.

Rodzicom

Acknowledgments

Na wstępie chciałbym podziękować moim promotorom, bez których ta praca by nie powstała: profesor Marii Gaździe oraz doktorowi Tadeuszowi Miruszewskiemu. Pani profesor dziękuję szczególnie za merytoryczne wsparcie i cierpliwość okazywaną na każdym kroku wspólnej pracy. Natomiast Tadeuszowi za przekazanie mi swojej filozofii bycia naukowcem, bycie ogromnym źródłem pomysłów oraz motorem do działania.

Ogromny merytoryczny wkład w napisanie tej pracy mieli również profesor Truls Norby oraz doktor Amir Masoud Dayaghi. Dziękuję im za możliwość odwiedzenia Uniwersytetu w Oslo i rozwój pod ich okiem w kontekście prowadzenia oraz analizowania pomiarów elektrycznych materiałów ceramicznych.

Chciałbym również podziękować członkom Zakładu Ceramiki oraz Instytutu Nanotechnologii i Inżynierii Materiałowej, którzy mieli swój wkład w powstanie tej pracy, w szczególności doktorowi Sebastianowi Wachowskiemu, doktorowi Wojciechowi Skubidzie, doktorowi Piotrowi Winiarzowi oraz doktorowi Kacprowi Dzierzgowskiemu za współpracę w laboratorium i chęć dzielenia się swoją wiedzą.

Za pozytywną atmosferę pracy i czas wspólnie spędzony w laboratorium dziękuję Jagodzie Budnik, Joannie Pośpiech, Kasi Wiciak-Pawłowskiej oraz Marcie Prześniak-Welenc.

Dziękuję również studentom, których miałem okazję spotkać, uczyć i wspierać w czasie pisania swoich prac dyplomowych. Szczególne podziękowania kieruję do Sandry Szczupaczyńskiej-Zalewskiej i Dominiki Krzyszczyk za rozwijającą współpracę naukową oraz całej ekipie Stowarzyszenia Umarłych Piromanów, z którymi miałem przyjemność podzielenia się swoją pasją do materiałów wysokoenergetycznych i współpracowania w przerwach od pracy nad doktoratem.

Nie jestem w stanie też w pełni ocenić wsparcia jakie uzyskałem od znajomych i przyjaciół, którzy pomagali mi nie zwariować od natłoku obowiązków i zdobywanej wiedzy. Szczególnie dziękuję Bognie Stormie, Krzysztofowi Hope oraz Damianowi Koszelowowi, za wsparcie mentalne, udzielane mi już od początku studiów na Politechnice Gdańskiej.

Na koniec chciałbym podziękować rodzinie za wiarę we mnie i moje możliwości, zwłaszcza rodzicom, którzy otoczyli mnie troską i zadbali o mój rozwój od najmłodszych lat. Dziękuję również mojej dziewczynie Oli, za ciepło i towarzyszenie mi przy końcu tej przygody.

This research has been supported by the National Science Centre Poland under the OPUS scheme “High-entropy oxides for energy conversion” (ref. no 2019/35/B/ST5/00888). The authors acknowledge the CERIC-ERIC Consortium for the access to experimental facilities. We acknowledge European Synchrotron Radiation Facility for providing access to its synchrotron radiation facilities and we thank Francesco D’Acapito for assistance in using LISA beamline (proposal no. 20227122).

TABLE OF CONTENTS

Abstract 13

Streszczenie 15

Abbreviations and Symbols 17

1. Introduction and aim of this work 22

2. High-entropy materials 23

2.1 High-entropy alloys 23

2.2 High-entropy oxides 26

2.2.1 Rock-salt structure 26

2.2.2 Fluorite structure 27

2.2.3 Spinel structure 28

2.2.4 Perovskite structure 29

2.2.5 Other crystal structures 30

2.3 Determination of configurational entropy 32

3. Electrical transport in oxides 34

3.1 Mechanisms of charge transport in conducting oxides 34

3.2 Proton conduction 35

4. Perovskite oxides 38

4.1 General information 38

4.2 Selected properties of $Ba(Ce,Zr)O_3$ proton conductors 40

5. Experimental procedures 43

5.1 Solid-state synthesis 43

5.2 X-Ray Diffraction 43

5.3 Dilatometry 44

5.4 X-Ray Absorption Spectroscopy 45

5.5 Scanning electron microscopy 47

5.6 Thermal analysis 47

5.7 Electrical measurements 50

6. Results and discussion 54

6.1 Solid state synthesis 54

6.2 X-Ray Diffraction 55

6.2.1 Phase analysis 55
6.2.2 High Temperature X-ray Diffraction 59
6.3 Dilatometry 62
6.4 X-Ray Absorption Spectroscopy 64
6.4.1 XANES 64
6.4.2 EXAFS 72
6.5 Scanning Electron Microscopy 75
6.5.1 Morphology 76
6.5.2 Energy Dispersive X-ray Spectroscopy 79
6.6 Thermal analysis 87
6.6.1 Isothermal thermogravimetry 87
6.6.2 Isobaric thermogravimetry 88
6.6.3 High-temperature drop calorimetry 92
6.7 Electrical measurements 94
6.7.1 Electrical conductivity in dry conditions 95
6.7.2 Electrical conductivity in wet conditions and isotope effect 98
6.7.3 Grain and grain boundary specific electrical conductivity 102
6.7.4 Electrical conductivity – oxygen and water vapor partial pressure dependence . 107
6.7.5 Electrical conductivity relaxation 110
6.7.5.1 Oxygen Diffusion 110
6.7.5.2 Water Diffusion 111
7. Conclusions 113
8. List of figures 116
9. List of tables 120
Bibliography 121

ABSTRACT

With the beginning of the 21st century, a new family of materials known as high-entropy alloys emerged. They exhibit properties not previously observed in conventional alloys, such as high hardness and corrosion resistance. Over time, research began to investigate more and more materials exhibiting high configurational entropy, including nitrides, carbides, and oxides. The first high-entropy oxide with the chemical formula $Mg_{0.2}Ni_{0.2}Co_{0.2}Cu_{0.2}Zn_{0.2}O$ was described less than ten years ago. The extensive base of various elements and disorder present in multi-component high-entropy materials can influence, among other things, the concentration and mobility of charge carriers. In the current era of energy transformation, significant work is being conducted on materials exhibiting proton conductivity, related to the transport of proton defects in the material's structure. Moreover, proton conductivity in multi-component oxides exhibiting high entropy is an interesting and poorly understood property.

This work aimed to synthesize multi-component oxides based on barium zirconate with a perovskite structure and determine a range of physicochemical properties of these compounds. Special emphasis was placed on investigating proton conductivity. An important variable in the synthesized samples was the concentration of oxygen vacancies resulting from the different amounts of acceptor dopants, ranging from 20% to 60% molar. The base cations in the B sublattice were zirconium, hafnium, tin, and titanium. The dopants included yttrium, ytterbium, samarium, indium, cerium, and zinc. These oxides were synthesized by the solid-state synthesis method and characterized using various techniques, including X-ray diffraction, dilatometry, X-ray absorption spectroscopy, scanning electron microscopy, thermogravimetry, drop-solution calorimetry, electrochemical impedance spectroscopy, and electrical conductivity relaxation. A major focus was placed on analyzing thermodynamic hydration parameters and determining partial electrical conductivities.

All obtained materials exhibited a regular perovskite structure with the $Pm\bar{3}m$ space group, with the lattice parameter linearly dependent on the average ionic radius of the dopants. The thermal expansion coefficients determined by various methods were similar to values reported in the literature for acceptor-doped barium cerate-zirconates. Measurements of absorption edges of different metals showed a low degree of octahedral distortion, except for the titanium K-edge, where a significant influence of oxygen vacancies around the cation on the absorption properties was observed. Based on scanning electron microscope images, large, well-sintered grains were observed in samples containing 10 or 8 elements in the B sublattice. However, samples containing only 5 elements in the B sublattice required the addition of a sintering aid in the form of nickel oxide to form large grains with few pores between them. Although all samples hydrated in a steam-rich atmosphere, the proton concentrations were much lower than those observed in well-known proton conductors based on barium cerate-zirconates. Drop solution calorimetry studies showed that the examined multi-component oxides were not entropy-stabilized. Electrical property measurements revealed lower electrical conductivity than in yttrium-doped barium cerate-zirconates, with a significant contribution from grain boundaries to the electrical resistance of the samples. On the

other hand, kinetic parameters of oxygen diffusion, such as the chemical diffusion coefficient and surface exchange rate, were significantly higher in selected multi-component oxide compared to values published for acceptor-doped barium cerate-zirconates. It is worth noting that all the oxides studied in this dissertation exhibited increased total electrical conductivity in the presence of water vapor, and some of them demonstrated an isotope effect.

STRESZCZENIE

Wraz z początkiem XXI wieku pojawiła się nowa rodzina materiałów zwanych stopami wysokoentropowymi. Wykazują one właściwości dotąd nieobserwowane w konwencjonalnych stopach tj. wysoka twardość i odporność na korozję. Z czasem zaczęto badać coraz to więcej materiałów wykazujących wysoką entropię konfiguracyjną m. in. azotki, węgliki lub tlenki. Pierwszy tlenek wysokoentropowy o wzorze sumarycznym $Mg_{0.2}Ni_{0.2}Co_{0.2}Cu_{0.2}Zn_{0.2}O$ został opisany niespełna dziesięć lat temu. Obszerna baza różnych pierwiastków i nieporządek obecne w wieloskładnikowych materiałach wysokoentropowych mogą wpływać m.in. na koncentrację, czy ruchliwość nośników ładunku. W obecnej erze transformacji energetycznej istotne prace prowadzone są nad materiałami wykazującymi przewodnictwo protonowe, związane z transportem defektów protonowych w strukturze materiału. Co więcej, przewodnictwo protonowe w tlenkach wieloskładnikowych wykazujących wysoką entropię jest interesującą i słabo poznaną właściwością.

Celem niniejszej pracy była synteza wieloskładnikowych tlenków na bazie cyrkonianu baru o strukturze perowskitu i określenie szeregu właściwości fizykochemicznych tych związków. Duży nacisk w rozprawie postawiono na badanie przewodnictwa protonowego. Istotną zmienną w wytworzonych próbkach była koncentracja wakansów tlenowych wynikająca z różnej ilości akceptorowych podstawników, od 20 do 60% molowych. Kationami bazowymi w podsieci B były: cyrkon, hafn, cyna oraz tytan. Natomiast rozpatrywanymi podstawnikami były itr, iterb, samar, ind, cer oraz cynk. Tlenki te wytworzono metodą syntezy w fazie stałej i scharakteryzowano przy użyciu m. in. dyfrakcji rentgenowskiej, dylatometrii, rentgenowskiej spektroskopii absorpcyjnej, obrazowania skaningowym mikroskopem elektronowym, termograwimetrii, kalorymetrii typu drop-solution, elektrochemicznej spektroskopii impedancyjnej oraz relaksacji przewodnictwa elektrycznego. Duży nacisk położono na analizę termodynamicznych parametrów uwodnienia i określenie parcjalnych przewodności elektrycznych.

Wszystkie otrzymane materiały wykazywały regularną strukturę perowskitu o grupie $Pm\bar{3}m$, z parametrem komórki zależnym liniowo od średniego promienia podstawników. Wyznaczone różnymi metodami współczynniki rozszerzalności termicznej były zbliżone i podobne do wartości podanych w literaturze dla akceptorowo podstawianych ceranów-cyrkonianów baru. Pomiary krawędzi absorpcji różnych metali wykazały niski stopień deformacji oktaedrów, oprócz krawędzi K tytanu, gdzie zauważono duży wpływ obecności wakansów tlenowych wokół kationu na właściwości absorpcyjne. Na podstawie zdjęć z mikroskopu elektronowego, duże, dobrze spieczone ziarna można było zaobserwować w próbkach posiadających 10 lub 8 pierwiastków w podsieci B. Natomiast próbki zawierające tylko 5 pierwiastków w podsieci B wymagały dodatku spiekającego w formie tlenku niklu, by uformować duże ziarna z małą ilością porów pomiędzy nimi. Mimo, że wszystkie próbki uwadniały się w atmosferze bogatej w parę wodną, to koncentracje protonów były o wiele niższe od tych obserwowanych w znanych przewodnikach protonowych na bazie ceranów-cyrkonianów baru. Na podstawie badań kalorymetrii drop solution ustalono, że rozpatrywane tlenki wieloskładnikowe nie są stabilizowane entropowo. Pomiary właściwości elektrycznych wykazały niższą przewodność elektryczną od podstawianych itrem ceranów-cyrkonianów baru, z dużym

wkładem granic międzyziarnowych do oporu elektrycznego próbek. Z drugiej strony, parametry kinetyczne dyfuzji tlenu, takie jak współczynnik dyfuzji chemicznej i chemicznej wymiany powierzchniowej okazały się znacznie wyższe w wybranym tlenku wieloskładnikowym niż te, opublikowane dla akceptorowo podstawianych ceranów-cyrkonianów baru. Warto zaznaczyć, że wszystkie badane w niniejszej rozprawie tlenki materiały miały podwyższoną całkowitą przewodność elektryczną w obecności pary wodnej, a część z nich wykazywała efekt izotopowy.

ABBREVIATIONS AND SYMBOLS

8YSZ – 8 mol% Yttrium Stabilized Zirconia,

AC – Alternating Current,

BLM – Brick Layer Model,

BPR – Ball-to-Powder Ratio,

BSE – Back-Scattered Electrons,

BSED – Back-Scattered Electron Detector,

BZCY/BCZY – Yttrium-doped Barium Cerate/Zirconate solid solution,

BZO – Barium Zirconate,

BZY – Yttrium-doped Barium Zirconate,

COD – Crystallography Open Database,

CPE – Constant Phase Element,

DC – Direct Current,

DFT – Discrete Fourier Transform,

DOS – Density of States,

DSC – Differential Scanning Calorimetry,

DTA – Differential Thermal Analysis,

ECR – Electrical Conductivity Relaxation,

EDS – Energy-Dispersive Spectroscopy,

EGA – Evolved Gas Analysis,

EIS – Electrochemical Impedance Spectroscopy,

EM – Entropy Metric,

ESO – Entropy-Stabilized Oxide,

ETD – Everhart-Thornley Detector,

EXAFS – Extended X-Ray Absorption Fine Structure,

FCC – Face-Centered Cubic structure,

HEA – High-Entropy Alloy,

HEC – High-Entropy Ceramic,

HEO – High-Entropy Oxide,

HTXRD – High-Temperature X-Ray Diffraction,

LSF – Strontium-doped Lanthanum Ferrite,

MEA – Multiprincipal-Element Alloy,

MEO – Medium-Entropy Oxide,

PVB – Polyvinyl Butyral,

SCL – Space Charge Layer,

SE – Secondary Electrons,

SEM – Scanning Electron Microscope,

TEC – Thermal Expansion Coefficient,

TEM – Transmission Electron Microscope,

TG – Thermogravimetry,

TTT – Time-Temperature-Transformation diagram,

WDS – Wave-Dispersive Spectroscopy,

XANES – X-Ray Absorption Near Edge Structure,

XAS – X-Ray Absorption Spectroscopy,

XPS – X-Ray Photoelectron Spectroscopy,

XRD – X-Ray Diffraction,

α – thermal expansion coefficient,

α_{DIL} – thermal expansion coefficient from dilatometry measurements,

α_{HTXRD} – thermal expansion coefficient from high-temperature X-ray diffraction,

ΔE_{Hf} – crystal field split for hafnium orbitals,

ΔG_{mix} – Gibbs free energy of mixing,

ΔH_{ass} – enthalpy of association,

ΔH_{ds} – enthalpy of drop solution,

ΔH_{form} – enthalpy of formation of given compound,

$\Delta H_{f,V_O^{\bullet\bullet}}$ – enthalpy of formation of oxygen vacancies,

ΔH_{hydr} – enthalpy of hydration reaction,

$\Delta H_{m,h}$ – enthalpy of mobility of electron holes,

ΔH_{mix} – enthalpy of mixing,

$\Delta H_{m,V_O^{\bullet\bullet}}$ – enthalpy of mobility of oxygen vacancies,

ΔH_{ox} – enthalpy of oxidation reaction,

Δm – sample mass change upon hydration,

ΔS_{conf} – configurational entropy,

ΔS_{conf}^{SL} – configurational entropy calculated from sublattice model,

ΔS_{conf}^{SS} – configurational entropy calculated from solid solution model,

ΔS_{hydr} – entropy of hydration reaction,

ΔS_{mix} – entropy of mixing,

ΔS_{ox} – entropy of oxidation reaction,

δ – oxygen non-stoichiometry,

δ_{GB} – thickness of space charge layer,

ε – strain,

ε_0 – vacuum permittivity,

ε_r – relative permittivity,

κ – thermal conductivity,

λ – wavelength,

λ^* – space charge layer width,

μ_e – mobility of electrons,

μ_h - mobility of electron holes,

μ_i – mobility of given species i,

μ_{ion} – mobility of ions,

μ_h^0 – pre-exponential factor for electron-hole mobility,

ρ_{Arch} – density of the sample obtained using Archimedes' method,

ρ_{rel} – relative density of the sample,

ρ_{th} – theoretical density of the material,

σ_{D2O} – total electrical conductivity in atmosphere humidified with heavy water,

σ_e – partial electrical conductivity of a material related to electrons,

σ_{el} – electrical conductivity,

σ_{H2O} – total electrical conductivity in atmosphere humidified with water,

σ_h – partial electrical conductivity of a material related to electron-holes,

σ_g – partial electrical conductivity of grains,

σ_{gb} – partial electrical conductivity of grain boundaries,

$\sigma_{gb-spec}$ – partial specific electrical conductivity of grain boundaries,

σ_{ion} – partial electrical conductivity of ions,

σ_O – partial electrical conductivity of a material related to oxygen ions,

σ_{OH} – partial electrical conductivity of a material related to protons,

σ_{tot} – total electrical conductivity,

σ_{D2O}^0 – pre-exponential factor for total electrical conductivity in atmosphere humidified with heavy water,

σ_{el}^0 – pre-exponential factor for electrical conductivity,

σ_{H2O}^0 – pre-exponential factor for total electrical conductivity in atmosphere humidified with water,

σ_{ion}^0 – pre-exponential factor for partial electrical conductivity of ions,

σ_{tot}^0 – pre-exponential factor of total electrical conductivity,

φ_0 – Schottky potential,

$[\dots]$ – concentration of given point defect, e.g. $[V_O^{\bullet\bullet}]$ is the concentration of oxygen vacancies,

$[Acc_B']$ – concentration of acceptor constituent in the B-sublattice,

$[X_i]$ – concentration of selected element in the crystal structure,

a_0 – lattice parameter,

a_{SL} – multiplicity of the sublattice,

C_g – capacitance of the grains,

C_{gb} – capacitance of grain boundaries,

c_i – the concentration of charge carrier i,

c_{ion} – concentration of ions,

D_{chem} – chemical diffusion coefficient,

D_{chem}^O – chemical diffusion coefficient of oxygen,

D_{chem}^{OH} – chemical diffusion coefficient of protons,

d_{BaO} – bond length between barium and oxygen,

d_{BO} – bond length between B-site cation and oxygen,

d_m – molar density,

E_a – activation energy of selected process,

E_g – energy band gap,

e – elementary charge,

e_g, t_{2g} – molecular orbitals,

F – Faraday constant,

$h^{\bullet}$ – electron holes,

I_0 – intensity of an incident photon beam,

I_1 – intensity of a photon beam after the interaction with the sample,

K_{H2O} – equilibrium constant for hydration reaction,

K_{ox} – equilibrium constant for oxidation reaction,

k_B – Boltzmann constant,

k_{chem} – chemical surface exchange coefficient,

k_{chem}^{O} – chemical surface exchange coefficient for oxygen,

k_{chem}^{OH} – chemical surface exchange coefficient for protons,

L – number of sublattices in the crystal structure,

L_B – Biot number,

L_D – Debye length,

l – thickness of the sample for electrical measurements,

m – mass of the sample for thermogravimetric measurements,

m_c – molar mass of the sample,

m_{H2O} – molar mass of water molecule,

N_c – density of states of electrons,

N_v – density of states of electron-holes,

O_O^X – oxygen in the oxygen site,

$OH_O^{\bullet}$ – proton defect,

pD_2O – heavy water vapor partial pressure,

pH_2O – water vapor partial pressure,

pO_2 – oxygen partial pressure,

R – gas constant,

R_{exp} – expected condition number from Rietveld refinement,

R_i – resistance of the selected element,

R_p – profile condition number from Rietveld refinement,

R_{wp} – weighted profile condition number from Rietveld refinement,

r_A – radius of an atom in A sublattice,

r_B – radius of an atom in B sublattice,

r_X – radius of an atom in anion sublattice,

S – sample cross-section,

T – absolute temperature in kelvin,

t – Goldschmidt tolerance factor,

t_{OH} – transfer number for protons,

$V_O^{\bullet\bullet}$ – oxygen vacancy,

x – thickness of the sample in XAS measurements,

Z_0 – magnitude of impedance,

Z' – real part of impedance,

Z'' – imaginary part of impedance,

$Z(\omega)$ – electrical impedance,

z – charge number.

1. INTRODUCTION AND AIM OF THIS WORK

Since the beginning of civilization, humans have been developing techniques for producing materials, which means that Materials Engineering may be one of the oldest professions in the world. Since the beginning of the Stone Age, we have been looking for new raw materials to satisfy our needs. Thus, successive eras were based on the dominant material, from bronze to iron and then steel, and the current era of superalloys. About 20 years ago, new materials appeared that could revise the perspective on material design, namely high entropy alloys. Increasing configurational entropy allows for achieving previously unexplored stabilization of exotic compositions. Many new families of materials started emerging, including high entropy oxides.

So-called high-entropy oxides may be considered a group with unexpected properties, so knowledge of their structures, properties, and synthesis technology contributes to a new development of materials engineering. High-entropy perovskite oxides have been known since 2018, and only a few of them have been examined in terms of their electrical transport properties and, in particular, their proton conductivity. It should be stressed that proton-conducting oxides are interesting materials for the next generation of solid oxide fuel cells. Currently, emphasis is placed on developing renewable and green technologies, including photovoltaics, nuclear energy or hydrogen technologies. For this reason, it is crucial to develop techniques for transporting and storing hydrogen, where proton conduction in materials is highly desirable. Therefore, the results of the studies carried out within this work will constitute an important contribution to the basic knowledge of materials and their potential application development.

The aim of this work is to synthesize and study a new group of proton-conducting oxides exhibiting a medium and high configurational entropy. The base structure for all samples is barium zirconate perovskite structure. The B sublattice will be occupied by a minimum of five different cations and a maximum of ten cations to obtain medium/high entropy in the compounds. The isovalent elements like Zr, Hf, Sn, and Ti are selected to create the base medium-entropy matrix. The other elements will be selected based on the Goldschmidt tolerance factor and the valency state. Acceptor substitution will be employed to induce the formation of oxygen vacancies, and to ensure the appearance of proton conductivity.

The dissertation is divided into six chapters. In Chapter 2, the theory and literature reports about the high-entropy materials are described. Chapter 3 introduces the charge transport models in considered types of materials and describes the proton conductivity. The next chapter discusses the perovskite oxides and presents the state-of-art of perovskite proton conductors. Chapter 5 describes the experimental techniques used in this work and provides details of the experiments performed. Chapter 6 presents the results with a discussion, divided into subsections for each experimental technique. The last chapter contains conclusions derived from the conducted analysis.

2. HIGH-ENTROPY MATERIALS

2.1 High-entropy alloys

The history of high-entropy oxides is not long; it has been less than 10 years. However, to fully describe the beginning and development of high-entropy materials, it is essential to start with the case of high-entropy alloys.

The first mentions of materials exhibiting high entropy date back to the 18th century, although those compounds were called multiprincipal-element alloys (MEA)[1]. German scientist and metallurgist Franz Karl Achard synthesized in the 80s of 18th century roughly 900 alloys consisting of two up to seven elements in the equimolar composition, selected from the group of 11 metals (among which were i.e. Fe, Cu, Sn, Pb, Zn, Co, Pt). In his book “Recherches sur les Propriétés des Alliages Métallique”, he included information such as the density of alloy, hardness, ductility, polishability, and results of exposition to various atmospheres (from dry air to highly acidic). Unfortunately, all data is presented in tabular form and with little discussion. F.K. Achard only summarized that the properties of those alloys differ from those of pure metals and are unpredictable. For almost two centuries, no new insight concerning MEA emerged until the second part of the 20th century and the beginning of the 21st century. Here must be noted the contribution of 3 scientists: Brian Cantor, Srinivasa Ranganathan, and Jien-Wei Yeh.

B. Cantor started his interest in MEA in the 80s of the twentieth century. He and one of his students prepared some equimolar alloys mixing from five to even twenty different elements in one alloy, using the molar contributions from 20% to 5%, respectively. They noticed that only one alloy formed a single-phase composition. It was $Fe_{20}Cr_{20}Ni_{20}Mn_{20}Co_{20}$ that crystallized in the face-centered cubic (FCC) structure. Unfortunately, these findings were only included in the student’s thesis, and no new experiments were conducted in the next 20 years. In 2004, another student’s work appeared and was finally published under Cantor’s directions[2]. They described findings regarding $Fe_{20}Cr_{20}Ni_{20}Mn_{20}Co_{20}$ and presented results of expanding this structure to six or even nine different atoms. Some elements, such as Nb, Ti, and V were found to be able to dissolve substantially in the dendritic microstructure. On the other hand, more electronegative elements, such as Cu and Ge, tended to agglomerate in the regions between dendrites. They also described an alloy containing 20 different atoms – the material was brittle and multiphase but with the predominant FCC structure. It is worth noting that the number of phases observed in all those multi-principal-element alloys, even in those exhibiting a few phases, is below the limit derived from the Gibbs phase law.

The second scientist who contributed to the popularization of high-entropy alloys was Srinivasa Ranganathan. In his article published in 2003[3], he described three new areas in alloy development, one of which was multicomponent alloys exhibiting high mixing entropy. This entropy was supposed to stabilize a single phase in compositions that, according to the Gibbs phase law, should consist of many phases and intermetallic species. In this type of alloy, establishing phase

diagrams requires a hyperdimensional space, and simulating possible structures is quite challenging. This short article was the first official paper containing information about high-entropy alloys, so it prepared the entire alloy community for ground-breaking findings in the upcoming years. Ranganathan gained information about HEA from the most prominent contributor and precursor in this matter: Jien-Wei Yeh.

Jien-Wei Yeh started his research on high-entropy alloys in 1995. He thought that increasing the mixing entropy would reduce the number of phases in multi-element compounds and may improve various properties of alloys. In the late 1990s, one of his students synthesized numerous alloys containing between five and nine different elements from 11 commonly used metals. These alloys were found to crystallize in a typical dendritic structure and have a high hardness level, depending on the type and number of elements. Moreover, adding 3 at.% of boron enhanced the hardness even further. From this moment, Yeh supervised many MS and PhD theses and conducted experiments concerning the annealing, wear and deformation behavior of HEA, thin film deposition and corrosion resistance. The most important conclusions were that the hardening of these alloys has roots in severe crystal lattice distortion and low Gibbs free energy resulting from high configurational entropy, which contributes to the rise of corrosion resistance. After patenting HEA in Japan, Taiwan, China, and the United States, Yeh published the first article on high-entropy alloys in 2004[4]. Apart from the first official usage and popularization of the term 'HE alloys', Yeh et al. described the theory of configurational entropy and experimental results of XRD patterns, SEM/TEM images and plots of mechanical properties (yield strength and hardness). In the end, they summed up that with the base of 13 mutually miscible metals, there are 7099 possible alloy systems composed of from 5 up to 13 elements in equimolar ratio and minor additions to those alloys can reinforce structure stabilization and processing.

According to Yeh's findings, high-entropy alloys possess many unique properties. Their origin can result from four core effects in HEA: high-entropy effect, severe lattice distortion, sluggish diffusion kinetics, and cocktail effect.

High-entropy effect

The high-entropy effect is the most prominent and concerns the second law of thermodynamics. The most stable compound under given conditions is the one with the lowest free energy. This energy depends on the enthalpy and entropy of mixing:

$$\Delta G_{mix} = \Delta H_{mix} - T\Delta S_{mix}. \tag{2.1}$$

Typically, in standard synthesis, the enthalpy term is the dominant one and governs the direction of the reaction. In the system with a few different elements, the compound(s) that will stabilize is(are) the one(s) with the lowest enthalpy of mixing. On the other hand, elements with positive enthalpy of mixing or those exceeding the solubility limit tend to separate from other elements and form secondary phases. The entropic contribution is often negligible when comparing numeric values. However, two phenomena may occur when we increase the number of elements. First, considering

the formation of a random solid solution, the enthalpy of mixing of such a system is less negative than that of an ordered system.

Nevertheless, with more elements in the system, those enthalpies become closer to each other. Second, equimolarity and many elements maximize the entropy of mixing, thus making the entropy term significant, especially at high temperatures. Combining these two issues may stabilize a single-phase random solid solution named by Yeh high-entropy alloys. To consider an alloy as 'high-entropy', its ΔS_{mix} should equal $1.5R$ or higher, where R is an ideal gas constant.

Lattice Distortion

When various metal elements form one crystal structure, the neighborhood of each cation is different: the differences between the atoms include their atomic radii, valency, bonding energy, etc. This leads to a strong lattice strain that distorts the atom positions, reflected in the XRD pattern as the crystal structure with an average lattice parameter. This lattice distortion influences not only the mechanical but also the transport properties of an alloy[4]. Mechanically, HEAs have a larger hardness and strength than binary or ternary parent alloys. Also, the transport properties, including electrical and thermal properties, strongly depend on the lattice distortion. Severely distorted lattice scatter phonons more strongly than unstrained ones, which in turn hinders thermal conductivity. In the case of electrons, their restrained mobility in the distorted lattice reduces both the electrical and thermal conductivity contributions[4].

Sluggish Diffusion Kinetics

We can also consider hindered ('sluggish') diffusion in a disordered system. A large pool of elements in the system restrains the diffusion of cations by increasing the activation energy of migration. During synthesis, this sluggishness not only helps stabilize a single-phase composition by inhibiting possible phase separation but also allows for achieving desirable properties. Through proper selection of metals and their quantities and synthesis conditions, such parameters as nucleation time or grain structure may be controlled. With a strictly defined microstructure, synthesized alloys can maintain high strength, toughness, and improved creep resistance.

Cocktail effect

The idea of synergistic effects between elements in the given composition is mainly represented in the 'cocktail effect' presented by Ranganathan[3]. HEAs are atomic-scale multicomponent composites with properties that depend mainly on the interactions between the cations and not the overall properties of elements in the structure. This approach results in unexpected outcomes emerging in an alloy. Furthermore, high-entropy alloys can contain more than one crystalline and intermetallic phase, so they can also be called composites on a microscale. Thus, the properties of an alloy depend not only on the quantity of all phases and their distribution in an alloy but also on the synergy between them.

In the following years, scientists have developed the high-entropy alloy family, adding new representatives with outstanding properties. For example, some researchers tried to nitride or

carburize alloys to create coatings to tune their properties[1,5]. Although in the form of thin films, these were the first attempts to broaden the group of high-entropy materials. Further investigations led to the development of a new family of compounds called high-entropy ceramics. High-entropy ceramics include oxides[6], nitrides[7], carbides[8], borides[9], hydrides[10], silicides[11], sulfides[12], fluorides[13] and many other compounds. This thesis is focused on high-entropy oxides.

2.2 High-entropy oxides

The first mention of the importance of entropy in the phase stabilization of oxides can be found in the work of Navrotsky and Kleppa[14]. The authors determined the enthalpies of the formation of several spinels and described the relations between metal ions building spinels and the possibilities of occurrence of the repulsion effect. Upon comparing those enthalpies with the free energies, they calculated the entropies of formation. It turned out that spinels with a random distribution of cations in the tetrahedral and octahedral sites and several inverse spinels have a more positive entropy of formation than normal spinels. Thus, the authors suggested that this configurational disorder can lead to 'entropy stabilization' of the spinel structure at high temperatures. It took some time to elaborate further on the importance of entropy in stabilizing oxides. With time, experiments confirmed the acquisition of high entropy oxides in rock-salt[15,16], fluorite[17,18], spinel[19,20], perovskite [21–23], and other more complex structures[24].

2.2.1 Rock-salt structure

In 2015, inspired by findings in HEA and supported by some theoretical principles, Rost et al.[15] applied the idea of 'high-entropy material' and entropy stabilization in the case of oxides. They synthesized a five-component high-entropy oxide consisting of MgO, NiO, CoO, CuO, and ZnO in equimolar quantities. The selection of cations was made with an emphasis on inducting diversity by electronegativity, cation coordination, and co-solubility. Only then could the influence of entropy on phase stabilization be examined. They obtained high entropy (Mg,Ni,Co,Cu,Zn)O oxide at 1000 °C using the solid-state reaction. It had a rock-salt crystal structure. Below 1000°C, two crystal phases, i.e. rock-salt and tenorite, were present. Two experiments were performed to test the entropy stabilization. The first one was related to the reversibility of phase stabilization through temperature.

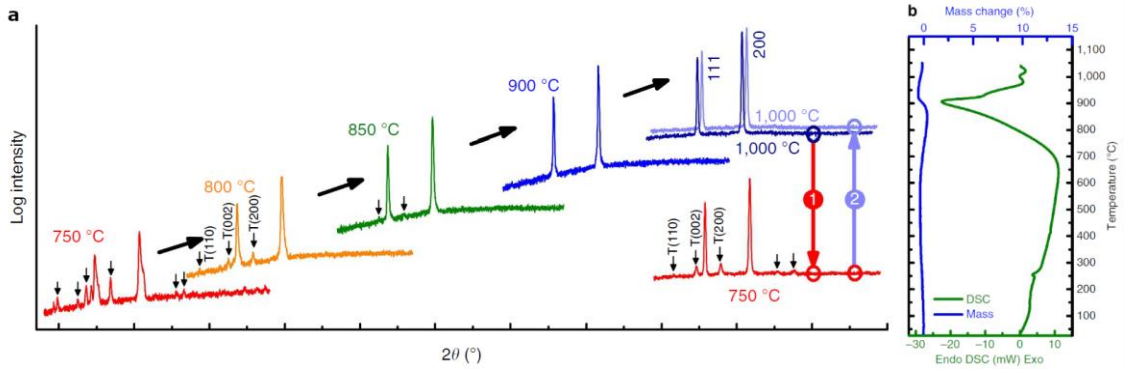

Figure 2.1 a) The evolution of the XRD pattern depending on the temperature of synthesis and the reversibility phenomenon, b) the phase change signal from the DSC[15].

They took the stable sample synthesized at 1000 °C, heated it to 750 °C in a similar annealing cycle, and tested it using XRD analysis. The sample was then reheated at 1000 °C and checked again. It turned out that when heated at a temperature below 1000 °C, the sample tended to separate into two phases, whereas after reheating at 1000 °C, the single-phase rock-salt structure was regained (Figure 2.1a). The authors also performed the DSC/TG analysis to determine the presence of any thermal processes. They observed an endothermic reaction between 700 and 1000 °C, connected with the transition from the multiphase- to the single-phase system (Figure 2.1b). The second experiment was related to lowering the configurational entropy of the system. They found that varying the amounts of constituent cations showed that nonequimolarity leads to increasing the transition temperature between multiphase and single-phase systems. Moreover, the synthesis of quaternary oxides revealed that a single rock-salt phase did not form in this case. The authors concluded that they obtained a single-phase high-entropy oxide stabilized with entropy (ESO). Moreover, they noticed that the anion sublattice present in the oxides is crucial in maintaining a high configurational entropy. Each cation occupies an oxygen octahedron and has a similar neighborhood, thus creating a high number of microstates, increasing the entropy. It is also worth emphasizing that not all high-entropy materials are entropy-stabilized, but every entropy-stabilized material has high configurational entropy.

Those findings began the research of a new branch of compounds that could be further explored in the scope of materials engineering. At first, scientists wanted to know more about this primal HEO because of its potentially interesting properties. A substantial contribution to the research on rock-salt HEO can be attributed to Berardan et al.[16]. His team examined the influence of aliovalent substitutions on the (Mg,Ni,Co,Cu,Zn)O parent compound and its properties. They found that acceptor substitution with Li^+ cations does not influence phase stability, while the lattice parameter changes according to Vegard's rule. XPS analysis confirmed that the samples with added Li show the signal characteristic of Co^{3+} cations. On the other hand, adding trivalent gallium caused severe phase changes and caused the samples to become multiphase. However, adding both cations in equal quantities resulted in the acquisition of single-phase compounds. Additionally, they checked the transport properties of a few selected compounds. The electrical resistivity of the parent compound was high and decreased exponentially with increasing temperature, which corresponded to the 1 eV bandgap. On the other hand, samples with Li^+ had reduced resistivity values by two orders of magnitude, and the band gap decreased with increasing Li content. Interestingly, every sample exhibited a very high relative permittivity ($\sim 10^{-5}$). To test if it is a unique feature of this family of high-entropy oxides, the authors repeated the measurements on the multiphase sample, that is, reheated at 750 °C. It turned out that the resistance at room temperature dropped substantially, but the sample did not exhibit any capacitance response. Therefore, this new family of rock-salt HEO shows unique dielectric properties.

2.2.2 Fluorite structure

The first high-entropy fluorite oxides were reported by Chen et al.[17]. Using solid-state reaction, they synthesized quinary fluorite oxide consisting of Zr, Hf, Sn, Ti, and Ce in the equimolar

ratio. The scientists checked if this compound could also be accounted for as ESO. After the last synthesis stage at 1500 °C, they found that the sample started to show a second phase after heating at 1100 °C; however, it became a single phase after reheating at 1500 °C. Interestingly, these changes in phase composition were also visible in the SEM images (Figure 2.2). Measurements of transport properties showed that the electrical conductivity changes linearly in Arrhenius coordinates with the activation energy E_a = 1.43 eV, probably related to ion oxygen transport. Furthermore, thermal conductivity equal to 1.28 W/K·m, which is half that of 7 wt% yttria-stabilized zirconia's, confirmed that high entropy influences phonon transport by lattice distortion. This material could be used as a thermal insulator.

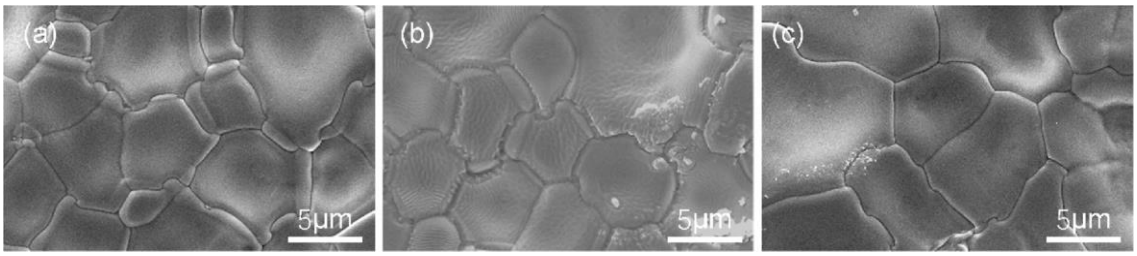

Figure 2.2 SEM images of $(Zr,Hf,Sn,Ti,Ce)O_2$ a) after synthesis at 1500 °C, b) after annealing at 1100 °C, c) after reheating at 1500 °C[17].

Gild et al. synthesized high-entropy oxides based on fluorites such as ZrO_2, HfO_2, and CeO_2 stabilized with trivalent elements, that is, Y, Yb, or Gd[18]. The single-phase samples were then compared with the 8 wt% yttria-stabilized zirconia (8YSZ) in terms of electrical and thermal conductivity and hardness. Although the HEO fluorite activation energies of the electrical conductivity process are comparable to 8YSZ, they have three orders of magnitude lower ionic conductivity. In the case of hardness (Figure 2.3a), the fluorites maintained values similar to that of 8YSZ. Thermal conductivity values are twice lower than that of 8YSZ (Figure 2.3b). These findings are in agreement with the results acquired by Chen et al.[17].

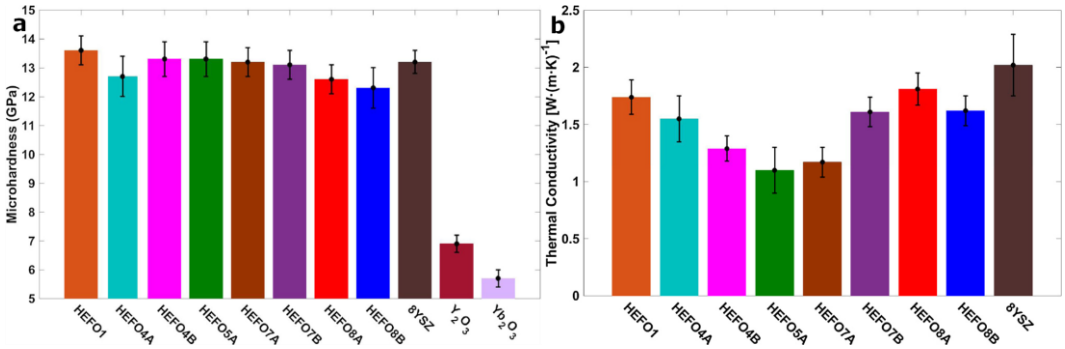

Figure 2.3 a) Measured hardness of HEO fluorites and reference compounds, b) thermal conductivity values for HEO fluorites and 8YSZ[18].

2.2.3 Spinel structure

Dąbrowa et al. obtained $(Cr,Co,Mn,Fe,Ni)_3O_4$ in the spinel structure ($Fm\bar{3}m$) by solid-state reaction and examined it using XRD analysis, SEM imagining with EDS analysis and Raman spectroscopy[19]. For reference, the authors also synthesized the rock-salt HEO sample. Each sample was a single phase with a homogeneous cation distribution. This spinel and its derivatives

were later studied by Mao et al.[20]. The authors, using the solution combustion method, synthesized $(Cr,Co,Mn,Fe,Ni)_3O_4$ and two other HEOs with Zn instead of Co or Ni. The XRD pattern showed that the Zn substitution influences the lattice parameter and the SEM images confirmed that the obtained powders are nanocrystalline. All samples were also subjected to room-temperature magnetic measurements, and the results indicated that magnetic super-exchange interactions occurred. However, in the case of compositions consisting of non-magnetic Zn, the magnetic responses were weaker than in the parent compound. It gives the possibility to tailor the magnetic properties of HEO by altering the oxide composition.

2.2.4 Perovskite structure

Jiang et al. reported the first high-entropy ABO_3 perovskite oxides[21]. They synthesized various oxides with 4 or 5 different cations in the B sublattice and barium, strontium or both in the A sublattice. The ones with four cations in the B sublattice were not single phase in the selected temperature range (1300-1500 °C), while those with five cations, in most cases, were single phase perovskites. It also turned out that single-phase materials had a Goldschmidt tolerance factor between 0.97 and 1.03. In this way, Jiang et al. have proposed a criterion that should be considered when designing new species in this family of compounds. Furthermore, they found that the difference in atomic size, which was used as a criterion for the possible stability of high-entropy alloys, in HEO perovskites was not as reliable as Goldschmidt's factor. Thorough research on entropy stabilization in HEO perovskites was done by Sarkar et al.[22]. The authors prepared various high-entropy perovskite oxides with five different elements in either A or B sublattice. They also prepared $(Gd_{0.2}La_{0.2}Nd_{0.2}Sm_{0.2}Y_{0.2})(Co_{0.2}Cr_{0.2}Fe_{0.2}Mn_{0.2}Ni_{0.2})O_3$ with both positions occupied by five constituents. To check the entropy stabilization, the scientists performed high-temperature X-ray diffraction (HTXRD) from room temperature to 1000 °C. The presence of entropy stabilization could be seen in two different cases. Some compounds that were not single phase (e.g. $(Gd_{0.2}La_{0.2}Nd_{0.2}Sm_{0.2}Y_{0.2})MnO_3$, Figure 2.4) became single phase at elevated temperatures due to an increase in the entropy term compared to the enthalpy term (Equation 2.1). In other cases, single-phase samples had the entropy term much bigger than the enthalpy term in a wide range of temperatures that governed the phase stabilization.

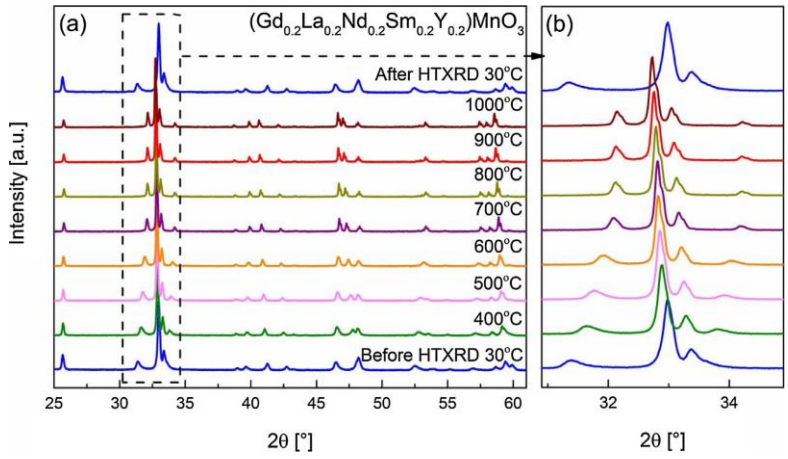

Figure 2.4 a) Full range and b) magnified fragment of HTXRD patterns of $Gd_{0.2}La_{0.2}Nd_{0.2}Sm_{0.2}Y_{0.2}MnO_3$[22].

Finally, it is worth mentioning that an attempt to use high-entropy oxides in a ceramic fuel cell has been recently reported by Yang et al.[23]. They prepared the non-equimolar HEO perovskite $La_{0.2}Pr_{0.2}Nd_{0.2}Sm_{0.2}Ba_{0.1}Sr_{0.1}Co_{0.2}Fe_{0.6}Ni_{0.1}Cu_{0.1}O_3$ using a one-pot combustion method and tested it as a cathode in a fuel cell. The tested fuel cell consisted of the NiO-YSZ cermet as an anode, dense YSZ as an electrolyte, and gadolinium-doped ceria as a buffer layer on the cathode-electrolyte interface. The selected HEO had six times higher total conductivity at 800 °C than the conventional $La_{0.8}Sr_{0.2}FeO_3$ (LSF). Regarding cell performance, the one with the HEO cathode achieved a low polarization resistance of 0.3 Ωcm^2, which is half that of the fuel cell using LSF as the cathode. The maximum cell power density at 800 °C reached a value of 714.5 mW/cm^2, placing this HEO perovskite as a promising cathode for solid oxide fuel cells.

2.2.5 Other crystal structures

Another widely researched oxide group is a group of pyrochlore oxides – $A_2B_2O_7$. One of the first high-entropy pyrochlore oxides was $Dy_2(Zr_{0.2}Hf_{0.2}Sn_{0.2}Ti_{0.2}Ge_{0.2})_2O_7$ reported by Vayer et al.[25]. Their team not only managed to synthesize the material in cubic pyrochlore structure but also determine some of its properties. In terms of thermal properties, they estimated the value of the thermal conductivity κ to be around 1.4 W/K·m, which is close to ones found in amorphous-like materials. The thermal expansion coefficient (TEC) was 10.3×10^{-6} 1/K, within the observed ranges for nickel-based superalloys: $9\text{-}16 \times 10^{-6}$ 1/K. These findings predispose this material as a promising thermal barrier coating. On the other hand, high resistivity, which is 8×10^{10} Ωm at room temperature, and relative permittivity of 78 make this material attractive for ceramic capacitors.

We previously reported the electrical transport properties for a group of calcium-doped pyrochlores based on the aforementioned oxide: $(Dy_{1-x}Ca_x)_2(Zr_{0.2}Hf_{0.2}Sn_{0.2}Ti_{0.2}Ge_{0.2})_2O_7$[26]. The electrical studies were performed in different ambient gasses and water partial pressures. Temperature dependencies of electrical conductivity are shown in Figure 2.5. The base pyrochlore exhibited low total electrical conductivity $<10^{-3}$ S/cm and a high activation energy for charge transport – 1.28 eV, even at 800 °C. The introduction of calcium causes the conductivity to decrease. Moreover, after the introduction of the water vapor, the conductivity did not change, indicating poor hydration.

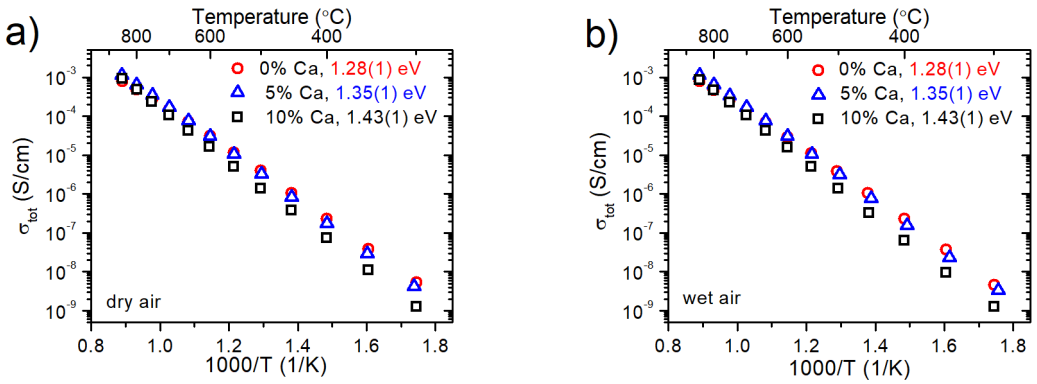

Figure 2.5 Temperature dependence of total conductivity in a) dry and b) wet air for $(Dy_{1-x}Ca_x)_2(Zr_{0.2}Hf_{0.2}Sn_{0.2}\ Ti_{0.2}Ge_{0.2})_2O_7$ with x = 0, 0.05 and 0.1[26].

One of the most interesting cases of entropy-stabilized oxides is the family of materials with the formula $A_6B_2O_{17}$. The first research around this family reached the 50s in the previous century when Roth et al. reported the formation of $6ZrO_2 \cdot Nb_2O_5$ pseudobinary system in orthorhombic symmetry ($Ima2$)[27]. However, only quite recently, Voskanyan et al. describe the thermal stability of materials where A = Zr, Hf and B = Nb, Ta[28]. They found that these compounds exhibit positive enthalpy of formation and a high degree of disorder. This would mean that these materials should have high configurational entropy. The astounding ΔS_{mix} equal to $4.5R$, according to the authors, stems from the structural complexity of these materials. The structure contains layers formed from A and B-centered polyhedra of different shapes, where cations can occupy various positions (Figure 2.6). This multiplicity of possible positions, not the number of elements, increases the configurational entropy, challenging proposed rules for designing high-entropy materials.

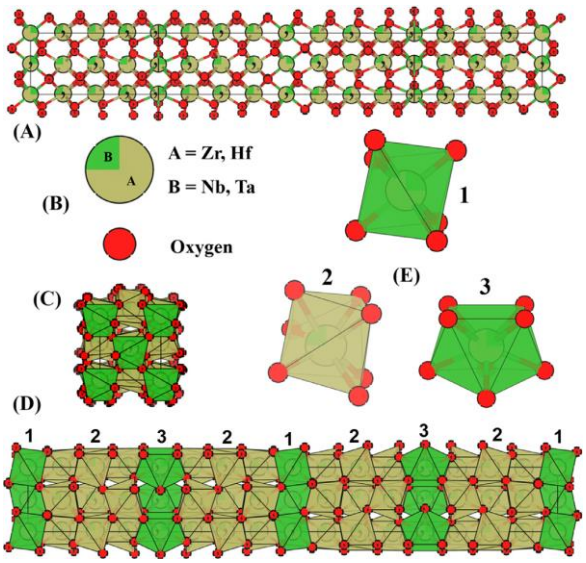

Figure 2.6 A depiction of the $A_6B_2O_{17}$ disordered structure looking down the c-axis (A) along with a key for A (Zr, Hf), B (Nb, Ta) and oxygen atoms (B). A depiction of the polyhedra in the $A_6B_2O_{17}$ structure looking down the a-axis (C), and the c-axis (D) along with a key for the different types of polyhedron present (E): 1– a six-coordinated distorted octahedron, 2– a seven coordinated capped trigonal prism and 3– an eight-coordinated distorted bicapped trigonal prism[28].

Regarding properties, Kleger et al. performed the DFT simulations of $Hf_6Ta_2O_{17}$, determining mechanical and thermal properties and the band structure[29]. Mechanically, this compound is ductile (according to the Pugh ratio) and has a wide (2.67 eV) indirect band gap, which makes it a promising material for coatings and high-temperature applications. We conducted a more detailed investigation of the electrical properties of materials reported by Voskanyan et al.[30]. The charge transport in these oxides is thermally activated, concerning the oxygen ions and electron/electron-holes, with activation energies ranging from 1 eV to 2 eV. Additionally, from conductivity measurements in different oxygen partial pressures, we inferred that electrons play an important role in the conduction of $A_6Nb_2O_{17}$, while electron holes are significant for conduction in $A_6Ta_2O_{17}$ (see Figure 2.7).

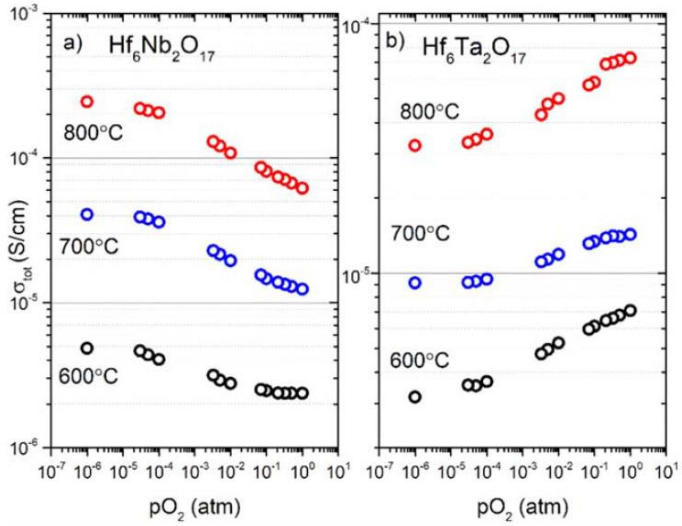

Figure 2.7 Total conductivity of a) $Hf_6Nb_2O_{17}$ and b) $Hf_6Ta_2O_{17}$ at 600, 700 and 800 °C as a function of oxygen partial pressure[30].

2.3 Determination of configurational entropy

Over the years, several methods have emerged to calculate the theoretical value of mixing entropy, also known as configuration entropy. The classical method of determining ΔS_{conf} is based on the second law of thermodynamics and Boltzmann's hypothesis on the relation between system complexity and entropy[31]. According to these assumptions, one can derive the formula for configurational entropy:

$$\Delta S_{conf}^{SS} = -R \sum_i [X_i] \ln[X_i], \tag{2.3}$$

where $[X_i]$ is the molar fraction of element i. If the elements in the system are in equimolar amounts, the Equation 2.3 can be reduced to Equation 2.4:

$$\Delta S_{conf}^{SS} = -Rln\left(\frac{1}{u}\right) = Rln\, u, \tag{2.4}$$

where u is the number of elements that are forming the solid solution. Each element is considered an entropic species and has an equal probability of occupying possible positions in the crystal structure. As described by Yeh et al., his so-called 'solid solution' model is reliable for calculating the ΔS_{conf} in high-entropy alloys[4]. The main criterion in designing HEA that the minimum number of elements should be 5 was proposed because the configurational entropy of such a system is $1.61R$. The threshold value of $1.5R$ for 'high-entropy' material was established considering the Richards' Rule. This rule concerns the maximum value of configurational entropy in melted metals to be equal to R. Apart from high-entropy alloys there are also 'medium entropy' and 'low entropy' alloys, possessing $\Delta S_{conf} \in \langle 1R; 1.5R)$ and $\Delta S_{conf} < 1R$, respectively.

However, Equation 2.4 is applicable in materials with only one lattice position which is occupied by the cations[32]. In other materials, e.g. oxides, where different elements occupy different sublattices and there is more than one atom per unit cell, they cannot be considered entropic

species for the whole crystal structure. To address this issue, another equation was proposed that considers the presence of different sublattices in the system and their multiplicity. The sublattice model defines the configurational entropy as follows:

$$\Delta S_{conf}^{SL} = \frac{-R \sum_{SL} \sum_i a_{SL}[X_i] \ln[X_i]}{\sum_{SL} a_{SL}}, \tag{2.5}$$

where a_{SL} is the multiplicity of the selected sublattice. For $a_{SL} = 1$, the Equation 2.5 reduces to Equation 2.4. What is interesting, the point defects can also be considered as an entropic species when their concentration is significant. The ΔS_{conf}^{SL} obtained from above equation is calculated per atoms in the system. To obtain the value per mole of formula unit, the denominator should be omitted. For example, the ΔS_{conf}^{SL} for $BaZr_{0.2}Hf_{0.2}Sn_{0.2}Ti_{0.2}Y_{0.2}O_{2.9}$ multicomponent perovskite oxide can be written as:

$$\Delta S_{config}^{SL-pero} = -R \frac{\left([Ba]\ln[Ba]+[Zr]\ln[Zr]+[Hf]\ln[Hf]+[Sn]\ln[Sn]+[Ti]\ln[Ti]+[Y]\ln[Y]+3\cdot\left([O_O^X]\ln[O_O^X]+[V_O^{\bullet\bullet}]\ln[V_O^{\bullet\bullet}]\right)\right)}{5}, \tag{2.6}$$

$$\Delta S_{config}^{SL-pero} = 3.41 \ \frac{J}{K \cdot mol} \ per \ atoms, \tag{2.7}$$

where $[O_O^X]$ is the concentration of oxygen at oxygen sites and $[V_O^{\bullet\bullet}]$ is the concentration of oxygen vacancies.

While more representative of oxide materials, this model does not allow the comparison of the values of configurational entropy between different crystal structures. The tool that would help unify the description of the disorder in different materials was proposed by Dippo et al.[32]. They formulated the Entropy Metric (EM). This dimensionless parameter joins the configurational entropy per atom with the complexity of a given material:

$$EM = \frac{\Delta S_{conf}^{SL}}{R} \cdot L, \tag{2.8}$$

where L is the number of the sublattices in the system. The division of types of entropic materials is retained for Entropy Metric i.e. materials with EM above 1.5 are considered, high-entropy and so on. The EM value for the configurational entropy from Equation 2.7, assuming $L = 3$, is equal to 1.23, indicating that this material is a medium entropy oxide (MEO). The different types of high-entropy materials and their entropic parameters are presented in Table 2.1.

Table 2.1 Quantification of entropy and new entropy metric; $\sum_{SL} a_{SL}$ is the number of atoms per formula unit and $(5M), (5N)$ are 5 different elements in given sublattice (reproduction from[32]).

Structure type	L	$\sum_{SL} a_{SL}$	$\Delta S_{conf}/R$	EM	EM classification
$(5M)$ metal	1	1	1.61	1.61	high entropy
$(5M)_1C_1$ carbide	2	2	0.80	1.61	high entropy
$(5M)_1B_1O_3$ perovskite	3	5	0.32	0.97	low entropy
$(5M)_1(5N)_1O_3$ perovskite	3	5	0.64	1.93	high entropy

3. ELECTRICAL TRANSPORT IN OXIDES

3.1 Mechanisms of charge transport in conducting oxides

Scientists have studied and described the topic of electric charge transport in perovskite oxides and oxide materials for several decades. The phenomenon of electric conduction is based on the transfer of electric charges under the influence of an electric field by mobile carriers, which can be electrons, electron-holes or ions (anions or cations). The expression for electrical conductivity can be written in the form of Equation 3.1:

$$\sigma_{tot} = \sum_i z_i e \cdot \mu_i \cdot c_i, \tag{3.1}$$

where z_i is the charge number, μ_i is the mobility and c_i is the concentration of the mobile charge carrier i.

The total electrical conductivity of a material in which ions, electrons and electron-holes are mobile can be defined as:

$$\sigma_{tot} = \sigma_{ion} + \sigma_e + \sigma_h, \tag{3.2}$$

where σ_{ion} is ionic conductivity of the material (cationic and anionic), σ_e is electronic conductivity and σ_h is electron-hole conductivity. For materials that exhibit low ionic conductivity and dominant electron/electron-hole conductivity Equation 3.2 can be reduced to the following:

$$\sigma_{tot} = \sigma_{el} = \sigma_e + \sigma_h. \tag{3.3}$$

Such a case is found in intrinsic semiconductors. For this type of materials, the conduction mechanism is a thermally activated motion of electrons and electron holes. The expression for electronic conductivity is a function of many factors, including the density of states of electron holes N_v and electrons N_c or the width of the energy band gap E_g. According to Equation 3.1, the electrical conductivity of intrinsic semiconductors can be expressed as the Arrhenius relation:

$$\sigma_{el} = e(\mu_e + \mu_h)(N_c N_v)^{1/2} e^{-\frac{E_g}{2k_B T}} = \sigma_{el}^0 e^{-\frac{E_g}{2k_B T}}, \tag{3.4}$$

where σ_{el}^0 is a pre-exponential constant of electrical conductivity and k_B denotes Boltzmann constant. Worth noting is that the intrinsic conductivity of oxide materials described by Equation 3.4, does not depend on the oxygen partial pressure[33,34]. When the thermally activated band-type electrical conduction mechanism dominates in the material, as in intrinsic semiconductors, the activation energy shown in Equation 3.4 is approximately half of the energy gap: $E_g \approx 2E_a$. Doping the material with both donors or acceptors causes a significant change in the value of electrical conductivity and affects the temperature dependence of conductivity. Charge transport in oxide materials is determined, among others, by the level of non-stoichiometry in the oxygen sublattice. In a doped semiconductor with non-stoichiometry in the oxygen sublattice, the total conductivity is determined by the concentrations and mobilities of electron/electron-holes and oxygen vacancies[35].

The so-called polaron conduction mechanism may occur in oxide materials. This mechanism refers to quasiparticles called polarons, which are formed due to the interaction of a mobile electron or electron hole with the crystal lattice, leading to its local deformation. In materials characterized by a strong interaction of electrons or electron holes with the lattice, the so-called small polaron mechanism dominates[36]. For this type of mechanism, Equation 3.5 has the form:

$$\sigma_{el}T = \sigma_{el}^{0} e^{-\frac{E_a}{k_B T}}, \tag{3.5}$$

where E_a is the activation energy of the conduction process, in this case, a small polaron hopping.

On the other hand, the ionic conductivity in crystalline materials is described by the lattice diffusion model, based on ions hopping between their positions in the crystal lattice[37]. This process is thermally activated and depends on the energy barrier of the hopping between adjacent positions. For example, in oxide materials, where the mobile charge carrier is the oxygen ion O^{2-}, the ionic conductivity can be described using Equation 3.1 as follows:

$$\sigma_{ion} = 2e\mu_{ion}c_{ion}, \tag{3.6}$$

The concentration of ionic species c_{ion} depends on many factors, mainly the temperature and enthalpy of the formation of a given defect. For materials with oxygen vacancies and vacancy-mechanism of conduction, the concentration of mobile oxygen ions depends on the deviation from stoichiometry in the oxygen sublattice δ and the temperature. Temperature dependence of oxygen ionic conductivity describes Equation 3.7:

$$\sigma_{ion}T = \sigma_{ion}^{0} e^{-\frac{E_a}{k_B T}}, \tag{3.7}$$

where σ_{ion}^{0} is a pre-exponential factor for ionic conductivity, dependent on e.g. oxygen vacancy concentration, migration entropy and lattice parameters[33,34]. It can be seen that Equations 3.5 and 3.7 are similar, due to the similarity of the electron and electron-hole hopping process in the trap state to the process of ionic diffusion through the vacancy mechanism, in which the ion mobility depends on the temperature like $\mu_{ion} \propto \frac{1}{T}$.

3.2 Proton conduction

The first works on proton conduction date back to 1964 and the work of Forrat et al. who suggested proton conduction in lanthanum aluminate[38]. However, the description of the high-temperature hydration process, through the filling of oxygen vacancies by hydroxyl ions, was proposed by Stotz and Wagner in 1966[39]. The systematic investigation of high-temperature proton conductors started with the work of Takahashi and Iwahara in 1980[40] in which they showed proton conductivity in indium-doped zirconates. Later, many oxides have been reported to reach proton conductivity between 500 and 1000 °C of at least 10^{-2} S/cm[41–43]. High-temperature ceramic proton conductors have become a field of great interest, but understanding these interesting materials is still unsatisfactory.

One of the most important features of proton-conducting oxides is that protons are not intrinsic for these materials but are present as defects originating from synthesis or in equilibrium with ambient hydrogen or water vapor[44]. Thus, the concentration and distribution of protons in the oxide structure depend not only on the composition of the material and its temperature but also on the atmosphere and the conditions of protonation. Proton conductivity requires a high proton concentration and mobility. The most commonly occurring process of proton defect formation is hydration. In this process, the water molecule dissociates into the hydroxide ion, which fills an oxygen vacancy, and the proton, which forms a covalent bond with lattice oxygen. In the Kröger-Vink notation[45], this process may be written as:

$$H_2O + V_O^{\bullet\bullet} + O_O^x \leftrightarrow 2OH_O^{\bullet}. \tag{3.8}$$

Since the hydration reaction involves oxygen vacancies, to obtain a high proton concentration in an oxide, a high concentration of $V_O^{\bullet\bullet}$ is necessary. This may be achieved by substituting one of the cations with an acceptor-type substituent. Such substitutions through ionic charge compensation lead to the formation of oxygen vacancies. At high oxygen pressure, the charge compensation mechanism involving the appearance of electron holes may also occur, which makes the material a mixed ionic-electronic conductor:

$$[h^{\bullet}] + [OH_O^{\bullet}] + 2[V_O^{\bullet\bullet}] = [Acc_B{}'], \tag{3.9}$$

where $[h^{\bullet}]$ is the concentration of electron holes, $[OH_O^{\bullet}]$ is the concentration of proton defects, $[V_O^{\bullet\bullet}]$ is the concentration of oxygen vacancies and $[Acc_B{}']$ is the concentration of acceptors in the perovskite B-sublattice.

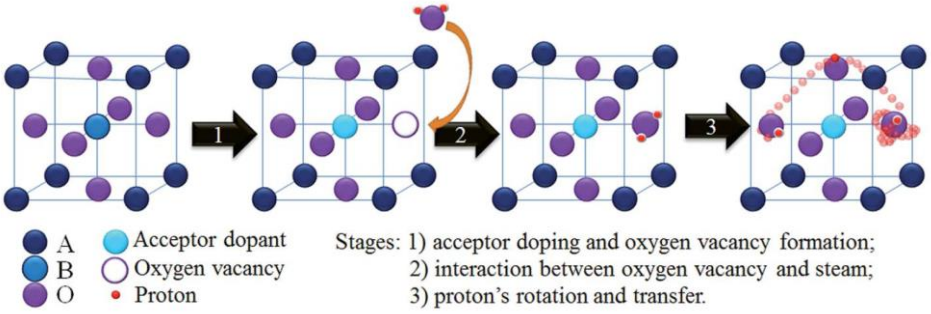

Figure 3.1 The proton defect formation and migration in the ABO_3 perovskite structure[46].

Two models of proton transport in oxide materials are considered: vehicle mechanism and hopping transport mechanism, often called Grotthuss hopping mechanism[33]. In the vehicle model, the whole proton defect $OH_O^{\bullet}$ diffuses in the system[47]. The transport may take place through oxygen vacancies or through interstitial positions. Since $OH_O^{\bullet}$ is smaller than oxygen ion, it is expected to have lower activation energy of diffusion than oxygen ion. The second hopping transport model treats proton movement separately from oxygen[46]. The scheme of the proton defect formation and migration is presented in Figure 3.1. As can be seen, the hopping mechanism involves two stages: the rotation of the proton around the oxygen that forms a proton defect and the proton transfer to a neighboring oxygen ion. After such a sequence, the proton reorients itself in the electron cloud of

the new oxygen and aligns for the next jump. The rotation and reorientation involve a low activation energy, below 0.1 eV thus, the jump of the proton is the most crucial part that defines the proton transport rate. Overall, the bond between oxygen and hydrogen in proton defect is weaker than in hydroxyl ion. Thus, protons are more likely to move as individual particles, making the hopping mechanism the principal mode of proton transport in oxides.

Considering the free transport mechanism, the oxygen sublattice should be dynamic for the high mobility of protons. This means that polarizable, large cations and lattices with low packing factors support the high mobility of protons. In contrast, small cations and dense, stiff oxygen sublattices promote lower mobility of protons and higher activation energy of proton conduction. The transport of protons in oxides is a thermally activated process, so it can be described similarly to oxygen ions transport (Equation 3.7). For the hopping mechanism, activation energy is correlated with the energy required to break the bond between oxygen and hydrogen and to move the proton to another oxygen in the lattice.

4. PEROVSKITE OXIDES

4.1 General information

Perovskite oxides, which are oxides of alkali metals, alkaline earth metals and transition metals, are a significant subgroup of ceramic materials with diverse properties. The first discovered perovskite was calcium titanate, with the structural formula $CaTiO_3$, found in the Ural Mountains in 1839 by the German chemist and mineralogist Gustav Rose. Its name, 'perovskite', originates from the last name of the Russian mineralogist Lev Perovsky. The crystal structure of calcium titanite was first described by Victor Goldschmidt in 1926 in a work describing the mismatch factor, which indicates the stability and deformation of perovskite crystal structures[48]. The group of perovskite minerals includes compounds that crystallize in the same or similar structure to $CaTiO_3$. The first diffraction pattern of a perovskite crystal structure was presented later, in 1945, thanks to the research of Helen Dick Megaw on barium titanate $BaTiO_3$[49].

The ideal perovskite is described by the general formula ABX_3, where A and B are alkali metals, alkaline earth metals or transition metal cations. X is most often an oxygen anion but can also be a halogen anion. The A cation has a larger ionic radius than the B cation. The oxidation states of the A and B cations in perovskites should sum up to 6, so there are three possible combinations of atomic charges: 1 + 5, 2 + 4 and 3 + 3[50]. The ideal perovskite structure is a cubic structure with the space group $Pm\bar{3}m$ (no. 221), in which the A cations with the coordination number of 12 occupy the positions in the eight corners of the cube, and the B cation with the coordination number 6 is located in the geometric center of the cell and is surrounded by six X anions. The B cations surrounded by X anions form a BX_6 octahedron. The unit cell diagram of the ABX_3 perovskite is shown in Figure 4.1.

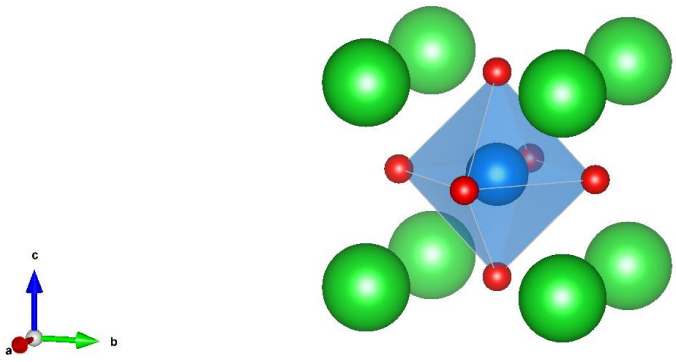

Figure 4.1 Exemplary unit cell of ABX_3 perovskite, simulated in VESTA[51].

The stability of a given perovskite depends largely on the properties of the bonds in the octahedron shown in Figure 4.1 and on the location of the B cation in its center. Helen Dick Megaw was the first to propose the formulation of the parameter that would determine the stability of the perovskite in terms of the anions and cations present in the structure. Although, the relation was lastly established by Victor Goldschmidt, in accordance with the following reasoning[48].

Taking into account the geometry of the previously described, ideal perovskite oxide structure with the unit cell edge length equal to a, one can conclude that: the distance from the centers of A and X atoms is $a/\sqrt{2}$; the distance from the centers of B and X atoms is $a/2$. This allows to formulate the following relation[35]:

$$r_A + r_X = \sqrt{2}(r_B + r_X), \tag{4.1}$$

where r_A is the ionic radius of cation A, $\mathrm{r_B}$ is the ionic radius of cation B and $\mathrm{r_X}$ is the ionic radius of anion X. As a consequence of the above relation, Victor Goldschmidt determined the tolerance factor t, also called the Goldschmidt factor, described by the equation[35]:

$$t = \frac{r_A + r_X}{\sqrt{2}(r_B + r_X)}. \tag{4.2}$$

The highest stability is characteristic for perovskites for which the Goldschmidt factor ranges from 0.8 to 1.05. The structure is more isometric when the t value is closer to 1. For t equal to 1, the structure is not strained. This situation occurs for barium zirconate with the formula $BaZrO_3$, crystallizing in a cubic system. The crystallographic structure of perovskites can also be tetragonal, trigonal or other, similar to the above structures, but with even lower symmetry. When radius of cation A increases, the factor t is larger than 1. In the case when radius of cation B increases, Goldschmidt factor is lower than 1[52]. The factor t is also correlated with the packing of atoms in the crystal lattice; e.g. for t < 1, the lattice is densely packed. The crystallographic structures and Goldschmidt factor values for selected perovskite oxides are gathered in Table 4.1.

Table 4.1 Goldschmidt factor values and crystal structure of selected perovskite oxides.

Compound	Formula	Tolerance factor	Crystallographic system
Barium zirconate[53]	$BaZrO_3$	1.01	Cubic
Barium cerate[52]	$BaCeO_3$	0.94	Cubic
Barium titanate[54]	$BaTiO_3$	1.07	Tetragonal
Barium stannate[55]	$BaSnO_3$	1.03	Cubic
Barium hafnate[56]	$BaHfO_3$	1.02	Cubic

The deviation from symmetry in perovskite materials is assumed to be caused by the octahedra tilting. This phenomenon is strongly composition-dependent. It occurs when the ionic radius of the A cation is not large enough for the ions to fill the entire volume that can be occupied. As a result, at a given temperature, the octahedra tilt reduces the cubo-octahedral space in the oxygen sublattice. The degree of deviation depends on the Goldschmidt factor t, temperature and material composition[52]. Possible configurations of octahedra are shown in Figure 4.2.

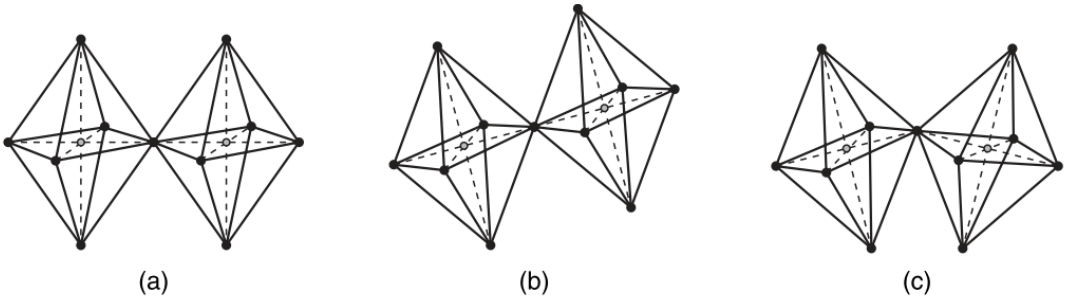

Figure 4.2 Possible arrangement of BX_6 octahedra in perovskites: a) untilted, b) tilted in the same phase, c) tilted in opposite phase[57].

Due to their diverse properties, perovskites are used in various fields. Materials with a perovskite structure can be pyro- or piezoelectrics, dielectrics, conductors of various types (electronic, ionic, mixed), and superconductors. They can also exhibit nonlinear optical effects, and can be used in electronics, electrical engineering, electrochemistry, energy and optics. In the following subsection, examples of perovskite materials and their properties, with the emphasis on electrical properties, will be discussed.

4.2 Selected properties of Ba(Ce,Zr)O_3 proton conductors

The most researched and important perovskite oxides in the context of this thesis are barium cerate $BaCeO_3$ and barium zirconate $BaZrO_3$.

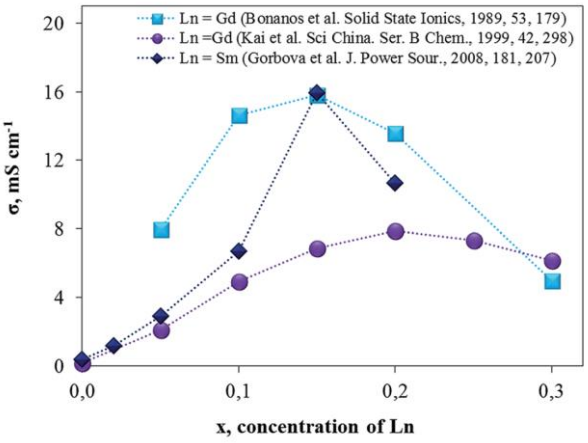

Figure 4.3 Electrical conductivity of $BaCe_{1-x}Ln_xO_{3-\delta}$ materials at 600 °C in wet air[58].

The materials based on the barium cerate exhibit the highest proton conductivity among other ceramic proton conductors[46]. It might be caused by the large ionic radii of barium and cerium that promote the formation of wide channels for protons to pass through. Undoped $BaCeO_3$ exhibit three phase transitions in the temperature range between room temperature and 1000 °C[59]. At 300 °C it undergoes the second-order transition concerning polymorphous change of an orthorhombic perovskite structure from $Pmcn$ to $Incn$. Around 400 °C first-order transition from orthorhombic $Incn$ to rhombohedral $R3c$ occurs. At high temperatures (~900 °C) second-order transition between the rhombohedral and cubic ($Pm\bar{3}m$) structure takes place. To stabilize desirable

phases doping with various elements is employed[60]. $BaCeO_3$ is usually substituted with other rare-earth metals in the place of cerium to tune up the proton conductivity through acceptor doping. It can be seen in Figure 4.3, the optimal concentration of acceptor ranges from 10 to 25 mol%. Further introduction of the substituents results in the formation of defect associates that impede the proton conductivity. The main problem with $BaCeO_3$-based materials is related to the thermodynamic stability of the material in the presence of water or acidic compounds e.g. H_2S or CO_2. The co-doping strategy was employed to overcome this issue, but in the end, stability was achieved at the expense of the proton conductivity level[46].

Barium zirconate-based materials exhibit exceptional stability under various environmental conditions[46]. This results from a shorter and stronger Zr-O bond than Ce-O, producing a nearly ideal tolerance factor t = 1.004. Barium zirconate retains its cubic perovskite structure down to 2 K[61]. One of the often used acceptors for $BaZrO_3$ is yttrium, which provides high bulk proton conductivity in the 300-600 °C range and robust thermodynamic stability[62]. The influence of yttrium substituent concentration on the electrical conductivity is presented in Figure 4.4. However, the problem in systems based on barium zirconate is high grain boundary resistance. Due to high sintering temperatures required to achieve dense material (1800-2000 °C), barium zirconates pose a great challenge in the synthesis process. If the temperature is not high enough, the microstructure will not be properly resolved, and grain boundaries will decrease the electrical conductivity. If the temperature is sufficiently high, there is a high risk of barium evaporation that will influence the chemical composition at the grain boundary, creating residual phases that will block the charge transport. Wet chemistry methods were employed to decrease the synthesis and sintering temperature[63,64], or sintering aids were added during the sintering step[58,65].

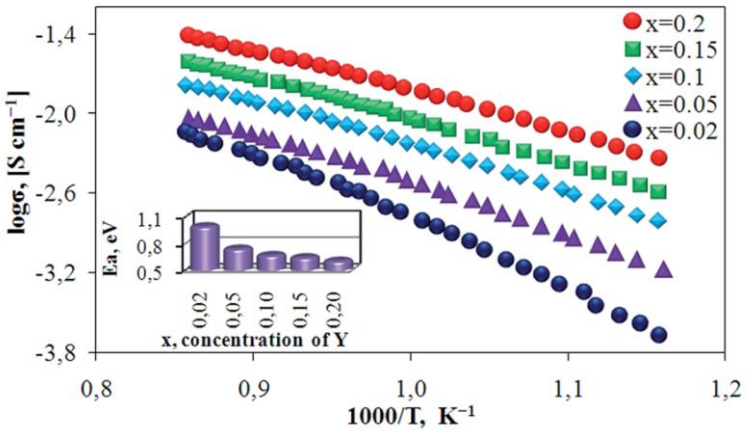

Figure 4.4 Total electrical conductivity and activation energy for conduction of $BaZr_{1-x}Y_xO_{3-\delta}$ in dry air[66].

To achieve a consensus between the proton conductivity level and material stability, solid solutions of $BaZrO_3$ and $BaCeO_3$ were synthesized. By varying the amounts of cerium, zirconium, and acceptor dopant, it is possible to obtain many compositions with suitable properties. The influence of Zr content on the total electrical conductivity of BCZY in wet air is presented in Figure 4.5. Compositions containing 10 mol% of yttrium exhibit significant conductivity decrease after introducing zirconium, retaining the value with increasing amounts of Zr. On the other hand,

for the solid solution with 20 mol% of Y, the exchange of cerium with zirconium results in nearly one order of magnitude decrease in electrical conductivity. In Figure 4.6. the total electrical conductivity of $BaCe_{0.5}Zr_{0.3}Ln_{0.2}O_{3-\delta}$ with different substituting elements is shown. The conductivity level and activation energy change depend on the lanthanide introduced. Also, different dopants modify the electrical conductivity behavior with the change of ambient gas.

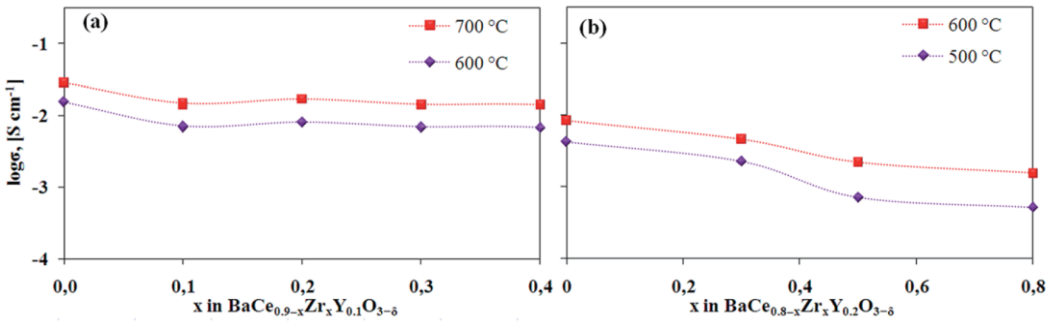

Figure 4.5 Influence of increasing Zr content on the total electrical conductivity in a) $BaCe_{0.9-x}Zr_xY_{0.1}O_{3-\delta}$, b) $BaCe_{0.8-x}Zr_xY_{0.2}O_{3-\delta}$ in wet air[67,68].

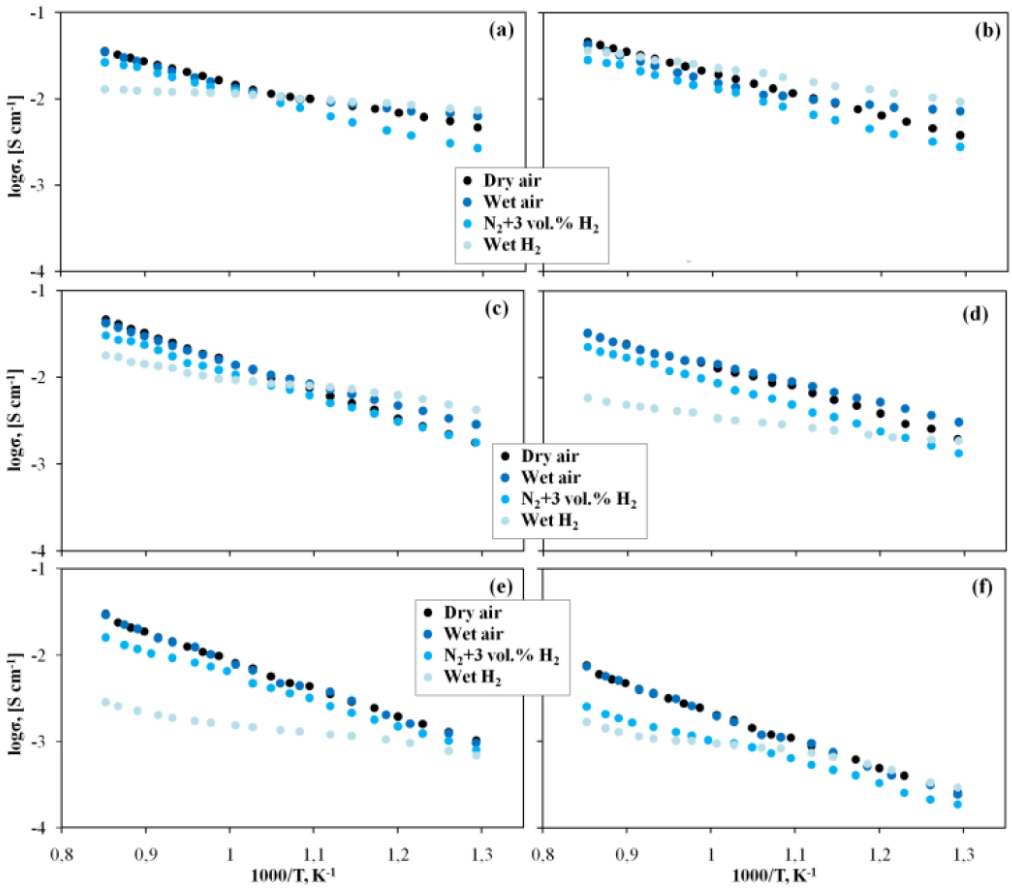

Figure 4.6 The temperature dependences of conductivity for $BaCe_{0.5}Zr_{0.3}Ln_{0.2}O_{3-\delta}$ ceramics in different atmospheres: a) Ln = Yb, b) Ln = Y, c) Ln = Gd, d) Ln = Sm, e) Ln = Nd and f) Ln = La[69].

5. EXPERIMENTAL PROCEDURES

5.1 Solid-state synthesis

The synthesis of the samples utilized the solid-state reaction method. This synthesis method was chosen based on previous literature reports describing the synthesis of high entropy perovskite oxides[21].

The samples were formed under high-temperature conditions from constituent oxides and carbonates mixed in stoichiometric amounts. In most cases, the synthesis consisted of two steps of high-temperature treatment; however, some compounds needed only one step of heat treatment. Reactants were first mixed and ground in a planetary ball mill with zirconia grinding bowls and balls for high homogeneity and intimate contact. The rotation speed was 600 rpm, the BPR (ball-to-powder ratio) was equal to 3:1, and one whole milling procedure was divided into 24 cycles, where each cycle consisted of 50 min of milling and 10 min of pause. The first synthesis step, calcination, was conducted to remove the carbonate residues of barium carbonate. Using barium carbonate as a reactant in solid-state synthesis provides a large number of nucleation sites. Because of that, the reaction proceeds at a high rate. Heating the powders at 950 °C for 24 h with a heating/cooling rate of 5 °C per minute and synthetic air flux was enough to decompose all the present carbonates. Thus, the obtained powders were pressed into pellets with a diameter of 12 mm using a cylindrical die and a uniaxial pressure of 350 MPa generated by a hydraulic press. The second step of synthesis was the main one in which the samples in the form of pellets were heated in a furnace at a rate of 5 °C per minute to a temperature varying from 1100 °C to 1500 °C. After dwelling at the target temperature for 10 h, the samples were cooled with the furnace. An additional procedure was applied if the obtained pellets did not reach a relative density above 90%. First, the powders from the first synthesis step were manually ground in 2-propanol with 1 wt% polyvinyl butyral (PVB) or 1 wt% NiO, or both. PVB was added as a binder to aid powder densification during pressing[70], while NiO acts as a sintering aid[71]. After this, the mixture is dried at 80 °C for 24 h and pelletized as previously mentioned.

5.2 X-Ray Diffraction

X-Ray Diffraction (XRD) is one of many non-destructive analysis techniques that can give information about solid-state materials' phase composition, crystallinity, and crystal structure. The idea of this technique is to emit X-ray radiation on a sample and collect reflected beams in a detector. X-rays are used because their wavelengths are comparable to the distances between crystal planes, which in turn allows diffraction to occur, according to Braggs' Law:

$$n\lambda = 2d \sin\theta, \tag{5.1}$$

where n is a diffraction order, λ is wavelength of incident beam, d is the interplanar distance and θ is X-ray diffraction reflection angle.

As a result of constructive and destructive interference of the reflected beams, a diffraction pattern in the form of peaks (for polycrystalline samples) or dots (for monocrystals) is obtained. There are two ways to perform the analysis. In classic Bragg diffraction, monochromatic radiation is applied to a sample and the incidence and reflection angle change. In Laue diffraction, the angles are fixed, and the analysis is performed as a function of the wavelength. Moreover, apart from the mode of analysis, we can also distinguish two analysis geometries: reflective (Bragg-Brentano) and transmissive (Debye-Scherrer). For monochromatic sources, X-ray tubes that emit radiation with a wavelength depending on the anode material (e.g. Cu or Mo) are used. Also, synchrotron radiation may be a monochromatic source of high intensity and brightness.

In my doctoral research, a Phillips X'Pert PRO MDP diffractometer with an X-ray source based on the copper anode ($\lambda_{K_{\alpha_1}}$ = 1.54056 Å and $\lambda_{K_{\alpha_2}}$ = 1.54439 Å) was used. This diffractometer operates in the Bragg-Brentano geometry with θ-θ PW3050/60 goniometer and 1D PIXCEL detector. X-ray diffraction measurements were carried out under 40 kV and 30 mA, at room temperature in air. High-temperature X-ray analyses have been performed in the temperature range between room temperature and 800 °C using an Anthon-Paar high-temperature camera. The phase analysis and Rietveld refinements of the patterns were done using HighScore Plus software[72]. For strain and grain size analysis, LaB_6 was used as a standard.

5.3 Dilatometry

Dilatometry measurements were performed to acquire information about the thermal properties of bulk materials. The idea behind it is simple – a sample placed in a measuring unit is subjected to a small initial force in one direction, and a change in length upon different conditions (temperature, time, atmosphere) is recorded. By performing measurements in other directions, it is possible to gain information on whether or not isotropic effects occur in the sample.

This technique has been used to formulate the time-temperature-transformation (TTT) diagrams for steels or establish glass transition temperatures in polymers[73]. In the case of ceramics, dilatometry is frequently used to determine the phase transition temperatures[74], shrinkage rate on account of sintering[75,76] and most importantly, the thermal expansion coefficient (TEC[1])[77,78].

In general, TEC is given as a temperature derivative of strain ε:

$$\alpha(T) = \frac{d\varepsilon}{dT}. \tag{5.2}$$

For materials that do not exhibit phase transition in a given temperature range, Equation 5.2 can be rewritten as:

$$\varepsilon(T) \cong \varepsilon(T_0) + \alpha(T - T_0). \tag{5.3}$$

[1] Often in literature one can find also CTE as the abbreviation, which stands for 'coefficient of thermal expansion'

Generally, there is always some strain in the structure, but for calculations at high temperatures (starting from 300 K), one can assume that $\varepsilon(T_0) = 0$. Additionally, strain is defined as the relative change of length l of the sample:

$$\varepsilon(T) = \frac{l(T) - l(T_0)}{l(T_0)}. \tag{5.4}$$

To evaluate the thermal expansion coefficients of the materials, dilatometry measurements were performed using the Netzsch 402 PC/4 instrument. Measurements were carried out on samples in the form of bars of length 18 mm. The temperature program of the measurement consists of heating at a rate of 2 °C/min from room temperature to 800 °C and cooling down at the same rate. During this temperature cycle, the flux of dry synthetic air ($pO_2 \approx 0.21$ atm, $pH_2O \approx 6 \times 10^{-5}$ atm) with 50 ml/min flow was set.

5.4 X-Ray Absorption Spectroscopy

X-Ray Absorption Spectroscopy (XAS) is a method that involves the usage of high-energy photons to excite the electrons from the closed shells of an atom, called core electrons, and observing the absorption profile as a function of the energy of photons, according to the basic absorption principle:

$$I_1(E) = I_0(E) \cdot e^{-\mu(E)x}, \tag{5.5}$$

where $I_0(E)$ is the intensity of an incident photon beam with energy E, $I_1(E)$ is the intensity of the beam after the interaction with the sample, $\mu(E)$ is a linear absorption coefficient and x is the sample thickness.

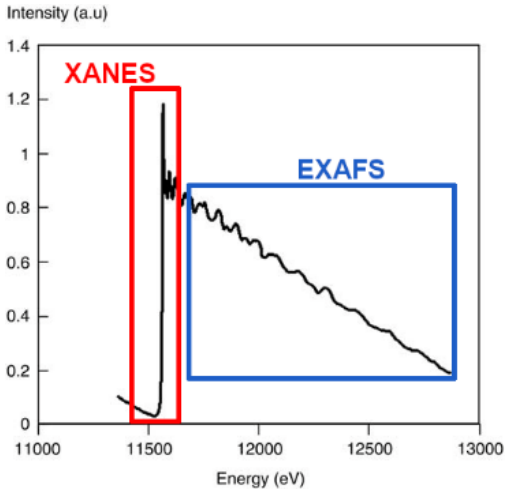

Figure 5.1 L_3 edge of platinum metal with marked two distinctive parts of XAS spectra[79].

The energy range used in these measurements starts from fractions of keV to dozens of keV, depending on the shell from which we would like to transfer the electron. Each atom has a few possible shells to work with, each with discrete values of energy (called binding energy) that are necessary to move the electron from its bound state to the lowest available unoccupied state.

Exciting electrons from the 1s orbital is referred to as examining the K edge, from 2s and 2p orbitals as L edge, etc.

A typical absorption edge is presented in Figure 5.1. One can distinguish two prominent features in the spectra[80]: XANES (X-ray Absorption Near Edge Spectra) and EXAFS (Extended X-ray Absorption Fine Structure). XANES region concerns the energy range of about 50 eV around the absorption edge, whereas EXAFS comprises oscillations far behind the XANES region, even above 1 keV. In the first region, we can further discern the pre-edge peak, actual edge and NEXAFS (Near-Edge X-ray Absorption Fine Structure). By analyzing the XANES region, it is possible to derive information about the electronic and geometric state of an atom, i.e. the coordination adopted by the atom, its valence state, orbitals' hybridization (crystal/ligand field) and type of ligands from the scattering of induced photoelectrons. It also serves as a 'fingerprint' of an atom in an exact environment of a given material. On the other hand, from the EXAFS region, we can obtain geometrical information such as the distance of nearest neighbors around the examined atom and their number.

XAS measurements can be conducted in different configurations, depending on the type of detected signal:

- transmission detection – classic measurement mode using I_0 and I_1 to evaluate the absorption of the sample, preferable for high energy photons (hard X-rays), susceptible to sample's thickness variations and inhomogeneity but covers the whole cross-section of the sample,
- fluorescence yield – in this mode, the signal is collected in the form of fluorescent decay of a core hole, usable in a wide range of photon energy, suitable for dilute materials, in more concentrated samples, saturation and self-absorption take place,
- electron yield – absorption cross-section of the material is evaluated based on the detected electrons emerging from the sample, used in low vacuum and with soft X-rays, a signal is gathered from a few nanometer layers of the surface,
- ion yield – there is a possibility of creating positive ions on the surface during core hole decay; analysis of escaping ions as a function of X-ray energy can yield information about the absorption, and it is a very surface-sensitive technique.

In this thesis, XAS measurements were conducted on the LISA beamline at the European Synchrotron Radiation Facility in Grenoble. XANES and EXAFS regions for the following edges: K-edges of titanium (4.9664 keV), zirconium (17.9976 keV), tin (29.2001 keV), yttrium (17.0384 keV), indium (27.9399 keV) and L_3-edges of barium (5.2470 keV), hafnium (9.5607 keV), ytterbium (8.9436 keV), samarium (6.7162 keV) were examined. The data acquisition was performed using transmission or fluorescence detection. Post-processing of obtained results and analysis of EXAFS data were performed using the DEMETER software package.

5.5 Scanning electron microscopy

Scanning electron microscopy (SEM) is a technique that provides information about the surface and microstructure of the considered samples. In contrast to standard microscopes using visible light, electron microscopy offers much more detailed insight and a wider range of extractable information. A scanning electron microscope consists of a source of electrons, a system of electron beam formation, and detectors. Electrons in the source guns are generated by thermal emission, field emission, or a combination of both (Schottky emission). Thus, the generated beam is accelerated in the electric field and concentrated by sets of electromagnets to give a 'spot' of a specific size at the end. Upon interaction of the beam with the sample, multiple events happen, depending on the electron penetration depth, which is related to the acceleration voltage. Three types of signals may be detected:

- secondary electrons (SE) – electrons emitted from the examined specimen after being excited by the electrons of the beam,
- backscattered electrons (BSE) – elastically reflected electrons originating from the scanning beam,
- characteristic X-ray radiation – the radiation emitted by the atoms of the specimen, excited by the interaction of beam electrons. Its energy is characteristic of the element.

The secondary electron signal collected with the Everhart-Thornley Detector (ETD) gives a high-resolution image, the brightness of which depends on the surface morphology. On the other hand, the backscattered electron detector (BSED) collects the information from deeper parts of the sample. The image seems to be more 'flat', but thanks to the dependence of the color intensity on the atomic number difference it points out the occurrence of different atomic compositions. Characteristic X-ray radiation is detected by two types of spectrometers: energy-dispersive (EDS) or wavelength-dispersive (WDS) and gives information on the atomic composition of the specimen. It is possible to perform mapping of elements, which can provide information about sample homogeneity and possible element separation in a studied material.

In this work, the morphology of cross-sections of HEO samples was studied by a FEI Quanta FEG 250 scanning electron microscope. The imaging was performed with secondary electrons using the Everhart-Thornley detector and with backscattered electrons using BSED. Each experiment was carried out under high vacuum conditions (10^{-5} mbar) with an acceleration voltage of 20 kV. The distribution of elements in all compounds were analyzed with Thermo Fisher Scientific Phenom XL utilizing an EDS detector.

5.6 Thermal analysis

The thermal analysis in this work was conducted using various thermogravimetric measurements and high-temperature drop calorimetry.

The thermogravimetric (TG) analysis principle is that a sample weight is measured as a function of temperature during heating or cooling in a precisely controlled atmosphere. Various reactions can be observed depending on the selected measurement setup, like decomposition, crystallization, oxidation, reduction, etc. TG analysis may be combined with differential scanning calorimetry (DSC) to obtain more information about the ongoing reactions. Furthermore, detecting gases emitted from the sample during the experiment is also possible. A special quadrupole mass spectrometer attached to a gas outlet is used. This helps further in the interpretation of reactions that take place in the measured sample. Such an examination is called evolved gas analysis (EGA).

In this work, thermogravimetric analysis was utilized to determine the water uptake. If a sample is held in the stabilized environment of a dry gas, e.g. air, upon the change to the humidified environment, a sample's mass may change. The mass changes under various conditions depend on water incorporation or desorption processes. After the acquisition of the mass change, one can calculate the protonic defect concentration from the following equation:

$$[OH_O^{\bullet}] = \frac{2\Delta m \cdot m_C}{m_{H2O} m}, \tag{5.6}$$

where m_{H2O} is the molar mass of water, m_C is the molar mass of the analysed compound, m is the mass of the sample powder, and Δm is the mass change determined from the TG curve. Carrying out this analysis in different temperatures makes it possible to determine the temperature dependence of proton defect concentration, enabling one to calculate the enthalpy of protonic defect creation.

TG analysis of water uptake was performed using a Netzsch Jupiter® 449 F1 instrument (Netzsch GmbH, Selb, Germany). Approximately 1.5 grams of as-prepared powder was placed in an alumina 5 ml crucible, heated to 800°C and held at this temperature for 5 h under dry air to remove water and surface carbon dioxide. To perform the isothermal measurement, the sample was cooled to 300 °C and held for 2 h to reach equilibrium. Subsequently, the switch was made from dry ($pH_2O \approx 6 \times 10^{-5}$ atm) to humidified ($pH_2O \approx 1.9 \times 10^{-2}$ atm) air. The flowing gas (synthetic air or nitrogen) was thus saturated with water and the weight change was recorded. After 2 h the purge gas was switched back to dry. For isobaric measurements, water partial pressure was changed at 800 °C and remained fixed for the whole measurement. The temperature was changed by 50 °C every 3h to reach equilibrium until 300 °C was reached. Before each measurement, a blank run was performed to determine the baseline correction.

Calorimetry studies refer to measurements conducted to gain insight into heat changes in examined materials. Those changes can be caused by chemical or physical reactions occurring during the measurement e.g. decomposition, first-order phase transitions (e.g. melting) or second-order phase transitions (e.g. magnetic transformations). By examining the changes quantitatively, one can derive the enthalpies of the considered reaction, which then allows to estimate the entropy and free Gibbs enthalpy values[81].

Depending on the type of calorimeter, different types of enthalpies can be derived. One of the most frequently used techniques is differential calorimetry, namely DTA (Differential Thermal Analysis) and DSC (Differential Scanning Calorimetry). During the measurement, the studied and reference materials undergo the same thermal cycle (heating/cooling) and changes in heat flux are recorded. This way, it is possible to derive the crystallization or glass transition enthalpies. Another technique is bomb calorimetry, which allows the determination of the heat of combustion by igniting the sample in a strongly isolated measuring unit and observing the temperature evolution in the system. The bomb calorimetry is commercially used in food and military industries.

The technique used in this thesis – drop calorimetry – enables us to determine the specific heat or enthalpy of formation by examining the heat effects during the dropping of the sample into the calorimeter chamber. In Figure 5.2, the schematic of the exemplary drop calorimeter is presented. Generally, the whole measuring unit consists of a large thermally isolated enclosure with high thermal capacity and two measuring chambers with narrow tubes allowing the dropping of samples inside. Two chambers are required for the measurement since the second one serves as a reference for heat flux change. The measurement can be conducted in two ways:

- the heated sample is dropped into the calorimeter maintained at room temperature,
- the sample at room temperature is dropped into the calorimeter held at elevated temperature.

After introducing the sample, a change in heat flux is recorded by thermopiles, which transform the thermal signal into an electrical one. This analogue signal is then recalculated to give information about released or absorbed heat in the system[82]. In a heated calorimeter, pure (single-phase) samples, and a mixture of substances, can be examined. In the first case, the heat content and specific heat can be derived. In the latter case, the enthalpies of reaction or formation can be achieved. Additionally, one can use a particular solvent to obtain the formation enthalpy for pure samples through dissolution. The most frequently used solvents are lead borate ($2PbO \cdot B_2O_3$) and sodium molybdate ($3Na_2O \cdot 4MoO_3$) because they are suitable to dissolve various oxides[83,84]. The most important concerns relating to this type of measurement are precise calibration of the calorimeter cell and reasonable temperature control of the whole device.

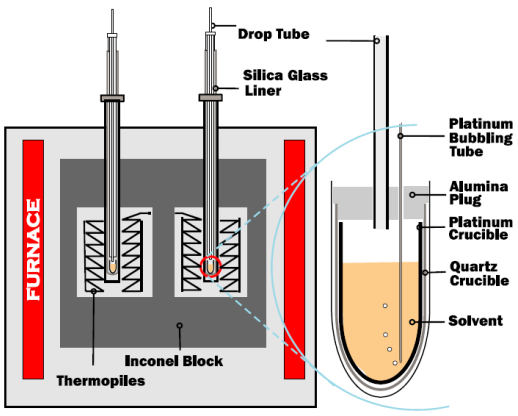

Figure 5.2 Schematic of twin-Calvet calorimeter used in high-temperature drop calorimetry[84].

On pre-dried samples, high-temperature oxide melt solution calorimetry was carried out using a Setaram AlexSYS Tian-Calvet twin microcalorimeter. The calorimeter was calibrated against the heat content of high-purity α-Al_2O_3 (99.99%). Pressed sample pellets (~5 mg) were dropped from ambient temperature into the calorimeter containing the solvent in the form of molten sodium molybdate ($3Na_2O \cdot 4MoO_3$), in a silica glass crucible at 800 °C. All experiments used oxygen bubbling through the solvent at 5 mL/min to aid dissolution and prevent local saturation of the solvent. To achieve statistically reliable data, the measurements for each sample were repeated several times.

5.7 Electrical measurements

Determining the electrical transport properties of materials is based on supplying the studied sample with an electrical signal and detecting the electrical response of another kind. For example, a sample is supplied with an electrical current and a voltage drop is measured. The information that can be extracted from the results depends on the selected setup and the measurement conditions. Those selected conditions are, for example, a type of ambient gas, the temperature range, or a combination of the two. The most essential decision is whether to use direct current (DC) or alternating current (AC). Using direct current to study materials with low electronic conductivity may lead to some parasitic effects, such as double-layer formation. AC measurements are more appropriate for studying such materials as ionic conductors, especially if one performs AC measurements as a function of frequency. Then, valuable information can be derived from the results. Such an experimental methodology is used in electrochemical impedance spectroscopy (EIS). Every electrical phenomenon occurring in the material depends on the supplied current frequency. It is connected with different relaxation times of ongoing processes. By using EIS, one can acquire full information about a sample complex impedance:

$$Z(\omega) = \frac{E}{I} = Z_0 exp(i\varphi) = Z' + iZ'', \tag{5.7}$$

where $E = E_0 exp(i\omega t)$ is supplied voltage, E_0 - the voltage amplitude; $I = I_0 \exp\big(i(\omega t + \varphi)\big)$ is current response, I_0 - the current amplitude; φ is phase shift; Z' is the real part of impedance and Z'' is the imaginary part of the impedance. By plotting results in $Z''(Z')$ coordinates, one acquires a Nyquist plot where charge transport processes are differentiated by their time constants corresponding to individual semicircles. This, in turn, allows one to distinguish the contributions of the conductivity of grains, grain boundaries, and other conduction mechanisms. The Bode plots should be considered to get information about the sample impedance as a function of the applied signal's frequency.

From each Nyquist plot, the information about resistivity and capacitance of specific processes can be derived. With the usage of the resistances, it is possible to calculate the overall conductivity of the material σ_{tot} as well as partial grain σ_g and grain boundary σ_{gb} conductivities:

$$\sigma_i = \left(\frac{l}{S} \cdot \frac{1}{R_i}\right) \cdot {\rho_{rel}}^{-3/2}, \tag{5.8}$$

where R_i – resistance corresponding to the selected process, l – distance between working electrodes, S – electrode surface area, ρ_{rel} – relative density of the sample. The ${\rho_{rel}}^{-3/2}$ part is called Bruggeman factor and is often incorporated to the calculations to compensate non-ideal densification of the sample pellet[85,86].

The conductivity of grain boundaries calculated with Equation 5.8 is, in fact, apparent. Grain boundaries fill only a small part of the sample volume and the geometric factor $\frac{l}{S}$ is insufficient to obtain the specific grain boundary conductivity. To achieve this, it is necessary to assume a microstructure model representing the material. For ceramic materials, the most reliable and well-regarded microstructure model is the Brick Layer Model (BLM)[87]. In this model, the polycrystalline material consists of uniformly distributed cubic grains, forming a characteristic brick wall pattern. According to this model, the specific grain boundary conductivity can be established as:

$$\sigma_{gb-spec} = \sigma_{gb} \cdot \frac{C_g}{C_{gb}}, \tag{5.9}$$

where σ_{gb} is obtained from Equation 5.8 and C_g, C_{gb} correspond to capacitances of grains and grain boundaries, respectively.

Two configurations (2- and 4-probe) of electrical measurements may be applied. If the studied materials are of high resistance, a 2-probe method can be applied. In this case, two electrodes deposited on the sample surface are connected with a measuring device by two metal wires composed of highly conducting material, i.e. silver, gold, or platinum (as depicted in Figure 5.3a). If the sample resistance is low (single ohms or even less), another configuration must be considered. The four-probe configuration is used to eliminate the ohmic contribution of the wires and electrodes. The external electrodes apply the known electric current, while the internal electrodes measure the voltage drop (Figure 5.3b). Knowing the resistance of the sample, the distance between the internal electrodes and the dimensions of the sample, the conductivity of the material can be determined. For the deposition of electrodes on the sample surface, evaporation, sputtering, or brush painting of a special paste are used. Silver and gold paste are often used for good electronic conductors such as materials with pure electronic conductivity. However, it tends to block oxygen movement in an ionic conductor. Porous platinum electrodes are more suitable for this type of samples since they are reversible for oxygen.

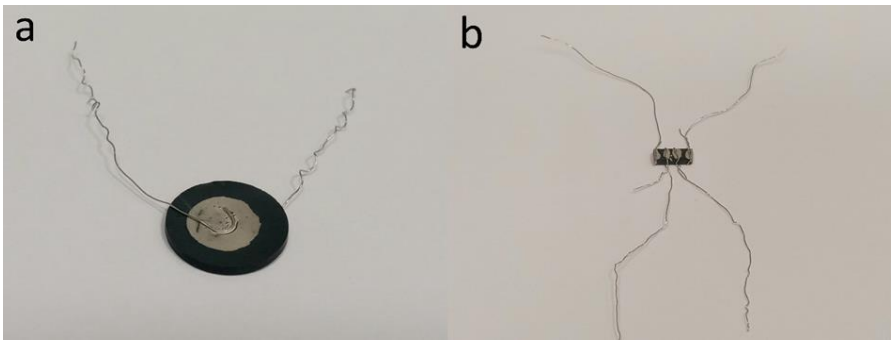

Figure 5.3 Examples of samples with a) 2-probe configuration and b) 4-probe configuration.

The aim of studying the electrical properties of ceramics in atmospheres with different water vapor pressures was to find ones that can conduct protons. If the conductivity is higher in the humidified gas than in the dry one, it confirms the occurrence of the hydration reaction (Equation 3.8) and suggests the proton conductivity. To further confirm the contribution of protons to electrical conductivity, measurements carried out using D_2O as a humidifying agent are necessary. Since deuterium ions behave as 'heavy protons' if they participate in the conduction process, the conductivity in the atmosphere containing D_2O is expected to be lower than in the atmosphere humidified with H_2O. If the conductivity of the sample in D_2O is between those in H_2O and dry atmosphere, then one can say that the isotope effect is present and proton conductivity is confirmed.

Primarily, electrical measurements are performed when the sample reaches a steady state. However, some electrical measurement techniques are concerned with the continuous observation of the output signal, after the abrupt change of one of the measurement conditions - temperature or water/oxygen partial pressure. One such technique is electrical conductivity relaxation (ECR)[88]. The essence of this method is a fast change of the chemical potential of oxygen in the atmosphere surrounding the sample. After some time, due to the incorporation or release of oxygen from the structure in the sample, a new thermodynamic equilibrium is established. Experimentally, an abrupt change in the chemical potential of oxygen is obtained by a rapid gas exchange in the chamber with the sample, after which the conductivity of the sample is measured as a function of time. The same idea can be applied to measurements conducted during the hydration of the sample.

From the obtained curves, it is possible to attain the kinetic parameters describing ionic transport, namely the chemical diffusion coefficient D_{chem} and the chemical surface exchange coefficient k_{chem}. These two parameters are connected by the I Fick's law, concerning the flux of ionic species J at the surfaces of the flat, thin sheet of material:

$$J = -D_{chem}\frac{\partial C}{\partial x} = k_{chem}[C(x,t) - C_\infty], \tag{5.10}$$

where $C(x,t)$ is the concentration of considered species in specific position and time, and C_∞ is the concentration after the equilibrium in new conditions is reached. Above equation can be solved analytically and for one-dimensional profile of charge carrier concentration $C(x,t)$ presents itself as follows[89]:

$$\frac{C(x,t)-C_0}{C_\infty-C_0} = 1 - \sum_{n=1}^{\infty}\frac{2L_B\cdot\cos\left(\frac{2\beta_n x}{l}\right)}{(\beta_n^2+L_B^2+L_B)\cos(\beta_n)}\exp\left(-\frac{4\beta_n^2\cdot D_{chem}\cdot t}{l^2}\right), \tag{5.11}$$

where l is the thickness of the sample, C_0 is the initial ionic concentration, β_n are the non-zero roots of the following function:

$$\beta_n \tan\beta_n = L_B, \tag{5.12}$$

where L is a dimensionless parameter called Biot number and is defined:

$$L_B = \frac{l}{2}\cdot\frac{k_{chem}}{D_{chem}}. \tag{5.13}$$

Additionally, by assuming that there is a linear dependence between concentration and electrical conductivity, one can rewrite the concentration expression from Equation 5.11 into conductivity:

$$\frac{C(x,t)-C_0}{C_\infty-C_0} = \frac{\sigma(x,t)-\sigma_0}{\sigma_\infty-\sigma_0}, \tag{5.14}$$

where $\sigma(x,t)$ is a sample conductivity as a function of position and time, σ_0 is the initial conductivity before the gas switch and σ_∞ is the conductivity after the stabilization of the sample in the new atmosphere.

Depending on the value of the Biot number it is possible to assess the characteristics of ion kinetics in the sample. According to den Otter et al., if the value of L_B is between 0.03 and 30 it is possible to estimate simultaneously k_{chem} and D_{chem}[90]. If the value of Biot number is more than 30, the ionic transport is controlled by the internal diffusion through the vacancy mechanism, and only D_{chem} is valid. On the other hand, if Biot number is less than 0.03, the ionic transport is controlled by the surface exchange due to the limited and finite efficiency of redox reactions caused by intrinsic catalytic activity. In this case, only estimated k_{chem} is valid.

In this work, two probe EIS measurements were carried out to study the total electrical conductivity because of the high resistance of HEO samples and their dominant ionic conductivity. Electrodes were brush-painted with ESL 5542 Platinum Conductor Paste and connected to the appropriate terminals by platinum wires with a 0.15 mm diameter. The total conductivity measurements were performed in dry ($pO_2 \approx 0.199$ atm, $pH_2O \approx 6 \times 10^{-5}$ atm) and humidified air ($pO_2 \approx 0.195$ atm, $pH_2O \approx 2.3 \times 10^{-2}$ atm). Samples with high differences in conductivity between these ambient conditions were additionally measured in D_2O-saturated air ($pO_2 \approx 0.196$ atm, $pH_2O \approx 6.3 \times 10^{-5}$ atm, $pD_2O \approx 2.03 \times 10^{-2}$ atm). Impedance spectra were collected with the Gamry Instruments potentiostat model Reference 3000 between 300 °C and 800 °C with 50 °C steps, in the frequency range 1 Hz–1 MHz and 1 V amplitude. The sample was held at each temperature for an appropriate time until a steady-state condition was reached. For the conductivity examination as a function of oxygen partial pressure, the measurements were conducted at a fixed temperature with changing pO_2 from 1 atm (oxygen) to 10^{-6} atm (pure nitrogen) with various mixtures in between. On the other hand, for examining conductivity as a function of water partial pressure, the measurements were conducted at a fixed temperature with changing pH_2O from ~6×10^{-5} atm to ~2.3×10^{-2} atm with a few mixtures in between. Between gas switches in pO_2 and pH_2O measurement, the conductivity relaxation curves were collected, which allowed acquiring information about the kinetics of charge transport, i.e. k_{chem} and D_{chem} for oxygen ions and protons. Obtained Nyquist plots were assessed using ZView 2 software (Scribner Associates Inc., USA), whereas $\sigma_{tot}(pO_2)$ were fitted using TableCurve2D software (Grafiti LLC, USA). Chemical surface exchange coefficients, as well as chemical diffusion coefficients, were evaluated using the NETL ECR script[91].

6. RESULTS AND DISCUSSION

6.1 Solid state synthesis

All compositions prepared and examined within this thesis are listed in Table 6.1. They were considered derivatives of barium zirconate. However, in the case of multicomponent or high-entropy oxides, all elements occupying one crystallographic position are assumed to be equivalent so that no one is regarded as a host. A different number and type of elements in the B sublattice were applied, which influenced the configurational entropy of compounds. The compositions labelled H1 and H2, have been taken from the work of Jiang et al.[21], while the others have been developed for the first time, utilizing the multicomponent perovskite framework consisting of Zr, Hf, Sn and Ti in the B sublattice – $Ba(Zr,Hf,Sn,Ti,X_{sub})O_3$. The X_{sub} elements were selected following the rules used in designing perovskite proton conductors and based on two principles:

- their ionic radii (in preferred coordination) should fit with other elements to yield the Goldschmidt tolerance factor (Equation 4.2) close to 1,
- the valence state of an element should be the same or lower than that of Zr, Hf, Sn, and Ti, i.e. 4+ or lower.

Most of the studied multicomponent perovskites contained 5 B-cations. Additionally, to examine the influence of many elements and high oxygen vacancy concentration on the properties, the samples with 8 (H38) and 10 (H40) elements in the B sublattice have been prepared. According to the Entropy Metrics (Equation 2.8) the 5B compositions can be regarded as 'Medium Entropy Oxides' (MEO) and only the 8B and 10B compositions as 'High Entropy Oxides' (HEO).

As can be seen in Table 6.1, the tolerance factor in all compounds is between 0.98 and 1.02, which corresponds to the value indicating the formation of cubic perovskite. Moreover, all multicomponent perovskites required high temperatures to form a single phase except the H40. It might be caused by the high number of elements in the structure and low melting oxide in reagents like ZnO.

Table 6.1 Compositions, labels, Goldschmidt tolerance parameters, Entropy Metrics and the synthesis temperatures of multicomponent perovskite oxides

Composition	Label	Goldschmidt factor	EM	Synthesis temperature (°C)
$BaZr_{0.2}Hf_{0.2}Sn_{0.2}Ti_{0.2}Ce_{0.2}O_{3-\delta}$	H1	1.012	0.966	1500
$BaZr_{0.2}Hf_{0.2}Sn_{0.2}Ti_{0.2}Y_{0.2}O_{2.9}$	H2	1.008	1.227	1500
$BaZr_{0.2}Hf_{0.2}Sn_{0.2}Ti_{0.2}Yb_{0.2}O_{2.9}$	H20	1.011	1.227	1500
$BaZr_{0.2}Hf_{0.2}Sn_{0.2}Ti_{0.2}In_{0.2}O_{2.9}$	H22	1.019	1.227	1500
$BaZr_{0.2}Hf_{0.2}Sn_{0.2}Ti_{0.2}Sm_{0.2}O_{2.9}$	H25	1.003	1.227	1500
$BaZr_{0.125}Hf_{0.125}Sn_{0.125}Ti_{0.125}Y_{0.125}Yb_{0.125}Sm_{0.125}In_{0.125}O_{2.75}$	H38	0.982	1.764	1500
$BaZr_{0.1}Hf_{0.1}Sn_{0.1}Ti_{0.1}Ce_{0.1}Y_{0.1}Yb_{0.1}Sm_{0.1}In_{0.1}Zn_{0.1}O_{2.7}$	H40	0.980	1.965	1150

6.2 X-Ray Diffraction

6.2.1 Phase analysis

In Figure 6.1, diffraction patterns for all synthesized oxides are gathered. The reference pattern for barium zirconate (COD no. 1532743) is included at the top of the graph. As it can be seen, every compound pattern corresponds to that of the cubic perovskite $Pm\bar{3}m$ (space group no. 221). The positions of the reflections change across all samples, which indicates different values of the lattice parameter. In the patterns of H2 and H25, the right-hand side of the reflections is asymmetric. This could imply the existence of more than one cubic perovskite structure with gradual changes in lattice parameters in one multicomponent sample.

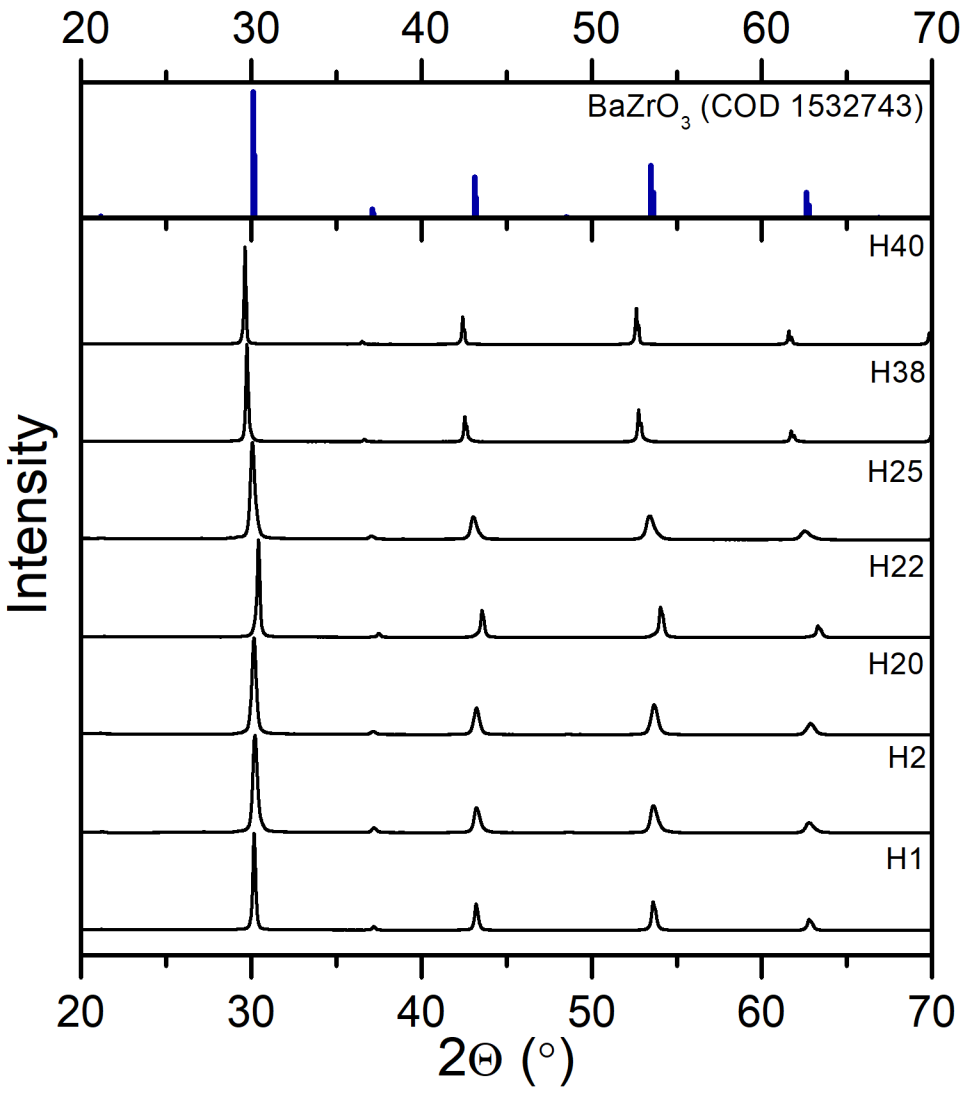

Figure 6.1 XRD patterns of synthesized multicomponent oxides and the $BaZrO_3$ reference.

Overall, no significant secondary phases were observed. However, upon magnification between 20-30° region, several minute peaks emerge from the background level. A few examples of observable cases are presented in Figure 6.2. The residual phase identified in the samples was titanium oxide in the rutile phase ($P4_2/mnm$) with the main reflection around 27.5°. Other detected

phases were oxides of substituting elements like yttrium oxide ($Ia\bar{3}$), ytterbium oxide ($Ia\bar{3}$) or cerium oxide ($Fm\bar{3}m$) and seldom zirconium oxide ($Fm\bar{3}m$). All those oxides are compounds of metals that should occupy the B-site in the perovskite structure. The deviation from the stoichiometry might be caused by the barium evaporation during the synthesis[92]. According to the site ratio balance, excess B-site metals separate from the main phase, forming residual phases. This phenomenon is often observed in A-site deficient materials based on strontium titanate[93].

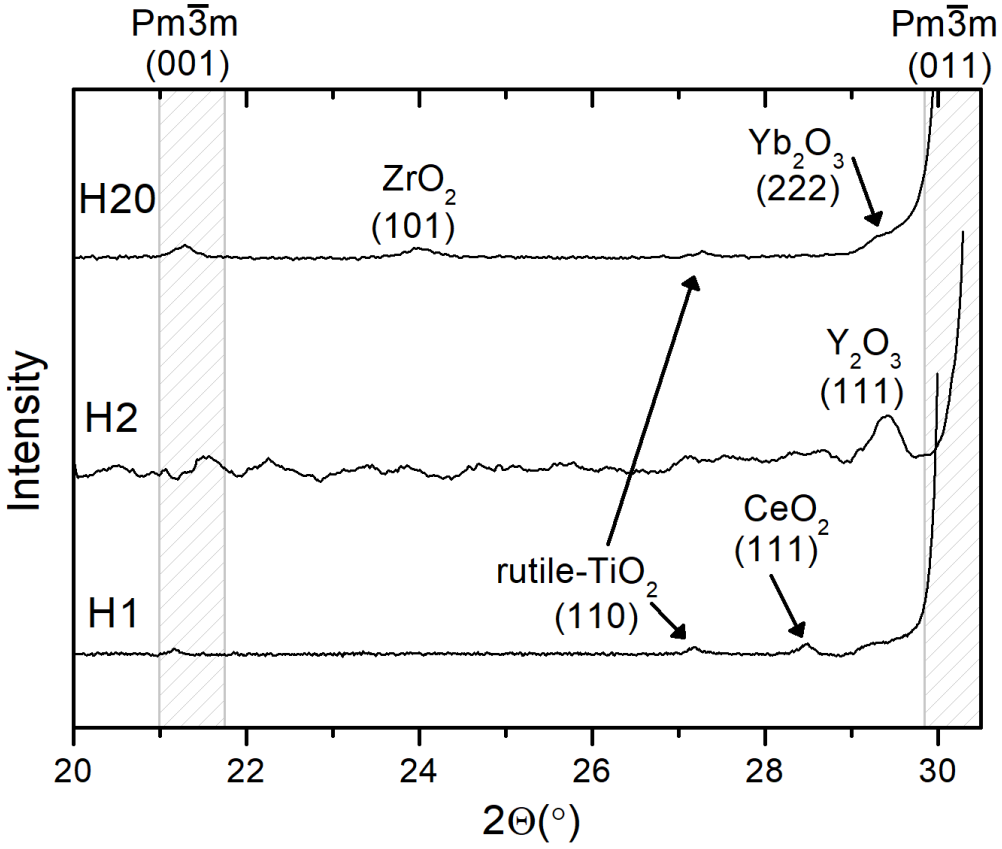

Figure 6.2 A magnified fragment of the XRD patterns showing small reflections of non-reacted oxides.

In Figure 6.3, the exemplary Rietveld refinement profile for $BaZr_{0.2}Hf_{0.2}Sn_{0.2}Ti_{0.2}Ce_{0.2}O_{3-\delta}$ is shown. The .cif file used in the refinement is based on the BZO oxide from the COD database with changed element contribution that reflected the stoichiometry of the specific multicomponent compound. The data from the Rietveld refinements for all samples without sintering aid and the reference values for BZO, are collected in Table 6.2. The average B-site radii were determined by calculating the weighted average of radii with mol% of the selected element as an importance factor. In these calculations six-coordinated Ce^{4+}, Y^{3+}, Yb^{3+}, Sm^{3+}, In^{3+} and Zn^{2+} were assumed. The agreement indices reveal that the cubic perovskite structure fits well with the obtained diffractograms; thus, derived structural information is reliable.

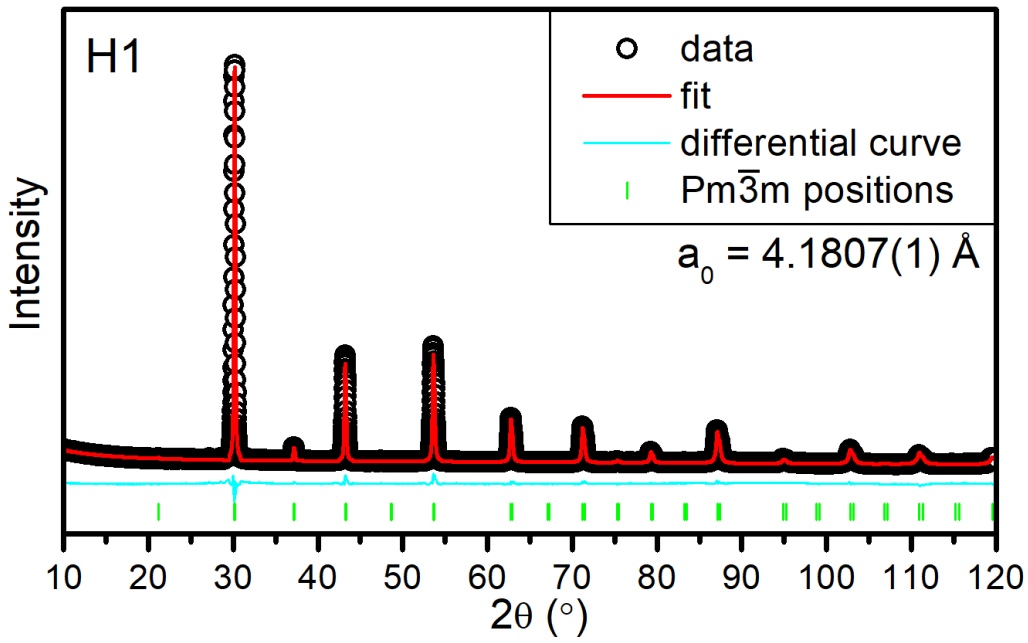

Figure 6.3 Diffractogram of $BaZr_{0.2}Hf_{0.2}Sn_{0.2}Ti_{0.2}Ce_{0.2}O_{3-\delta}$ (H1) with Rietveld refinement results, performed in HighScore Plus software using the pseudo Voigt profile function.

Table 6.2 Data derived from Rietveld analysis for all samples with obtained agreement indices.

Sample	Average B-site radius (Å)	Lattice parameter a_0 (Å)	Theoretical density ρ_{th} (g/cm^3)	Crystallite size (nm)	Strain (%)	R_{exp}	R_p	R_{wp}
H1	0.719	4.1807(1)	6.83	772.3	0.108	0.79455	3.50065	4.58081
H2	0.725	4.1863(1)	6.54	444.3	0.268	0.72324	3.64943	4.91302
H20	0.7186	4.1735(1)	6.98	456.9	0.248	0.8244	3.05118	3.98956
H22	0.705	4.1516(1)	6.82	952.9	0.100	0.83595	3.98727	5.88821
H25	0.7366	4.1982(1)	6.76	545.0	0.332	0.72601	3.032	4.1787
H38	0.7814	4.2490(1)	6.53	1617.9	0.085	0.75987	5.60992	7.83236
H40	0.7861	4.2564(1)	6.40	2334.5	0.176	0.78597	5.70355	8.12766
BZO	0.72	4.179	6.21					

Firstly, the values of lattice parameters a_0 depend on the material compositions, as expected from the initial qualitative analysis. Figure 6.4 presents a_0 values as a function of the average B-site radius. As it can be seen, with the increase of the average radius of elements occupying the B-site, the lattice parameter also increases. Moreover, the values are distributed in a linear pattern with respect to the reference BZO, as emphasized by the dashed line. This would confirm the agreement with Vegard's rule. A similar result was achieved by Imashuku et al. for barium zirconate doped with different trivalent elements[94].

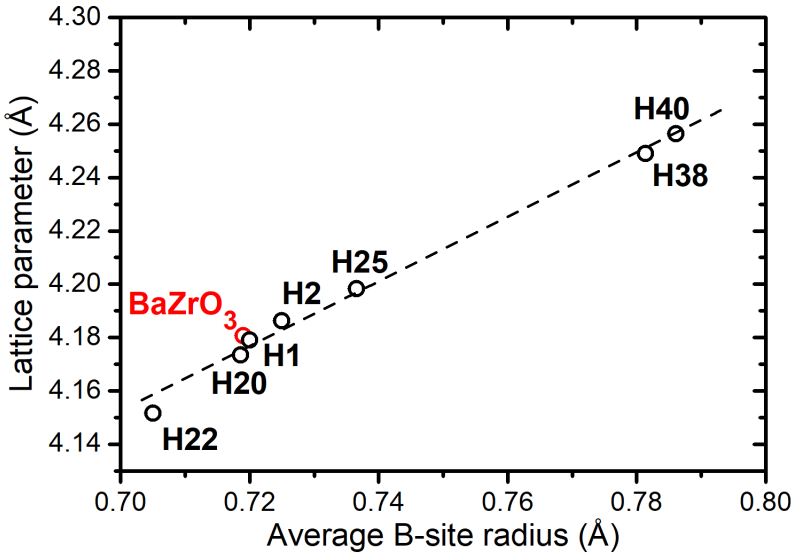

Figure 6.4 The lattice parameter values obtained from Rietveld refinement of synthesized samples as a function of average B-site radii.

By having the theoretical densities from the XRD measurements ρ_{th} it was possible to calculate the relative density of the synthesized pellets ρ_{rel}The parameter is crucial in assessing the sintering process and is required to adjust the electrical conductivity (through the Bruggeman factor). The density of pellets ρ_{Arch}, was determined using the Archimedes method with kerosene as a liquid medium. The relative density was calculated using the following formula (Equation 6.1):

$$\rho_{rel} = \frac{\rho_{Arch}}{\rho_{th}} \cdot 100\%. \quad (6.1)$$

All obtained values for samples synthesized with and without the addition of the sintering aid are collected in Table 6.3. The samples that did not need NiO to reach the desirable relative density (> 90%) are $BaZr_{0.2}Hf_{0.2}Sn_{0.2}Ti_{0.2}Ce_{0.2}O_{3-\delta}$ (H1) and the 8B and 10B high entropy oxides (H38 and H40). The other 5B samples reached low relative density values and had to be introduced with the sintering aid. The addition of nickel oxide had a significant impact on the density, where 1 mol% was sufficient to let them reach the required level of ρ_{rel}.

Table 6.3 Apparent and relative density values for composition pellets sintered with and without sintering aid.

Sample	Density without sintering aid		Density with sintering aid	
	Pellet density ρ_{Arch} (g/cm^3)	Relative density ρ_{rel} (%)	Pellet density ρ_{Arch} (g/cm^3)	Relative density ρ_{rel} (%)
H1	6.24	91	N/A	N/A
H2	3.73	57	6.33	97
H20	4.21	60	6.42	92
H22	5.26	77	6.80	99
H25	4.38	65	6.72	99
H38	6.31	97	N/A	N/A
H40	6.38	99	N/A	N/A

In Figure 6.5, the microstructural parameters obtained from the Rietveld refinements are presented. Those parameters are not dependent on the average B-site radii (Figure 6.5a,b), but they seem to be related to the relative density (Figure 6.5c,d). The grain size increases with the rising density, forming arc-shaped dependence, whereas strain decreases with rising density. Samples which reach high relative densities consist of large crystallites and have a low level of microstrain. On the other hand, the compositions with a low ρ_{rel} have smaller crystallites and high strain values. Thus, it can be concluded that samples like H38 and H40 can develop the well-sintered microstructure during the synthesis and samples like $BaZr_{0.2}Hf_{0.2}Sn_{0.2}Ti_{0.2}Sm_{0.2}O_{2.9}$ (H25) have unfavorable conditions during the synthesis and form weakly sintered microstructure with small unrelaxed grains.

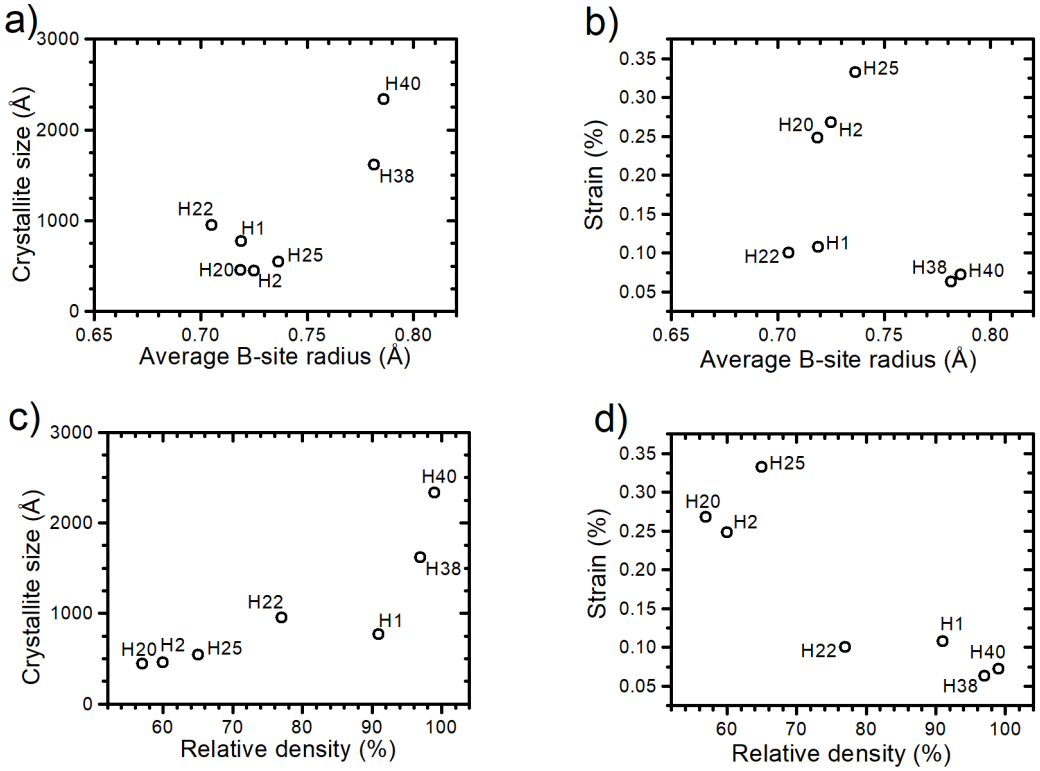

Figure 6.5 Microstructure parameters derived from Rietveld refinement, plotted as a function of average B-site radii (a, b) and relative density (c, d).

6.2.2 High Temperature X-ray Diffraction

For HT-XRD measurements, samples in the form of powders were first hydrated in a tube furnace at 300 °C for 24h with the internal flow of air containing 2% of water vapor. Afterwards, all powders were measured in two heating cycles. The first, denoted as 'wet', concerns as-hydrated specimens, whereas the second, denoted as 'dry', relates to reheating of the samples in the chamber after cooling down from the first cycle. In Figure 6.6, two exemplary results for HT-XRD measurements are presented. In the first example (Figure 6.6a), the lattice parameter of $BaZr_{0.2}Hf_{0.2}Sn_{0.2}Ti_{0.2}Ce_{0.2}O_{3-\delta}$ (H1) increases linearly with the rising temperature in both cycles, overlapping each other. This phenomenon displays the typical thermal expansion of the unit cell. On the other hand, in $BaZr_{0.1}Hf_{0.1}Sn_{0.1}Ti_{0.1}Ce_{0.1}Y_{0.1}Yb_{0.1}Sm_{0.1}In_{0.1}Zn_{0.1}O_{2.7}$ two regions of changes can be highlighted (Figure 6.6b). In the beginning, from room temperature to 400 °C, there is a non-

monotonic behavior with a local maximum. At higher temperatures, the change of a_0 switches to a linear increase with temperature. In the first region, apart from thermal expansion, a chemical expansion caused by water incorporation through proton defects also occurs[95]. Above 180 °C formed $OH_O^{\bullet}$ starts to leave the sample and in the second region only thermal expansion is visible. Interestingly, this phenomenon is also present in dried samples but not on the same scale since most of the proton defects disappeared from the sample. It is also worth noting the significant difference in lattice parameters between hydrated and dried H40 at room temperature.

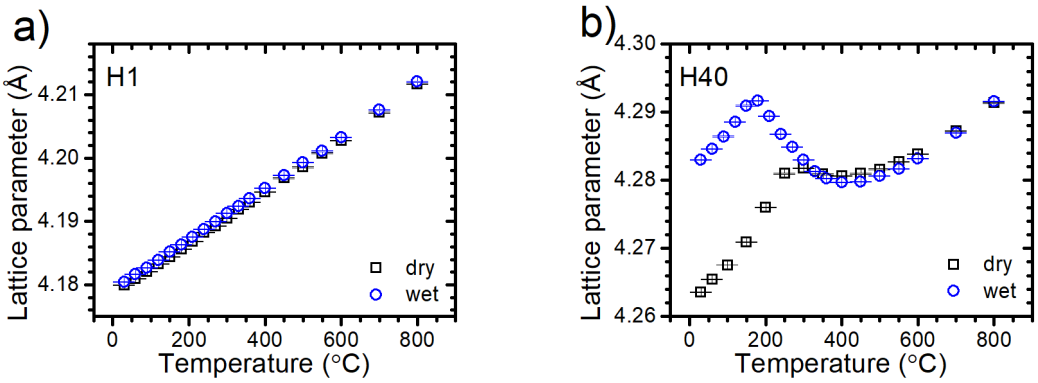

Figure 6.6 The lattice parameter expansion from HT-XRD measurements for dried and hydrated samples: a) $BaZr_{0.2}Hf_{0.2}Sn_{0.2}Ti_{0.2}Ce_{0.2}O_{3-\delta}$, b) $BaZr_{0.1}Hf_{0.1}Sn_{0.1}Ti_{0.1}Ce_{0.1}Y_{0.1}Yb_{0.1}Sm_{0.1}In_{0.1}Zn_{0.1}O_{2.7}$.

In Figure 6.7, the HT-XRD results for all multicomponent samples are collated. In all of them, the lattice parameter increases with the temperature with a similar slope. The chemical expansion region (grey dashed area) occurs between 100 and 300 °C with a local maximum of a_0 at temperatures, depending on the sample.

These results allow to calculate the thermal expansion coefficients (TECs) for each sample. According to Equations 5.3 and 5.4, for HT-XRD technique it can be rewritten:

$$\frac{\Delta a_0}{a_0} = \alpha_{HTXRD} \cdot \Delta T, \tag{6.2}$$

where α_{HTXRD} is considered TEC and $\frac{\Delta a_0}{a_0}$ is a relative increase of lattice parameter caused by the temperature difference ΔT. All thus obtained thermal expansion coefficients with the distinguished low (LT) and high temperature (HT) regions are collected in Table 6.4. There is a significant discrepancy in the obtained values of TEC in all multicomponent oxides. Apart from H1, all other samples have different coefficients in higher and lower temperatures, with H40 having the largest difference and the highest uncertainty. Additionally, all those values are slightly higher than the reported values of TEC for acceptor-doped barium zirconates/cerates achieved using HT-XRD measurements[96,97]. It might be caused by the distorted, more expanded crystal structure of HEO samples due to having equimolar amounts of different elements throughout the lattice.

For visual comparison in Figure 6.8, TEC values in the HT region of dried samples as a function of average B-site radius were plotted. No clear tendency can be seen. After the first heating step, the samples were not fully dried, so even in dry conditions, unit cell size changes related to the water release are observed.

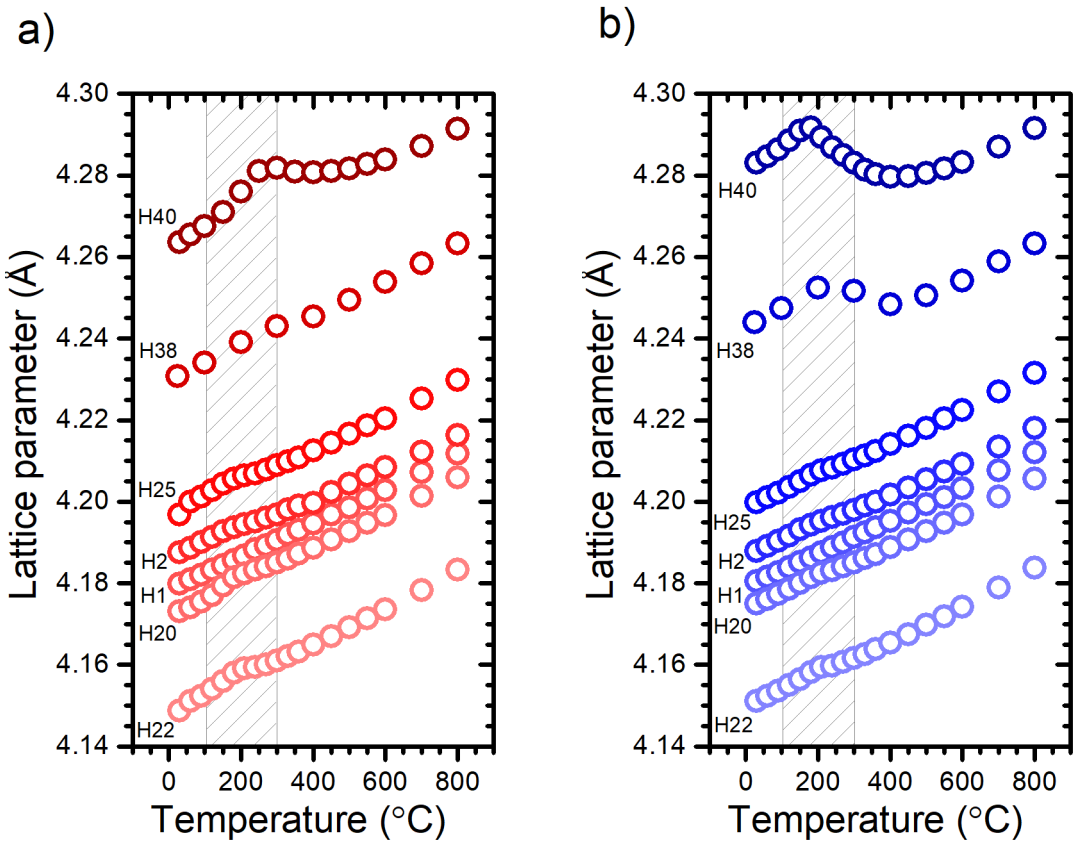

Figure 6.7 The lattice parameter evolution with temperature in all multicomponent samples: a) dried, b) hydrated.

Table 6.4 Thermal expansion coefficients obtained from HT-XRD measurements for all synthesized samples.

Sample	TEC of hydrated sample (10^{-6} 1/K)		TEC of dried sample (10^{-6} 1/K)	
	LT region	HT region	LT region	HT region
H1	9.73(4)		9.83(5)	
H2	10.23(33)	9.94(19)	10.46(26)	9.54(7)
H20	9.57(37)	10.27(11)	9.15(63)	10.45(23)
H22	10.70(16)	11.22(12)	12.05(74)	11.22(17)
H25	9.98(45)	10.56(10)	11.05(79)	10.46(24)
H38	11.40(46)	11.75(29)	11.12(37)	12.07(25)
H40	15.48(71)	9.24(49)	14.29(46)	8.80(54)
$BaCe_{0.4}Zr_{0.4}Y_{0.2}O_{3-\delta}$[96]			10.9	8.5
$BaCe_{0.8}Y_{0.2}O_{3-\delta}$[96]			11.6	8.3
$BaZr_{0.8}Y_{0.2}O_{3-\delta}$[96]			8.2	
$BaZr_{0.8}Sm_{0.2}O_{3-\delta}$[97]				9.2

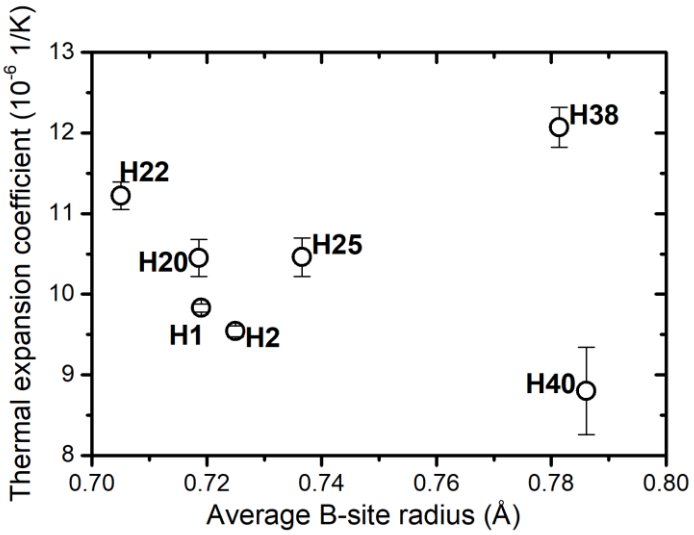

Figure 6.8 Thermal expansion coefficients of dried HEO samples, obtained from HT-XRD in the high-temperature range, as a function of average B-site radius.

6.3 Dilatometry

For dilatometry studies, as-sintered samples in the form of bars were applied. In Figure 6.9, the results of measurements performed during cooling are presented. As can be seen, the obtained curves are linear in the entire measurement range and have slopes similar to those of HT-XRD measurements. Moreover, all curves exhibit two temperature regions with distinctive inclinations. Using Equation 5.3, it was possible to derive the TEC values α_{DIL} in all considered samples.

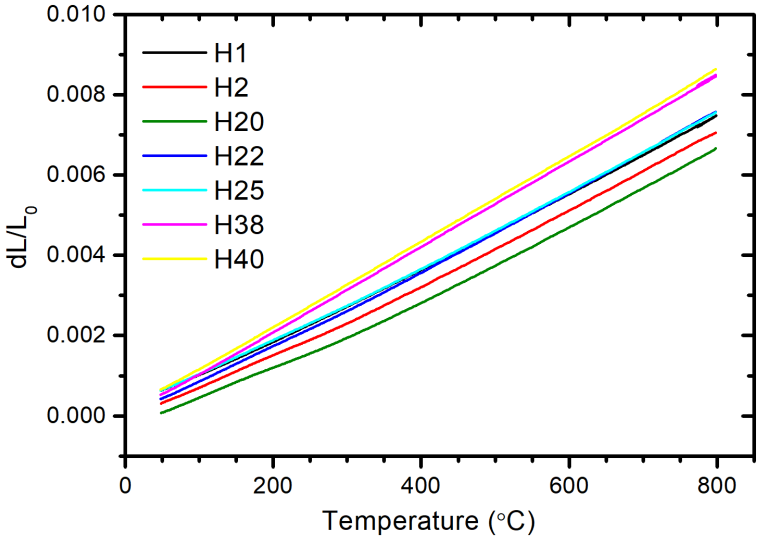

Figure 6.9 Relative elongation of multicomponent oxide pellets during cooling.

In Table 6.5, all obtained and reference values reported in the literature are displayed. The first notable feature is that for all multicomponent oxides, the TEC tends to be higher in high-temperature ranges (above 500 °C) than in lower temperatures. However, compared to values reported by other authors for similar compounds, they all are in good agreement[77,98,99].

In Figure 6.10, the thermal expansion coefficients achieved from high-temperature regions for HEO samples are plotted. With the increase of average B-site radii, the TEC also increases. Only $BaZr_{0.2}Hf_{0.2}Sn_{0.2}Ti_{0.2}In_{0.2}O_{2.9}$ (H22) is not in line with this relation.

Table 6.5 Thermal expansion coefficients obtained from dilatometry measurements for all synthesized samples.

Sample	TEC during cooling (10^{-6} 1/K)	
	LT region	HT region
H1	8.14(2)	9.75(1)
H2	7.71(1)	9.85(1)
H20	7.43(2)	9.81(1)
H22	8.74(1)	10.22(1)
H25	8.36(2)	9.94(1)
H38	10.33(2)	10.74(2)
H40	10.29(2)	11.03(2)
$BaZr_{0.9}Y_{0.1}O_{3-\delta}$[77]	13	
$BaZr_{0.85}Y_{0.15}O_{3-\delta}$[98]	8	
$BaCe_{0.7}Zr_{0.1}Y_{0.2}O_{3-\delta}$[99]	10.2	

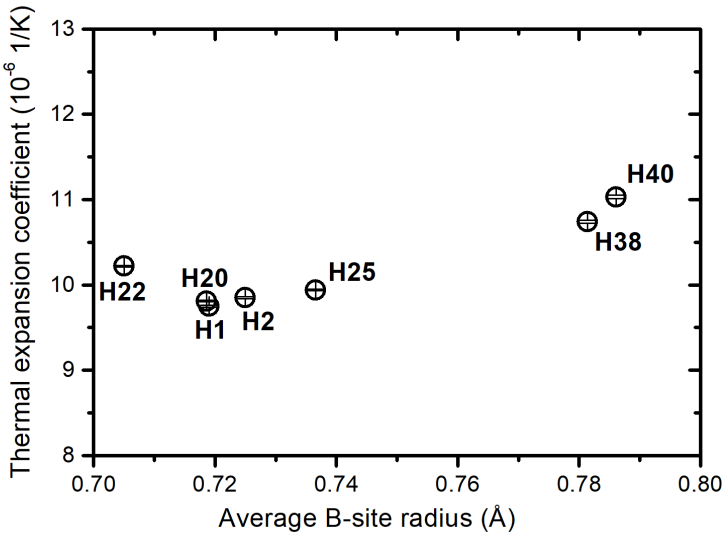

Figure 6.10 Thermal expansion coefficients of HEO samples, obtained from dilatometry measurements in high temperatures, as a function of average B-site radius.

In Figure 6.11, TEC values from HT-XRD and dilatometry for dried samples at high temperatures are compared. The dashed line represents equal TEC values in both techniques. $BaZr_{0.2}Hf_{0.2}Sn_{0.2}Ti_{0.2}Ce_{0.2}O_{3-\delta}$ (H1) is the only compound on this line, whereas the others show different TEC values from HT-XRD and dilatometry. In the case of H40, the difference seems especially high. What should be considered is that for XRD and dilatometry analyses, the powdered and solid samples, respectively, are used. This means that samples studied by HTXRD, especially those with a high acceptor constituent content, are more susceptible to oxygen stoichiometry changes. On the other hand, as shown in Fig. 6.7a, it has not been fully dried, so a strangely low thermal expansion coefficient may be caused by the water release still occurring during heating.

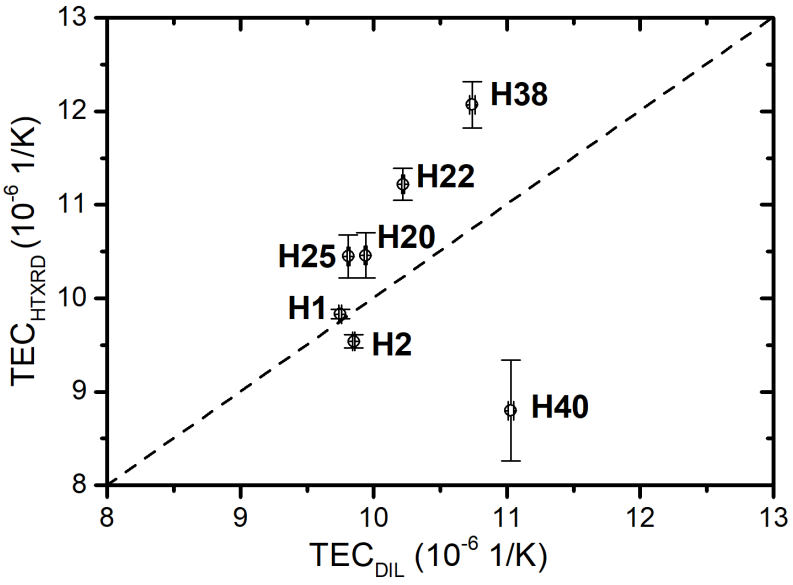

Figure 6.11 Comparison of thermal expansion coefficients obtained based on the dilatometry and HTXRD analyses.

6.4 X-Ray Absorption Spectroscopy

All absorption edges obtained during measurements are shown and discussed in this section, though it was impossible to study all the elements. The results are normalized and compared regarding selected elements shared between samples.

6.4.1 XANES

Figure 6.12 presents absorption edges for barium in all samples and the reference $BaTiO_3$ foil. This absorption edge consists of one main feature, the white line around 5250 eV associated with the transition from Ba 2p to unoccupied Ba 5d[100]. The spectrum observed at higher energies is connected with delocalized states emerging from near neighbors i.e. EXAFS oscillations. All absorption spectra are close in shape, which confirms that barium is at the 2+ oxidation state surrounded by 12 oxygen atoms. However, there are some discrepancies, as visible in Figure 6.12b. HEO samples have more intense white lines and a small -0.2 eV shift in maximum absorption energy compared to the reference. Also, the shape is more acute but retains the width at the base of the peak, with H38 and H40 being slightly wider. The energy shift can be ascribed to a small change in the effective oxidation state of barium in the presence of increased oxygen vacancy concentration or different Ba-O bond lengths. There is a notable difference between lattice parameters in HEO samples (a from 4.15 to 4.26 Å) and pure $BaTiO_3$ (a = 3.99 Å, c = 4.04 Å)[101]. The intensity of the white line might be increased through stronger overlapping of the Ba 5d orbital with O 2p orbitals and ones from diverse B-site elements. There is a strong correlation between peak width and symmetry of the position that the atom occupies[102]. Interestingly, Yoshii et al.[100,103] proposed that a wide absorption edge indicates strong hybridization of localized Ba 5d orbitals.

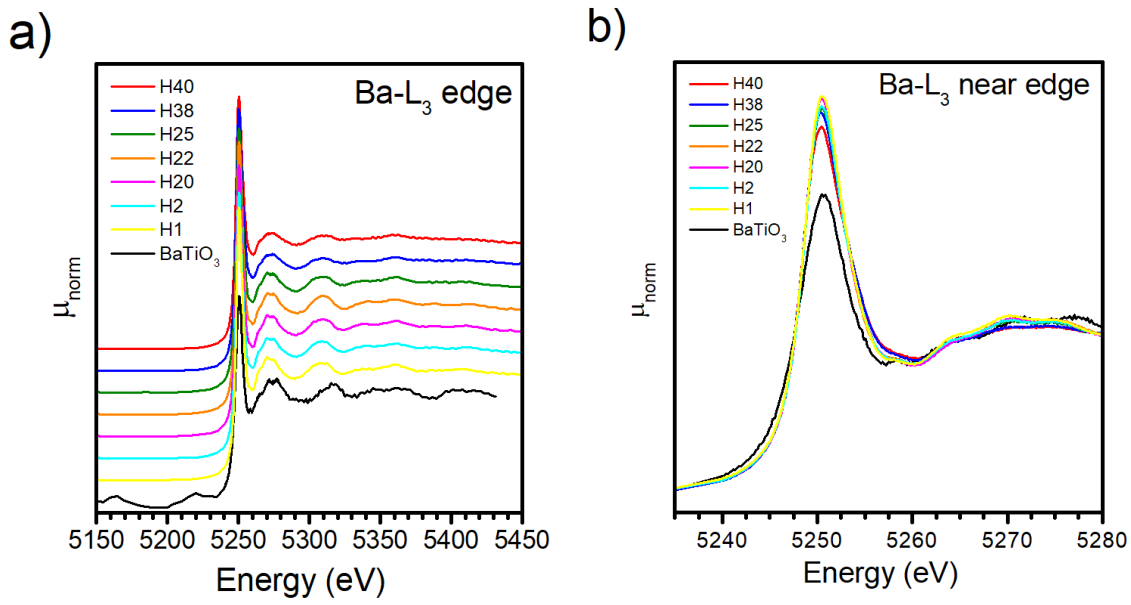

Figure 6.12 a) Absorption spectra in all examined samples for Ba-L_3 edge, with offset, b) close up around the edge, without offset.

XAS measurement results for zirconium in samples H2 and H22 are presented in Figure 6.13. Several different features in the spectra can be seen. The first significant feature in the Zr-K edge which is marked A in Figure 6.13b, is a pre-peak correlated with the transition of the 1s core electron to the lowest unoccupied state available, which is 4d for zirconium. Features B and C are ascribed to the transition from 1s orbital to 5s and 5p orbitals, respectively. Far from the edge, feature D, indicates multiple scattering and the onset of EXAFS signal. According to Choy et al.[104,105] and Jung et al.[106], the intensity of the A feature indicates the deviation from the centrosymmetry. Since the 1s → 4d transition is forbidden it requires some d-p orbital mixing. Thus, the so-called quadruple transition is weak in symmetrical positions (like octahedron) and strong in positions deviating from centrosymmetry (like tetrahedron). The main edge features also can give insight into the coordination of the zirconium atom. These orbitals are strongly hybridized with the surrounding oxygen atoms and are responsible for the multiple-scattering effects[106]. Feature C is more prominent in samples with cubic symmetry, while feature B is higher in non-centrosymmetric positions, with higher coordination numbers[107]. Lastly, the shift of feature D to higher energies can indicate the shortening of the Zr-O bond[104]. Acquired spectra for H2 and H22 are in good agreement with reported absorptions for cubic ZrO_2[108] and $Ba(Zr,Sc)O_3$[109]. This means that the Zr atom occupies octahedral positions with six neighboring oxygen atoms, and there are no distortions in the polyhedron. Overall, both samples have very similar spectra with only a little difference in feature C position, with the one for H2 shifted by -0.5 eV and less intense. It might indicate a slight difference in the concentration of oxygen around the zirconium atom, namely more oxygen vacancies are around Zr in H2 than in H22. A similar tendency was found by Hoshino et al. in ab initio calculations of the XAS Zr-K spectrum of ZrO_5 in $BaZrO_3$ supercell[109].

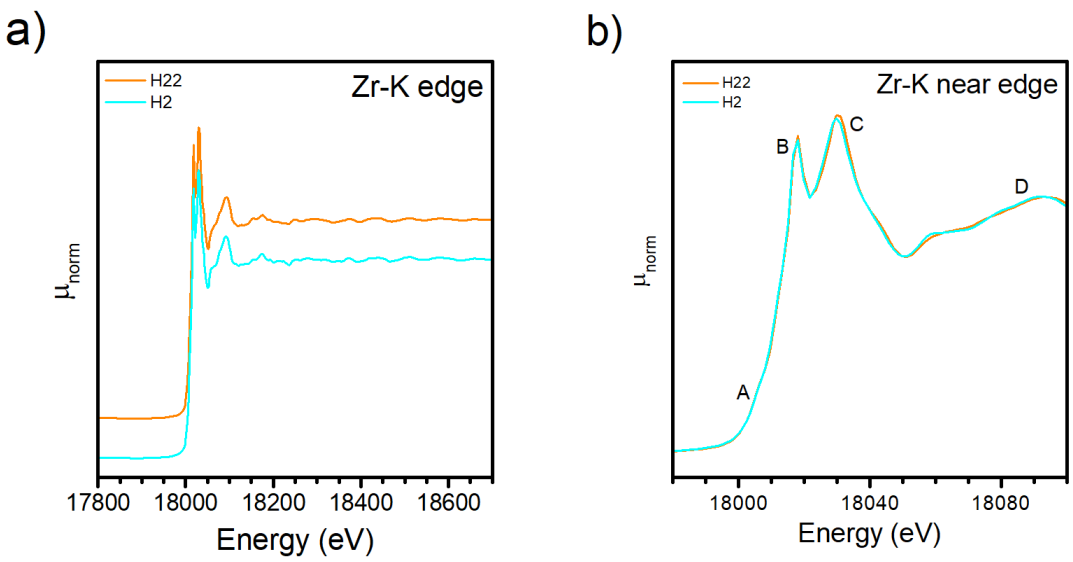

Figure 6.13 a) Absorption spectra in H2 and H22 samples for Zr-K edge, with offset, b) close up around the edge, without offset.

In Figure 6.14, absorption spectra for hafnium edge of all samples and reference HfO_2 are presented. The most important feature in this spectrum is the strong absorption at the edge caused by the transition of the core 2p electron to the molecular orbital comprised of 5d Hf hybridized with 2p O and 5d Ba[110,111]. A weak feature right above the edge at 9585 eV is caused by multiple scattering processes occurring at the second shell B-site metals. The features emerging above 9600 eV are ascribed to the EXAFS signal. HEO samples and HfO_2 have the edge in the same energy range thus, it is safe to assume that hafnium exists at the 4+ oxidation state. However, this is the only thing they have in common: the shape and intensity of the white line are different. The tip of the edge in HEO samples is split (Figure 6.14b), and since the absorbing orbital is the 'd' one, it can be assumed that it is caused by the presence of the t_{2g} and e_g orbitals. The peak positions, as well as the difference between them ΔE_{Hf} and average value are gathered in Table 6.6. The average values are close to the reference thus the split is roughly symmetrical and the values of the crystal field split for all samples are around 3 eV. Similar tendency with the split L_3 edge was observed for zirconium in borosilicate oxide glasses by Galoisy et al.[112]. They obtained the value of the split equal to 3.1 eV and found out that such a split is visible when the zirconium atoms have coordination number 6. In higher coordinations, the split was not visible. On the other hand, Soriano et al. determined the values of the crystal field split for different transition metal oxides, including hafnium oxide, from O K edge analysis[113]. They discovered that this split increases with the atomic number of the transition metal, yielding 3.7 eV for the hafnium oxide, which is more than that observed for the HEO samples. The weaker split in multicomponent oxides might result from a low hafnium content in all samples, where the maximum value is 20 mol% and thus weaker overlapping with the oxygen orbitals. As for the intensity of the white line, the difference is between all of the samples, not only the reference. The strongest absorption is observed for H22, while the weakest for H2 and the reference. The difference between the intensity of the white line of HfO_2 and the HEO samples may stem from the presence of barium, whose orbitals form molecular

orbitals and thus increase the density of states. So, as the intensity is dependent on the available states on the d orbital, this may serve as an indicator of the local oxidation state[114]. Tongpeng et al. proposed that weaker intensity of absorption in La-doped HfO_2 results from the existence of Hf^{3+} and partially filled 5d orbital caused by oxygen vacancies induced by acceptor[115]. This way, it can be proposed that in the HEO samples, oxygen vacancies differ in the tendency to be located around hafnium, with the strongest tendency in H2, the weakest in H22, and the other samples in between. However, as mentioned earlier, there is no apparent energy shift in the edge, so the change in the oxidation state is less likely to occur.

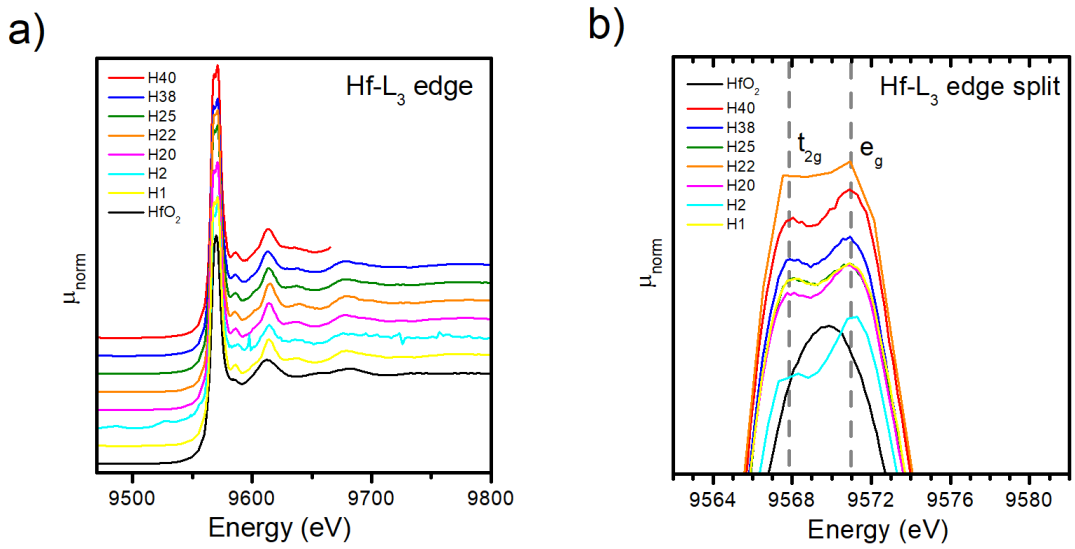

Figure 6.14 a) Absorption spectra in all samples for Hf-L_3 edge, with offset, b) close up around the edge, without offset.

Table 6.6 Positions of absorption maxima for all HEO samples and the reference with calculated crystal field split.

Sample	t_{2g} peak (eV)	ΔE_{Hf} (eV)	e_g peak (eV)	Average band maximum (eV)
H1	9568.11	2.71	9570.82	9569.47
H2	9567.91	3.18	9571.09	9569.50
H20	9567.91	2.91	9570.82	9569.36
H22	9568.18	2.70	9570.88	9569.53
H25	9568.03	2.79	9570.82	9569.43
H38	9567.97	2.91	9570.88	9569.43
H40	9568.03	2.85	9570.88	9569.46
HfO_2				9569.81

Figure 6.15 displays absorption spectra for tin in H2 and H22. Here, absorption takes place through the transition from core 1s level to hybridized Sn 5sp orbitals with O 2p orbitals[116]. The obtained spectra are nearly identical, with a slight difference in intensity of the white line. The lower value of peak height for H2 is similar to the difference described in the paragraph about Zr XAS results. Despite this, both measurements are in good agreement with Sn K edge measurements of SnO_2[117,118]. This oxide consists of Sn in a 4+ oxidized state and forms the rutile structure with six oxygen neighbors, similarly to oxygen octahedra around B-site ions in perovskites.

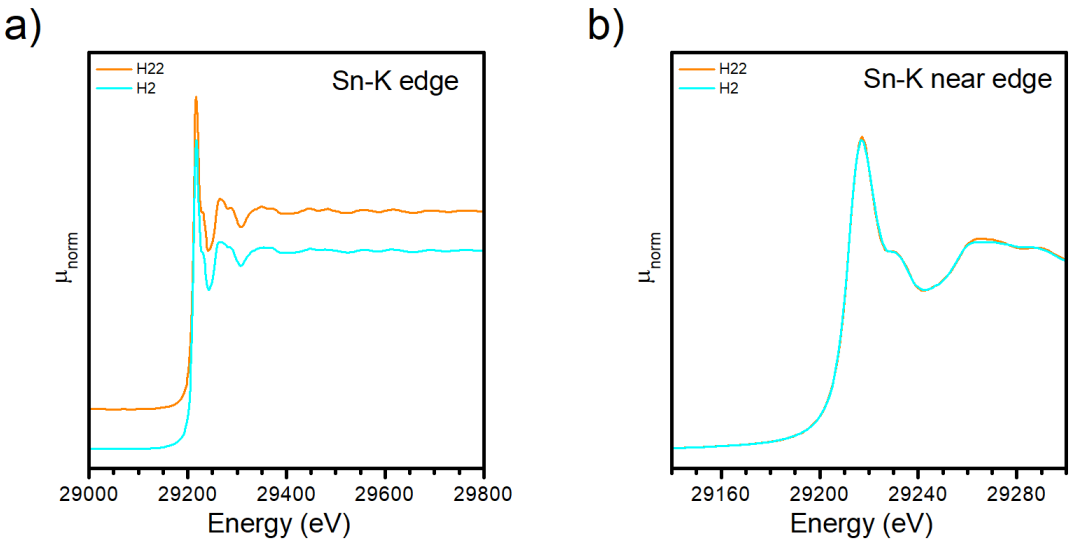

Figure 6.15 a) Absorption spectra in H2 and H22 samples for Sn-K edge, with offset, b) close up around the edge, without offset.

In Figure 6.16 the results of the measurements for all samples (including reference $BaTiO_3$) for titanium absorption edge, with the emphasis on significant parts of the spectrum, are gathered. In particular, Figure 6.16b contains all important features indexed with the A-E letters. The features A-C are interpreted as 1s → 3d transition[119], and D and E are ascribed to transitions to hybridized 4s and 4p orbitals, respectively[120,121]. Two phenomena occur at the pre-edge region: simple quadruple transition to local 3d states in lower energies and more complex dipole-allowed the transition to non-local 3d states (deriving from other shells Ti) in higher energies. The latter is possible because of a weak hybridization of Ti 4p, O 2p and Ti 3d orbitals[122]. Moreover, both energy levels split into t_{2g} and, e.g. sublevels, but two of them overlap, generating three pre-peaks. Thus, feature A relates to the local t_{2g} transition, feature B is a mix of local e_g and non-local t_{2g} states and lastly feature C is formed from electrons on non-local e_g states. The reference $BaTiO_3$ spectrum is in good agreement with the profiles reported in the literature[123] but HEO samples exhibit some differences. Firstly, in the pre-edge region (Figure 6.16c), the most prominent feature is the B one. Its intensity is the lowest for the H1 sample, followed by the reference, the other 5 B-site compositions, and the highest for H38 and H40. What is more, with the increase in intensity, feature B shifts towards lower energies. The highest B energy shift is observed in H38 and H40 and it reaches -1 eV in comparison with $BaTiO_3$. The increase in the feature B intensity means that there is a stronger overlap between Ti 3d and O 2p orbitals caused by the distortion of the symmetry of the octahedral site or the transition from octahedral to the tetrahedral site, in which the p-d hybridization is strong. It can be seen that the more vacancies are present, the stronger is the B feature. So, it seems reasonable that the vacancies deform TiO_6 octahedra. Also, titanium reacts to the presence of $V_O^{\bullet\bullet}$ by reducing the oxidation state, hence the energy shift. The lower intensity for H1 than for the reference might be caused by the difference in crystal structure. Barium titanate at room temperature exhibits a tetragonal structure where the octahedral sites are natively distorted. On the other hand, H1 is cubic with high octahedra symmetry. The white line (feature E) is the most

intense for H1, then there is the reference, 5 B-site HEO and H38 and H40 with the lowest intensity. Also, the feature E energy range spans from the reference to -1.9 eV, as indicated in Figure 6.16d, which further supports the reduction of titanium. Additionally, Farges et al. determined that A-site metal is important in forming the feature E[124]. Thus, it is possible that breaking of the symmetry weakens the hybridization of the Ti 4p orbitals with barium and oxygen orbitals, decreasing the DOS around the edge. This DOS is also decreased by the partially filled energy states in Ti^{3+}. So, ultimately, the increase of the acceptor concentration influences the titanium oxidation state which is responsible for the distortion of the TiO_6 octahedra shape.

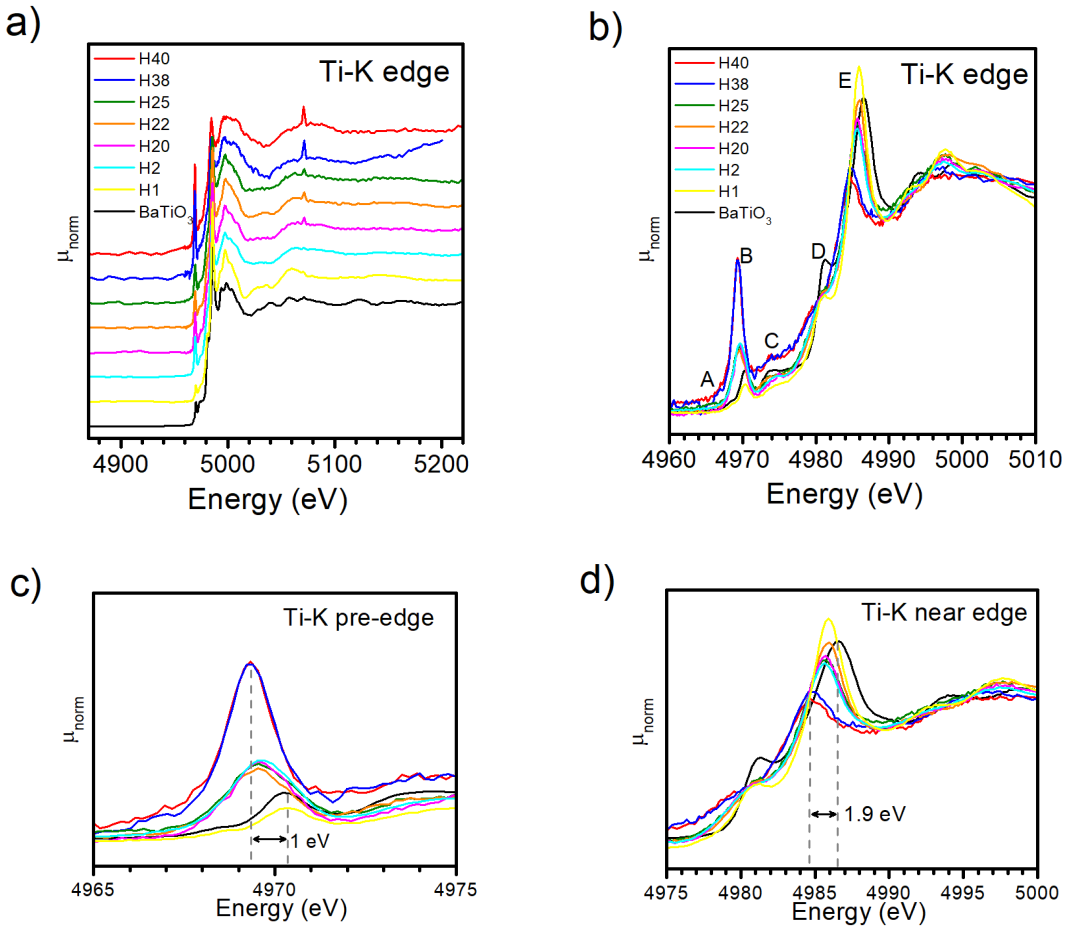

Figure 6.16 a) Absorption spectra in all samples for Ti-K edge, with offset, b) XANES region with all main features marked, c) close up around the pre-edge region, without offset, d) close up around the edge, without offset.

In Figure 6.17, absorption for the Y-K edge in H2 is presented. Since Y and Zr have the same electronic configuration in the ionic form, their absorption spectra are similar, as seen in Figure 6.13b and Figure 6.17b. Feature A is ascribed to a weak quadrupole transition to 4d orbital, while features B and C are present thanks to dipole s-p transition[125]. The yttrium absorption edge for H2 is in good agreement with reported data about Y-doped barium cerate[126]. However, unlike for Zr, the Y-K edge feature B is more intense than the C one. The relation between the B-C features indicates the symmetry of the sites occupied by the metal ion. Thus, this difference might be caused by the non-ideal symmetry of octahedra induced by the acceptor nature of yttrium in the B-site lattice, which is proposed by Longo et al.[126].

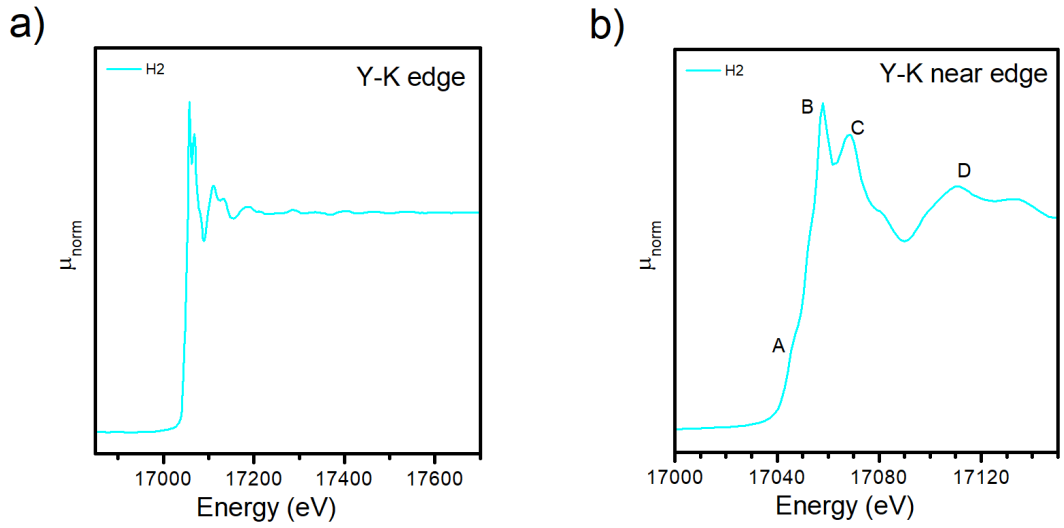

Figure 6.17 a) Absorption spectra in H2 sample for Y-K edge, with offset, b) close up around the edge, without offset.

In Figure 6.18, the single spectrum for Yb-L_3 absorption in H20 is presented. This absorption edge is similar in shape to the Hf-L_3 edge, although here, the main absorption occurs through the Yb 5d and 4f orbitals hybridized with O 2p[127]. The broad white line is due to the degeneracy of the 5d orbital and the formation of the crystal field. Also, no features emerging around 8940 eV indicate the absence of Yb^{2+}. In the case of H20, the spectrum resembles the Yb-L_3 XANES spectrum obtained for $Yb_2Cu_2O_5$ by Asakura et al.[128]. In this ytterbium compound, Yb occupies the octahedra sites and is coordinated by six oxygen ions, forming YbO_6 units.

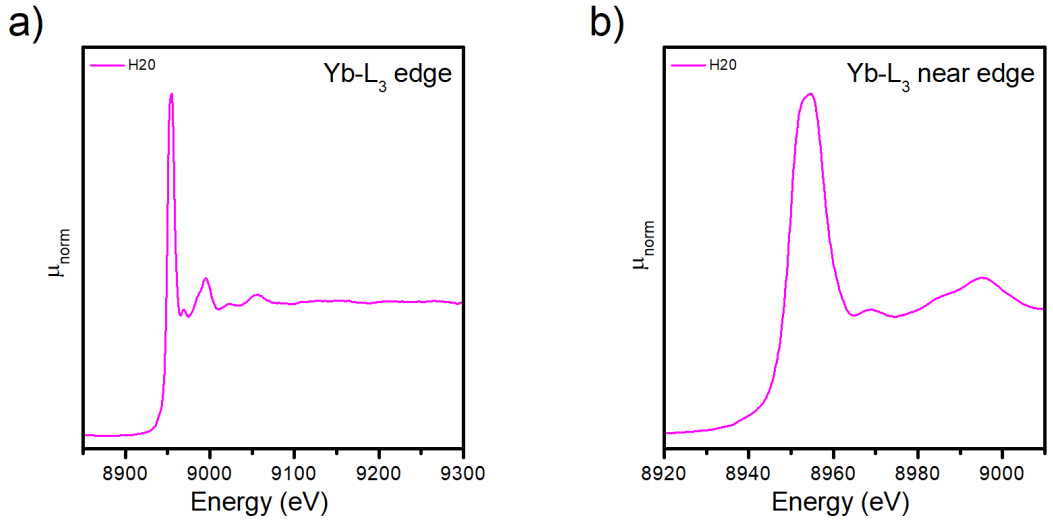

Figure 6.18 a) Absorption spectra in H20 sample for Yb-L_3 edge, b) close up around the edge.

In Figure 6.19 all spectra of Sm-L_3 absorption in the samples containing samarium are gathered. As for the lanthanides, like Yb, the main absorption feature is formed by 2p → 5d transition, albeit in this case, the white line is more narrow[129]. Since there is no pre-peak seen in the spectra, no Sm^{2+} is present in the sample[130]. The shape of all HEO sample spectra is similar to one another and to those reported by Asakura et al. for Sm complex oxides[129]. The intensity of the

white line for H40 is significantly decreased in relation to the others, whereas the highest intensity is seen for H38. These differences in intensity might be caused by the differences in the B-site element number and types. Thus the distortions in the crystal structure may weaken the hybridization of the orbitals.

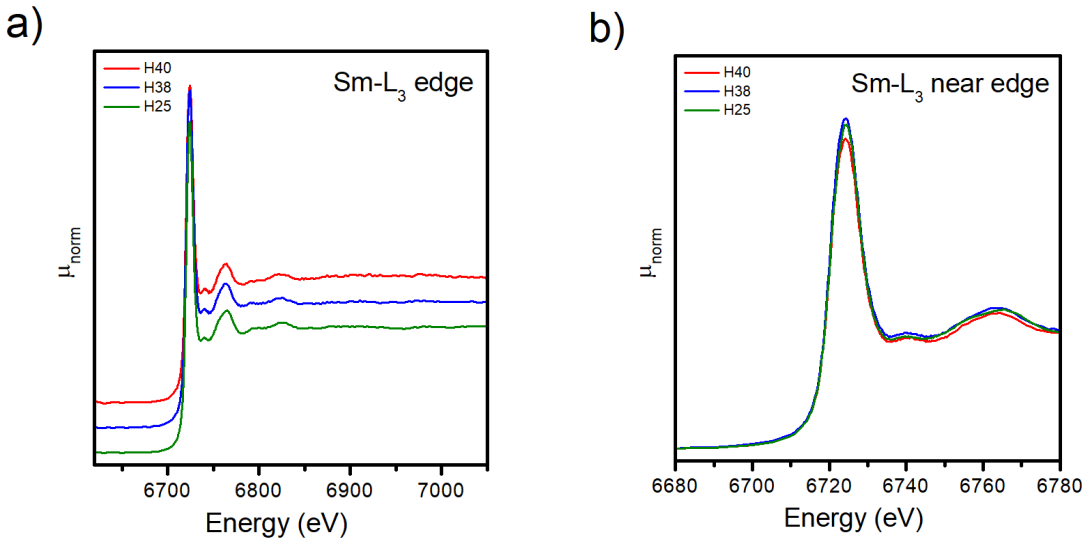

Figure 6.19 a) Absorption spectra in H25, H38 and H40 samples for Sm-L_3 edge, with offset, b) close up around the edge, without offset.

In Figure 6.20, a single spectrum for In-K edge in H22 is presented. Since indium in ionic form has the same electronic configuration as tin, their K edge absorption refers to the same transition, i.e. 1s → 5sp. This spectrum is similar to the results obtained for In_2O_3 where indium is at a 3+ oxidation state and is sixfold coordinated with oxygen[131,132]. The only difference with the reference oxide is the more prominent post-edge feature around 27970 eV. It might be caused by the presence of barium in the crystal structure, which orbitals take part in the formation of DOS around the absorption edge.

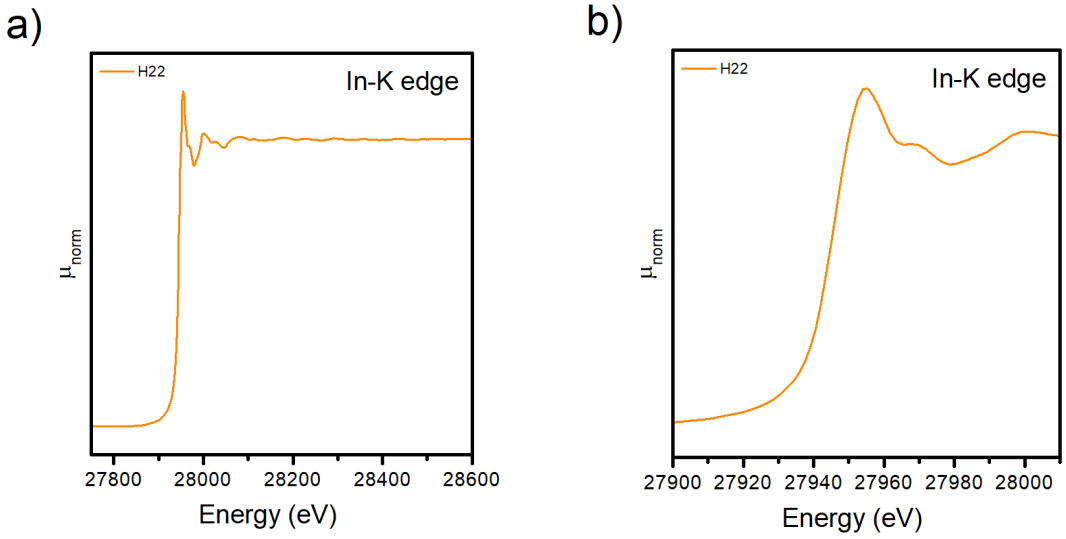

Figure 6.20 a) Absorption spectra in H22 sample for In-K edge, b) close up around the edge.

6.4.2 EXAFS

After the normalization, the $\chi(k)$ relations were derived from the data to perform the EXAFS analysis. The $Pm\bar{3}m$ structure was assumed in the model, and the wave vector range was set mostly from 2 to 8 Å^{-1} (in lower quality data, the highest value was 6 Å^{-1}, and in higher quality data – 10 Å^{-1} or more). The main goal of this analysis was to extract the bond lengths between metal ions and oxygen. All obtained values, as well as calculated average bond lengths in the HEO samples, are gathered in Tables 6.7 and 6.8. For better visualization, the cases with several representatives are plotted in Figure 6.21. The dashed lines in the figures represent a distance between the metal ion and oxygen ion estimated using the ionic radii in proper coordination and oxidation state[133].

Table 6.7 The M-O bond lengths in HEO samples for the core matrix elements.

Sample	M				
	Ba	Zr	Hf	Sn	Ti
H1	2.9052 ± 0.0461	-	2.0771 ± 0.0199	-	1.9140 ± 0.0373
H2	2.8997 ± 0.0383	2.1136 ± 0.0138	2.0807 ± 0.0294	2.0442 ± 0.0063	1.9274 ± 0.0163
H20	2.8758 ± 0.0394	-	2.0631 ± 0.0301	-	1.9367 ± 0.0200
H22	2.9215 ± 0.0445	2.1178 ± 0.0178	2.0719 ± 0.0252	2.0501 ± 0.0059	1.9359 ± 0.0259
H25	2.8906 ± 0.0363	-	2.0516 ± 0.0358	-	1.9327 ± 0.0193
H38	3.0172 ± 0.0508	-	2.0409 ± 0.0245	-	1.9427 ± 0.0689
H40	3.0169 ± 0.0315	-	-	-	-
HEO	2.9324 ± 0.0157	2.1157 ± 0.0113	2.0642 ± 0.0114	2.0471 ± 0.0043	1.9316 ± 0.0148
$BaTiO_3$	2.9461 ± 0.0344				1.8916 ± 0.0291
Theor.	2.96	2.07	2.06	2.04	1.955

Table 6.8 The M-O bond lengths in HEO samples for the other constituent elements.

Sample	M					
	Ce	Y	Yb	Sm	In	Zn
H1	-					
H2		2.2384 ± 0.0088				
H20			2.1830 ± 0.0237			
H22					2.1177 ± 0.0118	
H25				2.2807 ± 0.0324		
H38		-	-	2.2823 ± 0.0182	-	
H40	-	-	-	2.2876 ± 0.0172	-	-
HEO	-	2.2384 ± 0.0088	2.1830 ± 0.0237	2.2835 ± 0.0136	2.1177 ± 0.0118	-
Theor.	2.22	2.25	2.218	2.308	2.15	2.09

The first thing that becomes apparent from the data in Tables 6.7 and 6.8 is that there are different values of bond lengths for each B-site metal ion. This implies that corresponding octahedra have different sizes, which, in turn, indicates that the structural distortions in multicomponent materials manifest by the distribution of octahedra of different sizes. However, it should be remembered that the uncertainties of the data based on EXAFS analysis are quite large.

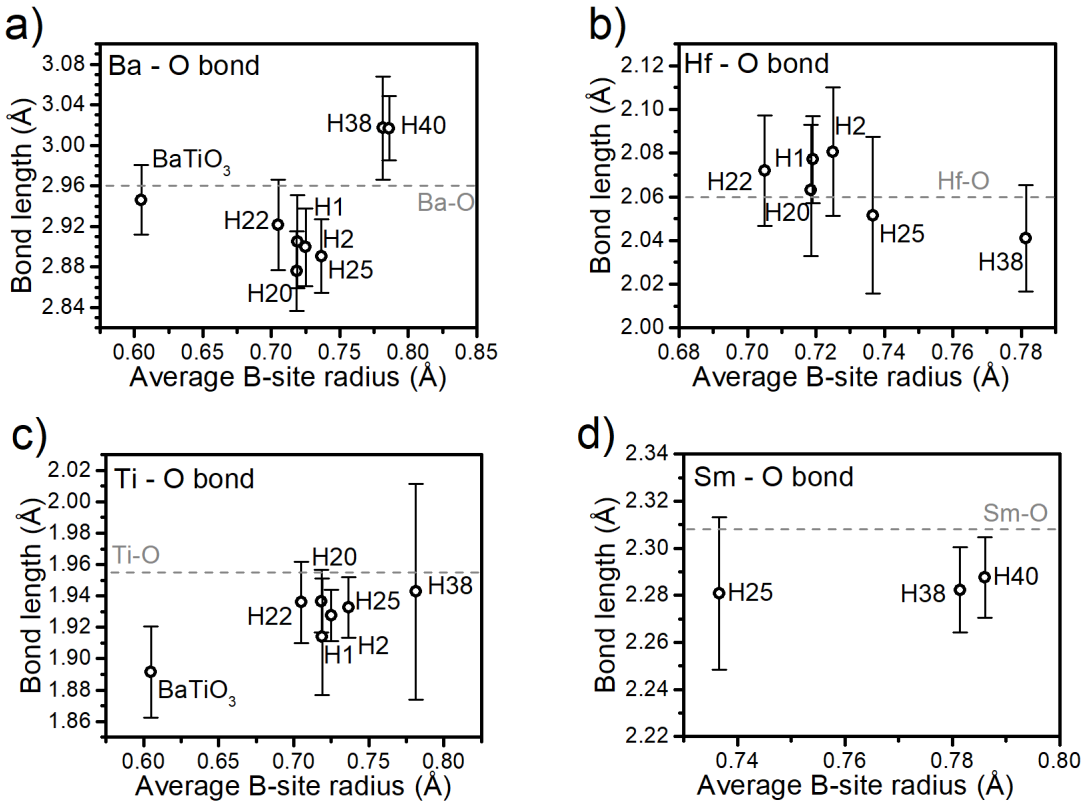

Figure 6.21 The comparison of M-O lengths for different HEO samples: a) Ba-O, b) Hf-O, c) Ti-O, d) Sm-O.

As for the comparison of bond lengths between different materials, the only notable difference is for H38 and H40, as presented in Figure 6.21a. Those 8- and 10-element perovskites have the longest Ba-O bonds, whereas 5-element perovskites have lower values than reference $BaTiO_3$. This is in accordance with Rietveld refinement results, which showed that the H38 and H40 materials have the largest lattice parameters. Additionally, the 5-B cation oxides show a quite unusual relation between the Ba-O bond length and the average B-site radius. As the radius increases, the Ba-O bond length decreases. This relation opposes that described in the XRD section in Figure 6.4, where a larger constituent causes an increase in the lattice parameter. Thus, this could mean that bigger octahedra somehow compress the A-sublattice. On the other hand, H38 and H40 break out from this relation, possibly because of the higher B element numbers and high oxygen vacancy concentration. This increase in the distance may signify the weakening of Ba-O bonds. In Figure 6.21b, there can be traced the decrease in the Hf-O bond length with the average B-site samples radius. Moreover, the Ti-O bond lengths (Figure 6.21c) are roughly similar in all multicomponent oxides and are longer than for reference barium titanate. For the Sm-O bond lengths (Figure 6.21d), there are no notable differences. However, even though there are some visible differences, a high degree of uncertainty overlap hinders the accuracy of the analysis.

Knowing the bond lengths enables the estimation of the lattice parameter from XAS measurements. In cubic perovskites (Goldschmidt factor equal unity), the following relations are fulfilled:

$$a_0 = 2 \cdot d_{BO} = \sqrt{2} \cdot d_{BaO}, \tag{6.3}$$

where d_{BO} denotes the distance between oxygen and the B-site ion and d_{BaO} denotes the distance between oxygen and barium ions. Estimations based on the Ba-O bonds can be performed for all samples. Additionally, for the H2 and H22, since all B-site elements were analyzed, the B-O distance was obtained as a simple arithmetic mean of all B-site bond lengths. The obtained values with uncertainties as well as a_0 values from the Rietveld refinement are presented in Table 6.9. As can be seen, the values estimated based on the XAS analysis differ from those of the Rietveld refinement, though they are in good agreement. In the case of H38 and H40, in contrast to the other oxides, the XAS-derived unit cell parameters are higher than those from the Rietveld analysis. Another interesting feature that can be noticed is that the best agreement between the unit cell parameters obtained based on the two methods was achieved for H22, H38, and H40. Chemical and structural differences/similarities between H38, H40, H22, and the other samples should be considered in order to discuss both issues. The first thing is the chemical composition: the B-cations common for all oxides are Zr, Hf, Ti and Sn. All of them form a strong bond with oxygen[134]. The fifth B-cation in H1, H2, H20, H22 and H25 is Ce, Y, Yb, In and Sm, respectively, while H38 and H40 contain additionally In or Zn and In. Among these cations, indium and zinc form the weakest bonds with O[135]. Based on that, it may be proposed that the better agreement between the XAS- and Rietveld-derived unit cell parameters is related to an easier adjustment of the B-O and Ba-O bond lengths one to another. Secondly, there are slight structural differences between H38, H40, and the other samples; namely, the Goldschmidt tolerance factors of H38 and H40 are around 0.98, whereas they are above 1 for the others. It may be linked to higher XAS a_0 than Rietveld a_0.

Table 6.9 The lattice parameters derived from Rietveld refinement and X-ray absorption spectroscopy for H2 and H22 samples.

Sample	Rietveld a_0 (Å)	XAS $a_0(d_{BaO})$ (Å)	XAS $a_0(d_{BO})$ (Å)
H1	4.1807 ± 0.0001	4.1085 ± 0.0651	
H2	4.1863 ± 0.0001	4.1007 ± 0.0541	4.1617 ± 0.0151
H20	4.1735 ± 0.0001	4.0670 ± 0.0557	
H22	4.1516 ± 0.0001	4.1316 ± 0.0630	4.1174 ± 0.0170
H25	4.1982 ± 0.0001	4.0879 ± 0.0514	
H38	4.2490 ± 0.0001	4.2669 ± 0.0718	
H40	4.2564 ± 0.0001	4.2666 ± 0.0445	

The values of bond lengths for all measured metal ions are comparable, but the data for all samples is incomplete; nevertheless, the analysis based on average bond length in HEO samples can give some insight into overall correlations in multicomponent oxides. In Figure 6.22, all averaged bond lengths are plotted as a function of the theoretical distance between metal ion and oxygen within the hard sphere approximation. The dashed line corresponds to the slope equal to 1, which represents the agreement between theoretical and experimental values. At first, all values are close to the line. The elements like Hf and Sn are located on the line, meaning that octahedra containing these metals are unstrained. However, several acceptor constituents are slightly below the line, which could imply that their octahedra are compressed. The same is observed for Ti. The XANES analysis found that extensive oxygen vacancy concentration around titanium caused the

deviation from the centrosymmetry. Thus, it is possible that the presence of $V_O^{\bullet\bullet}$ around the B-site ion makes the octahedron susceptible to deformations. The only element that falls out above the line is Zr. This would mean that the zirconium octahedron is larger.

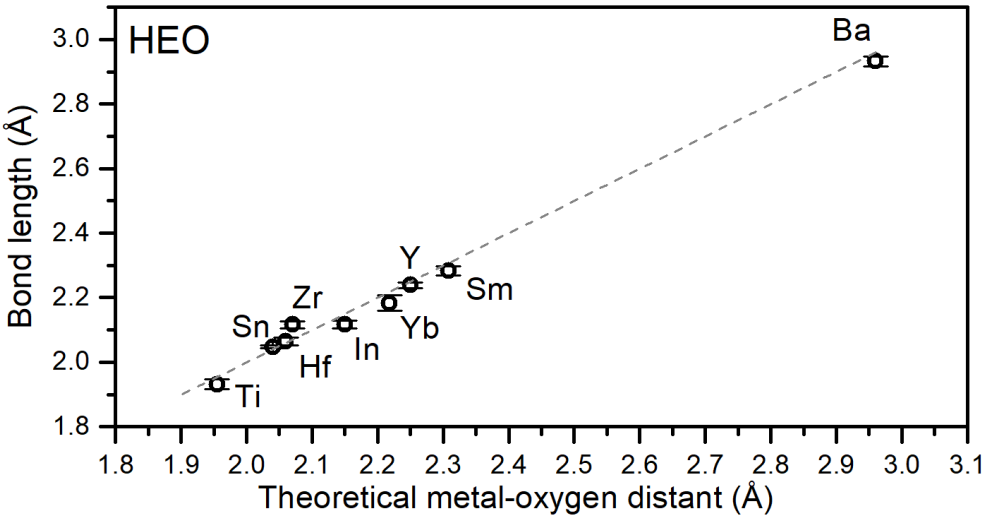

Figure 6.22 The average metal-oxygen bond length as a function of the theoretical metal-oxygen distance.

6.5 Scanning Electron Microscopy

In Figure 6.23, two exemplary SEM images of H22 and H25 synthesized in 1500 °C without the nickel oxide as a sintering aid are presented. Despite the high synthesis temperature, both compositions formed small (below 1 μm) grains that are moderately sintered with each other. Thus, each sample that did not achieve a relative density above 90% was prepared with an addition of 1 mol% of NiO. Figures 6.24 – 6.30 present SEM images made on dense pellets previously used for EIS measurements. For better visualization, all samples were covered with a thin 10 nm Au layer to prevent electron accumulation on the surface. The scale is set to the same magnification for easier comparison in all figures.

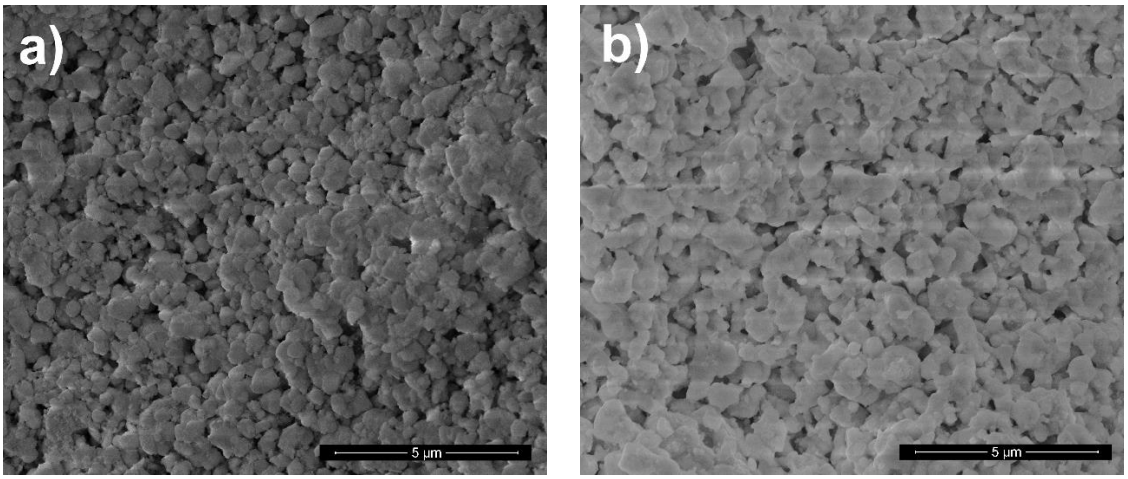

Figure 6.23 SEM images of morphology of the a) $BaZr_{0.2}Hf_{0.2}Sn_{0.2}Ti_{0.2}In_{0.2}O_{2.9}$ (H22), b) $BaZr_{0.2}Hf_{0.2}Sn_{0.2}Ti_{0.2}Sm_{0.2}O_{2.9}$ (H25) samples prepared without the sintering aid.

6.5.1 Morphology

Firstly, in Figure 6.24 the SEM images for $BaZr_{0.2}Hf_{0.2}Sn_{0.2}Ti_{0.2}Ce_{0.2}O_{3-\delta}$ (H1) are gathered. From Figure 6.24a, it can be seen that this ceramics forms quite dense microstructure with well-sintered grains. The size of grains varies from submicron to a few micrometers. Additionally, the BS electrons (Figure 6.24b) do not indicate the presence of any other phase in the bulk of the material. Worth noting is that H1 is the only 5B cation sample prepared within this work, that did not need the sintering aid to reach a high relative density.

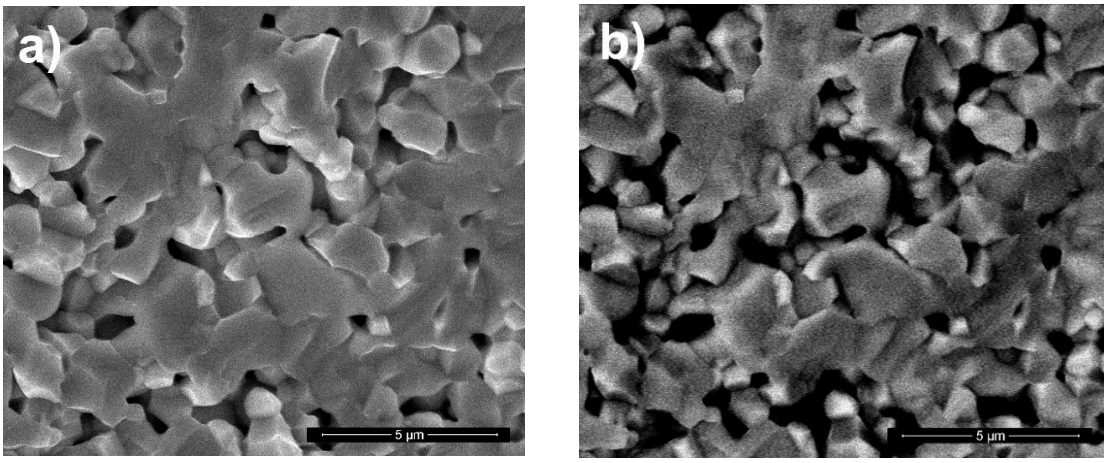

Figure 6.24 The SEM images of the cross section of $BaZr_{0.2}Hf_{0.2}Sn_{0.2}Ti_{0.2}Ce_{0.2}O_{3-\delta}$ (H1) sample, based on a) secondary electrons, b) back-scattered electrons.

In Figure 6.25 the SEM images for $BaZr_{0.2}Hf_{0.2}Sn_{0.2}Ti_{0.2}Y_{0.2}O_{2.9}$ (H2) containing yttrium are presented. The grain size range (between 1 µm and 5 µm) is comparable to H1 one, but the grains are barely distinguishable due to firm sintering. The BSE signal in Figure 6.25b presents a uniform image without phase separation or segregation. The visible bright spots are caused by the roughness of the cross-section, what is also apparent from Figure 6.25a.

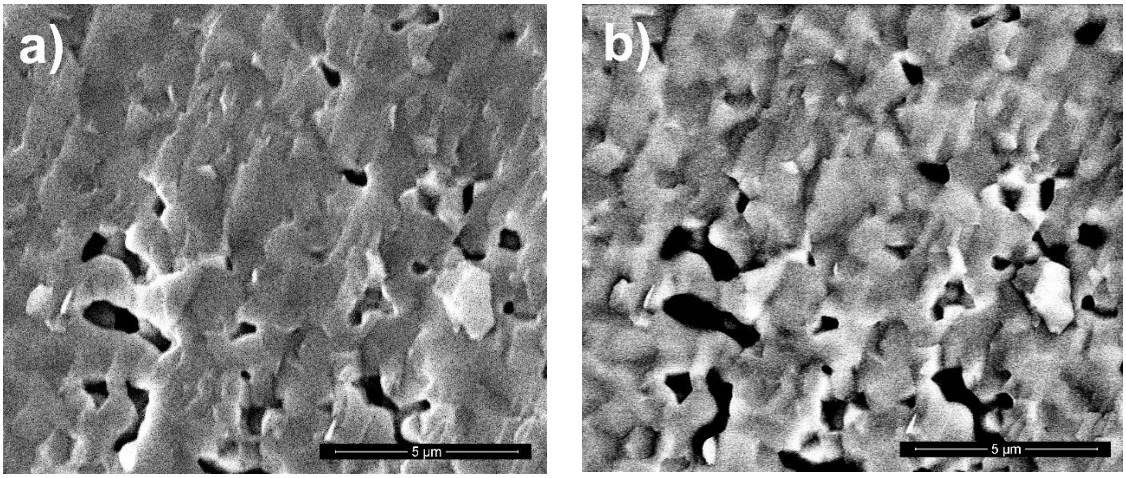

Figure 6.25 The SEM images of the cross-section of $BaZr_{0.2}Hf_{0.2}Sn_{0.2}Ti_{0.2}Y_{0.2}O_{2.9}$ (H2) sample, based on a) secondary electrons, b) back-scattered electrons.

In Figure 6.26, the SEM images for $BaZr_{0.2}Hf_{0.2}Sn_{0.2}Ti_{0.2}Yb_{0.2}O_{2.9}$ (H20) are displayed. Regarding the secondary electron signal, this sample exhibits a similar microstructure to the sample containing yttrium – a few closed pores and well-sintered, hardly distinguishable grains. However,

for the BSE signal shown in Figure 6.26b, bright spots that do not originate from the topographic distribution can be seen. This would mean some possibly separated binary oxide or other perovskite with altered stoichiometry. This is consistent with the XRD results, which showed very low reflections from unreacted oxides, as presented in Figure 6.2.

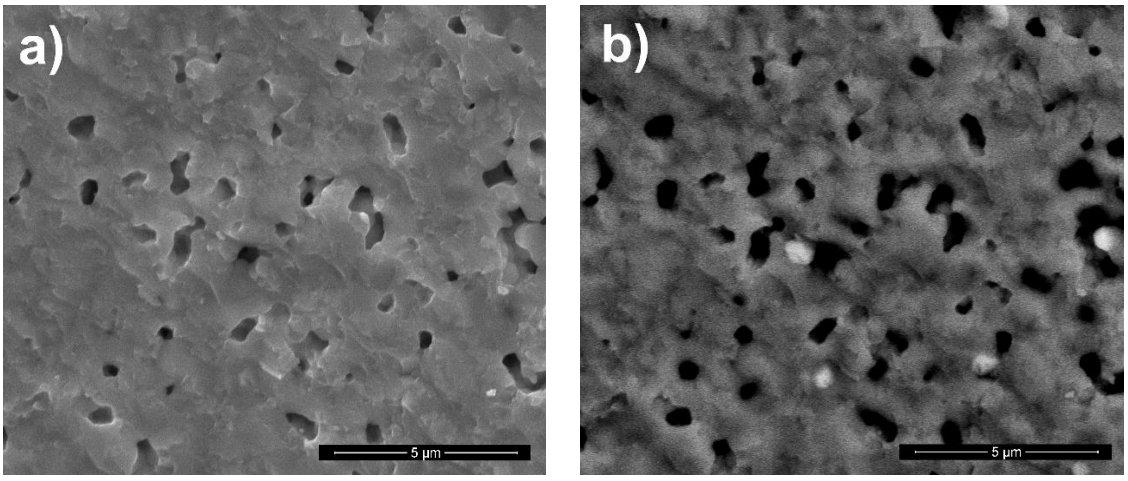

Figure 6.26 The SEM images of the cross section of $BaZr_{0.2}Hf_{0.2}Sn_{0.2}Ti_{0.2}Yb_{0.2}O_{2.9}$ (H20) sample, based on a) secondary electrons, b) back-scattered electrons.

In Figure 6.27, the SEM images $BaZr_{0.2}Hf_{0.2}Sn_{0.2}Ti_{0.2}In_{0.2}O_{2.9}$ (H22) are gathered. In this species, it can be seen that grains form well-resolved polyhedra with a size in the range of 1-2 micrometers. By comparing these images with Figure 6.27a, we see that the sintering aid significantly impacts the microstructure. Throughout the fracture, there is no sign of the porosity, meaning this pellet reached a high degree of densification. Apart from the large grains, many small, nanometric-size grains residing at the grain boundaries are also visible in Figure 6.27a. Yet, the BSE signal in Figure 6.27b shows no significant signs of the difference in intensity between both types of grains.

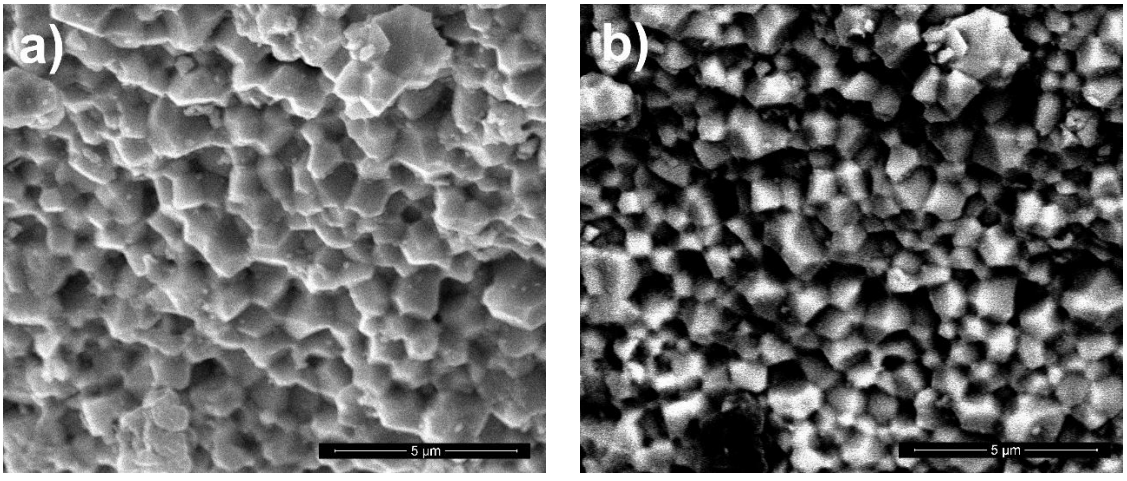

Figure 6.27 The SEM images of the cross section of $BaZr_{0.2}Hf_{0.2}Sn_{0.2}Ti_{0.2}In_{0.2}O_{2.9}$ (H22) sample, based on a) secondary electrons, b) back-scattered electrons.

In Figure 6.28, the SEM images for the last 5-B sample $BaZr_{0.2}Hf_{0.2}Sn_{0.2}Ti_{0.2}Sm_{0.2}O_{2.9}$ (H25) are presented. In this case, NiO also helped achieve a well-sintered microstructure without pronounced porosity. The grain size is comparable to H22 or even a little bigger, reaching 3-4 µm.

There are also visible nanometer-sized grains but in lower quantity than in indium-containing oxide. The backscattered electron signal does not pick up any differences in the phase content of this sample.

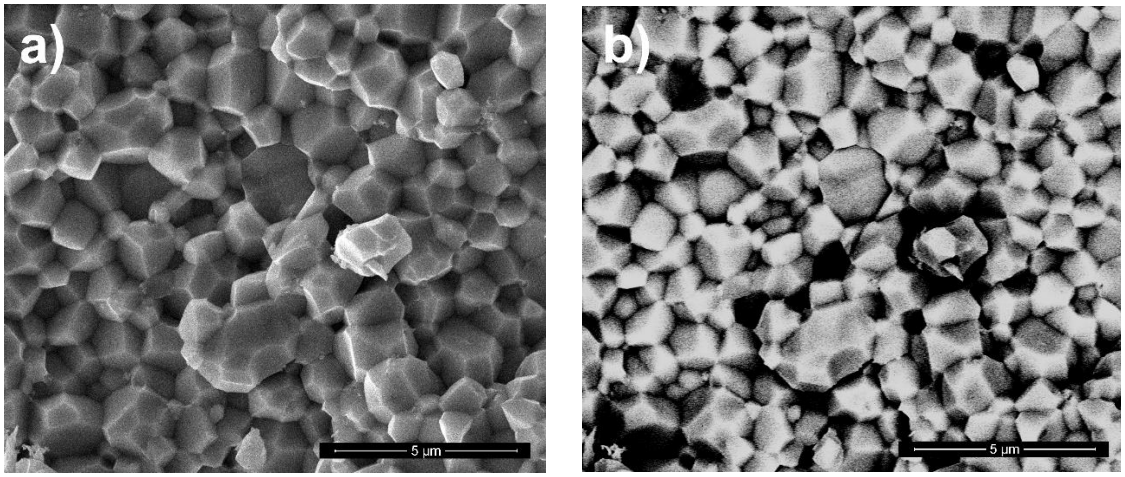

Figure 6.28 The SEM images of the cross-section of $BaZr_{0.2}Hf_{0.2}Sn_{0.2}Ti_{0.2}Sm_{0.2}O_{2.9}$ (H25) sample, based on a) secondary electrons, b) back-scattered electrons.

In Figure 6.29, the SEM images for $BaZr_{0.125}Hf_{0.125}Sn_{0.125}Ti_{0.125}Y_{0.125}Yb_{0.125}Sm_{0.125}In_{0.125}O_{2.75}$ (H38) sample are displayed. This sample reached a high relative density at 1500 °C without adding a sintering aid, achieving firmly sintered grains with minimal spaces that could be attributed to some closed pores. The grains form polyhedra of around a few micrometers in size. In Figure 6.29b, from the BSE signal, it can also be seen that no secondary phases are present.

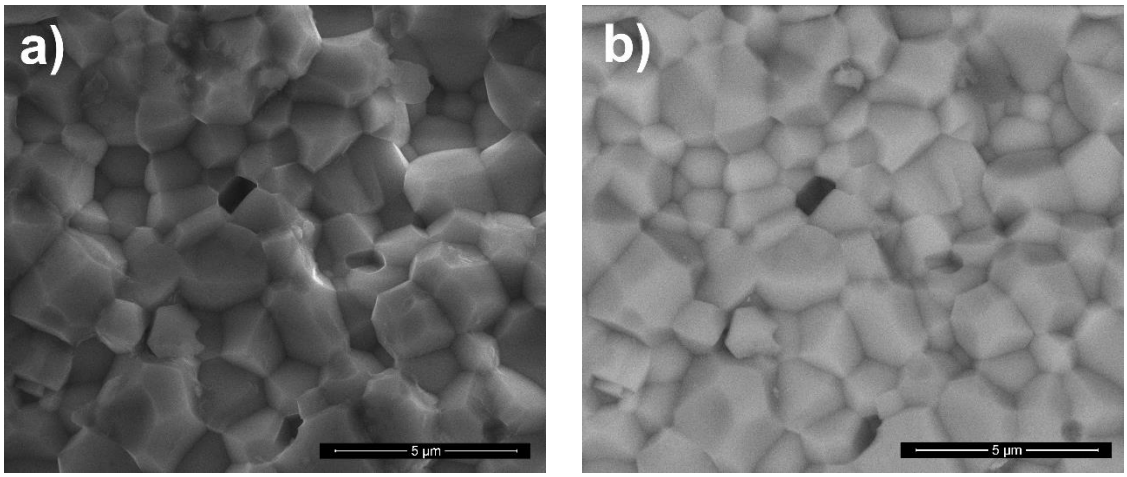

Figure 6.29 The SEM images of the cross section of $BaZr_{0.125}Hf_{0.125}Sn_{0.125}Ti_{0.125}Y_{0.125}Yb_{0.125}Sm_{0.125}In_{0.125}O_{2.75}$ (H38) sample, based on a) secondary electrons, b) back-scattered electrons.

Lastly, the SEM images for $BaZr_{0.1}Hf_{0.1}Sn_{0.1}Ti_{0.1}Ce_{0.1}Y_{0.1}Yb_{0.1}Sm_{0.1}In_{0.1}Zn_{0.1}O_{2.7}$ (H40) sample are gathered in Figure 6.30. The microstructure of this sample is similar to that of H38, although H40 was sintered at a lower temperature. H40 contains zinc, and using zinc oxide as a reagent during the synthesis also acts as a sintering aid. Also, there is no indication of any secondary phases in the BSE signal (Figure 6.30b).

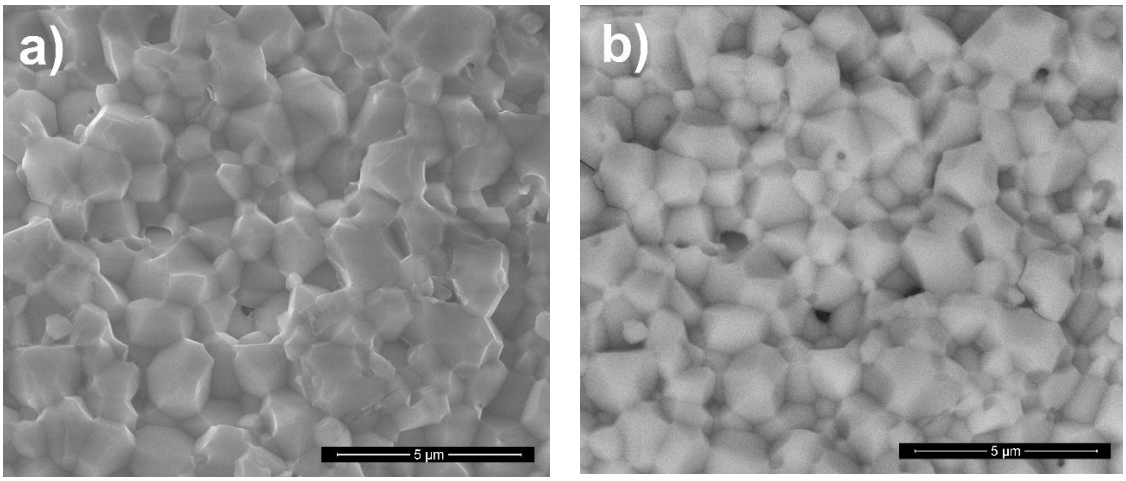

Figure 6.30 The SEM images of the cross-section of the H40 sample, based on a) secondary electrons b) back-scattered electrons.

6.5.2 Energy Dispersive X-ray Spectroscopy

The EDS analysis was conducted by performing surface scans with a spot diameter of 53.7 µm for 200 s. The exemplary EDS spectrum is presented in Figure 6.31, whereas quantitative results in the form of atomic concentration percentages are gathered in Table 6.10.

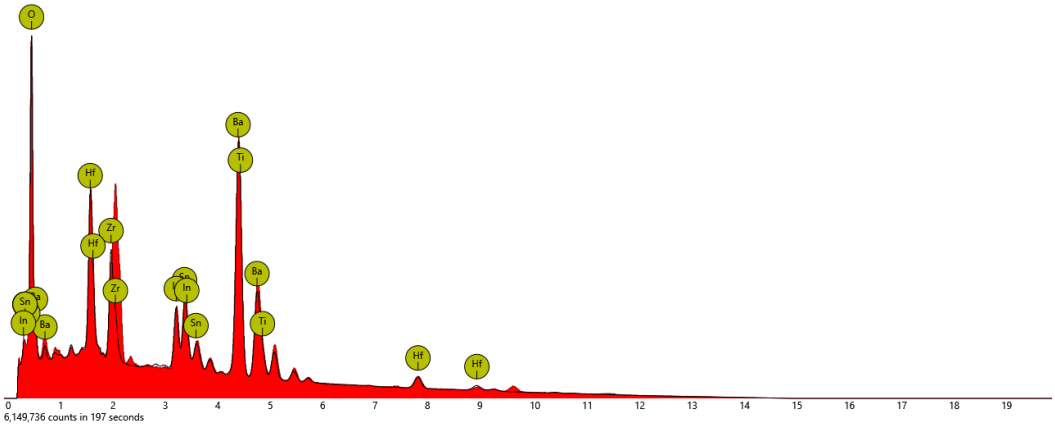

Figure 6.31 The exemplary EDS spectrum for $BaZr_{0.2}Hf_{0.2}Sn_{0.2}Ti_{0.2}In_{0.2}O_{2.9}$ (H22).

In Figure 6.32, maps of all elements present in $BaZr_{0.2}Hf_{0.2}Sn_{0.2}Ti_{0.2}Ce_{0.2}O_{3-\delta}$ (H1) are put together. As can be seen, there is no predominant signal on any map, and all elements are evenly distributed throughout the grains. The only notable variations visible in oxygen signal are due to examined surfaces being unpolished.

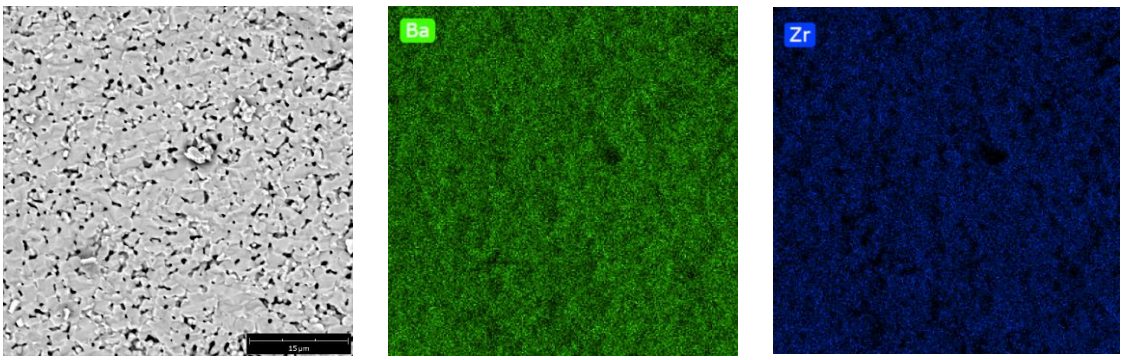

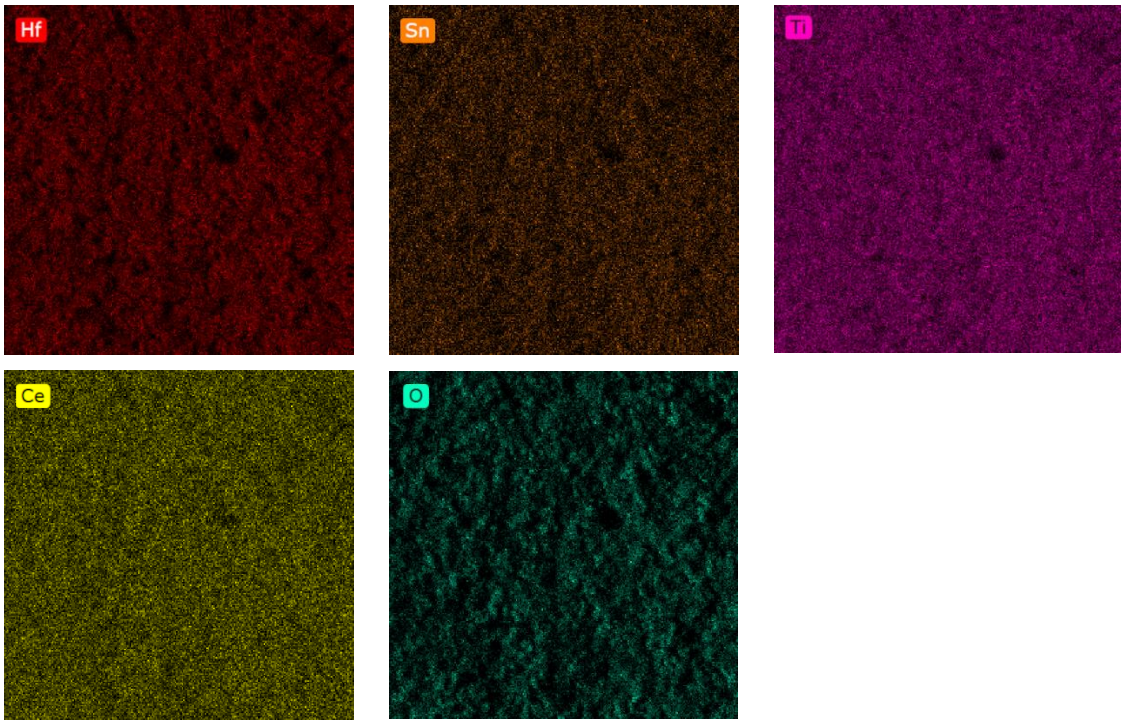

Figure 6.32 The area selected for EDS analysis in $BaZr_{0.2}Hf_{0.2}Sn_{0.2}Ti_{0.2}Ce_{0.2}O_{3-\delta}$ (H1) and maps obtained for each consisting element.

In Figure 6.33, maps of all elements that form $BaZr_{0.2}Hf_{0.2}Sn_{0.2}Ti_{0.2}Y_{0.2}O_{2.9}$ (H2) are gathered. Here, the pellet also looks homogeneous, with a similar to H1 difference in oxygen concentration stemming from the roughness of the cross-section.

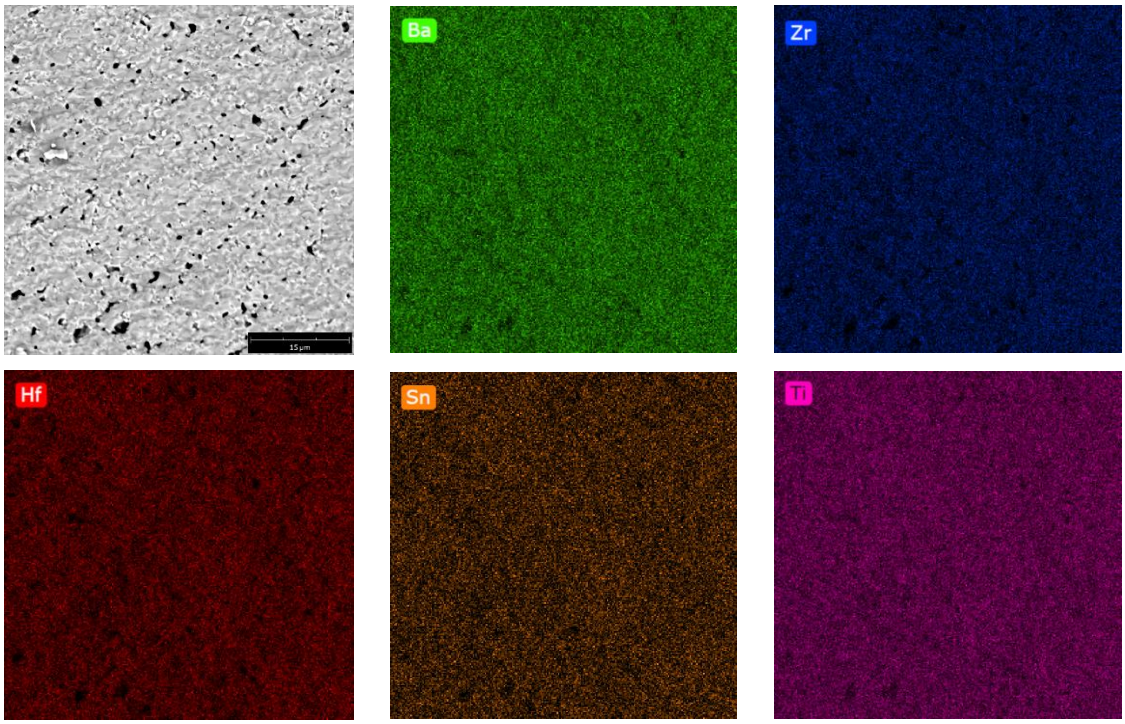

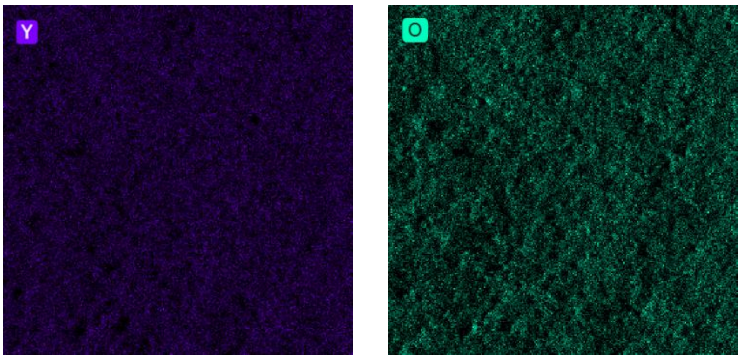

Figure 6.33 The area selected for EDS analysis in $BaZr_{0.2}Hf_{0.2}Sn_{0.2}Ti_{0.2}Y_{0.2}O_{2.9}$ (H2) and maps obtained for each consisting element.

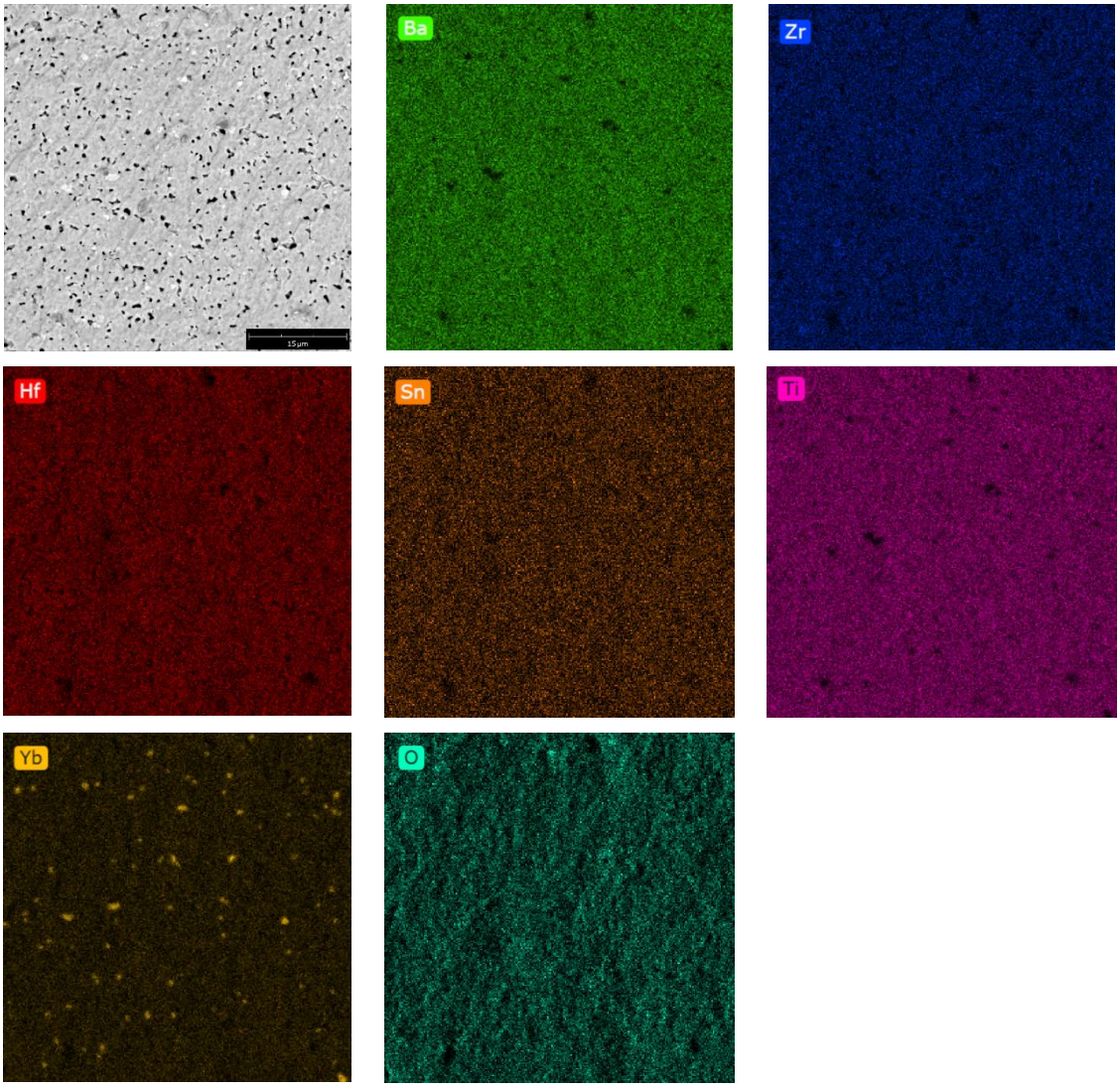

Figure 6.34 The area selected for EDS analysis in $BaZr_{0.2}Hf_{0.2}Sn_{0.2}Ti_{0.2}Yb_{0.2}O_{2.9}$ (H20) and maps obtained for each consisting element.

In Figure 6.34, the EDS analysis results for $BaZr_{0.2}Hf_{0.2}Sn_{0.2}Ti_{0.2}Yb_{0.2}O_{2.9}$ (H20) are displayed. In this case, the biggest difference in the distribution of elements is seen for ytterbium. There are multiple spots where the Yb concentration is higher than in other regions of the material.

Additionally, in these spots, some of the other elements have lowered concentration e.g. Ti and Ba. This could mean that ytterbium-enriched locations are pinpointing to a secondary phase containing mainly Yb, like Yb_2O_3. This observation is consistent with the bright spots found in the BSE signal for this sample (Figure 6.26b).

In Figure 6.35, the results of EDS analysis for $BaZr_{0.2}Hf_{0.2}Sn_{0.2}Ti_{0.2}In_{0.2}O_{2.9}$ (H22) are shown. In this sample, two types of grains are visible in the spot range (preview is made using BSE signal). However, element concentration maps do not distinguish any composition variation between those grains. There is only one heightened signal for oxygen in a large cavity.

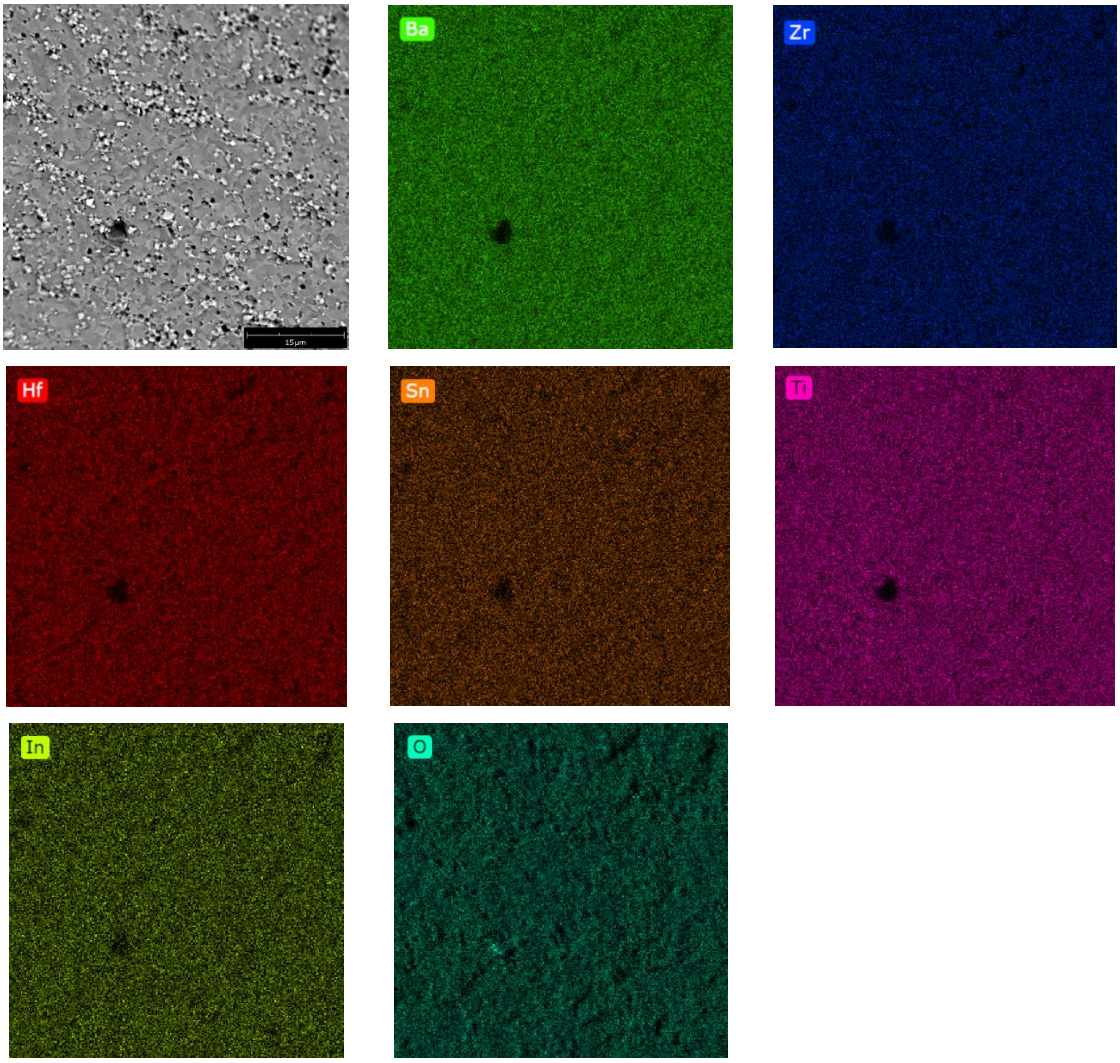

Figure 6.35 The area selected for EDS analysis in $BaZr_{0.2}Hf_{0.2}Sn_{0.2}Ti_{0.2}In_{0.2}O_{2.9}$ (H22) and maps obtained for each consisting element.

In Figure 6.36, maps of all elements present in $BaZr_{0.2}Hf_{0.2}Sn_{0.2}Ti_{0.2}Sm_{0.2}O_{2.9}$ (H25) are gathered. In this pellet, similarly to H2, the only notable changes are for oxygen concentration that reflects cross-section topography.

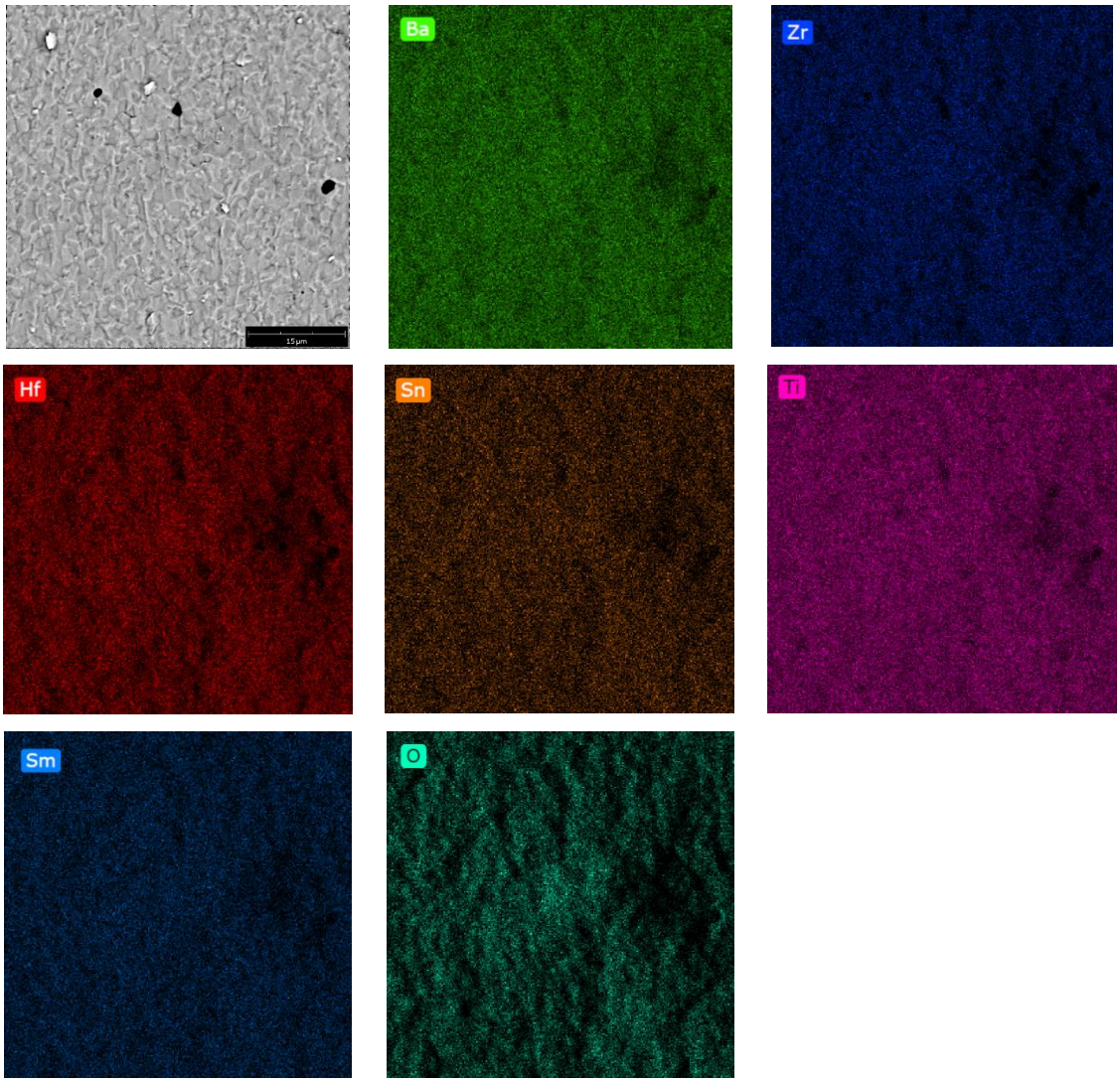

Figure 6.36 The area selected for EDS analysis in $BaZr_{0.2}Hf_{0.2}Sn_{0.2}Ti_{0.2}Sm_{0.2}O_{2.9}$ (H25) and maps obtained for each consisting element.

In Figure 6.37, EDS maps for $BaZr_{0.125}Hf_{0.125}Sn_{0.125}Ti_{0.125}Y_{0.125}Yb_{0.125}Sm_{0.125}In_{0.125}O_{2.75}$ (H38) are presented. As for 5-element B-site samples, elements are distributed uniformly across the grains. The oxygen concentration artefacts are also reflected in this sample.

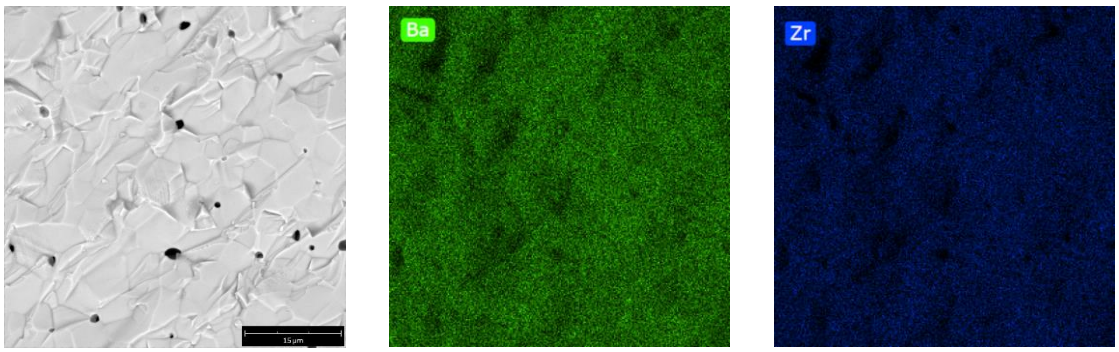

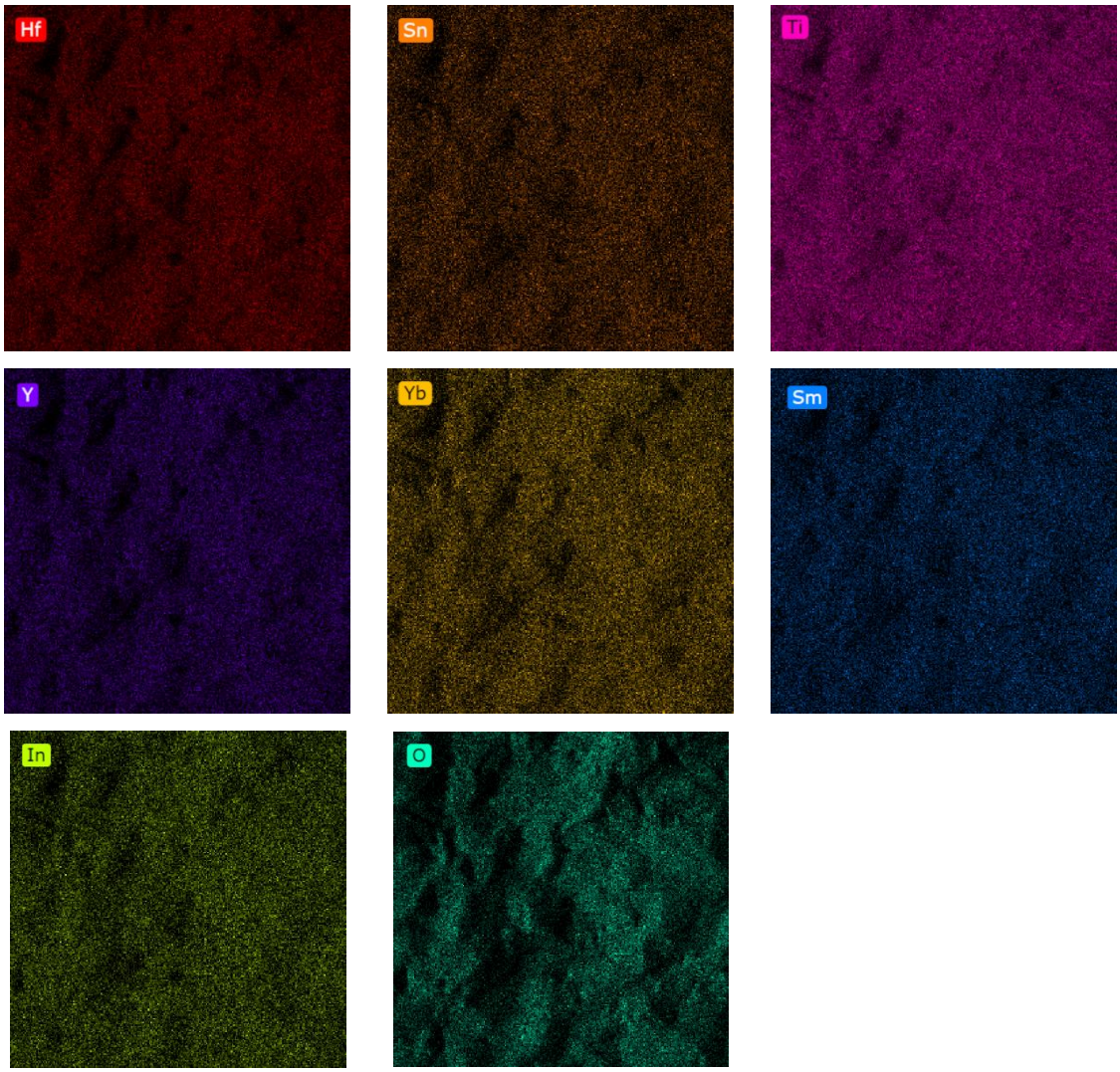

Figure 6.37 The area selected for EDS analysis in $BaZr_{0.125}Hf_{0.125}Sn_{0.125}Ti_{0.125}Y_{0.125}Yb_{0.125}Sm_{0.125}In_{0.125}O_{2.75}$ (H38) and maps obtained for each consisting element.

Lastly, EDS analysis maps for $BaZr_{0.1}Hf_{0.1}Sn_{0.1}Ti_{0.1}Ce_{0.1}Y_{0.1}Yb_{0.1}Sm_{0.1}In_{0.1}Zn_{0.1}O_{2.7}$ (H40) are shown in Figure 6.38. Here, the distribution of elements is comparable to that of the majority of previously described samples, including the oxygen concentration variation.

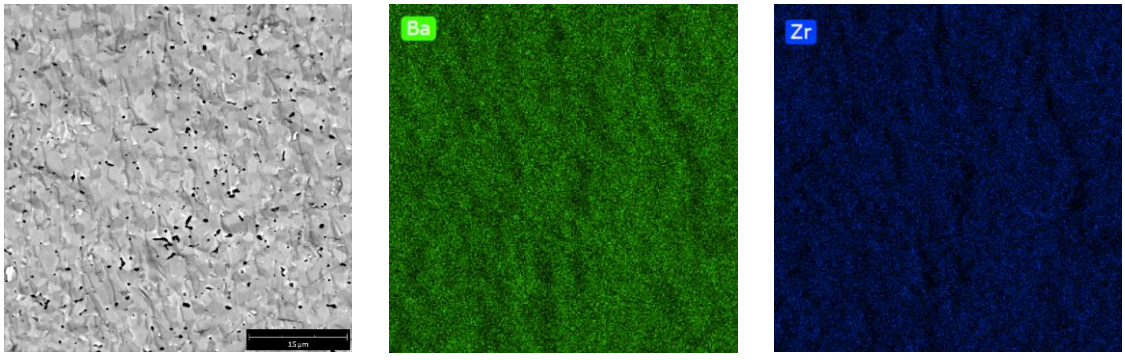

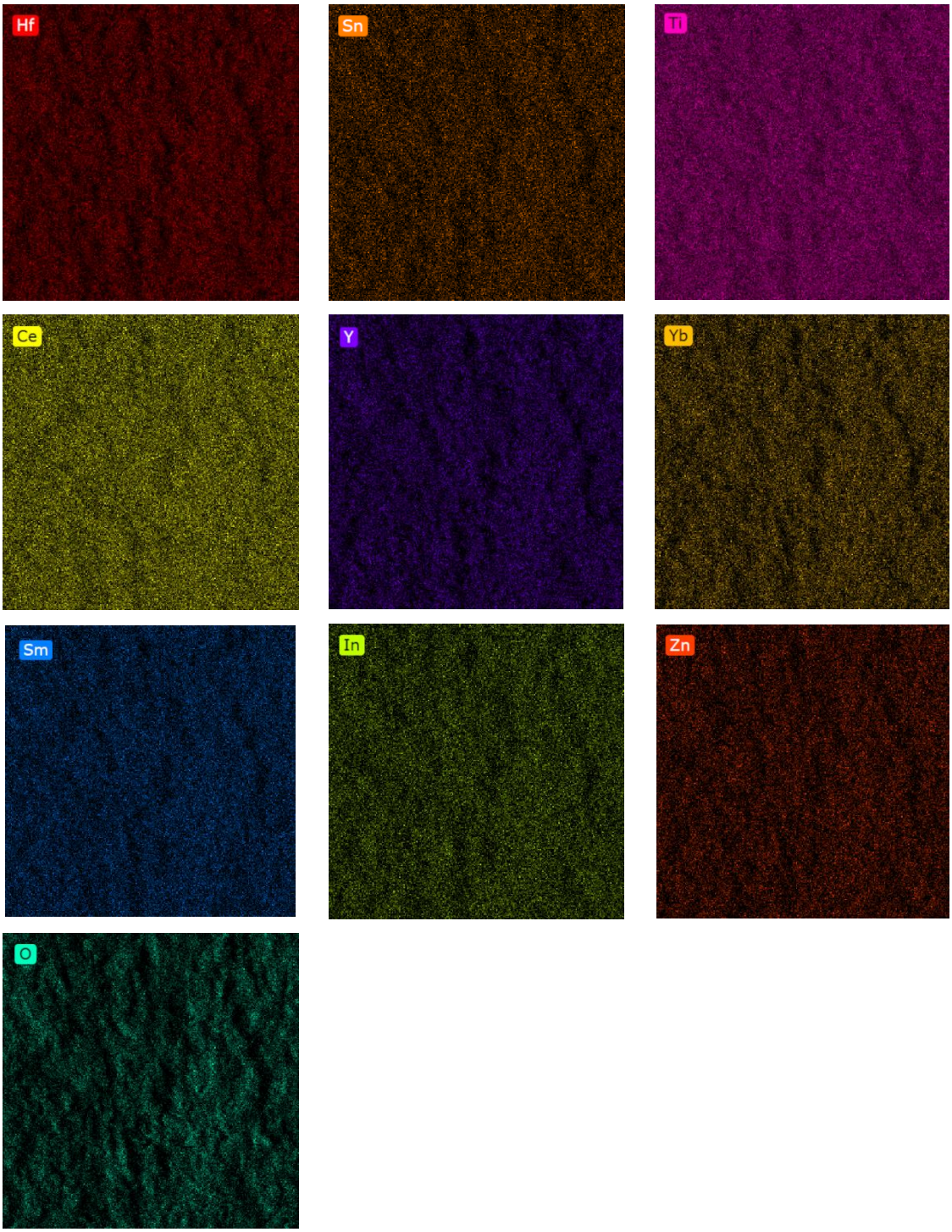

Figure 6.38 The area selected for EDS analysis in $BaZr_{0.1}Hf_{0.1}Sn_{0.1}Ti_{0.1}Ce_{0.1}Y_{0.1}Yb_{0.1}Sm_{0.1}In_{0.1}Zn_{0.1}O_{2.7}$ (H40) and maps obtained for each consisting element.

By looking at the values in Table 6.10, the conclusions about the actual composition of samples could be drawn. Firstly, the oxygen content in all of them is in an appropriate range for the nominal composition (around 60% or less). Since oxygen is regarded as a 'light' element and its recorded signal in EDS analysis exhibits significant uncertainty, those values are acceptable.

The concentrations of the concerned element are higher than stoichiometric values for titanium and zirconium and lower for hafnium and barium for all analyzed samples. Those related to Ba and Ti can be linked together and ascribed to the overlap of their energies in the EDS spectrum, as seen in Figure 6.31. Thus, it is challenging to deconvolute those peaks and determine the proper concentrations. A higher Zr and lower Hf content in all samples could be explained by the zirconium contamination of hafnium oxide. The XRD analysis of the HfO_2 reagent has been conducted. The resulting diffractogram with Rietveld analysis is presented in Figure 6.39. As can be seen, apart from the reflections of hafnium oxide, ZrO_2 has also been identified. Moreover, this impurity makes up to 30% of this reagent, causing an increase in Zr content at the expense of Hf. This means that synthesized samples should have a ratio of Zr:Hf around 2:1, consistent with values for zirconium and hafnium in Table 6.10.

Table 6.10 The atomic concentration of elements derived from the EDS analysis.

Sample	Atomic concentration (%)											
	Ba	O	Zr	Hf	Sn	Ti	Ce	Y	Yb	Sm	In	Zn
H1	13.21	61.67	5.37	2.88	3.51	8.96	4.41					
H2	13.53	58.69	6.83	3.17	3.94	9.24		4.59				
H20	13.08	61.15	6.70	3.59	3.51	8.80			3.18			
H22	14.22	59.97	5.84	3.56	3.62	8.94					3.85	
H25	12.58	60.55	5.98	3.58	4.32	8.68				4.31		
H38	15.14	54.30	6.63	1.89	2.32	8.76		3.12	2.65	2.77	2.42	
H40	14.19	58.22	5.16	1.59	2.23	7.26	3.03	2.01	1.45	1.74	1.66	1.47

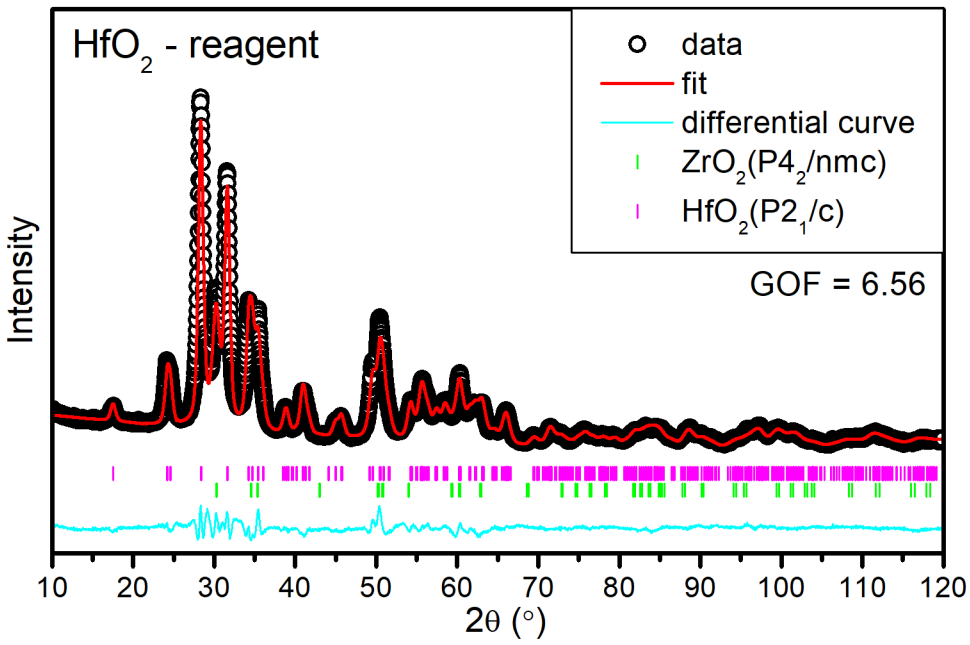

Figure 6.39 XRD pattern with Rietveld analysis for HfO_2 substrate.

6.6 Thermal analysis

6.6.1 Isothermal thermogravimetry

In Figure 6.40, mass changes during isothermal switches between wet and dry air are presented. $BaZr_{0.2}Hf_{0.2}Sn_{0.2}Ti_{0.2}Ce_{0.2}O_{3-\delta}$ (H1) exhibit weak water uptake since this sample contains no acceptors and oxygen vacancies stem from intrinsic sources, i.e. thermal equilibrium and charge compensation through aliovalent elements (Ti and Ce). On the other hand, $BaZr_{0.1}Hf_{0.1}Sn_{0.1}Ti_{0.1}Ce_{0.1}Y_{0.1}Yb_{0.1}Sm_{0.1}In_{0.1}Zn_{0.1}O_{2.7}$ (H40) shows a significant relative mass change upon change of water partial pressure. This is caused by the high acceptor concentration, which influences the oxygen vacancy concentration. Using Equation 5.6, the concentration of proton defects was determined for all samples and collected in Table 6.11 from the relative mass changes.

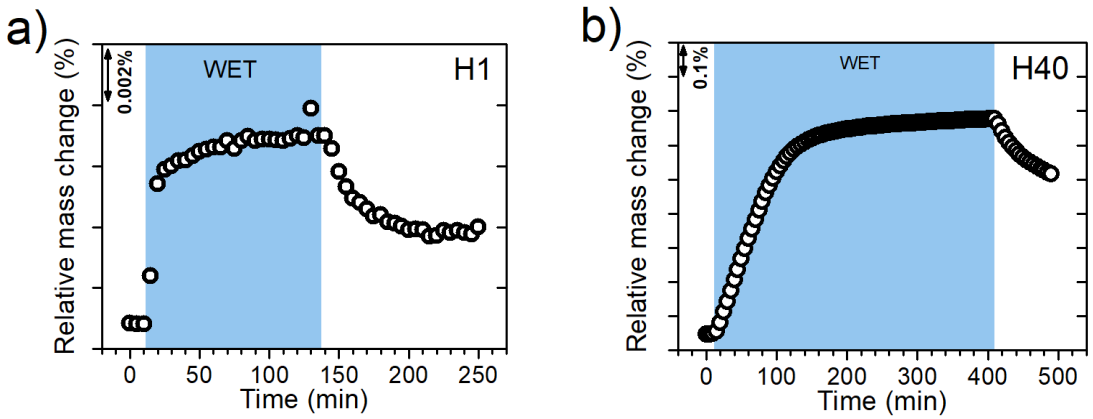

Figure 6.40 Isothermal thermograms of a) $BaZr_{0.2}Hf_{0.2}Sn_{0.2}Ti_{0.2}Ce_{0.2}O_{3-\delta}$ (H1) and b) $BaZr_{0.1}Hf_{0.1}Sn_{0.1}Ti_{0.1}Ce_{0.1}Y_{0.1}Yb_{0.1}Sm_{0.1}In_{0.1}Zn_{0.1}O_{2.7}$ (H40), recorded at 300 °C after the isothermal switch between dry and humidified air.

The values collected in Table 6.11 show that the concentration of proton defects in the multicomponent oxides containing acceptor constituents varies between samples. With the increase in nominal acceptor concentration, the concentration of $OH_O^{\bullet}$ also increases. Additionally, in selected samples, the proton defect concentration rises (by a maximum 16%) if the measurement is conducted using nitrogen as a working gas. This means inert gas promotes reduction processes that heighten the $[V_O^{\bullet\bullet}]$. The highest concentration of proton defects in synthesized high-entropy oxides has been observed in $BaZr_{0.1}Hf_{0.1}Sn_{0.1}Ti_{0.1}Ce_{0.1}Y_{0.1}Yb_{0.1}Sm_{0.1}In_{0.1}Zn_{0.1}O_{2.7}$ (H40) reaching about 0.2 mol/mol in both atmospheres. However, the reference sample $BaZr_{0.44}Ce_{0.35}Y_{0.2}O_{3,}$ under similar conditions, achieves higher values of proton defect concentration in comparison to most of the HEOs presented. This would imply the presence of two types of oxygen vacancies: active ones contributing to the water uptake and inert ones, which do not take part in the hydration mechanism, as mentioned by Leonard et al.[136].

Table 6.11 Proton defect concentration of synthesized high-entropy oxides at 300 °C.

Sample	Nominal acceptor concentration (mol%)	$[OH_O^{\bullet}]$ in air @ 300 °C (mol/mol)	$[OH_O^{\bullet}]$ in N_2 @ 300 °C (mol/mol)
H1	0	2.1×10^{-3}	2.1×10^{-3}
H2	20	3.6×10^{-2}	3.7×10^{-2}
H20	20	3.0×10^{-2}	3.5×10^{-2}
H22	20	3.7×10^{-2}	4.0×10^{-2}
H25	20	2.5×10^{-2}	2.9×10^{-2}
H38	50	1.5×10^{-1}	1.5×10^{-1}
H40	60	2.0×10^{-1}	2.1×10^{-1}
$BaZr_{0.44}Ce_{0.35}Y_{0.2}O_3$[136]	20		1.67×10^{-1}

Interesting observations concerning the water uptake can be made for 5-B samples. Figure 6.41 displays the proton defect concentrations for samples with 20 mol% of acceptors as a function of average B-cation radii. As can be seen, there is a somewhat linear decrease in proton concentration with radii increase caused by different substituting elements. This would mean that bigger elements in the B-site negatively influence the hydration process while smaller elements aid a higher proton defect concentration. It seems that with smaller octahedra in perovskite oxide, the proton has more space to fit into.

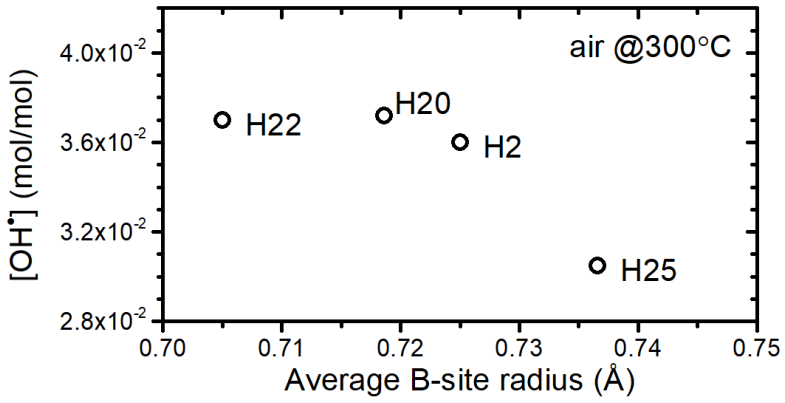

Figure 6.41 Proton defect concentration as a function of average B-cation radii in 5B multicomponent oxides.

6.6.2 Isobaric thermogravimetry

In Figure 6.42, an exemplary isobaric thermogravimetric curve is displayed. After the switch from dry to humidified air at 800 °C, the mass changes follow the step-type decrease in temperature. The mass differences recorded in each step increase with decreasing temperature. Such behavior is typical of proton conductors and was observed in, e.g. yttrium doped barium zirconates[137].

These steps make it possible to calculate the proton defect concentration at different temperatures. The temperature dependence of $[OH_O^{\bullet}]$ in all multicomponent samples are presented in Figure 6.43b. One can see that all samples exhibit an exponential increase in proton defect concentration with a decrease in temperature. Such behavior indicates that the hydration process is exothermic, i.e. its enthalpy is negative. This change is hardly visible for

$BaZr_{0.2}Hf_{0.2}Sn_{0.2}Ti_{0.2}Ce_{0.2}O_{3-\delta}$ (H1) due to a low proton concentration. Additionally, there is no saturation in proton defect concentration, while this type of feature is observed in many similar compounds[136,138].

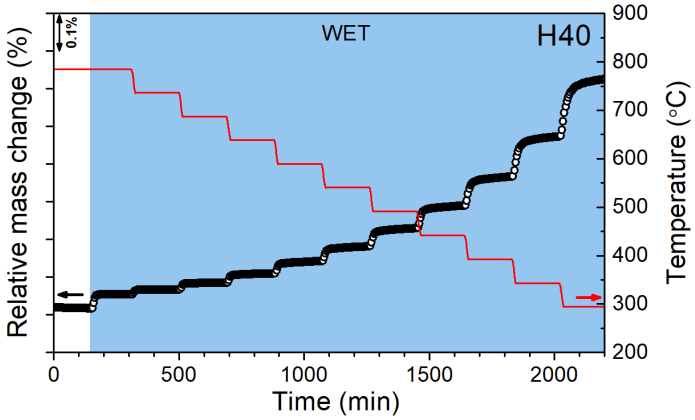

Figure 6.42 The weight change during isobaric thermogravimetry measurement for $BaZr_{0.1}Hf_{0.1}Sn_{0.1}Ti_{0.1}Ce_{0.1}Y_{0.1}Yb_{0.1}Sm_{0.1}In_{0.1}Zn_{0.1}O_{2.7}$ (H40).

By establishing $[OH_O^{\bullet}](T)$ dependence, it is possible to determine the hydration thermodynamic parameters, i.e. enthalpy (ΔH_{hydr}) and entropy (ΔS_{hydr}) of hydration. According to Guldberg-Waage Law, the reaction coefficient for Equation 3.8 referring to hydration can be written as:

$$K_{H2O} = \frac{[OH_O^{\bullet}]^2}{[V_O^{\bullet\bullet}][O_O^x]pH_2O} = exp\left(\frac{\Delta S_{hydr}}{R}\right) exp\left(-\frac{\Delta H_{hydr}}{RT}\right), \quad (6.4)$$

where $[O_O^x]$ is the concentration of oxygen ions in anionic sites in perovskite oxide. Electroneutrality conditions are also needed to solve this equation. For Equation 3.9, assuming that the hole concentration is negligible ($[h^{\bullet}] \approx 0$) in concerned oxides, the nominal acceptor content is compensated by oxygen vacancies and proton defects:

$$[OH_O^{\bullet}] + 2[V_O^{\bullet\bullet}] = [Acc_B{}']. \quad (6.5)$$

Additionally, it can be written that the oxygen sublattice consists of three different species:

$$[O] = [O_O^x] + [V_O^{\bullet\bullet}] + [OH_O^{\bullet}]. \quad (6.6)$$

By combining Equations 6.4-6.6 it is possible to achieve the equation where the reaction coefficient depends on proton defect concentration:

$$K_{H2O} = \frac{4}{pH_2O} \frac{[OH_O^{\bullet}]^2}{([O]-[OH_O^{\bullet}])^2-([O]-[Acc_B{}'])^2}. \quad (6.7)$$

In the case of $BaZr_{0.2}Hf_{0.2}Sn_{0.2}Ti_{0.2}Ce_{0.2}O_{3-\delta}$ (H1) the determination of K_{H2O} was not straightforward because the nominal acceptor concentration in this sample was 0. Thus, for the sake of calculations, the intrinsic acceptor concentration was assumed, considering the presence of Ce^{3+} ions. According to the literature, the amount of trivalent cerium in perovskite oxides ranges from 15% to 30% in similar conditions (oxidizing atmosphere)[139,140]. In Figure 6.43c, curves obtained for 1 mol% (5% of Ce^{3+}) and 4 mol% (20% Ce^{3+}) are presented. As can be seen, the

amount of intrinsic acceptor does not influence temperature dependence but rather the location on the vertical axis. For further analysis, K_{H2O} values obtained for 4 mol% Acc. are considered.

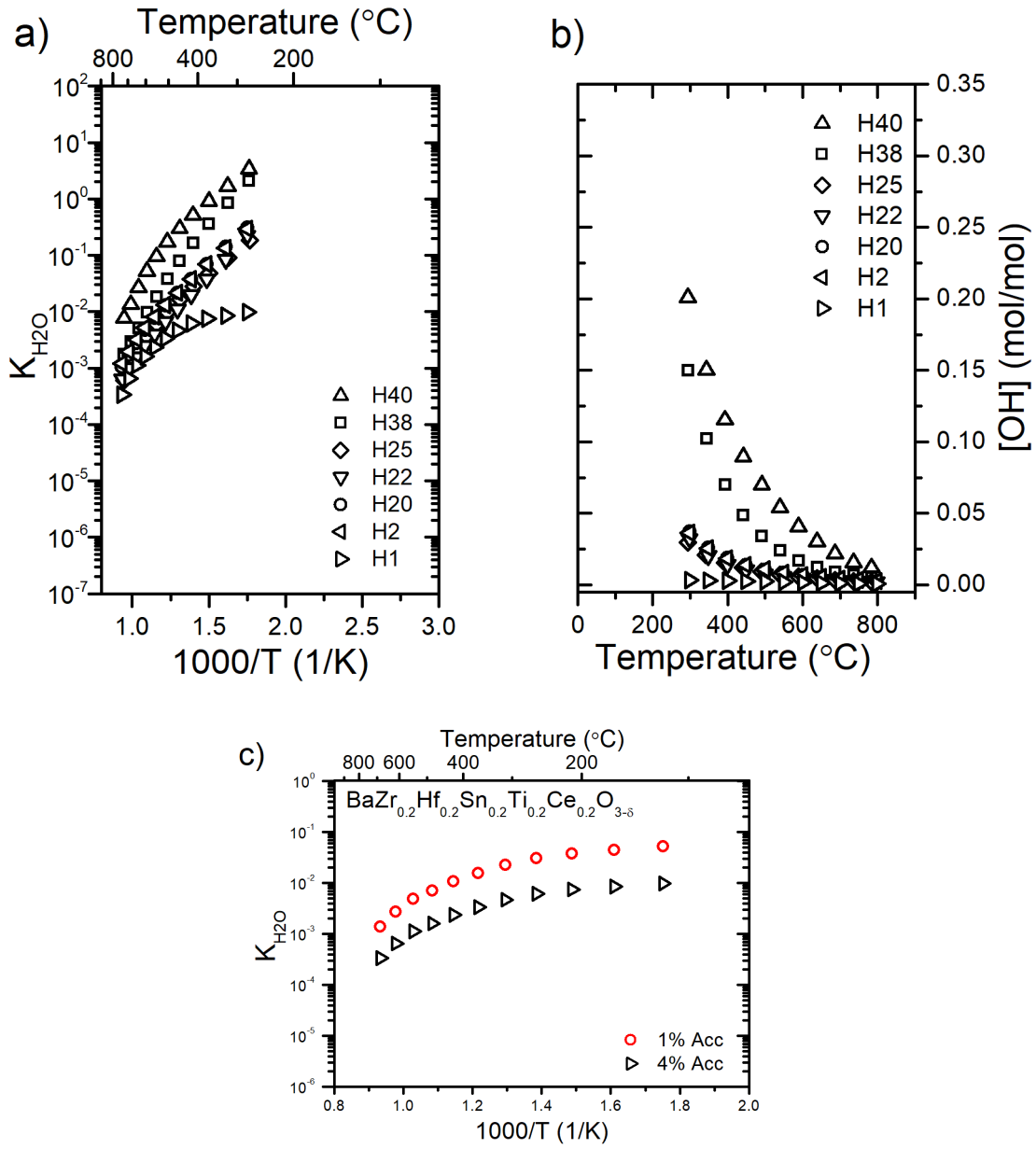

Figure 6.43 a) Hydration reaction equilibrium constant calculated from Equation 6.7, b) temperature dependence of proton defect concentration, c) influence of different intrinsic acceptor concentration on hydration coefficient in $BaZr_{0.2}Hf_{0.2}Sn_{0.2}Ti_{0.2}Ce_{0.2}O_{3-\delta}$ (H1).

In Figure 6.43a, the hydration coefficients versus inverted temperature (so-called van't Hoff plots) for all synthesized samples are presented. With the increase in acceptor concentration (and thus proton concentration), the reaction coefficient increases, which means that the hydration reaction is faster in acceptor-rich samples (H38/H40). Moreover, all samples form curves with two distinctive linear parts in different temperature regions, indicating that two hydration processes occur. By transforming Equation 6.4 into the following form:

$$f\left(\frac{1}{T}\right) = ln(K_{H2O}) = \frac{\Delta S_{hydr}}{R} - \frac{\Delta H_{hydr}}{RT}, \quad (6.8)$$

the thermodynamic parameters of hydration can be derived from linear approximations, where entropy is linked to the intercept of the line with OY axis and enthalpy is linked to the slope of the line. All thus derived hydration parameters as well as the reference values for similar compositions are gathered in Table 6.12.

For all samples, the enthalpies and entropies are more negative at higher temperatures (>500 °C) than at lower temperatures (<500 °C). One can assume that at higher temperatures (HT) hydration is more favorable since the proton concentration is low. In comparison, at lower temperatures (LT) where the proton concentration is significant, the rate of hydration decreases. Moreover, the comparison to other proton conductors is not explicit. For example, the zirconate reported by Gonçalves et al. with 20 mol% Y content exhibits in the HT region thermodynamic parameters close to the ones for $BaZr_{0.2}Hf_{0.2}Sn_{0.2}Ti_{0.2}Y_{0.2}O_{2.9}$. However, the difference between doped barium zirconate and H2 in the LT region is more prominent[137]. On top of that, BZCYs reported by Leonard et al. with composition complexity closer to oxides presented in this thesis have notably different hydration thermodynamic parameters than any reported HEO[136]. This indicates that the influence of multicomponent composition on hydration is a complex issue. More negative values for high entropy oxides in LT could mean that the hydration is more favorable than in low entropy counterparts. However, Putilov and Tsidilkovski suggested that proton trapping tends to be exothermic, which makes hydration entropy more negative[141]. Additionally, the enthalpies and entropies of hydration for H1 containing 1 mol% and 4 mol% of acceptors show no significant differences, indicating that the acceptor concentration does not influence the thermodynamics of water incorporation.

Table 6.12 Hydration energetics of studied high entropy oxides.

Sample	Atm.	Temperature range (°C)	p_{H2O} (atm)	ΔH_{hydr} (kJ/mol)	ΔS_{hydr} (J/Kmol)
H1 – 1% Acc	Air	800-550	0.019	-76 ± 9	-126 ± 9
		500-300		-15 ± 2	-50 ± 3
H1 – 4% Acc		800-550		-75 ± 9	-135 ± 9
		500-300		-13 ± 2	-61 ± 3
H2	Air	800-550	0.019	-75 ± 4	-125 ± 4
		500-300		-47 ± 1	-93 ± 1
H20	Air	800-550	0.019	-79 ± 3	-130 ± 3
		500-300		-49 ± 1	-95 ± 1
H22	Air	800-550	0.019	-72 ± 2	-128 ± 2
		500-300		-55 ± 1	-109 ± 1
H25	Air	800-550	0.019	-110 ± 5	-178 ± 5
		500-300		-45 ± 1	-100 ± 1
H38	Air	800-550	0.019	-90 ± 1	-138 ± 1
		500-300		-60 ± 2	-99 ± 3
H40	Air	800-550	0.019	-92 ± 4	-127 ± 5
		500-300		-44 ± 1	-67 ± 1

$BaZr_{0.9}Y_{0.1}O_{2.95}$[137]	Air	900-500	0.019	-94 ± 12	-131 ± 13
		500-100		-18 ± 2	-35 ± 3
$BaZr_{0.8}Y_{0.2}O_{2.9}$[137]	Air	900-500	0.019	-98 ± 12	-122 ± 13
		500-200		-22 ± 4	-25 ± 6
$BaZr_{0.7}Y_{0.3}O_{2.85}$[137]	Air	900-500	0.019	-141 ± 20	-166 ± 20
		500-300		-25 ± 6	-28 ± 9
$BaZr_{0.5}Ce_{0.4}Y_{0.1}O_{3-\delta}$[136]	N_2	1200-600	0.019	-41.64	-46.89
$BaZr_{0.44}Ce_{0.35}Y_{0.2}O_{3-\delta}$[136]	N_2	1200-600		-42.72	-47.15

To better analyze the hydration energetics of the studied oxides, the results were plotted in enthalpy-entropy coordinates with respect to high- and low-temperature regions. The graph is presented in Figure 6.44. The weakest hydration can be ascribed to H1, which is understandable since the oxygen vacancy concentration is minuscule in this sample. The most interesting observations can be made for acceptor-substituted 5B samples. In the HT region, the most negative values are recorded for H25 while the least negative for H22, with H2 and H20 in between. However, in the LT region, the relation is inverted - the most negative values are depicted for H22, and the least for H25 with H20 and H2 between them. On top of that, the relation from lower temperatures mirrors the observation in Figure 6.41. Therefore, one can conclude that the obtained thermodynamic parameters of hydration from isobaric measurements agree well with proton concentrations obtained from the isothermal measurements.

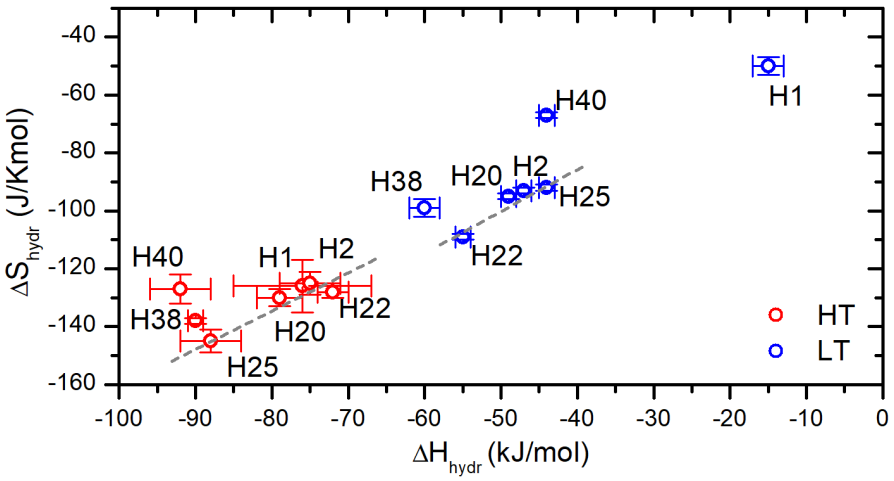

Figure 6.44 Hydration parameters of multicomponent perovskites, separated into temperature regions.

6.6.3 High-temperature drop calorimetry

The appropriate thermocycles should first be established to calculate the formation enthalpy correctly. The thermocycle for a given compound describes which reactions occur during the measurement and which drop solution enthalpies should be taken into account for calculations. In Table 6.13, the exemplary thermocycle for $BaZr_{0.2}Hf_{0.2}Sn_{0.2}Ti_{0.2}Ce_{0.2}O_{3-\delta}$ (H1) is presented.

Table 6.13 Thermodynamic cycle used for calculation of formation enthalpy of $BaZr_{0.2}Hf_{0.2}Sn_{0.2}Ti_{0.2}Ce_{0.2}O_{3-\delta}$.

Reaction	ΔH(kJ/mol)
$BaZr_{0.2}Hf_{0.2}Sn_{0.2}Ti_{0.2}Ce_{0.2})_{3-\delta}\ (s, 25\ °C) \rightarrow BaO\ (dis, 800\ °C) + 0.2ZrO_2\ (dis, 800\ °C) + 0.2\ HfO_2\ (dis, 800\ °C) + 0.2SnO_2\ (dis, 800\ °C) + 0.2\ TiO_2\ (dis, 800\ °C) + 0.2CeO_2\ (dis, 800\ °C)$	ΔH_{ds}^{H1}
$BaO\ (s, 25\ °C) \rightarrow BaO\ (dis, 800\ °C)$	ΔH_{ds}^{BaO}
$ZrO_2\ (s, 25\ °C) \rightarrow ZrO_2\ (dis, 800\ °C)$	ΔH_{ds}^{ZrO2}
$HfO_2\ (s, 25\ °C) \rightarrow HfO_2\ (dis, 800\ °C)$	ΔH_{ds}^{HfO2}
$SnO_2\ (s, 25\ °C) \rightarrow SnO_2\ (dis, 800\ °C)$	ΔH_{ds}^{SnO2}
$TiO_2\ (s, 25\ °C) \rightarrow TiO_2\ (dis, 800\ °C)$	ΔH_{ds}^{TiO2}
$CeO_2\ (s, 25\ °C) \rightarrow CeO_2\ (dis, 800\ °C)$	ΔH_{ds}^{CeO2}

s – solid; dis - dissolved

Generally, the thermocycle for the perovskite oxides consists of the dissolution of a given material and its constituent binary oxides. In such a complex composition, the information about the stability of ternary oxides could be unknown. However, the analysis based on binary oxides is sufficiently comprehensive and some of the possible ternary species are not stable in the perovskite structure. Thus, the final equation required to derive the enthalpy of formation for H1 is as follows:

$$\Delta H_{form}^{H1} = \Delta H_{ds}^{BaO} + \Delta H_{ds}^{ZrO2} + \Delta H_{ds}^{HfO2} + \Delta H_{ds}^{SnO2} + \Delta H_{ds}^{TiO2} + \Delta H_{ds}^{CeO2} - \Delta H_{ds}^{H1}. \quad (6.9)$$

The necessary drop solution enthalpies of binary oxides are gathered in Table 6.14, whereas the enthalpies from the measurement are presented in Table 6.15.

Table 6.14 Drop solution enthalpies of binary oxides in $3Na_2O \cdot 4MoO_3$ solvent at 800 °C.

Binary oxide	ΔH_{ds}(kJ/mol)
BaO	-176.48 ± 3.48[142]
ZrO_2	29.2 ± 1.2[143]
HfO_2	23.9 ± 1.1[144a]
SnO_2	52.85 ± 0.21[145]
TiO_2	73.74 ± 0.48[146]
CeO_2	76.78 ± 0.75[84a]
Y_2O_3	-116.34 ± 1.21[147]
Yb_2O_3	-82.65 ± 1.06[148]
Sm_2O_3	-132.0 ± 1.6[147]
In_2O_3	12.23 ± 1.03[145]
ZnO	20.68 ± 0.7[149]

[a] recalculated from 700 °C

Achieved values of formation enthalpy are negative for all considered multicomponent oxides. This means that they are thermodynamically stable, and the configurational entropy is unnecessary for their stabilization. According to Navrotsky and McCormack, such compounds should not be called ‘entropy-stabilized’ oxides[150]. In Figure 6.45 the formation enthalpies are displayed as a function of the average B-site radius and Entropy Metrics. In both cases, a similar

observation can be made. For lower B-site radius and lower EM, ΔH_{form} values are more negative and overlap to large extend. The formation enthalpy is less negative in the case of the H38 and H40 samples, with a higher average B-cation radius and higher EM. One could suppose that multicomponent oxides with a larger element number or a larger lattice parameter are less stable than compounds with fewer elements or smaller unit cells. However, by comparing calculated enthalpies with the values reported for acceptor-substituted barium zirconates, another conclusion can be derived. Firstly, values of enthalpy of formation for BZYs are close to those acquired for the samples in this thesis with a comparable acceptor content. Secondly, ΔH_{form} became less negative with the increase in acceptor concentration. Thus, the change in formation enthalpy in HEO samples is more influenced by the oxygen vacancy concentration than the number of elements in the structure.

Table 6.15 Enthalpies of drop solution and formation obtained for multicomponent oxides.

Sample	ΔH_{ds} (kJ/mol)	ΔH_{form} (kJ/mol)
H1	-25.72 ± 1.07	-99.47 ± 6.71
H2	-51.43 ± 0.89	-100.75 ± 6.51
H20	-46.75 ± 0.43	-102.06 ± 6.27
H22	-36.56 ± 0.55	-102.76 ± 6.27
H25	-39.49 ± 0.61	-114.25 ± 6.31
H38	-111.37 ± 1.20	-62.57 ± 6.81
H40	-106.04 ± 0.89	-58.66 ± 6.49
$BaZr_{0.8}Y_{0.2}O_{2.9}$[151]	-85.53 ± 1.96	-92.84 ± 3.87
$BaZr_{0.5}Y_{0.5}O_{2.75}$[151]	-126.97 ± 1.74	-77.09 ± 4.31

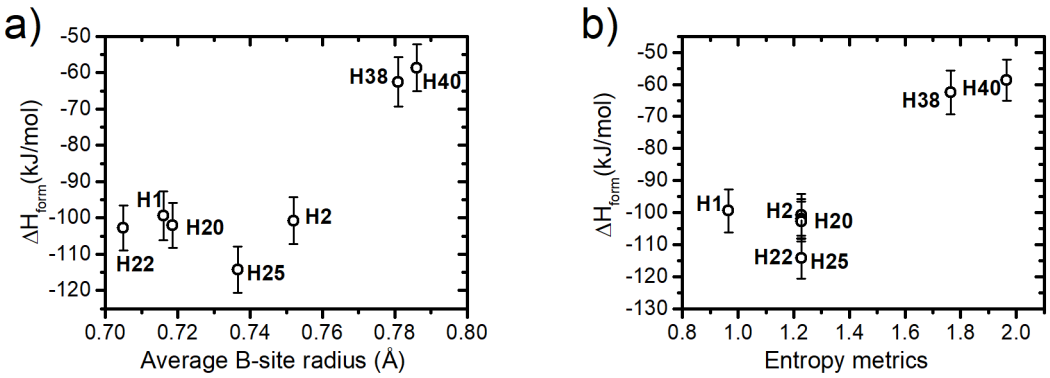

Figure 6.45 Enthalpies of formation for synthesized samples as a function of a) average B-site radii, b) Entropy Metrics.

6.7 Electrical measurements

For selected samples, the analysis of the obtained data will be divided based on temperature and pO_2/pH_2O dependencies of total electrical conductivity, as well as charge transport characteristics between grain and grain boundaries.

In Figure 6.46, the different types of acquired Nyquist plots are presented. Figure 6.46a shows the Nyquist plot observed at high temperatures for most samples. Due to the high inductance

of electrodes and wires at high temperatures and the high electronic transference number, the equivalent circuit consists of an inductance element representing the parasitic influence of the measuring cell and a resistor representing the total resistance of the sample. The impedance of the samples at intermediate temperatures is presented in Figure 6.46b. With the decrease in temperature, impedance plots start to form the semicircles. However, because of the upper-frequency limit of measurements, it was not possible to obtain the semicircle for grains in most cases. Thus, equivalent circuits consist of resistors representing the resistance of grains in series with a parallel connected resistor with a constant phase element (CPE) depicting grain boundary characteristics (Figure 6.46b). The semicircle representing grain conduction develops by further decreasing temperature, and the Nyquist plots presented in Figure 4.64c are observed. In this case, an equivalent circuit contained connected in a series of two parallel connections of a resistor and CPE corresponding to grain and grain boundary conduction.

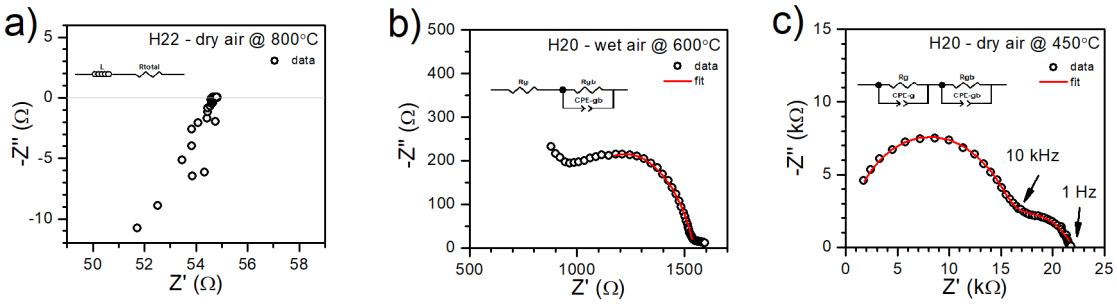

Figure 6.46 Different Nyquist plots obtained during the measurements.

6.7.1 Electrical conductivity in dry conditions

Figure 6.47 presents the temperature dependencies of total conductivities of multicomponent oxides in dry air, plotted in Arrhenius coordinates. The activation energies, E_a, and conductivity values at 600 °C are listed in Table 6.16. The activation energies were derived from plots of $\ln(\sigma T)$ vs $(1/T)$ plotted according to Equations 3.5 and 3.7:

$$\sigma_{tot} T = \sigma_{tot}^{0} e^{-\frac{E_a}{k_B T}} . \tag{6.10}$$

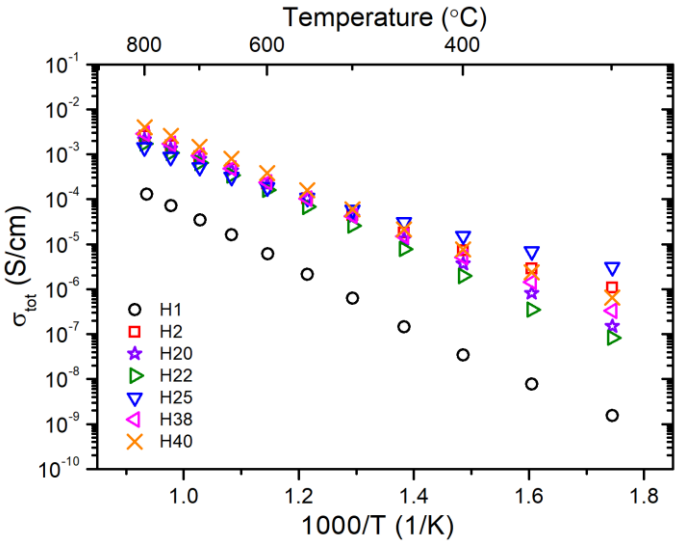

Figure 6.47 The temperature dependence of total conductivities of all samples in dry air.

As shown in Figure 6.47, the total conductivity for all samples decreases with decreasing temperature. This confirms that the charge transport is thermally activated, i.e. thermal energy is required to create and move the charge carrier. The values of conductivity in the studied temperature range span from a few 10^{-3} to 10^{-7} S/cm for acceptor substituted samples and from 10^{-4} to 10^{-9} S/cm for isovalent $BaZr_{0.2}Hf_{0.2}Sn_{0.2}Ti_{0.2}Ce_{0.2}O_{3-\delta}$ (H1). Moreover, at 600 °C the highest conductivity is recorded for $BaZr_{0.1}Hf_{0.1}Sn_{0.1}Ti_{0.1}Ce_{0.1}Y_{0.1}Yb_{0.1}Sm_{0.1}In_{0.1}Zn_{0.1}O_{2.7}$ (H40) and the lowest for H1. Additionally, the H1 sample exhibits the highest activation energy of conduction, whereas, for other samples, it is around 1 eV above 600 °C. In the case of H2, H22, H25, H38 and H40, a change in activation energy around 600 °C is observed. In comparison to the values presented in Figures 4.4-4.6 for $Ba(Ce,Zr,Y)O_3$ compounds, the synthesized multicomponent oxides exhibit from one to two orders of magnitude lower electrical conductivity than barium cerates and barium zirconates. Additionally, the activation energies are higher, nearly two times in some cases.

Table 6.16 Conductivities in dry air at 600 °C and activation energies of the conductivity for multicomponent oxides.

Sample	Total conductivity at 600 °C (S/cm)	Activation energy of conduction (eV)	
		above 600 °C	below 600 °C
H1	6.01×10^{-6}	1.38(1)	
H2	2.25×10^{-4}	1.05(1)	0.72(3)
H20	2.08×10^{-4}	1.09(1)	
H22	1.63×10^{-4}	1.01(1)	1.25(2)
H25	1.83×10^{-4}	0.94(3)	0.60(2)
H38	2.39×10^{-4}	1.09(1)	0.97(1)
H40	3.85×10^{-4}	1.00(2)	0.89(1)

$BaZr_{0.2}Hf_{0.2}Sn_{0.2}Ti_{0.2}Ce_{0.2}O_{3-\delta}$, which contains isovalent constituents in the B-sublattice, may be expected to have a close to stoichiometric oxygen content and be an electronic conductor. However, the change in the sample mass during TG hydration measurements indicates that some oxygen vacancies are present in the material. Thus, a small contribution of oxygen ion conduction is also possible. The mechanism of hole conduction in $BaZrO_3$ and related materials is still under study, though it is generally agreed that it is related to the processes of oxidation/reduction. This may lead to a band-hole ($h^{\bullet}$) or hole-polaron ($O_O^{\bullet}$) formation as described by reactions (Equation 6.11) and (Equation 6.12), respectively[152]:

$$\frac{1}{2}O_2 + V_O^{\bullet\bullet} + O_O^x \leftrightarrow 2h^{\bullet} + 2O_O^x, \tag{6.11}$$

$$\frac{1}{2}O_2 + V_O^{\bullet\bullet} + O_O^x \leftrightarrow 2O_O^{\bullet}. \tag{6.12}$$

DFT calculations showed that the energy of the small polaron formation is lower than that of the band hole, though the difference is low. Hence, both models agree with the experimental methods. The presence of acceptor constituents enhances hole localization. Moreover, the small-polaron hopping conduction mechanism was shown by Rowberg et al. in barium zirconates

and cerates[153] and by Tsunoda et al. in barium titanate[154]. Since there are many structural distortions in multicomponent perovskites, we assume that electronic conduction occurs by small polaron hopping. Moreover, oxides based on tetravalent elements are inevitably acceptor-doped, so the hole-polaron may be expected to be dominant. Low values of electrical conductivity and activation energy around 1.4 eV in this sample are consistent with the expected nature of these oxides as wide-bandgap dielectrics, similar to $BaSnO_3$, $BaZrO_3$, $BaHfO_3$ and $BaTiO_3$. Larramona et al. have found that barium stannate has a bandgap equal to 3.4 eV[155]. For other oxides, bandgaps equal 3.23 eV[156], 3.53 eV[157] and 3.2 eV[158], respectively.

Apart from H1, the acceptor content is significant in all studied materials, from 20 mol% in 5B oxides to 60 mol% in H40. The most probable charge compensation mechanism that takes place is through oxygen vacancies[159]:

$$[Acc_B{}'] = 2[V_O^{\bullet\bullet}]. \tag{6.13}$$

This equation shows that the expected concentration of oxygen vacancies compensating the acceptor charge in these samples should be between 10 mol% and 30 mol%. Thus, the oxygen ionic conductivity is expected to dominate the charge transport. Above 600 °C, the electrical conductivity in these samples is higher by an order of magnitude than in H1. At 300 °C this difference reaches two orders of magnitude for $BaZr_{0.2}Hf_{0.2}Sn_{0.2}Ti_{0.2}In_{0.2}O_{2.9}$ (H22) and 3.5 orders for $BaZr_{0.2}Hf_{0.2}Sn_{0.2}Ti_{0.2}Sm_{0.2}O_{2.9}$ (H25). Additionally, there is no significant difference between the temperature dependencies above 600 °C. The estimated activation energies of charge transport are around 1 eV, typical of oxygen ion conductors[160]. However, below 600 °C, the difference in activation energies between the samples can be seen. In most cases, E_a at lower temperatures is lower than that above 600 °C. In H22, it is higher, whereas in $BaZr_{0.2}Hf_{0.2}Sn_{0.2}Ti_{0.2}Yb_{0.2}O_{2.9}$ (H20), the same as at higher temperatures.

A change in the activation energy may be related to the transition between extrinsic and intrinsic conduction. For example, in H25, the activation energy of 0.6 eV in the lower temperature (extrinsic) region may be connected with the enthalpy of mobility of oxygen ions (Equation 6.14), while the high-temperature activation energy may additionally relate to the enthalpy of oxygen vacancy formation (Equation 6.15)[152]:

$$E_a^L = \Delta H_{m,V_O^{\bullet\bullet}} = 0.6\ eV \tag{6.14}$$

$$E_a^H = \frac{\Delta H_{f,V_O^{\bullet\bullet}}}{2} + \Delta H_{m,V_O^{\bullet\bullet}} = 0.94\ eV \rightarrow \Delta H_{f,V_O^{\bullet\bullet}} = 0.68\ eV. \tag{6.15}$$

In Table 6.17, the estimated enthalpies of mobility and oxidation are gathered. Such estimations are very rough, though the results seem reasonable. It can be seen that the mobility enthalpies are lower for the oxides containing 5 cations in B-site, which may be expected to be less disordered. On the other hand, the oxygen vacancy formation enthalpies are higher in the 5B materials. This is consistent with the tendencies found using drop-solution calorimetry. It showed

that the 5B oxides have higher formation enthalpy than the 8- and 10B ones, which indicates stronger bonds in H2 and H25 than in H38 and H40.

Table 6.17 The enthalpies of mobility and oxidation estimated based on activation energies of conduction

Sample	$\Delta H_{m,V_O^{\bullet\bullet}}$ (eV)	$\Delta H_{f,V_O^{\bullet\bullet}}$ (eV)
H2	0.72	0.66
H25	0.6	0.68
H38	0.97	0.24
H40	0.89	0.22

In the case of $BaZr_{0.2}Hf_{0.2}Sn_{0.2}Ti_{0.2}In_{0.2}O_{2.9}$ (H22), the activation energy of conduction in the low-temperature range was higher than that above 600 °C. A similar behavior was observed by Zhan et al. for samarium doped ceria[161]. They found that in lower temperature region, complex defects such as $[Sm'_{Ce} - V_O^{\bullet\bullet}]$ are present. The increased activation energy of conduction is related to additional enthalpy of formation of those associates. So, considering H22, at lower temperatures associates $[In'_B - V_O^{\bullet\bullet}]$ may be present and the association enthalpy may be estimated as:

$$\Delta H_{ass}^{In} = E_a^L - E_a^H = 0.24\ eV, \tag{6.16}$$

where, E_a^L is activation energy below 600 °C and E_a^H is activation energy above 600 °C. The reason why the properties of the $BaZr_{0.2}Hf_{0.2}Sn_{0.2}Ti_{0.2}In_{0.2}O_{2.9}$ perovskite differ from the others could be the highest content of indium.

6.7.2 Electrical conductivity in wet conditions and isotope effect

Figure 6.48 shows the total conductivity in dry and humidified air for all samples. In Table 6.18, the values of conductivity at 600 °C, and activation energies of conductivity in wet air are presented. Generally, the influence of water vapor on the electrical conductivity level and activation energies differs depending on the sample.

In all samples above 600 °C, there is no difference in conductivity between wet and dry air. It is caused by a negative enthalpy of protonic defect formation, which results in a low concentration of proton defects in this temperature range[50]. In the lower temperature range, the total conductivity in the presence of water vapor is either higher or does not change compared to dry conditions. In H22, H38 and H40, the relative difference between wet and dry conductivities reaches from 2-fold for H38 and H40 (Figure 6.48f,g) to an even 5-fold increase in the 5B sample with indium (Figure 6.48d) at 300 °C.

Activation energies of conduction are close to the ones in the dry air, apart from that of H22. This may indicate that the electrical conductivity in wet condition is mixed proton, oxide-ion and electron-hole conductivity. For $BaZr_{0.2}Hf_{0.2}Sn_{0.2}Ti_{0.2}In_{0.2}O_{2.9}$, the activation energy is lower than in dry air, indicating that the presence of protons prevents the formation of low-temperature $[In'_B - V_O^{\bullet\bullet}]$ associates. Overall, studied samples behave like typical ceramic proton conductors with hydration as a predominant reaction for water uptake (Equation 3.8)[98].

The influence of water vapor on the electrical conductivity is vague for H20 and H1. The conductivity in a wet atmosphere in $BaZr_{0.2}Hf_{0.2}Sn_{0.2}Ti_{0.2}Yb_{0.2}O_{2.9}$ (H20) is slightly below that measured in dry air below 450 °C and the activation energies are practically the same in both atmospheres. It could be caused by the presence of sintering aid – nickel oxide. It has been proposed, that nickel ions can act as doubly charged acceptors Ni_B'' and create trapping centers for protons, which lower the concentration of active proton defects[75]. For the H1 sample, the influence of water will be the weakest since the oxygen vacancies concentration is the lowest in this composition, considering all the samples studied in this thesis. Nevertheless, the activation energy reduces quite significantly at lower temperatures.

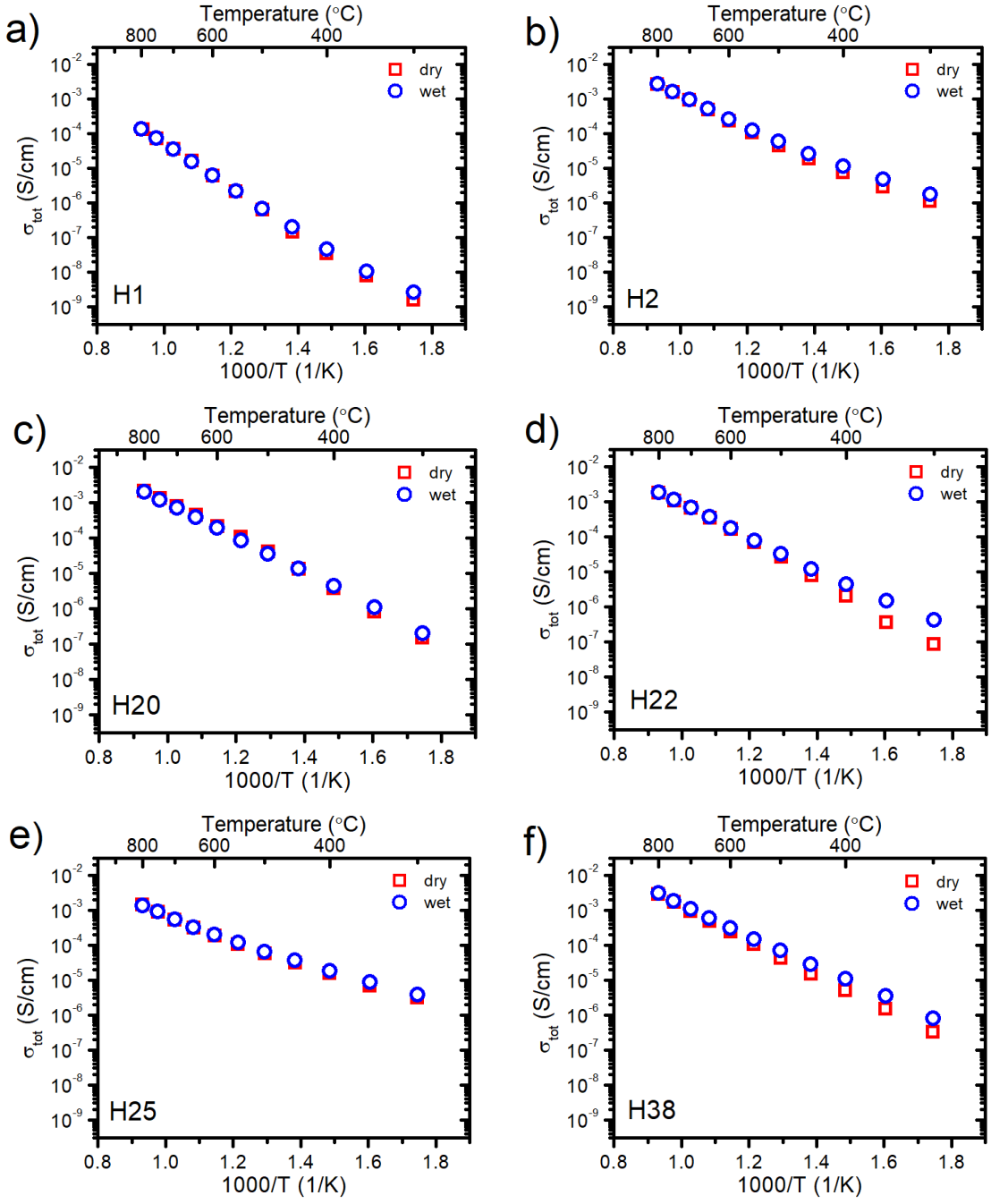

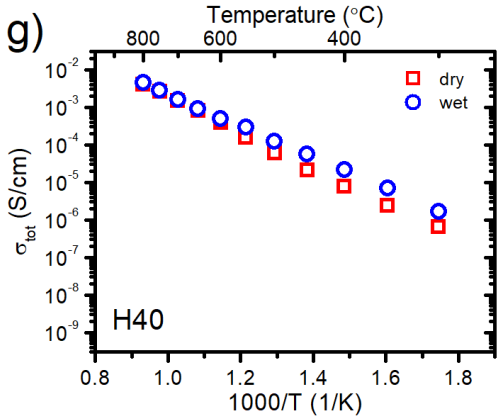

Figure 6.48 Total conductivities of synthesized samples in dry and humidified air.

Table 6.18 Conductivities in humidified air at 600 °C and activation energies of the conductivity for studied multicomponent oxides.

Sample	Total conductivity at 600 °C (S/cm)	Activation energy of conduction (eV)	
		above 600 °C	below 600 °C
H1	6.08×10^{-6}	1.34(1)	1.00(6)
H2	2.50×10^{-4}	0.99(1)	0.70(1)
H20	1.85×10^{-4}	1.04(1)	
H22	1.74×10^{-4}	1.00(2)	0.85(1)
H25	1.98×10^{-4}	0.90(1)	0.60(1)
H38	2.98×10^{-4}	0.98(1)	0.90(1)
H40	4.85×10^{-4}	1.00(2)	0.89(1)

Selected samples exhibiting a high difference between the electrical conductivity in dry and humidified air were studied in the flux of air humidified with heavy water. The conductivities measured in H_2O and D_2O-saturated air are presented in Figure 6.49a-c. The activation energies of conduction are gathered in Table 6.19. The conductivity in a D_2O-humidified atmosphere is below the conductivity in H_2O-humidified air and above the conductivity in dry air. Additionally, the activation energy of conduction in air with heavy water is higher than in H_2O-wet air and lower than in dry air (Table 6.16). These observations indicate the isotope effect typical of proton conductors.

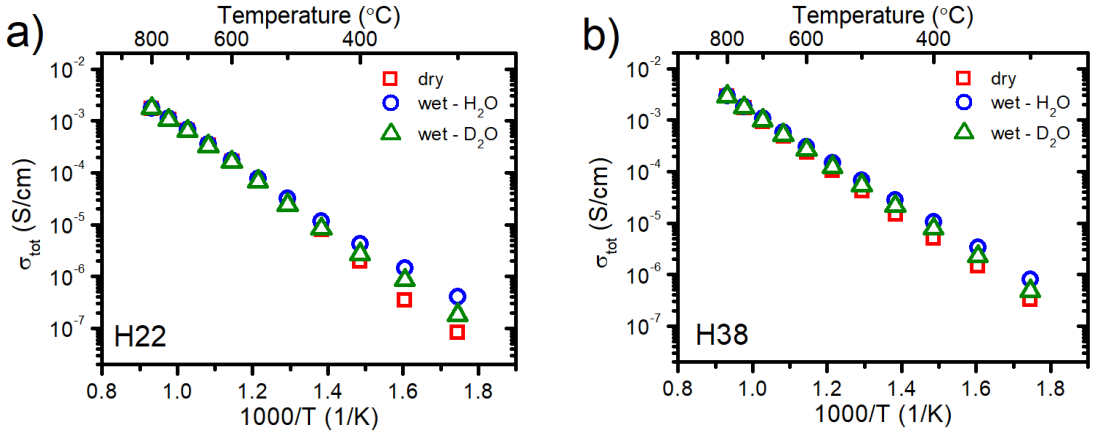

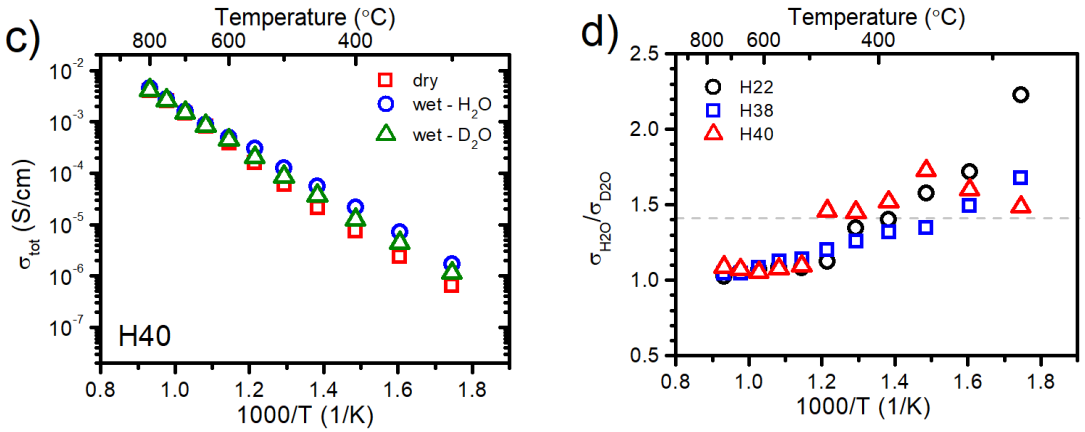

Figure 6.49 The total conductivity in dry, H_2O- and D_2O-humidified air for a) $BaZr_{0.2}Hf_{0.2}Sn_{0.2}Ti_{0.2}In_{0.2}O_{2.9}$, b) $BaZr_{0.125}Hf_{0.125}Sn_{0.125}Ti_{0.125}Y_{0.125}Yb_{0.125}Sm_{0.125}In_{0.125}O_{2.75}$, c) $BaZr_{0.1}Hf_{0.1}Sn_{0.1}Ti_{0.1}Ce_{0.1}Y_{0.1}Yb_{0.1}Sm_{0.1}In_{0.1}Zn_{0.1}O_{2.7}$, d) the ratio between conductivities measured at H_2O and D_2O conditions (dashed line indicate the $\sqrt{2}$ value).

The ratios of the conductivities of $\sigma_{H2O}/\sigma_{D2O}$ in water- and heavy water-saturated air are presented in Figure 6.49d, whereas the parameters describing isotope effect are gathered in Table 6.20. At temperatures below approximately 450 °C, the $\sigma_{H2O}/\sigma_{D2O}$ ratios yield values above 1 and close to $\sqrt{2}$. This indicates that the isotope effect in the samples follows a modified semi-classical model[162]. The proton-deuteron mass difference causes the deviation in activation energy for conduction up to 0.055 eV. Considering the values shown in Table 6.20, only $BaZr_{0.2}Hf_{0.2}Sn_{0.2}Ti_{0.2}In_{0.2}O_{2.9}$ (H22) material exhibits a value almost twice larger. It may be caused by the association of protonic defects around indium atoms. Another parameter to consider when analyzing the isotope effect is the relation between pre-exponential factors from Arrhenius plots in both atmospheres. Considering the semi-classical model the value of $\sigma^0_{H2O}/\sigma^0_{D2O}$ should be around $\sqrt{2}$. By incorporating quantum vibrational functions that account for discrete energy states, the pre-exponentials ratio can range between 0.5 and $\sqrt{2}$, with a strong probability of being close to unity[163]. However, H22 displays values that deviate from these expected ranges, resulting in a lower ratio. Overall, parameters describing the isotope effect in studied multicomponent oxides are similar to those reported for acceptor-substituted perovskites, excluding absolute values for pre-exponentials being one order of magnitude lower.

Table 6.19 Conductivities at 600 °C and activation energies of the conductivity for samples selected for measurements in D_2O-humidified air.

Sample	Total conductivity at 600 °C (S/cm)	Activation energy of conduction (eV)	
		above 600 °C	below 600 °C
H22	1.61×10^{-4}	1.03(2)	0.96(1)
H38	2.62×10^{-4}	1.03(1)	0.96(2)
H40	4.43×10^{-4}	1.00(1)	0.88(2)

Table 6.20 Characteristic conductivity values describing isotope effect in selected samples.

Sample	σ^0_{H2O} $(10^5\ K/\Omega \cdot cm)$	σ^0_{D2O} $(10^5\ K/\Omega \cdot cm)$	$\sigma^0_{H2O}/\sigma^0_{D2O}$	$\sigma_{H2O}/\sigma_{D2O}$ at 300 °C	$E_a^{D2O} - E_a^{H2O}$ below 600 °C
H22	0.07(1)	0.28(7)	0.25(7)	2.23	0.11(1)
H38	0.39(8)	0.79(25)	0.49(18)	1.68	0.06(1)
H40	0.64(15)	0.33(12)	1.97(85)	1.49	-0.01(2)
$Sr(Ce_{0.95}Yb_{0.05})O_3$[164]	3	-	0.60	1.5	0.04
$Sr(Zr_{0.9}Sc_{0.1})O_3$[165]	28	-	0.80	1.6	0.03
$Ba(Ce_{0.95}Nd_{0.05})O_3$[166]	9	-	0.41	1.6	0.04

6.7.3 Grain and grain boundary specific electrical conductivity

For certain compositions, it was feasible to differentiate the resistances attributed to the bulk grains and those associated with the grain boundaries. The analysis was made based on acquired capacitances of processes from the Nyquist plot fits, using characteristic ranges for grains and grain boundaries, proposed by Irvine et al.[167]. The comparison of grain and specific grain boundary electrical conductivity measured at different atmospheres is presented in Figure 6.50. The conductivity values for grains and specific grain boundaries at 600 °C and activation energies are gathered in Table 6.21.

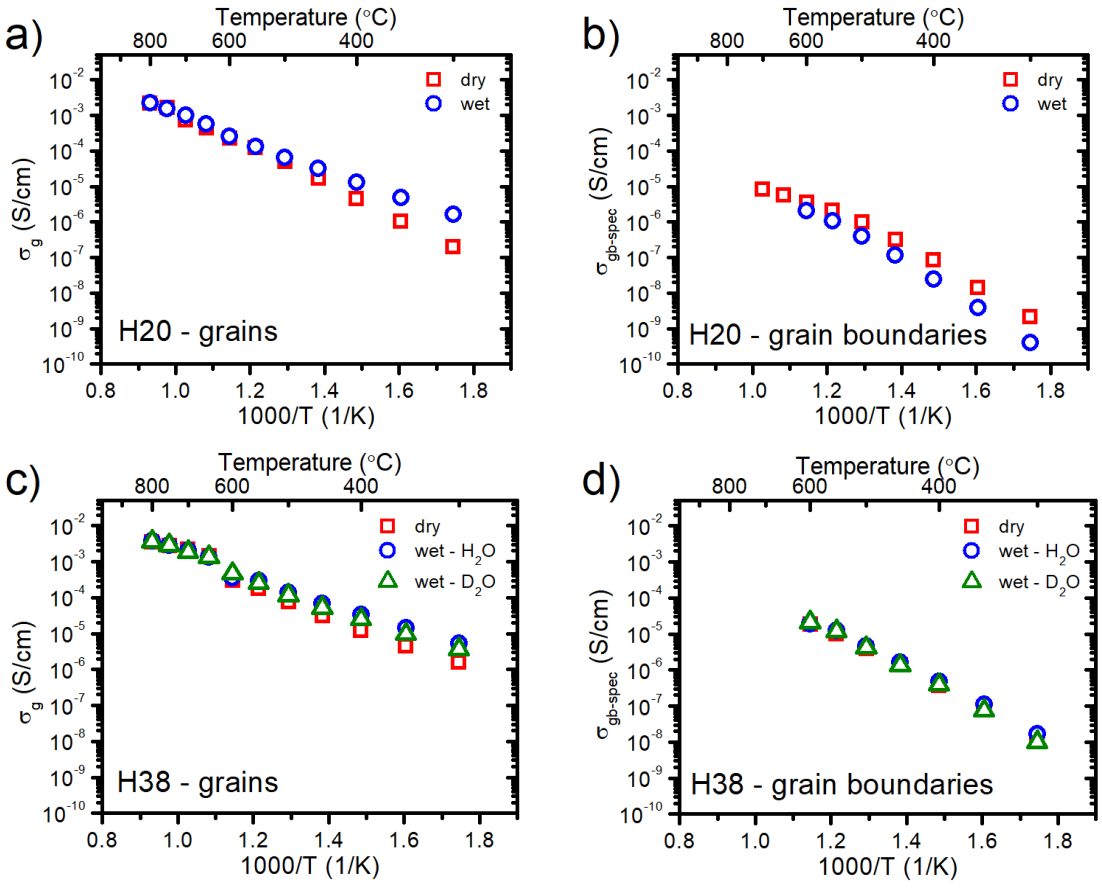

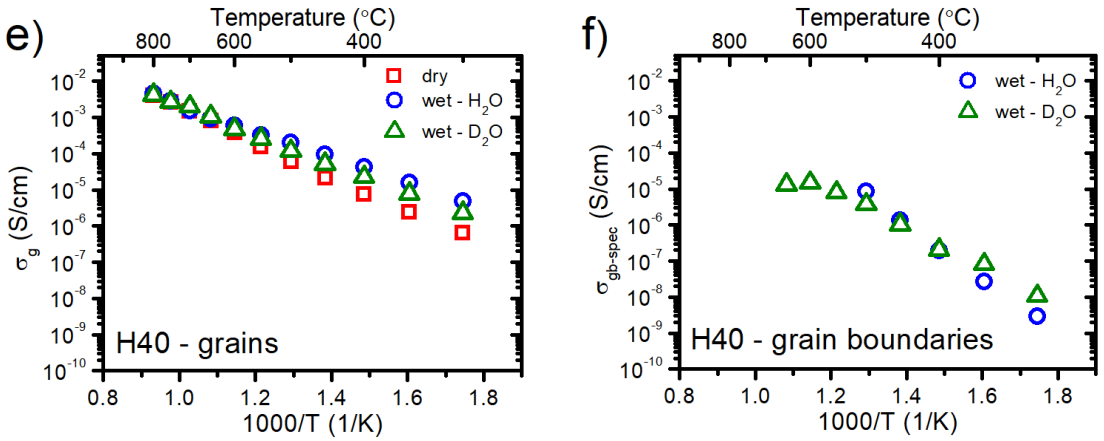

Figure 6.50 The grain and specific grain boundary conductivity for a,b) $BaZr_{0.2}Hf_{0.2}Sn_{0.2}Ti_{0.2}Yb_{0.2}O_{2.9}$, c,d) $BaZr_{0.125}Hf_{0.125}Sn_{0.125}Ti_{0.125}Y_{0.125}Yb_{0.125}Sm_{0.125}In_{0.125}O_{2.75}$, e,f) $BaZr_{0.1}Hf_{0.1}Sn_{0.1}Ti_{0.1}Ce_{0.1}Y_{0.1}Yb_{0.1}Sm_{0.1}In_{0.1}Zn_{0.1}O_{2.7}$, measured in different atmospheres.

Table 6.21 Grain and specific grain boundary conductivities at 600 °C and activation energies of the conductivity for selected samples measured in different atmospheres.

Atmosphere	Sample	Grain conductivity at 600 °C (S/cm)	Activation energy of conduction (eV)		Grain boundary conductivity at 600 °C (S/cm)	Activation energy of conduction (eV)	
			above 600 °C	below 600 °C		above 600 °C	below 600 °C
DRY	H20	2.27×10^{-4}	1.03(10)	1.11(1)	3.62×10^{-6}	-	1.24(2)
	H38	3.00×10^{-4}	0.59(4)	0.76(3)	1.82×10^{-5}	-	1.17(2)
	H40	3.85×10^{-4}	1.00(2)	0.89(1)	-	-	-
WET	H20	2.55×10^{-4}	0.85(3)	0.77(1)	2.05×10^{-6}	-	1.38(2)
	H38	3.63×10^{-4}	0.66(2)	0.67(1)	1.94×10^{-5}	-	1.13(2)
	H40	6.05×10^{-4}	1.01(2)	0.77(1)	-	-	1.57(5)
D_2O	H38	4.63×10^{-4}	0.67(3)	0.69(1)	2.09×10^{-5}	-	1.21(2)
	H40	4.71×10^{-4}	0.84(8)	0.80(1)	1.48×10^{-5}	-	1.14(6)

Firstly, in all studied samples, the specific electrical conductivity of the grains is higher than the specific conductivity of grain boundaries in the whole temperature range. The difference starts from one to two orders of magnitude at 600 °C and increases with the temperature decrease. The activation energies for grain boundaries are up to two times larger than E_a for conduction through the grains. Moreover, the grain conductivity increases in humidified atmospheres. Other relations are observed for specific grain boundary conductivity. In H38 and H40, the ambient atmosphere has practically no influence on the conduction process through grain boundaries. In $BaZr_{0.2}Hf_{0.2}Sn_{0.2}Ti_{0.2}Yb_{0.2}O_{2.9}$ (H20), the specific grain boundary conductivity decreases after the introduction of water vapor. This explains no noticeable change in total conductivity in humidified air (Figure 6.48c) while grain conductivity exhibits an evident increase. As proposed above, such a phenomenon may be caused by using nickel oxide during the sintering. The sintering additives tend to form various point defects in the structure, incorporating in both interstitial and lattice points[65,92]. This, in turn, alters the defect chemistry of the material and may change the electrical properties. For example, Babilo et al. examined the influence of ZnO as a sintering aid on electrical

conductivity in Y-doped $BaZrO_3$[75]. They found, that zinc tends to agglomerate at the grain boundaries, forming Zn''_{Zr} defects, that cause the proton trapping and decrease of the electrical conductivity.

Overall, it turns out that grain boundaries have a significant effect on the conduction process in the studied materials. Similar relations have been found for other conducting perovskite oxides like $BaZrO_3$[168,169] or $SrTiO_3$[170]. The high grain resistivity is caused by the depletion of major charge carriers in the space charge zones[169,171].

To further investigate the electrical properties of grain boundaries, the space charge layer (SCL) model was applied[172]. This model assumes that around the positively charged grain boundary core are located negatively charged point defects like Acc'_B (and Ni''_B in case of H20). Positively charged mobile defects are repulsed from the positive core and have to overcome a potential barrier φ_0 when moving through grain boundaries[173].

By applying the approach proposed by Fleig[174], it is possible to estimate the value of Schottky potential barrier φ_0 at the grain boundaries:

$$\frac{\sigma_g}{\sigma_{gb-spec}} = \frac{e^{\frac{ze\varphi_0}{k_BT}}}{2\frac{ze\varphi_0}{k_BT}}, \tag{6.17}$$

where z is the charge of dominating carrier in given conditions and e is the elementary charge. Moreover, by knowing the φ_0 it is possible to calculate the Debye length L_D and width of the space charge layer λ^*[173]:

$$L_D = \sqrt{\frac{kT\varepsilon_r\varepsilon_0}{2e^2c}}, \tag{6.18}$$

$$\lambda^* = L_D\sqrt{\frac{4e\varphi_0}{k_BT}}, \tag{6.19}$$

where ε_r is the relative permittivity and c is acceptor concentration ($c = [Acc'_B]$). The relative permittivity was estimated in accordance to capacitance of the grains in both atmospheres ($\varepsilon_r = \frac{C_g l}{\varepsilon_0 S}$, where ε_0 is vacuum permittivity). All calculated values from Equations 6.17-6.19 are presented in Figure 6.51.

In Figure 6.51a, the temperature dependencies of the Schottky barrier at grain boundaries are shown. As can be seen, φ_0 exhibits various temperature dependence. The height of the barrier decreases with temperature in humidified atmospheres or remains stable as for H40 in D_2O. In dry conditions, it increases with the temperature or remains the same, as is the case of sample H38. Vollman et al. demonstrated that Schottky potential barriers diminish with increasing temperature, attributed to the progressive broadening of the potential profile across the grain boundaries[170]. The temperature dependence of the grain boundary potential is described by Equation 6.20:

$$\varphi_0 = \frac{Q_{core}^2}{8e\varepsilon_r\varepsilon_0[Acc'_B]} + \frac{k_BT}{ez_{def}}, \tag{6.20}$$

where Q_{core} is the core charge and z_{def} is charge number of the defect. All variables in this expression are dependent on the temperature and water partial pressure. Thus relation of Schottky potential with temperature is determined by the relations between these temperature dependencies [175]. Worth noting are increased values of φ_0 for all samples in humidified conditions in relation to dry conditions. It is probably caused by the lower charge for $OH_O^{\bullet}$ than $V_O^{\bullet\bullet}$ defects and lower electrostatic energy of the hydrated grain boundary core[176]. Iguchi et al. obtained potential barrier for $BaZr_{0.95}Y_{0.05}O_3$ in wet nitrogen at 300 °C equal to 0.51 V[171] while Polfus et al. using DFT methods acquired Schottky barriers for BZO equal to 0.51 V and 0.28 V in hydrated and dehydrated state, respectively[176]. Moreover, values gathered by Chen et al. for Y-doped BZO obtained with various synthesis methods range from 0.3 to 0.9 V[168].

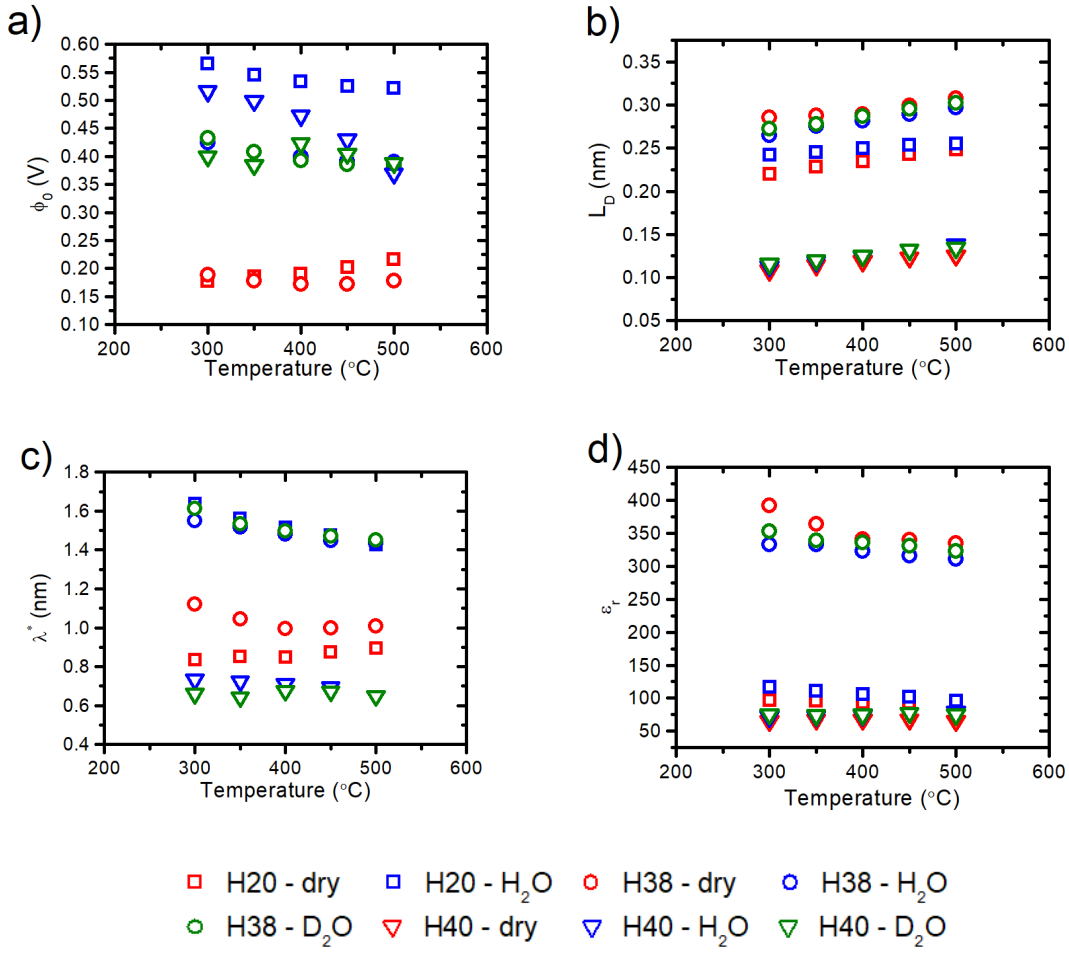

Figure 6.51 The characteristic values describing grain boundaries in selected samples, derived from SCL model: a) the charge potential at the grain boundary, b) Debye length, c) space charge layer thickness, d) relative permittivity.

Calculated Debye lengths, presented in Figure 6.51b for all samples, are between 0.1 and 0.35 nm. This means that the electric field from the SCL is permeating at the depth of a fraction of a unit cell. Moreover, L_D increases with the temperature for all examined samples and atmospheres. Interestingly, there is no difference between values for given samples in dry and wet air. The $BaZr_{0.1}Hf_{0.1}Sn_{0.1}Ti_{0.1}Ce_{0.1}Y_{0.1}Yb_{0.1}Sm_{0.1}In_{0.1}Zn_{0.1}O_{2.7}$ (H40) sample has the lowest Debye

length, three times lower than in other compositions. Barium zirconate doped with 1 at% of yttrium yields at 500 °C Debye length equal 0.8 nm, as reported by Shirpour et al.[169].

In Figure 6.51c, the space charge layer widths λ^* for all studied samples are presented. Their temperature dependencies vary between the samples. In most of them, the SCL width narrows at higher temperatures, but, e.g. for H20 in dry conditions, λ^* increases with temperature. In the case of H38 and H20 materials, the SCL width is larger in humidified air than in dry air. Additionally, in H40, these space charge layer in humid air are twice lower than in the other two samples. It might be influenced by the high oxygen vacancy concentration around the grain boundary in this sample. Chen et al. found that the width of the space charge layer around the grain boundary is reduced by the increased acceptor substitution[168]. With the use of λ^*, it is possible to estimate the thickness of the grain boundary $\delta_{GB} \approx 2\lambda^*$ (assuming the negligible contribution of the grain boundary core). According to values of δ_{GB} gathered by Chen et al., which are between 4 to 8 nm, grain boundary thicknesses in the studied multicomponent oxides are comparable to the ones found in acceptor doped $BaZrO_{3-\delta}$[168]. By confronting those values with grain sizes observed in SEM images one can conclude that space charge zone around grain boundary occupy one hundredth of the grain.

In Figure 6.51d, estimated relative permittivities in considered samples are displayed. The ε_r values exhibit weak dependence on temperature, but considering humidity, each sample behaves differently. In H20, relative permittivity increases in the wet atmosphere; in H38 decreases, while in H40, the change is hardly visible. The most noticeable observation is that ε_r for H38 is three times higher than in other samples. In acceptor-doped BZOs, the value of relative permittivity ranges from 40 to 120, depending on the amount of the acceptor and the method of the synthesis[168]. These values are in good agreement with ε_r acquired for H20 and H40. High dielectric permittivity in high entropy perovskites was reported for $Ba(Zr,Hf,Sn,Ti,Me)O_3$ (where Me = Ta, Nb) by Zhou et al.[177].

Overall, based on the established parameters from the SCL model, H40 exhibits smaller depletion zones around grain boundaries. In the case of decreased grain boundary conductivity in wet atmosphere for H20, it is suggested that protonic defects accumulate at the grain boundaries, contributing to the space charge layer. This SCL build-up could be increased by the presence of nickel trapping centers at grain boundaries because of the addition of sintering aid after the perovskite phase formation. Nevertheless, as concluded by Loureiro et al., even after the introduction of sintering aid before the phase formation, nickel ions were found evenly distributed throughout grains and grain boundaries[92]. Also, the values from Figure 6.51 do not indicate that SCL in H20 is more significant than in other samples. However, grains in H20 (Figure 6.26) are significantly smaller than in H38/H40 thus space charge's influence on conductivity could be more impactful.

6.7.4 *Electrical conductivity – oxygen and water vapor partial pressure dependence*

The chosen sample, $BaZr_{0.1}Hf_{0.1}Sn_{0.1}Ti_{0.1}Ce_{0.1}Y_{0.1}Yb_{0.1}Sm_{0.1}In_{0.1}Zn_{0.1}O_{2.7}$ (H40), was subjected to electrical measurements performed in fixed temperature with the change of oxygen partial pressure. The atmosphere ranged from pure oxygen (pO_2 = 1 atm) to pure nitrogen ($pO_2 \approx 10^{-6}$ atm). The model for fitting data is based on the elementary expression for the total electrical conductivity expressed by Equation 3.1. The following assumptions can be introduced for oxides that are oxygen deficient i.e. acceptor substituted:

- in dry atmosphere, the total conductivity is a sum of oxygen ionic σ_O and electron-hole σ_h conductivity:

$$\sigma_{tot} = \sigma_O + \sigma_h. \tag{6.22}$$

- the chemical reaction that takes place is oxidation/reduction of oxygen:

$$\frac{1}{2}O_2 + V_O^{\bullet\bullet} \leftrightarrow O_O^x + 2h^{\bullet}, \tag{6.23}$$

with the following reaction constant:

$$K_{ox} = \frac{[O_O^x][h^{\bullet}]^2}{[V_O^{\bullet\bullet}]pO_2^{1/2}} = \exp\left(\frac{\Delta S_{ox}}{R}\right)\exp\left(-\frac{\Delta H_{ox}}{RT}\right), \tag{6.24}$$

where ΔS_{ox} and ΔH_{ox} are entropy and enthalpy of oxidation, respectively. The mobility of electron-holes is described as:

$$\mu_h = \frac{\mu_h^0}{T}\exp\left(-\frac{\Delta H_{m,h}}{RT}\right), \tag{6.25}$$

where μ_h^0 is a pre-exponential factor of electron-hole mobility and $\Delta H_{m,h}$ is the enthalpy of electron-hole mobility. Using Equations 3.1, 6.24, and 6.25 one can obtain the expression for hole conductivity:

$$\sigma_h = Fd_m\frac{1}{T}[V_O^{\bullet\bullet}]^{1/2}pO_2^{1/4}[O_O^x]^{-1/2}\mu_h^0\exp\left(\frac{\Delta S_{ox}}{2R}\right)\exp\left(-\frac{\Delta H_{m,h}+\frac{1}{2}\Delta H_{ox}}{RT}\right), \tag{6.26}$$

where F is Faraday constant, d_m is molar density (for H40, it is equal to 0.021 mol/cm^3), R is gas constant. The oxygen ionic conductivity is assumed to be constant in the fitting and is equal to the total ionic conductivity in dry atmospheres: $\sigma_O = \sigma_{ion}$.

In wet atmospheres, three charge carriers - electron holes, oxygen vacancies and proton defects – are involved in the conduction process:

$$\sigma_{tot} = \sigma_O + \sigma_h + \sigma_{OH}. \tag{6.27}$$

where σ_{OH} is proton conductivity. Equation 6.26 is applicable for the electron-hole conductivity, while proton and oxygen ionic conductivities contribute to the sample's overall ionic conductivity. The results of conductivity measurements with the fitted model, according to Equations 6.22 and 6.27, are presented in Figure 6.52.

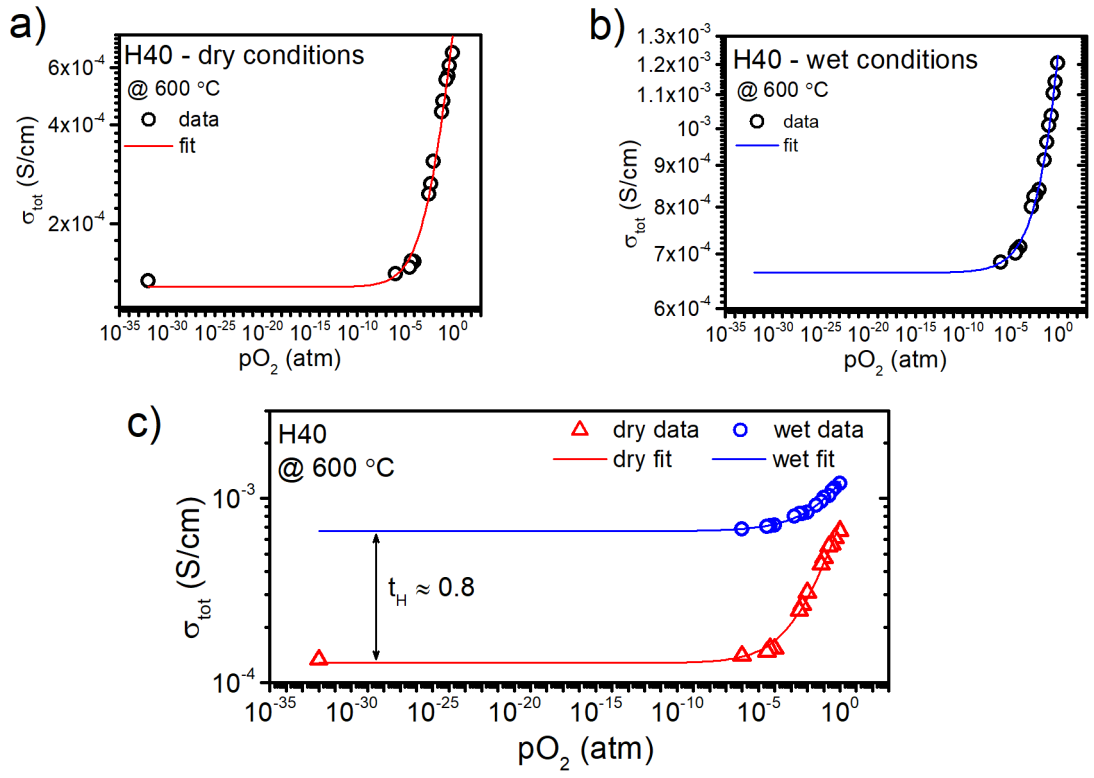

Figure 6.52 Conductivity of $BaZr_{0.1}Hf_{0.1}Sn_{0.1}Ti_{0.1}Ce_{0.1}Y_{0.1}Yb_{0.1}Sm_{0.1}In_{0.1}Zn_{0.1}O_{2.7}$ as a function of oxygen partial pressure measured at 600 °C in a) dry atmosphere, b) wet atmosphere, c) conductivities in different humidities.

As can be seen in Figure 6.52, the assumed model is in good agreement with the obtained data. The values obtained from the fitting of both curves are listed in Table 6.22. The first fitted parameter was the oxygen vacancy concentration. The value obtained in dry conditions coincides with the nominal concentration of oxygen vacancies in H40 resulting from the acceptor concentration. The reduced concentration of $V_O^{\bullet\bullet}$ in a humid atmosphere is likely attributable to the incorporation of protonic defects, as described in Equation 6.6. The values of $\mu_h^0 \exp\left(\frac{\Delta S_{ox}}{2R}\right)$ are similar in dry and wet air. It might be caused by the comparable oxidation entropy at different water partial pressures The variable 'Slope' is a parameterized exponent of pO_2 dependence of conductivity, and both in dry and wet conditions, it is close to the slope of 0.25. This confirms the adopted defect chemistry model, where $\sigma_h \approx pO_2^{1/4}$. The sum of electron-hole mobility and oxidation enthalpies is not changing after the introduction of water vapor during the measurements. Assuming that $\Delta H_{ox} = \Delta H_{f,V_O^{\bullet\bullet}}$, and knowing the enthalpy of oxygen vacancy formation for H40 from Table 6.17, it is possible to estimate the migration enthalpy of electron holes $\Delta H_{m,h}$. The enthalpy of electron-hole mobility is equal to 0.77 eV, which is one order of magnitude higher than 0.06 eV obtained for $BaZr_{0.9}Y_{0.1}O_{3-\delta}$ by Tsvetkov et al.[178]. Estimated values of ionic conductivity in dry and wet atmospheres for H40 are more than one order of magnitude lower than σ_{ion}, which we obtained for $BaCe_{0.6}Zr_{0.2}Y_{0.2}O_{3-\delta}$ in comparable temperature and gas conditions[179]. From the obtained ionic conductivities, it is possible to estimate the transfer number for protons, expressed as follows:

$$t_{OH} = \frac{\sigma_{ion}^{WET} - \sigma_{ion}^{DRY}}{\sigma_{ion}^{WET}}. \quad (6.28)$$

The transport number was estimated within the assumption that the ionic conductivity of oxygen ions does not change in dry and wet air, so this number should be treated only as a rough approximation. In $BaZr_{0.1}Hf_{0.1}Sn_{0.1}Ti_{0.1}Ce_{0.1}Y_{0.1}Yb_{0.1}Sm_{0.1}In_{0.1}Zn_{0.1}O_{2.7}$ (H40), the transfer number for protons at 600 °C is approximately 0.8, as indicated in Figure 6.52c. This result is lower than the value of $t_{OH} = 0.95$ reported by Heras-Juaristi et al. for $BaZr_{0.7}Ce_{0.2}Y_{0.1}O_{3-\delta}$ in wet nitrogen at the same temperature[180]. Nevertheless, the results show that the contribution of proton conduction in H40 is significant even at a high temperature of 600 °C.

Table 6.22 Parameters of $BaZr_{0.1}Hf_{0.1}Sn_{0.1}Ti_{0.1}Ce_{0.1}Y_{0.1}Yb_{0.1}Sm_{0.1}In_{0.1}Zn_{0.1}O_{2.7}$ derived from the fitting of conductivity data as a function of pO_2, according to Equation 6.22 or 6.27.

Fit parameter	Dry conditions	Wet conditions
$[V_O^{\bullet\bullet}]$ (mol/mol)	0.102	0.08
$\mu_h^0 exp(\Delta S_{oxy}/2R)$ (cm^2K/Vs)	100.54	92.98
Slope	0.29	0.24
$\Delta H_{m,h} + \frac{1}{2}\Delta H_{ox}$ (eV)	0.88	0.88
σ_{ion} (S/cm)	1.3×10^{-4}	6.6×10^{-4}

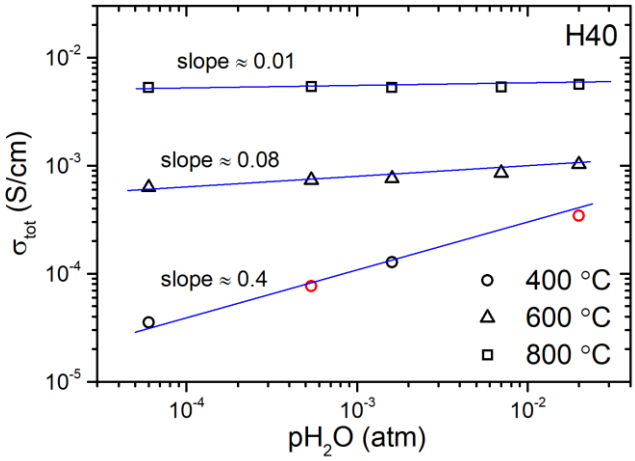

Figure 6.53 Conductivity of $BaZr_{0.1}Hf_{0.1}Sn_{0.1}Ti_{0.1}Ce_{0.1}Y_{0.1}Yb_{0.1}Sm_{0.1}In_{0.1}Zn_{0.1}O_{2.7}$ as a function of water partial pressure measured at different temperatures in air (Red points are estimated values).

The electrical conductivity of H40 as a function of water partial pressure at different temperatures, is presented in Figure 6.53. The measurements were performed in the air. The proton conductivity depends on the concentration of proton defects, which, according to Equation 6.4, is dependent on the water partial pressure:

$$\sigma_{OH} \propto [OH_O^{\bullet}] \propto pH_2O^{1/2}. \quad (6.29)$$

As can be seen, at 800 °C, there is no visible change in electrical conductivity due to the low concentration of proton defects at this temperature. With the decrease of the temperature, the concentration of protons increases, which results in a more significant change in electrical conductivity as a function of pH_2O. Figure 6.53 shows a linear function of log σ_{tot}(log pH_2O), and the slope increases with decreasing temperature. Concerning Equation 6.29, the slope value at 400 °C is close to the expected value of 0.5.

6.7.5 Electrical conductivity relaxation

6.7.5.1 Oxygen Diffusion

During the measurements of electrical conductivity as a function of pO_2, for the H40 sample, it was possible to record the impedance change during the gas switches. The real part of the impedance was recalculated to the electrical conductivity and normalized in a way that would be used according to Equations 5.14 and 5.11. The exemplary conductivity relaxation curve in the reduction step is presented in Figure 6.54. One exponential curve was observed, which indicates a sufficiently rapid gas exchange in the measurement chamber. The data derived from fitted relaxation curves are displayed in Figure 6.55. The values of pO_2 on the X-axis were estimated as an average of initial and final oxygen partial pressure in selected conductivity relaxation experiments. In some cases, it was possible to determine both ionic transport parameters, whereas in others, only one and the rest of the data was unphysical.

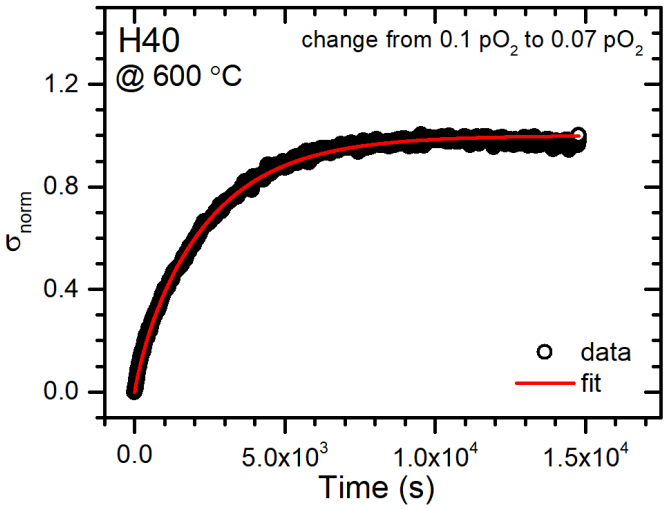

Figure 6.54 Exemplary electrical conductivity relaxation curve for $BaZr_{0.1}Hf_{0.1}Sn_{0.1}Ti_{0.1}Ce_{0.1}Y_{0.1}Yb_{0.1}Sm_{0.1}In_{0.1}Zn_{0.1}O_{2.7}$ during the change of the atmosphere from 0.1 pO_2 to 0.07 pO_2 at 600 °C.

In Figure 6.55a, the chemical oxygen surface exchange coefficients as a function of oxygen partial pressure in dry and wet gas are shown. The values of k^O_{chem} ranges from 10^{-4} to 10^{-3} cm/s in the studied pO_2 range. Also, there is a significant change in the type of dependence after the introduction of water into the system. In dry atmospheres, the chemical surface exchange coefficient oxygen partial pressure dependence is not monotonic. In a wet atmosphere and higher oxygen partial pressures the surface exchange coefficient for oxygen ions is three times lower than in dry. At lower pO_2, k^O_{chem} values are comparable in dry and wet gas. Unlike in dry atmosphere, in wet gas the k^O_{chem} increases with decreasing pO_2. This may be related to the increasing concentration of oxygen vacancies and a larger number of catalytic centers at lower pO_2. Lim et al. reported the chemical surface exchange coefficients in hydrated atmospheres ($pH_2O \sim 10^{-3}$ atm) for many perovskites-based barium cerate-zirconates[181–183]. They found that at 700°C in oxidizing conditions, the $BaCe_{0.85}Y_{0.15}O_{3-\delta}$, $BaZr_{0.2}Ce_{0.65}Y_{0.15}O_{3-\delta}$ and $BaZr_{0.6}Ce_{0.25}Y_{0.15}O_{3-\delta}$ materials reach k^O_{chem} in the

range of 10^{-3}-3 × 10^{-3} cm/s[181], 6 × 10^{-5}-2×10^{-4} cm/s[182] and 3 × 10^{-6}-5×10^{-6} cm/s[183] respectively. As can be seen, the obtained k^O_{chem} for multicomponent oxide studied in this thesis are closer to values exhibited by barium cerate than barium zirconate. Interestingly, Lim et al. observed that in compositions with more cerium than zirconium, the chemical surface exchange coefficient increases with the decrease of oxygen partial pressure whereas in perovskites with the majority of zirconium in the B-sublattice, k^O_{chem} decreases with the decrease of pO_2.

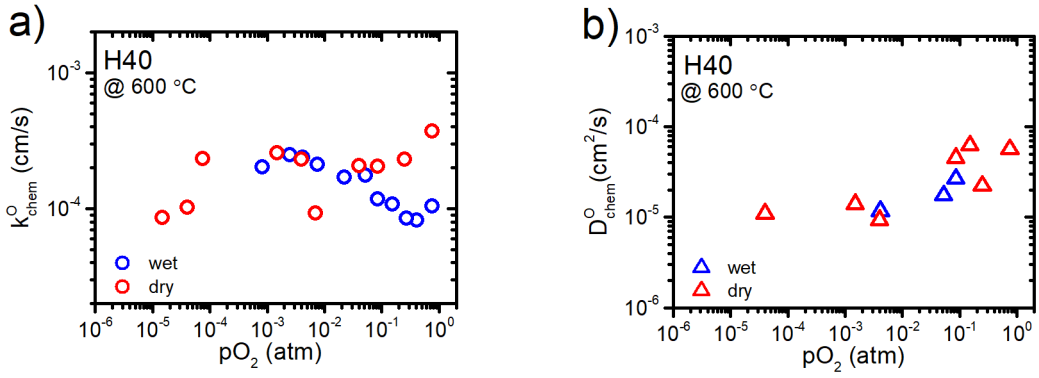

Figure 6.55 a) Surface exchange coefficient, b) diffusion coefficient for oxygen ions in $BaZr_{0.1}Hf_{0.1}Sn_{0.1}Ti_{0.1}Ce_{0.1}Y_{0.1}Yb_{0.1}Sm_{0.1}In_{0.1}Zn_{0.1}O_{2.7}$ as a function of oxygen partial pressure in dry and humidified conditions.

Figure 6.55b presents the chemical oxygen diffusion coefficients as a function of oxygen partial pressure at different pH_2O. The values of D^O_{chem} range from 10^{-5} to 10^{-4} cm^2/s in the studied pO_2 range. There is no change in oxygen diffusion coefficients in humidified atmospheres. This may indicate that in the presence of proton defects in the structure, the chemical diffusion of oxygen atoms does not change. Moreover, in both dry and wet conditions, D^O_{chem} slightly decreases with the decrease in oxygen partial pressure. Lim et al. also reported values of the oxygen diffusion coefficient in the same conditions as previously mentioned. According to $D^O_{chem}(T)$ functions proposed by Lim et al.[181–183], the chemical oxygen diffusion coefficients for reduction in $BaCe_{0.85}Y_{0.15}O_{3-\delta}$, $BaZr_{0.2}Ce_{0.65}Y_{0.15}O_{3-\delta}$ and $BaZr_{0.6}Ce_{0.25}Y_{0.15}O_{3-\delta}$ at 600 °C could be expected to reach values 1.1×10^{-5} cm^2/s, 5×10^{-7} cm^2/s and 2.6×10^{-8} cm^2/s, respectively. In comparison to values obtained in this work, the H40 exhibits higher values of D^O_{chem} in similar measuring conditions.

6.7.5.2 Water Diffusion

Similarly to pO_2 measurements, it was possible to observe the electrical conductivity relaxation upon water partial pressure changes in H40. A single diffusion coefficient typically characterizes the diffusion of water in solids. In this case, an ambipolar diffusion of $2H^+$ and O^{2-} can be observed. Consequently, the electrical conductivity behavior following a rapid change in pH_2O, is expected to exhibit a single-step process[184,185]. This is typical behavior of materials with a low electron transfer number. However, rapidly moving protons can independently respond to the chemical potential gradient of water while remaining decoupled from oxygen vacancies. Under these conditions, electroneutrality is maintained through variations in the concentration of electronic charge carriers within the sample. This phenomenon enables the characterization of two distinct diffusion coefficients corresponding to protons and oxygen vacancies[186–188]. Such a behavior was

observed in proton-conducting oxides[183,189]. In Figure 6.56 the exemplary relaxation curves at different temperatures are presented. At 800 °C, the electrical conductivity shows non-monotonic time evolution (Figure 6.56a). At first, the conductivity decreases after switching pH_2O from dry to wet conditions. Then, it reaches a minimum, starts to increase and at some point, achieves a stable value at the steady state. This behavior is caused by the decoupled transport of protons and oxygen ions. At the start, the mobile protons are incorporated into the material. Later, the oxidation/reduction reaction dominates, increasing σ_{tot}. This two-fold relaxation kinetics is visible at high temperatures when the electron-hole concentration is non-negligible[190]. On the other hand, at lower temperatures, the conductivity change is monotonic, as presented in Figure 6.56b. As can be seen, the single-fold type diffusion occurs in the studied H40 sample at 400 °C. After the increase of water partial pressure, the conductivity increases. At lower temperatures, the concentration of electron holes is low. Thus, a hydration reaction is dominant[191]. The diffusion coefficient of water could be estimated using the same approach as that used for oxygen ions. Only the values of kinetic parameters for single-fold diffusions were derived. For the curve in Figure 6.56b, the k_{chem}^{OH} was equal to 2.1×10^{-7} cm/s, whereas, the D_{chem}^{OH} was 1.2×10^{-8} cm^2/s. These values are one order of magnitude lower than the coefficients in $Ba_{0.9}La_{0.1}Zr_{0.25}Sn_{0.25}In_{0.5}O_{3-\delta}$ reported by Skubida et al.[190] and two orders of magnitude lower than in $BaCe_{0.9}Y_{0.1}O_{3-\delta}$ reported by Kreuer, for the same temperature[192].

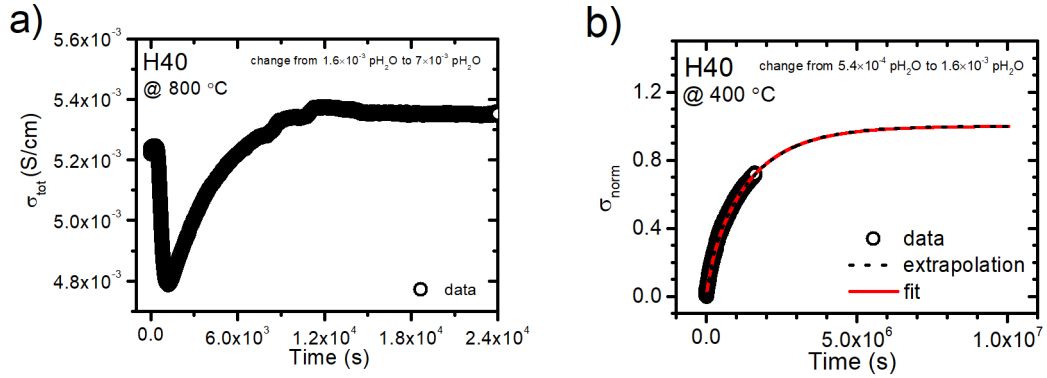

Figure 6.56 Exemplary electrical conductivity relaxation curves for $BaZr_{0.1}Hf_{0.1}Sn_{0.1}Ti_{0.1}Ce_{0.1}Y_{0.1}Yb_{0.1}Sm_{0.1}In_{0.1}Zn_{0.1}O_{2.7}$ during the change of the pH_2O a) at 800 °C, b) at 400 °C.

7. CONCLUSIONS

Within this thesis, five 5B cation perovskite oxides $BaZr_{0.2}Hf_{0.2}Sn_{0.2}Ti_{0.2}B_{0.2}O_{3-\delta}$ - (where B = Ce, Y, Yb, In and Sm), $BaZr_{0.125}Hf_{0.125}Sn_{0.125}Ti_{0.125}Y_{0.125}Yb_{0.125}Sm_{0.125}In_{0.125}O_{2.75}$ and $BaZr_{0.1}Hf_{0.1}Sn_{0.1}Ti_{0.1}Ce_{0.1}Y_{0.1}Yb_{0.1}Sm_{0.1}In_{0.1}Zn_{0.1}O_{2.7}$ were successfully synthesized and examined. The studies of the materials with different numbers of B-cations were focused on the structural, thermal and electrical properties. Special attention was paid to the proton, oxygen-ionic and electronic conductivity of the oxides. The research results may be summed up by the following conclusions.

The solid-state synthesis method proved to be appropriate to obtain single-phase or almost single-phase multicomponent oxides. The presence of a very small amount of TiO_2, Y_2O_3 or Yb_2O_3 detected by XRD and EDS in some samples was assumed insignificant and explained as a result of barium evaporation. The relative density of $BaZr_{0.2}Hf_{0.2}Sn_{0.2}Ti_{0.2}Ce_{0.2}O_{3-\delta}$, $BaZr_{0.125}Hf_{0.125}Sn_{0.125}Ti_{0.125}Y_{0.125}Yb_{0.125}Sm_{0.125}In_{0.125}O_{2.75}$ and $BaZr_{0.1}Hf_{0.1}Sn_{0.1}Ti_{0.1}Ce_{0.1}Y_{0.1}Yb_{0.1}Sm_{0.1}In_{0.1}Zn_{0.1}O_{2.7}$ was between 91 and 99% without sintering aids, while the other ceramics required using 1 wt% of NiO to achieve a high density. Additionally, 10-B sample reach high relative density at 1150 °C, thanks to high zinc content. The samples with high relative densities comprised large crystallites forming larger grains and showed a lower microstrain.

Multicomponent cubic perovskites with a Goldschmidt tolerance factor between 0.98 and 1.02 were obtained. Unit cell parameters of the perovskites, between 4.15 and 4.26 Å, followed the Vegard rule and were consistent with the average B-cation radii. The average long-term order of crystal structures of the studied oxides was demonstrated by well-resolved XRD patterns. On the other hand, the short-range disorder was indicated by the XAS results. The length of the B cation – oxygen bonds was found to depend on the B cation kind. The Ti-O bonds were shorter than the Zr-O, Hf-O, Sn-O, Y-O, Yb-O and In-O bonds. Moreover, the results suggested that titanium was present both in 4+ and 3+ valence states.

The multicomponent perovskites were thermodynamically stable, with a negative formation enthalpy of about -100 kJ/mol in 5-B cation perovskites and about -60 kJ/mol for eight and 10-B cation perovskites. These values are comparable to those typical of barium zirconate. Thus, the perovskites studied in this work do not belong to the group of entropy-stabilized oxides. Moreover, the values of the entropy metric show that only $BaZr_{0.125}Hf_{0.125}Sn_{0.125}Ti_{0.125}Y_{0.125}Yb_{0.125}Sm_{0.125}In_{0.125}O_{2.75}$ and $BaZr_{0.1}Hf_{0.1}Sn_{0.1}Ti_{0.1}Ce_{0.1}Y_{0.1}Yb_{0.1}Sm_{0.1}In_{0.1}Zn_{0.1}O_{2.7}$ are high-entropy oxides. The perovskites containing 5 B-cations are medium entropy oxides.

Thermal expansion coefficients of multicomponent oxides were between 8.15 and 11 × 10^{-6} 1/K. The higher TEC values were found for $BaZr_{0.125}Hf_{0.125}Sn_{0.125}Ti_{0.125}Y_{0.125}Yb_{0.125}Sm_{0.125}In_{0.125}O_{2.75}$ and $BaZr_{0.1}Hf_{0.1}Sn_{0.1}Ti_{0.1}Ce_{0.1}Y_{0.1}Yb_{0.1}Sm_{0.1}In_{0.1}Zn_{0.1}O_{2.7}$. This may be related to a less negative formation enthalpy and higher cation-oxygen bond lengths, signifying weaker bonds in these materials. Nevertheless, achieved values of TEC for multicomponent oxides are similar to those reported for barium zirconates/cerates, which suggests that these materials could be used in a similar application as the reference materials.

All studied perovskites undergo the hydration reaction that utilize the oxygen vacancies. In a hydrated state, the unit cells expand as a result of proton defect formation. Higher chemical expansion corresponded to higher proton defect contents. Proton defect concentration depends on the acceptor content. Even $BaZr_{0.2}Hf_{0.2}Sn_{0.2}Ti_{0.2}Ce_{0.2}O_{3-\delta}$ hydrated thanks to the presence of Ce^{3+} acting as an intrinsic acceptor. With the increase in acceptor concentration the proton concentration was also rising, reaching a maximum value of 0.21 mol/mol for $BaZr_{0.1}Hf_{0.1}Sn_{0.1}Ti_{0.1}Ce_{0.1}Y_{0.1}Yb_{0.1}Sm_{0.1}In_{0.1}Zn_{0.1}O_{2.7}$ at 300 °C in nitrogen atmosphere. In the case of the 5B-samples, it was found that the radius of the acceptor is important for water uptake. Smaller elements (like In) are more favorable for proton defect formation than larger elements (like Sm), which was confirmed by thermodynamic parameters of hydration. The thermodynamic parameters of hydration of the synthesized materials were more negative in high temperatures (between -72 and -110 kJ/mol) than in lower temperatures (between -15 and -60 kJ/mol). It was proposed that at higher temperatures hydration is more favorable since the proton concentration is low. In comparison to the $Ba(Ce,Zr)O_3$ materials, multicomponent oxides exhibit more preferable, nearly twofold lower, enthalpies of hydration. Despite this, the proton concentrations achieved by the HEO samples were much lower. This could indicate the clustering of oxygen vacancies, making them “inactive” in the hydration process.

The multicomponent perovskites exhibit mixed electron-hole and oxygen ionic conductivity following classical oxidation/reduction reactions. $BaZr_{0.2}Hf_{0.2}Sn_{0.2}Ti_{0.2}Ce_{0.2}O_{3-\delta}$ have the lowest electrical conductivity in the whole temperature range, while $BaZr_{0.1}Hf_{0.1}Sn_{0.1}Ti_{0.1}Ce_{0.1}Y_{0.1}Yb_{0.1}Sm_{0.1}In_{0.1}Zn_{0.1}O_{2.7}$ have the highest conductivity in high temperatures and $BaZr_{0.2}Hf_{0.2}Sn_{0.2}Ti_{0.2}Sm_{0.2}O_{2.9}$ have the highest conductivity in lower temperatures. This shows that the amount and the type of acceptor constituents have an influence on the level and temperature dependence of electrical conductivity. However, the electrical conductivity values of acceptor-doped materials were found to be lower by one order of magnitude than that of barium zirconates and two orders of magnitude than barium cerates. Estimated enthalpy values of oxygen vacancy formation and mobility indicate that 8B and 10B samples form $V_O^{\bullet\bullet}$ easier than 5B samples but oxygen ion motion is hindered. It is not clear if it is caused by the presence of more distorted cation lattice or the higher concentration of oxygen vacancies. The presence of proton conduction in all acceptor-doped compounds was confirmed by their higher electrical conductivity in wet conditions. The proton conductivity in the $BaZr_{0.2}Hf_{0.2}Sn_{0.2}Ti_{0.2}In_{0.2}O_{2.9}$, $BaZr_{0.125}Hf_{0.125}Sn_{0.125}Ti_{0.125}Y_{0.125}Yb_{0.125}Sm_{0.125}In_{0.125}O_{2.75}$ and $BaZr_{0.1}Hf_{0.1}Sn_{0.1}Ti_{0.1}Ce_{0.1}Y_{0.1}Yb_{0.1}Sm_{0.1}In_{0.1}Zn_{0.1}O_{2.7}$ was further confirmed by the isotope effect consistent with the semiclassical model. The grain boundaries turned out to be blocking for the charge carriers, which is also a feature of acceptor-doped barium zirconates. For $BaZr_{0.2}Hf_{0.2}Sn_{0.2}Ti_{0.2}Yb_{0.2}O_{2.9}$ it was found that smaller grains and the presence of nickel defects Ni_B'' have a negative impact on the grain boundary conductivity in humidified conditions.

Very interesting results were obtained in the studies of oxygen and water diffusion in $BaZr_{0.1}Hf_{0.1}Sn_{0.1}Ti_{0.1}Ce_{0.1}Y_{0.1}Yb_{0.1}Sm_{0.1}In_{0.1}Zn_{0.1}O_{2.7}$. The values of D_{chem}^{O} (10^{-5} to 10^{-4} cm^2/s) found

in dry and humidified atmospheres mean that the oxygen chemical diffusion is much faster than in yttrium-doped barium zirconate-cerate solid solutions. Interestingly, this shows that oxygen diffuses more easily through the vacancy mechanism in a more "disordered" structure. In the case of water diffusion, at high temperatures takes place two-fold transport of charge carriers and at lower temperatures the transport of protons and oxygen ions is coupled, resulting in single-fold diffusion. Estimated value of proton diffusion at 400 °C is two orders of magnitude lower than in yttrium-doped barium cerate indicating negative influence of distorted cation lattice on proton transport.

Author assures that this thesis was created in high entropy conditions, in order to preserve the established subject matter fully.

8. LIST OF FIGURES

Figure 2.1 a) The evolution of the XRD pattern depending on the temperature of synthesis and the reversibility phenomenon, b) the phase change signal from the DSC[15]. 26
Figure 2.2 SEM images of $(Zr,Hf,Sn,Ti,Ce)O_2$ a) after synthesis at 1500 °C, b) after annealing at 1100 °C, c) after reheating at 1500 °C[17]..... 28
Figure 2.3 a) Measured hardness of HEO fluorites and reference compounds, b) thermal conductivity values for HEO fluorites and 8YSZ[18]..... 28
Figure 2.4 a) Full range and b) magnified fragment of HTXRD patterns of $Gd_{0.2}La_{0.2}Nd_{0.2}Sm_{0.2}Y_{0.2}MnO_3$[22]. 29
Figure 2.5 Temperature dependence of total conductivity in a) dry and b) wet air for $(Dy_{1-x}Ca_x)_2(Zr_{0.2}Hf_{0.2}Sn_{0.2}\ Ti_{0.2}Ge_{0.2})_2O_7$ with x = 0, 0.05 and 0.1[26]. 30
Figure 2.6 A depiction of the $A_6B_2O_{17}$ disordered structure looking down the c-axis (A) along with a key for A (Zr, Hf), B (Nb, Ta) and oxygen atoms (B). A depiction of the polyhedra in the $A_6B_2O_{17}$ structure looking down the a-axis (C), and the c-axis (D) along with a key for the different types of polyhedron present (E): 1– a six- coordinated distorted octahedron, 2– a seven coordinated capped trigonal prism and 3– an eight-coordinated distorted bicapped trigonal prism[28]..... 31
Figure 2.7 Total conductivity of a) $Hf_6Nb_2O_{17}$ and b) $Hf_6Ta_2O_{17}$ at 600, 700 and 800 °C as a function of oxygen partial pressure[30]. 32
Figure 3.1 The proton defect formation and migration in the ABO_3 perovskite structure[46]. 36
Figure 4.1 Exemplary unit cell of ABX_3 perovskite, simulated in VESTA[51]. 38
Figure 4.2 Possible arrangement of BX_6 octahedra in perovskites: a) untilted, b) tilted in the same phase, c) tilted in opposite phase[57]. 40
Figure 4.3 Electrical conductivity of $BaCe_{1-x}Ln_xO_{3-\delta}$ materials at 600 °C in wet air[58]. 40
Figure 4.4 Total electrical conductivity and activation energy for conduction of $BaZr_{1-x}Y_xO_{3-\delta}$ in dry air[66]. 41
Figure 4.5 Influence of increasing Zr content on the total electrical conductivity in a) $BaCe_{0.9-x}Zr_xY_{0.1}O_{3-\delta}$, b) $BaCe_{0.8-x}Zr_xY_{0.2}O_{3-\delta}$ in wet air[67,68]. 42
Figure 4.6 The temperature dependences of conductivity for $BaCe_{0.5}Zr_{0.3}Ln_{0.2}O_{3-\delta}$ ceramics in different atmospheres: a) Ln = Yb, b) Ln = Y, c) Ln = Gd, d) Ln = Sm, e) Ln = Nd and f) Ln = La[69]. 42
Figure 5.1 L_3 edge of platinum metal with marked two distinctive parts of XAS spectra[80]. 45
Figure 5.2 Schematic of twin-Calvet calorimeter used in high-temperature drop calorimetry[84]. ... 49
Figure 5.3 Examples of samples with a) 2-probe configuration and b) 4-probe configuration. 51
Figure 6.1 XRD patterns of synthesized multicomponent oxides and the $BaZrO_3$ reference. 55
Figure 6.2 A magnified fragment of the XRD patterns showing small reflections of non-reacted oxides. 56
Figure 6.3 Diffractogram of $BaZr_{0.2}Hf_{0.2}Sn_{0.2}Ti_{0.2}Ce_{0.2}O_{3-\delta}$ (H1) with Rietveld refinement results, performed in HighScore Plus software using the pseudo Voigt profile function. 57

Figure 6.4 The lattice parameter values obtained from Rietveld refinement of synthesized samples as a function of average B-site radii. 58
Figure 6.5 Microstructure parameters derived from Rietveld refinement, plotted as a function of average B-site radii (a, b) and relative density (c, d). 59
Figure 6.6 The lattice parameter expansion from HT-XRD measurements for dried and hydrated samples: a) $BaZr_{0.2}Hf_{0.2}Sn_{0.2}Ti_{0.2}Ce_{0.2}O_{3-\delta}$, b) $BaZr_{0.1}Hf_{0.1}Sn_{0.1}Ti_{0.1}Ce_{0.1}Y_{0.1}Yb_{0.1}Sm_{0.1}In_{0.1}Zn_{0.1}O_{2.7}$. 60
Figure 6.7 The lattice parameter evolution with temperature in all multicomponent samples: a) dried, b) hydrated. 61
Figure 6.8 Thermal expansion coefficients of dried HEO samples, obtained from HT-XRD in the high-temperature range, as a function of average B-site radius. 62
Figure 6.9 Relative elongation of multicomponent oxide pellets during cooling. 62
Figure 6.10 Thermal expansion coefficients of HEO samples, obtained from dilatometry measurements in high temperatures, as a function of average B-site radius. 63
Figure 6.11 Comparison of thermal expansion coefficients obtained based on the dilatometry and HTXRD analyses. 64
Figure 6.12 a) Absorption spectra in all examined samples for Ba-L_3 edge, with offset, b) close up around the edge, without offset. 65
Figure 6.13 a) Absorption spectra in H2 and H22 samples for Zr-K edge, with offset, b) close up around the edge, without offset. 66
Figure 6.14 a) Absorption spectra in all samples for Hf-L_3 edge, with offset, b) close up around the edge, without offset. 67
Figure 6.15 a) Absorption spectra in H2 and H22 samples for Sn-K edge, with offset, b) close up around the edge, without offset. 68
Figure 6.16 a) Absorption spectra in all samples for Ti-K edge, with offset, b) XANES region with all main features marked, c) close up around the pre-edge region, without offset, d) close up around the edge, without offset. 69
Figure 6.17 a) Absorption spectra in H2 sample for Y-K edge, with offset, b) close up around the edge, without offset. 70
Figure 6.18 a) Absorption spectra in H20 sample for Yb-L_3 edge, b) close up around the edge. 70
Figure 6.19 a) Absorption spectra in H25, H38 and H40 samples for Sm-L_3 edge, with offset, b) close up around the edge, without offset. 71
Figure 6.20 a) Absorption spectra in H22 sample for In-K edge, b) close up around the edge. 71
Figure 6.21 The comparison of M-O lengths for different HEO samples: a) Ba-O, b) Hf-O, c) Ti-O, d) Sm-O. 73
Figure 6.22 The average metal-oxygen bond length as a function of the theoretical metal-oxygen distance. 75
Figure 6.23 SEM images of morphology of the a) $BaZr_{0.2}Hf_{0.2}Sn_{0.2}Ti_{0.2}In_{0.2}O_{2.9}$ (H22), b) $BaZr_{0.2}Hf_{0.2}Sn_{0.2}Ti_{0.2}Sm_{0.2}O_{2.9}$ (H25) samples prepared without the sintering aid. 75

Figure 6.24 The SEM images of the cross section of $BaZr_{0.2}Hf_{0.2}Sn_{0.2}Ti_{0.2}Ce_{0.2}O_{3-\delta}$ (H1) sample, based on a) secondary electrons, b) back-scattered electrons. 76
Figure 6.25 The SEM images of the cross-section of $BaZr_{0.2}Hf_{0.2}Sn_{0.2}Ti_{0.2}Y_{0.2}O_{2.9}$ (H2) sample, based on a) secondary electrons, b) back-scattered electrons. 76
Figure 6.26 The SEM images of the cross section of $BaZr_{0.2}Hf_{0.2}Sn_{0.2}Ti_{0.2}Yb_{0.2}O_{2.9}$ (H20) sample, based on a) secondary electrons, b) back-scattered electrons. 77
Figure 6.27 The SEM images of the cross section of $BaZr_{0.2}Hf_{0.2}Sn_{0.2}Ti_{0.2}In_{0.2}O_{2.9}$ (H22) sample, based on a) secondary electrons, b) back-scattered electrons. 77
Figure 6.28 The SEM images of the cross-section of $BaZr_{0.2}Hf_{0.2}Sn_{0.2}Ti_{0.2}Sm_{0.2}O_{2.9}$ (H25) sample, based on a) secondary electrons, b) back-scattered electrons. 78
Figure 6.29 The SEM images of the cross section of $BaZr_{0.125}Hf_{0.125}Sn_{0.125}Ti_{0.125}Y_{0.125}Yb_{0.125}Sm_{0.125}In_{0.125}O_{2.75}$ (H38) sample, based on a) secondary electrons, b) back-scattered electrons. 78
Figure 6.30 The SEM images of the cross-section of the H40 sample, based on a) secondary electrons b) back-scattered electrons. 79
Figure 6.31 The exemplary EDS spectrum for $BaZr_{0.2}Hf_{0.2}Sn_{0.2}Ti_{0.2}In_{0.2}O_{2.9}$ (H22). 79
Figure 6.32 The area selected for EDS analysis in $BaZr_{0.2}Hf_{0.2}Sn_{0.2}Ti_{0.2}Ce_{0.2}O_{3-\delta}$ (H1) and maps obtained for each consisting element. 80
Figure 6.33 The area selected for EDS analysis in $BaZr_{0.2}Hf_{0.2}Sn_{0.2}Ti_{0.2}Y_{0.2}O_{2.9}$ (H2) and maps obtained for each consisting element. 81
Figure 6.34 The area selected for EDS analysis in $BaZr_{0.2}Hf_{0.2}Sn_{0.2}Ti_{0.2}Yb_{0.2}O_{2.9}$ (H20) and maps obtained for each consisting element. 81
Figure 6.35 The area selected for EDS analysis in $BaZr_{0.2}Hf_{0.2}Sn_{0.2}Ti_{0.2}In_{0.2}O_{2.9}$ (H22) and maps obtained for each consisting element. 82
Figure 6.36 The area selected for EDS analysis in $BaZr_{0.2}Hf_{0.2}Sn_{0.2}Ti_{0.2}Sm_{0.2}O_{2.9}$ (H25) and maps obtained for each consisting element. 83
Figure 6.37 The area selected for EDS analysis in $BaZr_{0.125}Hf_{0.125}Sn_{0.125}Ti_{0.125}Y_{0.125}Yb_{0.125}Sm_{0.125}In_{0.125}O_{2.75}$ (H38) and maps obtained for each consisting element. 84
Figure 6.38 The area selected for EDS analysis in $BaZr_{0.1}Hf_{0.1}Sn_{0.1}Ti_{0.1}Ce_{0.1}Y_{0.1}Yb_{0.1}Sm_{0.1}In_{0.1}Zn_{0.1}O_{2.7}$ (H40) and maps obtained for each consisting element. 85
Figure 6.39 XRD pattern with Rietveld analysis for HfO_2 substrate. 86
Figure 6.40 Isothermal thermograms of a) $BaZr_{0.2}Hf_{0.2}Sn_{0.2}Ti_{0.2}Ce_{0.2}O_{3-\delta}$ (H1) and b) $BaZr_{0.1}Hf_{0.1}Sn_{0.1}Ti_{0.1}Ce_{0.1}Y_{0.1}Yb_{0.1}Sm_{0.1}In_{0.1}Zn_{0.1}O_{2.7}$ (H40), recorded at 300 °C after the isothermal switch between dry and humidified air. 87
Figure 6.41 Proton defect concentration as a function of average B-cation radii in 5B multicomponent oxides. 88
Figure 6.42 The weight change during isobaric thermogravimetry measurement for $BaZr_{0.1}Hf_{0.1}Sn_{0.1}Ti_{0.1}Ce_{0.1}Y_{0.1}Yb_{0.1}Sm_{0.1}In_{0.1}Zn_{0.1}O_{2.7}$ (H40). 89

Figure 6.43 a) Hydration reaction equilibrium constant calculated from Equation 6.7, b) temperature dependence of proton defect concentration, c) influence of different intrinsic acceptor concentration on hydration coefficient in $BaZr_{0.2}Hf_{0.2}Sn_{0.2}Ti_{0.2}Ce_{0.2}O_{3-\delta}$ (H1). 90
Figure 6.44 Hydration parameters of multicomponent perovskites, separated into temperature regions. 92
Figure 6.45 Enthalpies of formation for synthesized samples as a function of a) average B-site radii, b) Entropy Metrics 94
Figure 6.46 Different Nyquist plots obtained during the measurements. 95
Figure 6.47 The temperature dependence of total conductivities of all samples in dry air. 95
Figure 6.48 Total conductivities of synthesized samples in dry and humidified air. 100
Figure 6.49 The total conductivity in dry, H_2O- and D_2O-humidified air for a) $BaZr_{0.2}Hf_{0.2}Sn_{0.2}Ti_{0.2}In_{0.2}O_{2.9}$, b) $BaZr_{0.125}Hf_{0.125}Sn_{0.125}Ti_{0.125}Y_{0.125}Yb_{0.125}Sm_{0.125}In_{0.125}O_{2.75}$, c) $BaZr_{0.1}Hf_{0.1}Sn_{0.1}Ti_{0.1}Ce_{0.1}Y_{0.1}Yb_{0.1}Sm_{0.1}In_{0.1}Zn_{0.1}O_{2.7}$, d) the ratio between conductivities measured at H_2O and D_2O conditions (dashed line indicate the 2 value). 101
Figure 6.50 The grain and specific grain boundary conductivity for a,b) $BaZr_{0.2}Hf_{0.2}Sn_{0.2}Ti_{0.2}Yb_{0.2}O_{2.9}$, c,d) $BaZr_{0.125}Hf_{0.125}Sn_{0.125}Ti_{0.125}Y_{0.125}Yb_{0.125}Sm_{0.125}In_{0.125}O_{2.75}$, e,f) $BaZr_{0.1}Hf_{0.1}Sn_{0.1}Ti_{0.1}Ce_{0.1}Y_{0.1}Yb_{0.1}Sm_{0.1}In_{0.1}Zn_{0.1}O_{2.7}$, measured in different atmospheres. 103
Figure 6.51 The characteristic values describing grain boundaries in selected samples, derived from SCL model: a) the charge potential at the grain boundary, b) Debye length, c) space charge layer thickness, d) relative permittivity. 105
Figure 6.52 Conductivity of $BaZr_{0.1}Hf_{0.1}Sn_{0.1}Ti_{0.1}Ce_{0.1}Y_{0.1}Yb_{0.1}Sm_{0.1}In_{0.1}Zn_{0.1}O_{2.7}$ as a function of oxygen partial pressure measured at 600 °C in a) dry atmosphere, b) wet atmosphere, c) conductivities in different humidities. 108
Figure 6.53 Conductivity of $BaZr_{0.1}Hf_{0.1}Sn_{0.1}Ti_{0.1}Ce_{0.1}Y_{0.1}Yb_{0.1}Sm_{0.1}In_{0.1}Zn_{0.1}O_{2.7}$ as a function of water partial pressure measured at different temperatures in air (Red points are estimated values). 109
Figure 6.54 Exemplary electrical conductivity relaxation curve for $BaZr_{0.1}Hf_{0.1}Sn_{0.1}Ti_{0.1}Ce_{0.1}Y_{0.1}Yb_{0.1}Sm_{0.1}In_{0.1}Zn_{0.1}O_{2.7}$ during the change of the atmosphere from 0.1 pO_2 to 0.07 pO_2 at 600 °C. 110
Figure 6.55 a) Surface exchange coefficient, b) diffusion coefficient for oxygen ions in $BaZr_{0.1}Hf_{0.1}Sn_{0.1}Ti_{0.1}Ce_{0.1}Y_{0.1}Yb_{0.1}Sm_{0.1}In_{0.1}Zn_{0.1}O_{2.7}$ as a function of oxygen partial pressure in dry and humidified conditions. 111
Figure 6.56 Exemplary electrical conductivity relaxation curves for $BaZr_{0.1}Hf_{0.1}Sn_{0.1}Ti_{0.1}Ce_{0.1}Y_{0.1}Yb_{0.1}Sm_{0.1}In_{0.1}Zn_{0.1}O_{2.7}$ during the change of the pH_2O a) at 800 °C, b) at 400 °C. 112

9. LIST OF TABLES

Table 2.1 Quantification of entropy and new entropy metric; $\sum_{SL} a_{SL}$ is the number of atoms per formula unit and $5M, 5N$ are 5 different elements in given sublattice (reproduction from[32]). 33
Table 4.1 Goldschmidt factor values and crystal structure of selected perovskite oxides. 39
Table 6.1 Compositions, labels, Goldschmidt tolerance parameters, Entropy Metrics and the synthesis temperatures of multicomponent perovskite oxides 54
Table 6.2 Data derived from Rietveld analysis for all samples with obtained agreement indices. 57
Table 6.3 Apparent and relative density values for composition pellets sintered with and without sintering aid. 58
Table 6.4 Thermal expansion coefficients obtained from HT-XRD measurements for all synthesized samples. 61
Table 6.5 Thermal expansion coefficients obtained from dilatometry measurements for all synthesized samples. 63
Table 6.6 Positions of absorption maxima for all HEO samples and the reference with calculated crystal field split. 67
Table 6.7 The M-O bond lengths in HEO samples for the core matrix elements. 72
Table 6.8 The M-O bond lengths in HEO samples for the other constituent elements. 72
Table 6.9 The lattice parameters derived from Rietveld refinement and X-ray absorption spectroscopy for H2 and H22 samples. 74
Table 6.10 The atomic concentration of elements derived from the EDS analysis. 86
Table 6.11 Proton defect concentration of synthesized high-entropy oxides at 300 °C. 88
Table 6.12 Hydration energetics of studied high entropy oxides. 91
Table 6.13 Thermodynamic cycle used for calculation of formation enthalpy of $BaZr_{0.2}Hf_{0.2}Sn_{0.2}Ti_{0.2}Ce_{0.2}O_{3-\delta}$. 93
Table 6.14 Drop solution enthalpies of binary oxides in $3Na2O \cdot 4MoO3$ solvent at 800 °C. 93
Table 6.15 Enthalpies of drop solution and formation obtained for multicomponent oxides. 94
Table 6.16 Conductivities in dry air at 600 °C and activation energies of the conductivity for multicomponent oxides. 96
Table 6.17 The enthalpies of mobility and oxidation estimated based on activation energies of conduction 98
Table 6.18 Conductivities in humidified air at 600 °C and activation energies of the conductivity for studied multicomponent oxides. 100
Table 6.19 Conductivities at 600 °C and activation energies of the conductivity for samples selected for measurements in D_2O-humidified air. 101
Table 6.20 Characteristic conductivity values describing isotope effect in selected samples. 102
Table 6.21 Grain and specific grain boundary conductivities at 600 °C and activation energies of the conductivity for selected samples measured in different atmospheres. 103
Table 6.22 Parameters of $BaZr_{0.1}Hf_{0.1}Sn_{0.1}Ti_{0.1}Ce_{0.1}Y_{0.1}Yb_{0.1}Sm_{0.1}In_{0.1}Zn_{0.1}O_{2.7}$ derived from the fitting of conductivity data as a function of pO_2, according to Equation 6.22 or 6.27. 109

BIBLIOGRAPHY

1. Murty, B. S., Yeh, J.-W. & Ranganathan, S. *High-Entropy Alloys*. (Elsevier Inc, Londres, 2014).
2. Cantor, B., Chang, I. T. H., Knight, P. & Vincent, A. J. B. Microstructural development in equiatomic multicomponent alloys. *Materials Science and Engineering: A* **375–377**, 213–218 (2004).
3. Ranganathan, S. Alloyed pleasures: Multimetallic cocktails. *CURRENT SCIENCE* **85**, 3 (2003).
4. Yeh, J.-W. *et al.* Nanostructured High-Entropy Alloys with Multiple Principal Elements: Novel Alloy Design Concepts and Outcomes. *Adv. Eng. Mater.* **6**, 299–303 (2004).
5. Pogrebnjak, A. D., Bagdasaryan, A. A., Yakushchenko, I. V. & Beresnev, V. M. The structure and properties of high-entropy alloys and nitride coatings based on them. *Russ. Chem. Rev.* **83**, 1027–1061 (2014).
6. Sarkar, A. *et al.* High-Entropy Oxides: Fundamental Aspects and Electrochemical Properties. *Adv. Mater.* **31**, 1806236 (2019).
7. Moskovskikh, D. *et al.* Extremely hard and tough high entropy nitride ceramics. *Sci Rep* **10**, 19874 (2020).
8. Wang, Z., Li, Z.-T., Zhao, S.-J. & Wu, Z.-G. High-entropy carbide ceramics: a perspective review. *Tungsten* **3**, 131–142 (2021).
9. Zhang, Y. *et al.* Dense high-entropy boride ceramics with ultra-high hardness. *Scripta Materialia* **164**, 135–139 (2019).
10. Mohammadi, A. *et al.* High-entropy hydrides for fast and reversible hydrogen storage at room temperature: Binding-energy engineering via first-principles calculations and experiments. *Acta Materialia* **236**, 118117 (2022).
11. Qin, Y. *et al.* A high entropy silicide by reactive spark plasma sintering. *J Adv Ceram* **8**, 148–152 (2019).
12. Cui, M. *et al.* High-Entropy Metal Sulfide Nanoparticles Promise High-Performance Oxygen Evolution Reaction. *Advanced Energy Materials* **11**, 2002887 (2021).
13. Wang, T., Chen, H., Yang, Z., Liang, J. & Dai, S. High-Entropy Perovskite Fluorides: A New Platform for Oxygen Evolution Catalysis. *J. Am. Chem. Soc.* **142**, 4550–4554 (2020).
14. Navrotsky, A. & Kleppa, O. J. Thermodynamics of formation of simple spinels. *Journal of Inorganic and Nuclear Chemistry* **30**, 479–498 (1968).

15. Rost, C. M. *et al.* Entropy-stabilized oxides. *Nat Commun* **6**, 8485 (2015).

16. Bérardan, D., Franger, S., Dragoe, D., Meena, A. K. & Dragoe, N. Colossal dielectric constant in high entropy oxides. *Phys. Status Solidi RRL* **10**, 328–333 (2016).

17. Chen, K. *et al.* A five-component entropy-stabilized fluorite oxide. *Journal of the European Ceramic Society* **38**, 4161–4164 (2018).

18. Gild, J. *et al.* High-entropy fluorite oxides. *Journal of the European Ceramic Society* **38**, 3578–3584 (2018).

19. Dąbrowa, J. *et al.* Synthesis and microstructure of the (Co,Cr,Fe,Mn,Ni) 3 O 4 high entropy oxide characterized by spinel structure. *Materials Letters* **216**, 32–36 (2018).

20. Mao, A. *et al.* A new class of spinel high-entropy oxides with controllable magnetic properties. *Journal of Magnetism and Magnetic Materials* **497**, 165884 (2020).

21. Jiang, S. *et al.* A new class of high-entropy perovskite oxides. *Scripta Materialia* **142**, 116–120 (2018).

22. Sarkar, A. *et al.* Rare earth and transition metal based entropy stabilised perovskite type oxides. *Journal of the European Ceramic Society* **38**, 2318–2327 (2018).

23. Yang, Q. *et al.* A high-entropy perovskite cathode for solid oxide fuel cells. *Journal of Alloys and Compounds* **872**, 159633 (2021).

24. Dąbrowa, J. *et al.* Structure and transport properties of the novel (Dy,Er,Gd,Ho,Y)3Fe5O12 and (Dy,Gd,Ho,Sm,Y)3Fe5O12 high entropy garnets. *Journal of the European Ceramic Society* **41**, 3844–3849 (2021).

25. Vayer, F., Decorse, C., Bérardan, D. & Dragoe, N. New entropy-stabilized oxide with pyrochlore structure: Dy2(Ti0.2Zr0.2Hf0.2Ge0.2Sn0.2)2O7. *Journal of Alloys and Compounds* **883**, 160773 (2021).

26. Miruszewski, T. *et al.* High-temperature transport properties of entropy-stabilized pyrochlores. *Journal of Applied Physics* **135**, 085112 (2024).

27. Roth, R. S. & Coughanour, L. W. Phase equilibrium relations in the systems titania-niobia and zirconia-niobia. *J. RES. NATL. BUR. STAN.* **55**, 209 (1955).

28. Voskanyan, A. A., Lilova, K., McCormack, S. J., Kriven, W. M. & Navrotsky, A. A new class of entropy stabilized oxides: Commensurately modulated A6B2O17 (A = Zr, Hf; B = Nb, Ta) structures. *Scripta Materialia* **204**, 114139 (2021).

29. Kleger, A. & Meunier, V. Density functional theory study of the structural, electronic, mechanical, and thermal properties of Hf6Ta2O17. *Materials Today Communications* **34**, 105065 (2023).

30. Miruszewski, T. *et al.* Charge Transport in the $A_6 B_2 O_{17}$ (A = Zr, Hf; B = Nb, Ta) Superstructure Series. *J. Electrochem. Soc.* **171**, 034503 (2024).

31. Swalin, R. A. *Thermodynamics of Solids*. (J. Wiley, New York, 1972).

32. Dippo, O. F. & Vecchio, K. S. A universal configurational entropy metric for high-entropy materials. *Scripta Materialia* **201**, 113974 (2021).

33. Kofstad, P. & Norby, T. *Defects and Transport in Crystalline Solids*. (University of Oslo, 2007).

34. Gellings, P. J. *The CRC Handbook of SOLID STATE Electrochemistry*. (CRC Press, 2019). doi:10.1201/9780429121791.

35. Ishihara, T., Sammes, N. M. & Yamamoto, O. Chapter 4 - Electrolytes. in *High Temperature and Solid Oxide Fuel Cells* (eds. Singhal, S. C. & Kendall, K.) 83–117 (Elsevier Science, Amsterdam, 2003). doi:https://doi.org/10.1016/B978-185617387-2/50021-0.

36. Swift, M., Janotti, A. & Van de Walle, C. G. Small polarons and point defects in barium cerate. *Phys. Rev. B* **92**, 214114 (2015).

37. F. Krok & W. Bogusz. *Elektrolity stałe*. (Wydawnictwo Naukowo-Techniczne, Warszawa, 1995).

38. Forrat, F., Dauge, G., Trevoux, P., Danner, G. & Christen, M. Electrolyte solide à base de AlLaO3. Application aux piles à combustible. *Comptes Rendus de l'Académie des Sciences* 2813–2816 (1964).

39. Stotz, S. & Wagner, C. Die Löslichkeit von Wasserdampf und Wasserstoff in festen Oxiden. *Ber Bunsenges Phys Chem* **70**, 781–788 (1966).

40. Takahashi, T. & Iwahara, H. Solid-state ionics: protonic conduction in perovskite type oxide solid solutions. (1980).

41. Tu, C.-S., Chien, R. R., Schmidt, V. H., Lee, S. C. & Huang, C.-C. Temperature-dependent structures of proton-conducting $Ba(Zr_{0.8-x}Ce_xY_{0.2})O_{2.9}$ ceramics by Raman scattering and x-ray diffraction. *J. Phys.: Condens. Matter* **24**, 155403 (2012).

42. Slodczyk, A. *et al.* Structural modifications induced by free protons in proton conducting perovskite zirconate membrane. *Solid State Ionics* **225**, 214–218 (2012).

43. Norby, T. & Larring, Y. Concentration and transport of protons in oxides. *Current Opinion in Solid State and Materials Science* **2**, 593–599 (1997).

44. Norby, T. Solid-state protonic conductors: principles, properties, progress and prospects. *Solid State Ionics* **125**, 1–11 (1999).

45. Kröger, F. A. & Vink, H. J. Relations between the Concentrations of Imperfections in Crystalline Solids. in *Solid State Physics* vol. 3 307–435 (Elsevier, 1956).

46. Kochetova, N., Animitsa, I., Medvedev, D., Demin, A. & Tsiakaras, P. Recent activity in the development of proton-conducting oxides for high-temperature applications. *RSC Adv.* **6**, 73222–73268 (2016).

47. Hibino, T., Mizutani, K., Yajima, T. & Iwahara, H. Characterization of proton in Y-doped SrZr03 polycrystal by IR spectroscopy.

48. Goldschmidt, V. M. Die Gesetze der Krystallochemie. *Naturwissenschaften* **14**, 477–485 (1926).

49. Megaw, H. D. Crystal Structure of Barium Titanate. *Nature* **155**, 484–485 (1945).

50. *Perovskite Oxide for Solid Oxide Fuel Cells*. (Springer US, Boston, MA, 2009). doi:10.1007/978-0-387-77708-5.

51. Momma, K. & Izumi, F. *VESTA 3* for three-dimensional visualization of crystal, volumetric and morphology data. *J Appl Crystallogr* **44**, 1272–1276 (2011).

52. Sebastian, M. Chapter Six. ABO3 Type Perovskites. in *Dielectric Materials for Wireless Communication* 161–203 (2008). doi:10.1016/B978-0-08-045330-9.00006-6.

53. Davies, R. Dopant and proton incorporation in perovskite-type zirconates. *Solid State Ionics* **126**, 323–335 (1999).

54. Gomez, M. A., Griffin, M. A., Jindal, S., Rule, K. D. & Cooper, V. R. The effect of octahedral tilting on proton binding sites and transition states in pseudo-cubic perovskite oxides. *The Journal of Chemical Physics* **123**, 094703 (2005).

55. Bévillon, É., Chesnaud, A., Wang, Y., Dezanneau, G. & Geneste, G. Theoretical and experimental study of the structural, dynamical and dielectric properties of perovskite $BaSnO_3$. *J. Phys.: Condens. Matter* **20**, 145217 (2008).

56. Maekawa, T., Kurosaki, K. & Yamanaka, S. Thermal and mechanical properties of perovskite-type barium hafnate. *Journal of Alloys and Compounds* **407**, 44–48 (2006).

57. Glazer, A. M. The classification of tilted octahedra in perovskites. *Acta Crystallogr B Struct Crystallogr Cryst Chem* **28**, 3384–3392 (1972).

58. Medvedev, D. *et al.* BaCeO3: Materials development, properties and application. *Progress in Materials Science* **60**, 72–129 (2014).

59. Ohzeki, T., Hasegawa, S., Shimizu, M. & Hashimoto, T. Analysis of phase transition behavior of BaCeO3 with thermal analyses and high temperature X-ray diffraction. *Solid State Ionics* **180**, 1034–1039 (2009).

60. Yamaguchi, S. Thermal lattice expansion behavior of Yb-doped BaCeO3. *Solid State Ionics* **162–163**, 23–29 (2003).

61. Akbarzadeh, A. R., Kornev, I., Malibert, C., Bellaiche, L. & Kiat, J. M. Combined theoretical and experimental study of the low-temperature properties of BaZrO 3. *Phys. Rev. B* **72**, 205104 (2005).

62. Bi, L. & Traversa, E. Synthesis strategies for improving the performance of doped-$BaZrO_3$ materials in solid oxide fuel cell applications. *J. Mater. Res.* **29**, 1–15 (2014).

63. Lyagaeva, Yu. G. *et al.* Specific features of preparation of dense ceramic based on barium zirconate. *Semiconductors* **48**, 1353–1358 (2014).

64. Park, K.-Y. *et al.* Enhanced proton conductivity of yttrium-doped barium zirconate with sinterability in protonic ceramic fuel cells. *Journal of Alloys and Compounds* **639**, 435–444 (2015).

65. Medvedev, D. A., Murashkina, A. A. & Demin, A. K. Formation of dense electrolytes based on BaCeO3 and BaZrO3 for application in solid oxide fuel cells: The role of solid-state reactive sintering. *Ref. J. Chem.* **5**, 193–214 (2015).

66. Kuz'min, A. V., Balakireva, V. B., Plaksin, S. V. & Gorelov, V. P. Total and hole conductivity in the BaZr1 − x Y x O3 − α system (x = 0.02−0.20) in oxidizing atmosphere. *Russ J Electrochem* **45**, 1351–1357 (2009).

67. Katahira, K., Kohchi, Y., Shimura, T. & Iwahara, H. Protonic conduction in Zr-substituted BaCeO3. *Solid State Ionics* **138**, 91–98 (2000).

68. Fabbri, E., Depifanio, A., Dibartolomeo, E., Licoccia, S. & Traversa, E. Tailoring the chemical stability of Ba(Ce0.8−xZrx)Y0.2O3−δ protonic conductors for Intermediate Temperature Solid Oxide Fuel Cells (IT-SOFCs). *Solid State Ionics* **179**, 558–564 (2008).

69. Lyagaeva, J. *et al.* Acceptor doping effects on microstructure, thermal and electrical properties of proton-conducting BaCe0.5Zr0.3Ln0.2O3−δ (Ln = Yb, Gd, Sm, Nd, La or Y) ceramics for solid oxide fuel cell applications. *Electrochimica Acta* **192**, 80–88 (2016).

70. Fu, Z. & Roosen, A. Shrinkage of Tape Cast Products During Binder Burnout. *J. Am. Ceram. Soc.* **98**, 20–29 (2015).

71. Liu, Y., Yang, L., Liu, M., Tang, Z. & Liu, M. Enhanced sinterability of BaZr0.1Ce0.7Y0.1Yb0.1O3−δ by addition of nickel oxide. *Journal of Power Sources* **196**, 9980–9984 (2011).

72. Degen, T., Sadki, M., Bron, E., König, U. & Nénert, G. The HighScore suite. *Powder Diffr.* **29**, S13–S18 (2014).

73. Hunkel, M., Surm, H. & Steinbacher, M. Dilatometry. in *Handbook of Thermal Analysis and Calorimetry* vol. 6 103–129 (Elsevier, 2018).

74. Dzierzgowski, K., Wachowski, S., Łapiński, M., Mielewczyk-Gryń, A. & Gazda, M. Praseodymium Orthoniobate and Praseodymium Substituted Lanthanum Orthoniobate: Electrical and Structural Properties. *Materials* **15**, 2267 (2022).

75. Babilo, P. & Haile, S. M. Enhanced Sintering of Yttrium-Doped Barium Zirconate by Addition of ZnO. *J American Ceramic Society* **88**, 2362–2368 (2005).

76. Surzhikov, A. P., Frangulyan, T. S. & Ghyngazov, S. A. A thermoanalysis of phase transformations and linear shrinkage kinetics of ceramics made from ultrafine plasmochemical ZrO2(Y)–Al2O3 powders. *J Therm Anal Calorim* **115**, 1439–1445 (2014).

77. Goupil, G., Delahaye, T., Gauthier, G., Sala, B. & Joud, F. L. Stability study of possible air electrode materials for proton conducting electrochemical cells. *Solid State Ionics* **209–210**, 36–42 (2012).

78. Kozlovskii, Yu. M. & Stankus, S. V. Thermal expansion of beryllium oxide in the temperature interval 20–1550°C. *High Temp* **52**, 536–540 (2014).

79. Groot, F. de & Kotani, A. *Core Level Spectroscopy of Solids*. (CRC Press, Boca Raton, 2008).

80. Bare, S. R. XANES Measurements and Interpretation. (2003).

81. Meschel, S. V. & Nash, P. *HIGH-TEMPERATURE DROP CALORIMETRY*. (2012).

82. Razouk, R., Beaumont, O., Hameury, J. & Hay, B. Towards accurate measurements of specific heat of solids by drop calorimetry up to 3000 °C. *Thermal Science and Engineering Progress* **26**, 101130 (2021).

83. Navrotsky, A. Progress and new directions in high temperature calorimetry revisited. *Physics and Chemistry of Minerals* **24**, 222–241 (1997).

84. Navrotsky, A. Progress and New Directions in Calorimetry: A 2014 Perspective. *J. Am. Ceram. Soc.* **97**, 3349–3359 (2014).

85. Bruggeman, D. A. G. Berechnung verschiedener physikalischer Konstanten von heterogenen Substanzen. I. Dielektrizitätskonstanten und Leitfähigkeiten der Mischkörper aus isotropen Substanzen. *Annalen der Physik* **416**, 636–664 (1935).

86. Pal, R. On the Electrical Conductivity of Particulate Composites. *Journal of Composite Materials* **41**, 2499–2511 (2007).

87. Haile, S. M., West, D. L. & Campbell, J. The role of microstructure and processing on the proton conducting properties of gadolinium-doped barium cerate. *J. Mater. Res.* **13**, 1576–1595 (1998).

88. Ciucci, F. Electrical conductivity relaxation measurements: Statistical investigations using sensitivity analysis, optimal experimental design and ECRTOOLS. *Solid State Ionics* **239**, 28–40 (2013).

89. Crank, J. *The Mathematics of Diffusion*. (Clarendon Press, Oxford, 1976).

90. den Otter, M. W., Bouwmeester, H. J. M., Boukamp, B. A. & Verweij, H. Reactor Flush Time Correction in Relaxation Experiments. *J. Electrochem. Soc.* **148**, J1 (2001).

91. Abernathy, H., Yang, T., Liu, J. & Na, B. NETL Electrical Conductivity Relaxation(ECR) Analysis Tool. (2021) doi:10.18141/1762415.

92. Loureiro, F. J. A., Nasani, N., Reddy, G. S., Munirathnam, N. R. & Fagg, D. P. A review on sintering technology of proton conducting BaCeO3-BaZrO3 perovskite oxide materials for Protonic Ceramic Fuel Cells. *Journal of Power Sources* **438**, 226991 (2019).

93. Blennow, P., Hansen, K. K., Reine Wallenberg, L. & Mogensen, M. Effects of Sr/Ti-ratio in SrTiO3-based SOFC anodes investigated by the use of cone-shaped electrodes. *Electrochimica Acta* **52**, 1651–1661 (2006).

94. Imashuku, S. *et al.* Dependence of Dopant Cations on Microstructure and Proton Conductivity of Barium Zirconate. *J. Electrochem. Soc.* **156**, B1 (2009).

95. Løken, A., Ricote, S. & Wachowski, S. Thermal and Chemical Expansion in Proton Ceramic Electrolytes and Compatible Electrodes. *Crystals* **8**, 365 (2018).

96. Lyagaeva, Yu. G., Medvedev, D. A., Demin, A. K., Tsiakaras, P. & Reznitskikh, O. G. Thermal expansion of materials in the barium cerate-zirconate system. *Phys. Solid State* **57**, 285–289 (2015).

97. Han, D., Shinoda, K. & Uda, T. Dopant Site Occupancy and Chemical Expansion in Rare Earth-Doped Barium Zirconate. *J. Am. Ceram. Soc.* **97**, 643–650 (2014).

98. Kreuer, K. D. Proton-Conducting Oxides. *Annu. Rev. Mater. Res.* **33**, 333–359 (2003).

99. Zhu, Z., Tao, Z., Bi, L. & Liu, W. Investigation of SmBaCuCoO5+δ double-perovskite as cathode for proton-conducting solid oxide fuel cells. *Materials Research Bulletin* **45**, 1771–1774 (2010).

100. Yoshii, K. *et al.* Probing the Ba 5d states in BaTiO3 and BaSO4: A resonant x-ray emission study at the Ba-L3 edge. *Journal of Physics and Chemistry of Solids* **73**, 1106–1110 (2012).

101. Ghosez, Ph., Gonze, X. & Michenaud, J.-P. First-principles characterization of the four phases of barium titanate. *Ferroelectrics* **220**, 1–15 (1999).

102. Srwastava, U. & NIGAllf, N. L. X-RAY ABSORPTION EDGE SPE~RO~~RY (XAES) AS APPLIED TO COORDINATION CHEMISTRY.

103. Yoshii, K. *et al.* Electronic structure of BaTiO3 using resonant X-ray emission spectroscopy at the Ba-L3 and Ti-K absorption edges. *Journal of Physics and Chemistry of Solids* **75**, 339–343 (2014).

104. Choy, J.-H., Yoon, J.-B., Jung, H. & Park, J.-H. Zr K-Edge XAS and ^{29} Si MAS NMR Studies on Hexagonal Mesoporous Zirconium Silicate. *Journal of Porous Materials* **11**, 123–129 (2004).

105. Choy, J.-H., Yoon, J.-B. & Park, J.-H. *In situ* XAFS study at the Zr *K* -edge for SiO_2 /ZrO_2 nano-sol. *J Synchrotron Rad* **8**, 782–784 (2001).

106. Jung, H., Paek, S.-M., Yoon, J.-B. & Choy, J.-H. Zr K-edge XAS study on ZrO2-pillared aluminosilicate. *J Porous Mater* **14**, 369–377 (2007).

107. Rothensteiner, M., Bonk, A., Vogt, U. F., Emerich, H. & Van Bokhoven, J. A. Structural Changes in $Ce_{0.5}Zr_{0.5}O_{2-\delta}$ under Temperature-Swing and Isothermal Solar Thermochemical Looping Conditions Determined by in Situ Ce K and Zr K Edge X-ray Absorption Spectroscopy. *J. Phys. Chem. C* **120**, 13931–13941 (2016).

108. Li, P., Chen, I.-W. & Penner-Hahn, J. E. X-ray-absorption studies of zirconia polymorphs. I. Characteristic local structures. *Phys. Rev. B* **48**, 10063–10073 (1993).

109. Hoshino, K. *et al.* Probing Local Environments of Oxygen Vacancies Responsible for Hydration in Sc-Doped Barium Zirconates at Elevated Temperatures: In Situ X-ray Absorption Spectroscopy, Thermogravimetry, and Active Learning Ab Initio Replica Exchange Monte Carlo Simulations. *Chem. Mater.* **35**, 2289–2301 (2023).

110. Liu, Q.-J., Liu, Z.-T., Feng, L.-P. & Tian, H. Mechanical, electronic, chemical bonding and optical properties of cubic BaHfO3: First-principles calculations. *Physica B: Condensed Matter* **405**, 4032–4039 (2010).

111. Morais, J. *et al.* Environment of hafnium and silicon in Hf-based dielectric films: An atomistic study by x-ray absorption spectroscopy and x-ray diffraction. *Applied Physics Letters* **86**, 212906 (2005).

112. Galoisy, L. *et al.* Evidence for 6-Coordinated Zirconium in Inactive Nuclear Waste Glasses. *Journal of the American Ceramic Society* **82**, 2219–2224 (1999).

113. L. Soriano *et al.* The O 1s X-ray absorption spectra of transition-metal oxides: the TiO2-ZrO2-HfO2 and V2O5-Nb2O5-Ta2O5 series. *Solid State Communications* **87**, 699–703 (1993).

114. Wang, M. & Feng, Z. Pitfalls in X-ray absorption spectroscopy analysis and interpretation: A practical guide for general users. *Current Opinion in Electrochemistry* **30**, 100803 (2021).

115. Tongpeng, S., Wannapaiboon, S., Janphuang, P. & Jiansirisomboon, S. Effects of La Doping on Local Structure of Hafnium Oxide Studied by X-Ray Absorption Spectroscopy. *Integrated Ferroelectrics* **238**, 125–135 (2023).

116. Mohamed, A. Y. *et al.* X-ray spectroscopy study on the electronic structure of Sn-added p-type SnO films. *J. Phys.: Condens. Matter* **32**, 065502 (2020).

117. Lützenkirchen-Hecht, D., Scotti, N., Jacobs, H. & Frahm, R. XAFS investigations of tin nitrides. *J Synchrotron Rad* **8**, 698–700 (2001).

118. Caballero, A. & Ocaña, M. Synthesis and Structural Characterization by X-ray Absorption Spectroscopy of Tin-Doped Mullite Solid Solutions. *Journal of the American Ceramic Society* **85**, 1910–1914 (2002).

119. Bootchanont, A. *et al.* Investigation of local structure in BaTiO3–BaZrO3 system by synchrotron X-ray absorption spectroscopy. *Ceramics International* **39**, S579–S582 (2013).

120. A. Balzarotti *et al.* K-edge absorption of titanium in the perovskites SrTiO3, BaTiO3 and TiO2. *Solid State Communications* **35**, 145–149 (1980).

121. Fischer, D. W. X-Ray Band Spectra and Molecular-Orbital Structure of Rutile Ti O 2. *Phys. Rev. B* **5**, 4219–4226 (1972).

122. Groot, F. de. *Core Level Spectroscopy of Solids*. (CRC Press, Boca Raton, 2008).

123. Vedrinskii, R. V., Kraizman, V. L., Novakovich, A. A., Demekhin, P. V. & Urazhdin, S. V. Pre-edge fine structure of the 3d atom K x-ray absorption spectra and quantitative atomic structure determinations for ferroelectric perovskite structure crystals. *J. Phys.: Condens. Matter* **10**, 9561–9580 (1998).

124. Farges, F., Brown, G. E., Navrotsky, A., Gan, H. & Rehr, J. J. Coordination chemistry of Ti(IV) in silicate glasses and melts: II. Glasses at ambient temperature and pressure. *Geochimica et Cosmochimica Acta* **60**, 3039–3053 (1996).

125. Jollet, F., Noguera, C., Gautier, M., Thromat, N. & Duraud, J. Influence of Oxygen Vacancies on the Electronic Structure of Yttrium Oxide. *Journal of the American Ceramic Society* **74**, 358–364 (1991).

126. Longo, A. *et al.* Local Environment of Yttrium in Y-Doped Barium Cerate Compounds. *Chem. Mater.* **18**, 5782–5788 (2006).

127. Felner, I. *et al.* Ytterbium valence phase transition in Yb x In 1 − x Cu 2. *Phys. Rev. B* **35**, 6956–6963 (1987).

128. Asakura, H., Shishido, T., Teramura, K. & Tanaka, T. Local Structure and L_1 - and L_3 -Edge X-ray Absorption Near Edge Structure of Late Lanthanide Elements (Ho, Er, Yb) in Their Complex Oxides. *J. Phys. Chem. C* **119**, 8070–8077 (2015).

129. Asakura, H., Shishido, T., Fuchi, S., Teramura, K. & Tanaka, T. Local Structure of Pr, Nd, and Sm Complex Oxides and Their X-ray Absorption Near Edge Structure Spectra. *J. Phys. Chem. C* **118**, 20881–20888 (2014).

130. Mizumaki, M. *et al.* Determination of the valence in Sm-based filled skutterudite compounds. *Physica B: Condensed Matter* **383**, 144–145 (2006).

131. Proffit, D. E. *et al.* X-ray absorption spectroscopy study of the local structures of crystalline Zn–In–Sn oxide thin films. *Journal of Applied Physics* **106**, 113524 (2009).

132. Blackburn, L. R. *et al.* Underpinning the use of indium as a neutron absorbing additive in zirconolite by X-ray absorption spectroscopy. *Sci Rep* **13**, 9329 (2023).

133. R.D. Shannon. Revised effective ionic radii and systematic studies of interatomic distances in halides and chalcogenides. *Acta Crystallographica Section A* **32**, 751–767 (1976).

134. Moltved, K. A. & Kepp, K. P. The Chemical Bond between Transition Metals and Oxygen: Electronegativity, d-Orbital Effects, and Oxophilicity as Descriptors of Metal–Oxygen Interactions. *J. Phys. Chem. C* **123**, 18432–18444 (2019).

135. Yu-Ran Luo. *Comprehensive Handbook of Chemical Bond Energies*. (CRC Press, Boca Raton, 2007).

136. Leonard, K., Lee, Y.-S., Okuyama, Y., Miyazaki, K. & Matsumoto, H. Influence of dopant levels on the hydration properties of SZCY and BZCY proton conducting ceramics for hydrogen production. *International Journal of Hydrogen Energy* **42**, 3926–3937 (2017).

137. Gonçalves, M. D. *et al.* Systematic Water Uptake Energetics of Yttrium-Doped Barium Zirconate—A High Resolution Thermochemical Study. *J. Phys. Chem. C* **124**, 11308–11316 (2020).

138. Dayaghi, A. M. *et al.* Effects of sintering additives on defect chemistry and hydration of BaZr0.4Ce0.4(Y,Yb)0.2O3−δ proton conducting electrolytes. *Solid State Ionics* **401**, 116355 (2023).

139. Wu, Y., Ren, G., Ding, D., Yang, F. & Pan, S. Study on the cerium oxidation state in a Lu0.8Sc0.2BO3 host. *J. Mater. Chem.* **21**, 17805 (2011).

140. Begg, B. D., Vance, E. R. & Lumpkin, G. R. Charge Compensation and the Incorporation of Cerium in Zirconolite and Perovskite. *MRS Proc.* **506**, 79 (1997).

141. Putilov, L. P. & Tsidilkovski, V. I. Impact of bound ionic defects on the hydration of acceptor-doped proton-conducting perovskites. *Phys. Chem. Chem. Phys.* **21**, 6391–6406 (2019).

142. Gong, W. & Navrotsky, A. Thermodynamics of BaNd2O4 and phase diagram of the BaO–Nd2O3 system. *J. Mater. Res.* **34**, 3337–3342 (2019).

143. Drey, D. L. *et al.* Disorder in $Ho_2 Ti_{2-x} Zr_x O_7$: pyrochlore to defect fluorite solid solution series. *RSC Adv.* **10**, 34632–34650 (2020).

144. Lee, T. A. & Navrotsky, A. Enthalpy of formation of cubic yttria-stabilized hafnia. *J. Mater. Res.* **19**, 1855–1861 (2004).

145. Abramchuk, M., Lilova, K., Subramani, T., Yoo, R. & Navrostky, A. Development of high-temperature oxide melt solution calorimetry for p-block element containing materials – CORRIGENDUM. *Journal of Materials Research* **36**, 785–785 (2021).

146. Hayun, S. & Navrotsky, A. Formation enthalpies and heat capacities of rear earth titanates: RE2TiO5 (RE=La, Nd and Gd). *Journal of Solid State Chemistry* **187**, 70–74 (2012).

147. Mielewczyk-Gryn, A. & Navrotsky, A. Enthalpies of formation of rare earth niobates, $RE_3\ NbO_7$. *American Mineralogist* **100**, 1578–1583 (2015).

148. Qi, J., Guo, X., Mielewczyk-Gryn, A. & Navrotsky, A. Formation enthalpies of LaLn′O3 (Ln′=Ho, Er, Tm and Yb) interlanthanide perovskites. *Journal of Solid State Chemistry* **227**, 150–154 (2015).

149. Subramani, T. *et al.* Surface energetics of wurtzite and sphalerite polymorphs of zinc sulfide and implications for their formation in nature. *Geochimica et Cosmochimica Acta* **340**, 99–107 (2023).

150. McCormack, S. J. & Navrotsky, A. Thermodynamics of high entropy oxides. *Acta Materialia* **202**, 1–21 (2021).

151. Gonçalves, M. D., Maram, P. S., Muccillo, R. & Navrotsky, A. Enthalpy of formation and thermodynamic insights into yttrium doped $BaZrO_3$. *J. Mater. Chem. A* **2**, 17840–17847 (2014).

152. Lindman, A., Erhart, P. & Wahnström, G. Polaronic contributions to oxidation and hole conductivity in acceptor-doped BaZrO 3. *Phys. Rev. B* **94**, 075204 (2016).

153. Rowberg, A. J. E., Li, M., Ogitsu, T. & Varley, J. B. Polarons and electrical leakage in BaZrO 3 and BaCeO 3. *Phys. Rev. Materials* **7**, 015402 (2023).

154. Tsunoda, N., Kumagai, Y. & Oba, F. Stabilization of small polarons in BaTiO 3 by local distortions. *Phys. Rev. Materials* **3**, 114602 (2019).

155. Larramona, G., GutiCrrez, C., Pereira, I. & Nunes, M. R. Characterization of the Mixed Perovskite BaSn,_,Sb,O, by Elect1-01yte Electroreflectance, Diffuse Reflectance, and X-Ray Photoelectron Spectroscopy.

156. Terki, R., Feraoun, H., Bertrand, G. & Aourag, H. Full potential calculation of structural, elastic and electronic properties of $BaZrO_3$ and $SrZrO_3$. *Physica Status Solidi (b)* **242**, 1054–1062 (2005).

157. Vali, R. Lattice dynamics and electronic properties of the scintillator host material: Barium hafnate. *Solid State Communications* **147**, 1–3 (2008).

158. kumari, S., Padalia, D., Kumari, R., Srivastava, S. & Kalra, G. Effect of cerium substitution on structural and optical properties of barium titanate ceramics. *Materials Today: Proceedings* S2214785323031012 (2023) doi:10.1016/j.matpr.2023.05.466.

159. Smyth, D. M. Defect structure in perovskite titanates. *Current Opinion in Solid State and Materials Science* **1**, 692–697 (1996).

160. Badwal, S. P. S. Electrical conductivity of single crystal and polycrystalline yttria-stabilized zirconia. *J Mater Sci* **19**, 1767–1776 (1984).

161. Zhan, Z., Wen, T.-L., Tu, H. & Lu, Z.-Y. AC Impedance Investigation of Samarium-Doped Ceria. *J. Electrochem. Soc.* **148**, A427 (2001).

162. Nowick, A. S. & Vaysleyb, A. V. Isotope effect and proton hopping in high-temperature protonic conductors. *Solid State Ionics* **97**, 17–26 (1997).

163. Bell, R. P. *The Tunnel Effect in Chemistry*. (Springer US, Boston, MA, 1980). doi:10.1007/978-1-4899-2891-7.

164. Scherban, T. Bulk protonic conduction in Yb-doped SrCeO3. *Solid State Ionics* **35**, 189–194 (1989).

165. Liang, K., Du, Y. & Nowick, A. Fast high-temperature proton transport in nonstoichiometric mixed perovskites. *Solid State Ionics* **69**, 117–120 (1994).

166. Liu, J. F. & Nowick, A. S. The incorporation and migration of protons in Nd-doped BaCe03.

167. Irvine, J. T. S., Sinclair, D. C. & West, A. R. Electroceramics: Characterization by Impedance Spectroscopy. *Advanced Materials* **2**, 132–138 (1990).

168. Chen, C.-T., Danel, C. E. & Kim, S. On the origin of the blocking effect of grain-boundaries on proton transport in yttrium-doped barium zirconates. *J. Mater. Chem.* **21**, 5435 (2011).

169. Shirpour, M., Merkle, R., Lin, C. T. & Maier, J. Nonlinear electrical grain boundary properties in proton conducting Y–$BaZrO_3$ supporting the space charge depletion model. *Phys. Chem. Chem. Phys.* **14**, 730–740 (2012).

170. Vollman, M. & Waser, R. Grain Boundary Defect Chemistry of Acceptor-Doped Titanates: Space Charge Layer Width. *Journal of the American Ceramic Society* **77**, 235–243 (1994).

171. Iguchi, F., Chen, C.-T., Yugami, H. & Kim, S. Direct evidence of potential barriers at grain boundaries in Y-doped BaZrO3 from dc-bias dependence measurements. *J. Mater. Chem.* **21**, 16517 (2011).

172. Guo, X. & Maier, J. Grain Boundary Blocking Effect in Zirconia: A Schottky Barrier Analysis. *J. Electrochem. Soc.* **148**, E121 (2001).

173. Iguchi, F., Sata, N. & Yugami, H. Proton transport properties at the grain boundary of barium zirconate based proton conductors for intermediate temperature operating SOFC. *J. Mater. Chem.* **20**, 6265 (2010).

174. Fleig, J. The grain boundary impedance of random microstructures: numerical simulations and implications for the analysis of experimental data. *Solid State Ionics* **150**, 181–193 (2002).

175. De Souza, R. A., Munir, Z. A., Kim, S. & Martin, M. Defect chemistry of grain boundaries in proton-conducting solid oxides. *Solid State Ionics* **196**, 1–8 (2011).

176. Polfus, J. M., Toyoura, K., Oba, F., Tanaka, I. & Haugsrud, R. Defect chemistry of a BaZrO3 Σ3 (111) grain boundary by first principles calculations and space–charge theory. *Phys. Chem. Chem. Phys.* **14**, 12339 (2012).

177. Zhou, S. *et al.* Microstructure and dielectric properties of high entropy Ba(Zr0.2Ti0.2Sn0.2Hf0.2Me0.2)O3 perovskite oxides. *Ceramics International* **46**, 7430–7437 (2020).

178. Tsvetkov, D. S., Ivanov, I. L., Malyshkin, D. A., Sereda, V. V. & Yu. Zuev, A. Red-Ox Energetics and Holes Trapping in Yttrium-Substituted Barium Zirconate $BaZr_{0.9}$ $Y_{0.1}$ $O_{2.95}$. *J. Electrochem. Soc.* **166**, F232–F238 (2019).

179. Miruszewski, T. *et al.* Hebb–Wagner polarization method for determining the oxygen ion conductivity in barium cerate-zirconate. *J. Mater. Chem. A* **10**, 7218–7227 (2022).

180. Heras-Juaristi, G., Pérez-Coll, D. & Mather, G. C. Temperature dependence of partial conductivities of the BaZr 0.7 Ce 0.2 Y 0.1 O 3-δ proton conductor. *Journal of Power Sources* **364**, 52–60 (2017).

181. Lim, D.-K. *et al.* Conductivity Relaxation of Proton-Conducting BaCe0.85Y0.15O3−δ Upon Oxidation and Reduction. *J. Electrochem. Soc.* **158**, B852 (2011).

182. Lim, D.-K., Park, C.-J., Choi, M.-B., Park, C.-N. & Song, S.-J. Partial conductivities of mixed conducting BaCe0.65Zr0.2Y0.15O3–δ. *International Journal of Hydrogen Energy* **35**, 10624–10629 (2010).

183. Lim, D.-K., Im, H.-N., Jeon, S.-Y., Park, J.-Y. & Song, S.-J. Experimental evidence of hydrogen–oxygen decoupled diffusion into BaZr0.6Ce0.25Y0.15O3−δ. *Acta Materialia* **61**, 1274–1283 (2013).

184. Wagner, C. & Schottky, W. Theorie der geordneten Mischphasen. *Z. Phys. Chem. B* **11**, 163–210 (1930).

185. Kreuer, K., Schonherr, E. & Maier, J. Proton and oxygen diffusion in BaCeO3 based compounds: A combined thermal gravimetric analysis and conductivity study. *Solid State Ionics* **70–71**, 278–284 (1994).

186. Yoo, H.-I., Yoon, J.-Y., Ha, J.-S. & Lee, C.-E. Hydration and oxidation kinetics of a proton conductor oxide, $SrCe_{0.95}Yb_{0.05}O_{2.975}$. *Phys. Chem. Chem. Phys.* **10**, 974–982 (2008).

187. Yu, J. H., Lee, J. & Maier, J. Peculiar Nonmonotonic Water Incorporation in Oxides Detected by Local In Situ Optical Absorption Spectroscopy. *Angew Chem Int Ed* **46**, 8992–8994 (2007).

188. Yu, J.-H., Lee, J.-S. & Maier, J. Water incorporation in oxides: A moving boundary problem. *Solid State Ionics* **181**, 154–162 (2010).

189. Yoo, H.-I., Yeon, J. I. & Kim, J.-K. Mass relaxation vs. electrical conductivity relaxation of a proton conducting oxide upon hydration and dehydration. *Solid State Ionics* **180**, 1443–1447 (2009).

190. Skubida, W., Niemczyk, A., Zheng, K., Liu, X. & Świeczek, K. Crystal Structure, Hydration, and Two-Fold/Single-Fold Diffusion Kinetics in Proton-Conducting Ba0.9La0.1Zr0.25Sn0.25In0.5O3−a Oxide. *Crystals* **8**, 136 (2018).

191. Kim, E. & Yoo, H.-I. Two-fold -to-single-fold transition of the conductivity relaxation patterns of proton-conducting oxides upon hydration/dehydration. *Solid State Ionics* **252**, 132–139 (2013).

192. Kreuer, K. D. Aspects of the formation and mobility of protonic charge carriers and the stability of perovskite-type oxides. *Solid State Ionics* **125**, 285–302 (1999).